THE UNIVERSITY *of* EDINBURGH

Advancing our Understanding of Lipid Bilayer Interactions: A Molecular Dynamics Study

Matthew Carr

Doctor of Philosophy
The University of Edinburgh
March 2015

Abstract

In recent years, advances in computer architecture and lipid force field parameters have made Molecular Dynamics (MD) a powerful tool for gaining atomistic resolution of biological membranes on timescales that other tools simply cannot explore. With many key biological processes involving membranes occurring on the nanosecond timescale, MD allows us to probe the dynamics and energetics of these interactions in molecular detail. Specifically, we can observe the interactions taking place as a peptide or protein comes into contact with a lipid bilayer, and how this may shape or alter the bilayer either locally (changes in headgroup orientation, lipid fluidity) or in bulk (lipid demixing, membrane curvature). The resolution achieved through atomistic MD can be directly compared with other tools such as NMR and EPR to gain a full perspective of how these biological systems behave over different timescales. As my background is in computational physics, this thesis not only looks into broadening our understanding of various interactions with biological membranes, but also into the development of construction and analytical software to assist in my research and benefit others in the field.

One aspect of biological membranes that could vastly benefit from MD simulations is that of *antimicrobial peptides* (AMPs). These peptides primarily target and destroy microbes by permeabilising the cell membrane through a variety of proposed mechanisms, where each mechanism relies on the AMP to adopt specific conformations upon contact with bacterial membranes. In this thesis, I present an investigation into the interactions between a synthetic AMP and an inhibitor peptide designed to regulate antimicrobial activity through the formation of a *coiled coil* structure, which restricts the AMP from adopting new conformations. Simulations captured the spontaneous formation of coiled coils between these peptides, and specific residues in their sequences were identified that promote unfolding. This knowledge may lead to better design of coiled coil forming

peptides.

Another aspect of biological membranes that can be explored with MD is the interactions between model bacterial membranes and amphipathic helices, such as the MinD membrane targeting sequence (MinD-MTS). This 11-residue helix is responsible for anchoring the MinD protein to the inner membrane of *Bacillus subtilis* and plays a crucial role in bacterial cell division. MinD is known to exhibit sensitivity to transmembrane potentials (TMVs), whereby its localisation and binding affinity to bacterial membranes are disrupted upon removal of the TMV. Simulations revealed rapid insertions of MinD-MTS peptides into the headgroup region of a model bacterial membrane. Analytical software was constructed to measure the membrane properties of the lipids surrounding inserted MinD-MTS peptides, which revealed splayed lipid tails and suggests the MinD-MTS may be capable of inducing membrane curvature. Additional simulations were conducted to investigate the influence of a TMV on model bacterial membranes, where software was constructed to measure changes in membrane properties. An analysis of these simulations suggests that a TMV is capable of lowering the transition temperature of a model bacterial membrane by a few degrees, yielding increased fluidity in the lipids and increased perturbations on the membrane surface.

Finally, another aspect of biological membranes that can be explored through MD is that of electroporation. This induction of transient water pores in cell membrane provides an exciting aspect for drug delivery applications into cells, whereby electric fields are applied to cells to increase the uptake of therapeutic drugs. Simulations of membranes with high voltage TMVs were conducted that sought to investigate the implications of electroporation across a variety of bilayer compositions at different temperatures. Software was constructed to measure changes in membrane and system properties, which revealed that pore formation occurred at the same threshold voltage for different bilayer compositions in the fluid phase ($\sim$1.9 V) and a higher voltage for DPPC bilayers in the gel phase ($\sim$2.4 V). The TMV was found to be highly dependent on the area per lipid (APL), implying that bilayers with bulkier lipids or those transitioning from gel to fluid will experience smaller TMVs and fewer pore formations. These simulations also revealed lipid flip-flopping through pores, where charged lipids tended to translocate in the direction of the electric field to produce an asymmetrically charged bilayer. Finally, simulations utilising charged peptides with membranes yielded electroporation effects, whereby the charged peptides generate an identical

TMV to those produced by an ion imbalance of equal magnitude. This suggests that charged peptides, such as AMPs, may be capable of permeabilising cell membranes through electroporation mechanisms.

Lay summary

Biological cells play fundamental roles in the development and maintenance of living organisms; a detailed understanding of the mechanisms behind many cellular functions is crucial for the development of new treatments for human disease. As each cell is housed by a membrane, many drug therapies must overcome this barrier to gain access to the intracellular contents in order to assist, block or disrupt cellular functions to achieve therapeutic goals. Furthermore, certain drug therapies, such as a class of naturally occurring peptides known as *antimicrobial peptides* (AMPs), specifically target and disrupt the function of the cell membrane to achieve their therapeutic goal. Therefore, a detailed understanding of the mechanisms involved in the function of cell membranes, and the interactions of cell membranes with proteins, peptides, or other molecules, is crucial in the design of new therapies.

The research presented in this thesis uses Molecular Dynamics (MD) to investigate the effects of various biological processes and phenomenon broadly involved in lipid bilayer interactions. Chapter 3 presents `Membrainy`, a tool to analyse changes in membrane properties from lipid bilayer trajectories, where these changes are often a result of environmental perturbations. This tool was a necessary creation to allow for the analyses of the simulations presented in this thesis, and has since been published and made available for others in the scientific community. Additionally, this chapter presents tools aimed at the construction, maintenance and post-analysis of membrane systems.

Chapter 4 presents the concept of regulating the antimicrobial activity of AMPs through the binding of an inhibitor peptide to form a *coiled coil* structure. Coiled coils comprise two amphipathic α-helical regions wrapped around each other with their hydrophobic faces buried together, providing a strong cohesive bond between the helices. By binding to an AMP through coiled coil formation, these inhibitor peptides can target and disrupt the ability for AMPs to bind to membranes and

to adopt new conformations, thus disabling their antimicrobial action. In this chapter, a mutated version of the AMP Cecropin-B is used as a model system to investigate whether an inhibitor peptide is capable of coiled coil formation with this mutant. Simulations revealed that coiled coil formation between these peptides is possible but highly infrequent, where this infrequency is primarily due to specific residues which strongly disrupt the susceptibility for coiled coil formation. This analysis can therefore be used to improve the sequences of coiled coil forming peptides for future studies.

Chapter 5 investigates the insertion of the MinD membrane targeting sequence (MinD-MTS), an 11-residue amphipathic helix responsible for anchoring the MinD protein to the inner membrane of *Bacillus subtilis* and plays a crucial role in bacterial cell division. Previous studies have identified this sequence to be highly sensitive to membrane potentials, whereby an ionic gradient found across all bacterial cell membranes promotes peptide binding to the membrane. Simulations of MinD-MTS with a model bacterial membrane revealed that this peptide rapidly inserts into the headgroup region and results in splayed lipid tails, which may give rise to membrane curvature. Additional simulations were conducted that sought to understand what effect a membrane potential may have on membrane properties, and revealed that the membrane potential is capable of slightly lowering the transition temperature of a model bacterial membrane.

Chapter 6 investigates the electroporation phenomenon, whereby electric fields applied to lipid bilayers result in the formation of transient water pores. This phenomenon has also been shown to occur when an ionic gradient is placed between membrane compartments, generating a high voltage membrane potential. Simulations were conducted to explore the implications of electroporation on a variety of lipid bilayer compositions at different temperatures, which revealed that bilayers with bulkier lipids required a larger ionic gradient to achieve pore formation than those with smaller lipids. Furthermore, an increase in temperature reduced the strength of the membrane potential due to the bilayers expanding, reducing the frequency of pore formation. This was most noticeable in membranes that transition between gel and fluid phase. Furthermore, additional simulations revealed that charged peptides, such as AMPs, are capable of inducing pore formation via electroporation mechanisms. This may reveal an additional mechanism of how AMPs disrupt cell membranes and exhibit antimicrobial action.

Declaration

I declare that this thesis was composed by myself, that the work contained herein is my own except where explicitly stated otherwise in the text, and that this work has not been submitted for any other degree or professional qualification except as specified.

Part of this work has been published:

Publication 1: Matthew Carr and Cait E. MacPhee. Membrainy: a 'smart', unified membrane analysis tool. Source Code for Biology and Medicine, (1):3+, March 2015.

Publication 2: Lloyd Ryan, Baptiste Lamarre, Ting Diu, Jascindra Ravi, Peter J. Judge, Adam Temple, Matthew Carr, Eleonora Cerasoli, Bo Su, Howard F. Jenkinson, Glenn Martyna, Jason Crain, Anthony Watts and Maxim G. Ryadnov. Anti-antimicrobial Peptides FOLDING-MEDIATED HOST DEFENSE ANTAGONISTS. The Journal of Biological Chemistry, 288, 20162-20172, July 2013.

This thesis also includes one publication that is not presented in the chapters:

Publication 3: Paulina D. Rakowska, Haibo Jiang, Santanu Ray, Alice Pyne, Baptiste Lamarre, Matthew Carr, Peter J. Judge, Jascindra Ravi, Ulla I. M. Gerling, Beate Koksch, Glenn J. Martyna, Bart W. Hoogenboom, Anthony Watts, Jason Crain, Chris R. M. Grovenor, and Maxim G. Ryadnov. Nanoscale imaging reveals laterally expanding antimicrobial pores in lipid bilayers. Proceedings of the National Academy of Sciences, 110 (22), 8918-8923, May 2013. .

Matthew Carr
March 2015

Acknowledgements

First and foremost I would like to thank my supervisors Professor Cait MacPhee, Dr. Ulrich Zachariae and Professor Jason Crain for their invaluable guidance and support throughout my studies, with a special acknowledgement for Cait who has contributed significantly to the shape and direction of this thesis, and has allowed me creative freedom in the decisions involved in my final projects. I would also like to thank EPSRC for their funding, and Professor Arthur Trew for his generous allocation of HECToR time.

In addition, I would like to thank Dr. Peter Judge, Dr. Marieke Schor and Giovanni Brandani for their helpful discussions and continued efforts to ensure my studies have been fun, engaging and challenging. I would like to especially thank Peter for his time and effort during his many visits to Edinburgh, and for his regular taxi service between Heathrow Airport and the National Physical Laboratory. And a special thank you to Marieke for her incredible wealth of knowledge in biophysics, and for the useful discussions while walking our dogs.

Finally, I would like to thank my parents, Margaret and Frank Carr, for their endless support and guidance over the years. They have continually pushed me to do my best, and I would not be where I am today without them. I would also like to thank my beloved dog Eli, who has kept me sane, fit and healthy over the years. And of course, my fellow PhD office mates in Room 1511, Alys Jepson, Giulia Foffano, Fred Farrell and Steven Court, for their incredible support and entertainment, and their constant supply of edible treats brought back from their travels.

Contents

List of Figures

List of Tables

Preface

The fundamental area that I have been researching is that of computational biophysics, with a strong focus on antimicrobial peptides and their interactions with cell membranes on the nanoscale, and the effects of low and high voltage transmembrane potentials on the lipid properties of cell membranes. My research has been funded by EPSRC, and certain projects have involved collaborations with the National Physical Laboratory, London; the Department of Biochemistry, University of Oxford; the Institute for Cell and Molecular Biosciences, Newcastle University; and IBM's TJ Watson Research Center, New York. My research is purely computational driven through Molecular Dynamics (MD) simulations, with strong ties to collaborators focusing on other experimental techniques such as microbiology and nuclear magnetic resonance.

In 1928, the Scottish biologist Alexander Fleming made the first discovery of a class of antibiotics known today as *penicillins*, found in the molds produced by the Penicillium fungus. These molds were known for their antibiotic properties as early as 1640, but it was only in 1940 when two scientists, Howard Florey and Ernst Chain, isolated the penicillin molecules and began producing enough to experiment on mice. A year later, Charles Fletcher, a doctor who had heard of Florey and Chain's research, had a patient who was near death due to a simple wound infection. He managed to obtain a small quantity of penicillin and treated his patient, who initially made a spectacular recovery but unfortunately died a few weeks later when Fletcher ran out of penicillin. However this proved that penicillin had remarkable potential to treat bacterial infection. Florey and Chain tried to persuade British drug companies to produce penicillin in large quantities, but were largely unsuccessful due to these companies being preoccupied with the Second World War. Shortly after, Florey managed to persuade an American drugs company to mass produce penicillin and, by D-Day, it was widely used to treat wounded soldiers who showed signs of infection, saving hundreds of lives

and earning the nickname “the wonder drug”.

Since the discovery of the penicillin family, many new classes of antibiotics have been discovered. Today there are over one hundred antibiotics available for safe human use, many of which are derivatives from the same class. Antibiotics have revolutionised medicine as we know it, paving the way for a huge range of medical and surgical procedures that would almost certainly result in death from infection if left untreated.

However, there is a dark side to the story: antibiotic resistance. In the past 15 years, the number of documented cases where bacterial infections have not responded to current therapies has been increasing at an alarming rate. The ECDC (The European Centre for Disease Prevention and Control) has documented the levels of antibiotic resistance across Europe since 2001 and has observed a rise in antibiotic resistance for each class, some rising faster than others. Today, penicillin is largely ineffective. In the UK there is approximately 62% resistance to penicillin from Staphylococcal wound infections and, in some countries across Europe, the number of resistant cases reported is much higher. The outlook for future generations is certainly in doubt; there is a huge demand for new therapies targeted at the eradication or prevention of bacterial infection.

This is where I began my journey in 2010 at the start of my PhD. I began working alongside the National Physical Laboratory in London and IBM’s TJ Watson Research Centre in New York, looking specifically at antimicrobial peptides, a class of antimicrobials that have evolved in nature as a response to infection and show remarkably low levels of resistance. During my PhD, I became interested in how these antimicrobials interface with bacterial membranes. I developed computational tools to implant peptides on top of bacterial membranes, and tools to analyse how the shape and properties of these membranes may be modified by such peptides. I also became interested in membrane potentials, and eventually combined both interests into my final project where I explored how antimicrobial peptides may establish pores within bacterial membranes through a phenomenon known as electroporation.

It is my hope that my contributions to the ongoing research in antimicrobial peptides and cell membranes will have some benefit for the scientific community, and perhaps inspire other PhDs to continue my research from a microbiology perspective. I also hope that the computational tools I have developed and published will continue to benefit the MD community.

Chapter 1

Introduction

The work presented in this thesis aims to improve our understanding of a class of antimicrobials known as *antimicrobial peptides* (AMPs), and how they may influence cell membranes through the induction of a transmembrane potential. This chapter aims to give a broad introduction to the fundamental science and concepts discussed throughout this thesis. For a more detailed overview of the fundamental biology, and for the citations of the information discussed within this chapter, unless otherwise stated, see [1] and [2].

1.1 Cells, cell membranes, lipids and lipid bilayers

The biological cell is arguably one of the most fundamental evolutionary developments of life; it is the basic building block of all known living things. The name "cell" is derived from the Latin *cella* which translates to "small room" and describes the basic appearance of the cell, having a range of intracellular contents housed within a cell membrane. These intracellular contents range from simple proteins, peptides and other small molecules to highly complex molecular machines such as ribosomes and mitochondria, which are surrounded with a salty cytoplasm and enclosed within a plasma membrane. Cells also contain genetic material in the form of DNA or RNA, which are encoded with the information required to construct the building blocks for new cells. This means that cells are the smallest unit of life and are highly self sufficient, typically responsible for their own maintainence, replication and function, with the exception of certain cells

such as viruses which partly rely on host cells for various critical functions [3]. Cells can be divided into two categories: **eukaryotic** and **prokaryotic** (Figure 1.1).

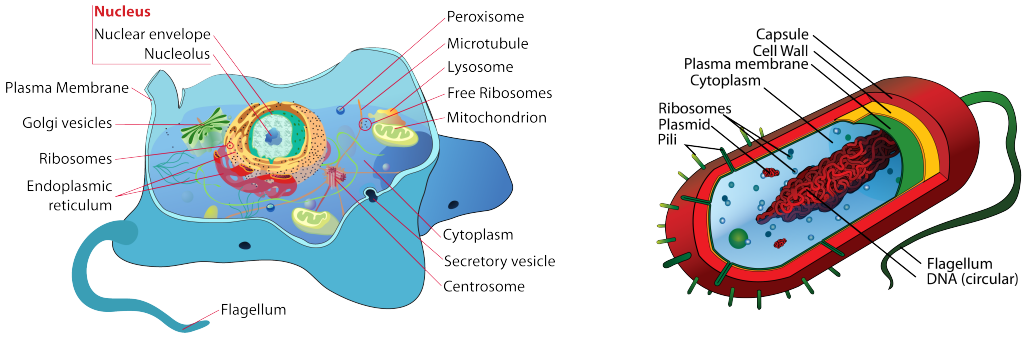

(a) *Eukaryote* **(b)** *Prokaryote*

Figure 1.1 *The two categories of biological cells. Source: [4].*

Eukaryotic cells (Figure 1.1a) are those that contain a nucleus, typically belonging to complex organisms including plants, animals and fungi. They are large (10-100μm), highly structured cells containing a cytoskeleton network and one or more linear DNA molecules within the nucleus. They contain internal structures known as organelles (e.g. mitochondria, plastids, lysosomes etc.) which are housed within their own membranes. Eukaryotic cells replicate through mitosis and cytokinesis, a process of replicating and dividing the contents of the cell that can take anywhere from a few minutes to over a year depending on the type of cell [5]. Exceptions to the eukaryotic classification exist, such as mature red blood cells which are eukaryotes but have their nucleus and most organelles ejected to maximise space for hemoglobin storage [6].

Prokaryotic cells (Figure 1.1b) are without a nucleus, typically belonging to single celled organisms such as bacteria and archaea. They are typically much smaller ($\sim 1\mu m$) and less complex than eukaryotes, containing very little internal structure and commonly house circular DNA. Exceptions to the prokaryotic classification exist, such as the gram-negative bacteria Thiomargarita namibiensis which can potentially reach sizes of 750 μm, large enough to be visible with the naked eye [7]. Prokaryotes replicate through a simple binary fission process where the DNA is copied and the cell divides near the midpoint. This division process is discussed in detail in Section 5.1.1.

The intracellular contents of both eukaryotes and prokaryotes are enclosed within a cell membrane. Cell membranes are remarkable multi-functional structures that

not only act as a protective barrier and container for the intracellular contents, but as an osmotic barrier, a platform for transmembrane proteins and fusion events, a capacitor and resistor for maintainance of chemical and electrostatic potentials, and a barrier for drug and antibody delivery into the cell [8]. It is the ability of the membrane to act as a flexible barrier that enables cells to thrive, allowing the transport of essential nutrients into the cell while protecting the cell from harmful extracellular molecules.

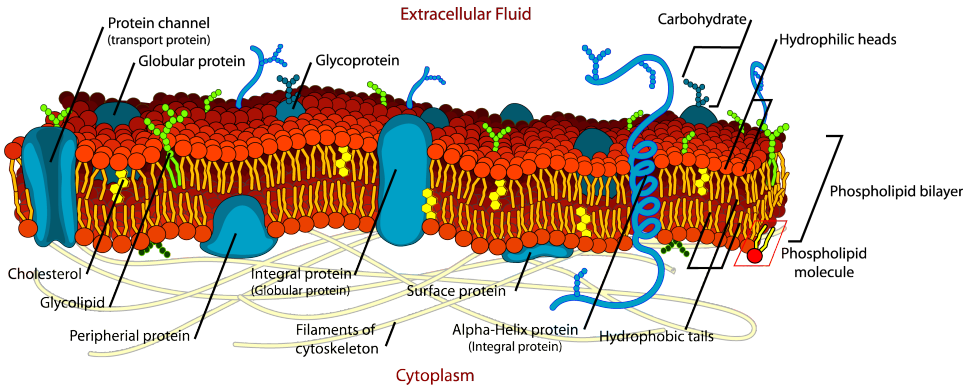

Figure 1.2 *Illustration of the complexities of biological cell membranes. Source: [4].*

Cell membranes are complex structures that contain a wide range of molecules including lipids, proteins and carbohydrates (Figure 1.2). The main building blocks of the membrane are the lipids, more commonly phospholipids. These are mostly derivatives of diglycerides that consist of a glycerol molecule attached to two fatty acids, and contain a phosphate group on the third carbon and usually another polar molecule adjacent to the phosphate group (Figure 1.3). Phospholipids are amphipathic; the fatty acid *tails* are hydrophobic while the phosphate *headgroup* is hydrophilic. They may also have zwitterionic headgroups where the phosphate group is negatively charged and the extra polar molecule on the headgroup may be positively charged. The lipid tails can contain a mixture of saturated and unsaturated hydrocarbons (containing one or more double bonds).

When many of these lipids are grouped together in water, they often exploit the hydrophobic effect by self assembling into a lipid bilayer, consisting of two layers or *leaflets* of parallel lipids with the hydrophobic regions buried together. This hydrophobic effect drives an entropic process that seeks to minimise the free energy of the system by minimising the interfacial surface between hydrophobic molecules and water. This means that lipid bilayers are semipermeable, allowing them to behave as a barrier by naturally excluding hydrophilic molecules (certain proteins, carbohydrates, ions etc.) while allowing other molecules to pass freely.

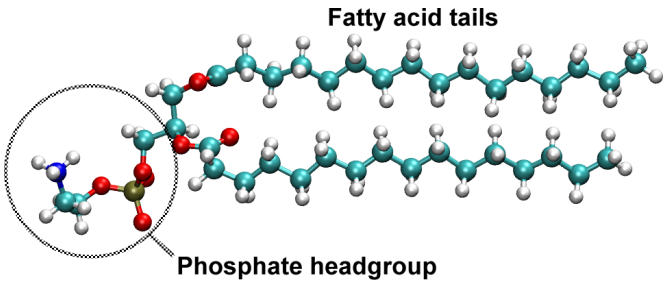

Figure 1.3 *Illustration of a phospholipid, specifically a DPPE phospholipid in the gel phase.*

Other forces also play a role in the stability of lipid bilayers, such as van der Waals interactions, electrostatics and hydrogen bonding. The bilayer also allows the inclusion and incorporation of various transmembrane proteins, carbohydrates, sterols and polysaccharides that play important roles in cell function, without compromising structural integrity.

Phospholipids can be categorised and identified by their two parts: the headgroup and the tail. Phospholipids are abbreviated to four letters, where the first two letters identify the two lipid tails attached to the first and second carbons of the glycerol molecule, and the final two letters identify the headgroup attached to the third carbon. As an example, the lipid *1-palmitoyl,2-oleoyl-sn-glycero-3-phosphocholine* can be abbreviated to POPC where the PO symbolises the two lipid tails comprising a saturated palmitoyl fatty acid containing 16 hydrocarbons and an unsaturated oleoyl fatty acid containing 18 hydrocarbons, with a double bond between the ninth and tenth carbons. The final two letters PC symbolise the headgroup which in this case is phosphocholine, a negatively charged phosphate group with a positively charged choline group.

In addition to phospholipids, there are many other types of molecules found in cell membranes, such as lipopolysaccharides (LPS) and sterols. LPS are common to gram-negative bacteria and serve a vital role in the structural integrity and protection of the membrane. Sterols, such as cholesterol or vitamin D, are common to eukaryotic cells, coexisting alongside phospholipids and play a role in modulating the structure and fluidity of the membrane.

1.2 Membrane fluidity and phase transitions

Membrane fluidity is the measure of the relative mobility of the lipids within a bilayer. Similarly to most materials, lipid bilayers undergo a first order phase transition at a certain temperature, experiencing two primary phases known as the fluid (L_d) phase and the gel (L_β) phase. The fluid (or liquid disordered) phase occurs at higher temperatures and is characterised by highly mobile lipids that are able to traverse great distances in a random walk manner [9]. The lipid tails are typically more disordered and energetic, causing a lateral expansion of the bilayer that results in a thinner membrane (Figure 1.4a). The gel (or solid) phase occurs at lower temperatures and is characterised by highly immobile lipids. The lipid tails are more ordered and linear, resulting in a thicker membrane with tighter packing of the lipids (Figure 1.4b). Other phases have also been proposed such as the ripple and subgel phase [10].

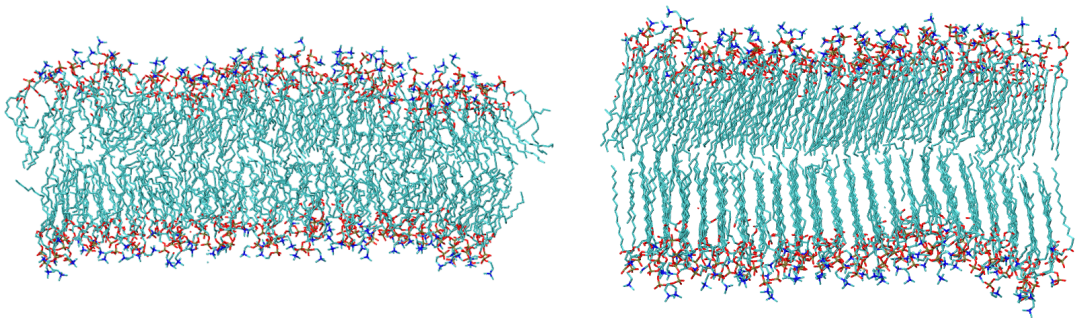

(a) *Fluid membrane* **(b)** *Gel membrane*

Figure 1.4 *Illustration of membranes in the fluid and gel phases. (a) POPC bilayer and (b) DPPC bilayer, both at 297K. The main difference between the two lipid types is the presence of a double bond in the POPC lipid tail.*

The transition temperature at which the lipids undergo a phase change is primarily defined by the types of lipids within the bilayer. Increasing the number of carbons in the lipid tails results in a higher transition temperature, due to the longer tails exerting additional van der Waals forces which decreases lipid mobility. Increasing the number of double bonds in the lipid tails results in a lower transition temperature, due to the double bond causing a kink in the lipid tails which disrupts the optimal packing of the acyl chains and creates additional free space for the lipid tails to occupy. Other factors also contribute to changes in transition temperature such as the presence of cholesterol which is known to raise the transition temperature [11]. Cholesterol enriched areas of the bilayer may also

induce *lipid rafts*; specialised highly ordered membrane microdomains that may play a role in many cellular processes such as signal transduction, membrane trafficking, cytoskeletal organisation, and pathogen entry [12, 13].

1.3 Antimicrobial and amphipathic peptides

Antimicrobial peptides (AMPs) are a class of antimicrobials that have evolved in nature as a direct immune response to microbial infection. Not only do they target and destroy both gram-positive and gram-negative bacteria, but they have also proved effective against viruses, fungi and even cancer cells [14–22]. They have been found in a wide variety of species across the planet, including plants, animals and invertebrates. They are also found all over the human body; on the surface of our eyes, between our gums, in our sweat etc. Examples of well established AMPs include the *Magainan* peptide originally found in the skin of African clawed frog [23], the *Cecropin* peptide originally found in the North American Cecropia moth [24], and *Dermcidin* secreted in the human sweat glands [25]. AMPs are currently being studied as an alternative or supplement to existing antimicrobial therapies. Their mechanisms differ from conventional antibiotics in that they primarily target and disrupt the cell membrane, increasing its permeability and ultimately resulting in cell death.

AMPs come in many shapes and sizes. They adopt a range of different conformations including alpha helical, beta stranded (due to the presence of two or more disulfide bonds), extended and mixed (containing a mixture of the three previous conformations) (Figure 1.5). AMPs often adopt a new conformation when in contact with lipid bilayers, commonly with part or all of the peptide adopting an amphipathic helical conformation. This amphipathicity is achieved by the helical peptide containing all of its hydrophobic residues on one side of the helix and polar residues on the other side (Figure 1.6). This change in conformation plays an important role in the inclusion of the AMP with lipid bilayers, as amphipathic helices exploit the hydrophobic effect by burying their hydrophobic residues with the lipid tails, and the polar residues remain in contact with the lipid headgroups and water. The resulting helical region of the peptide would sit amongst the lipid headgroups, parallel to the bilayer surface.

The mode of action of AMPs is somewhat unclear; the complex nature of cell membranes and rapid onset of cell death makes their exact mechanism difficult

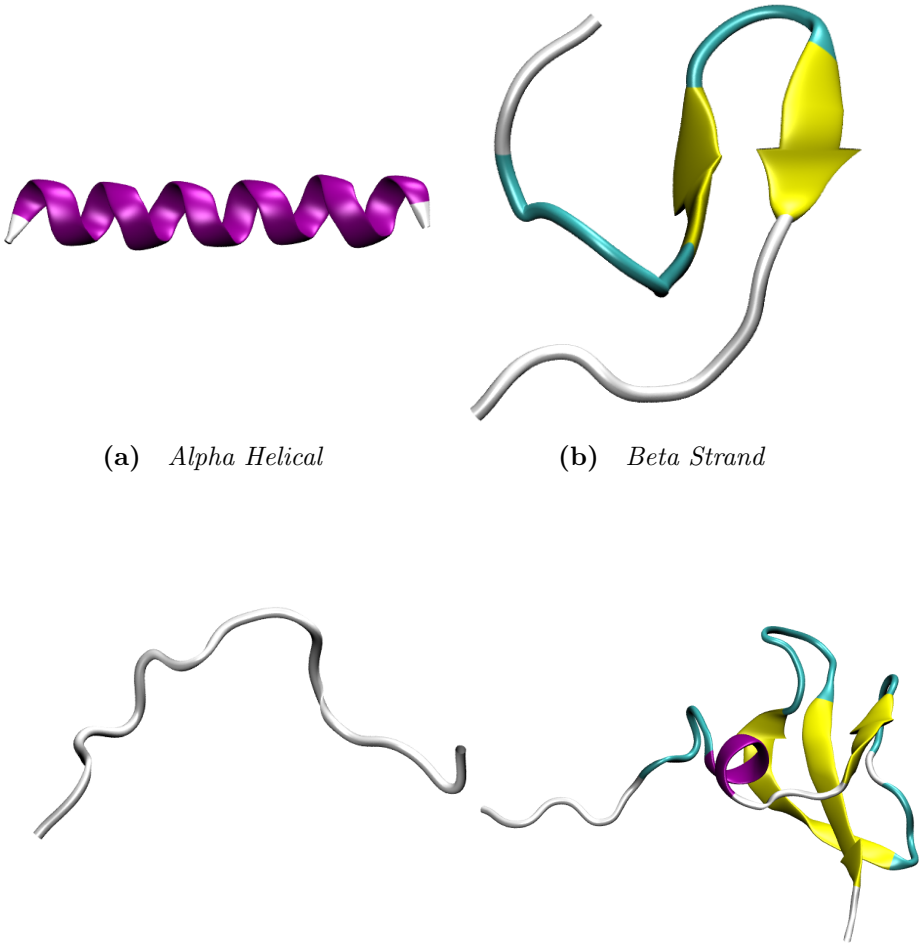

(a) *Alpha Helical* **(b)** *Beta Strand*

(c) *Extended* **(d)** *Mixed*

Figure 1.5 *Images of the secondary structure for different types of AMPs. (a) Pexiganan, (b) Tachyplesin 1, (c) Indolicidin, (d) Human Beta Defensin 3.*

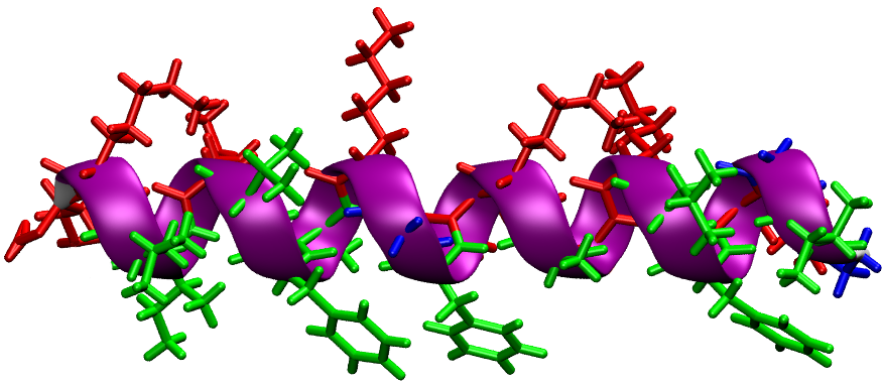

Figure 1.6 *Illustration of the amphipathic AMP Pexiganan. The amphipathic nature is achieved by the hydrophobic (green) residues orientated on one side, with the polar residues (red) orientated on the other side.*

to capture, with no single experimental technique able to provide a complete picture of their mechanism. AMPs must first navigate past the complex structures extruding from the lipid bilayer such as the lipopolysaccharides (LPS) or capsular polysaccharides. This is likely assisted by the electrostatic interactions between the peptides and charged lipids, since many species of microbes carry a slight negative charge on their membrane, achieved by acidic phospholipids such as phosphatidylglycerol [26], and many AMPs contain the cationic residues lysine and arginine [27]. Once they have reached the membrane surface, certain AMPs are thought to disrupt the membrane via one or more of three broad mechanisms: *toroidal pore formation*, *barrel-stave pore formation*, and *carpet* mechanism [28]. The toroidal pore formation mechanism applies to the shorter alpha helical peptides such as the magainins and protegrins. The helical peptides insert into the headgroup region of the lipid bilayer, parallel to the bilayer surface. They then reorientate themselves such that they are perpendicular to the membrane surface and perturb the membrane enough to establish transient water pores, lined with both peptide and lipid headgroups. Barrel-stave pore formers, such as dermcidin, assemble in a similar way to toroidal pores; however, these peptides bundle together to form a stable ion channel. Many of these channels often require zinc ions for antimicrobial activity [29, 30]. The carpet mechanism involves peptides that carpet the surface of the bilayer, and at high concentrations are thought to disrupt the bilayer in a detergent-like manner. There is also evidence that certain AMPs may interfere with intracellular workings, such as inhibiting cell-wall synthesis, nucleic-acid synthesis, protein synthesis and inhibiting enzymatic activity [31–34].

1.3.1 Antimicrobial peptide resistance mechanisms

Remarkably, microbes have shown very few resistance mechanisms to AMPs when compared to conventional antibiotics. This becomes even more remarkable when we consider that AMPs have fought off microbial assault for many thousands of years. This is likely because there is no single gene mutation that can completely alter the composition of the cell membrane - many gene mutations would have to occur simultaneously for the membrane to exhibit AMP resistance [28]. Furthermore, antimicrobial assaults often comprise many different types of AMPs, and therefore can employ a multi-strategic assault on microbes to bypass possible resistance mechanisms [16].

However resistance to AMPs is far from impossible. Certain species of bacteria such as *Serratia* and *Morganella* exhibit natural immunity by lacking appropriate levels of charged lipids in the outer membrane [35]. The gram-positive *Staphylococcus aureus* and *Staphylococcus xylosus* also exhibit natural resistance to cationic AMPs by having an increased number of positively charged D-alanines in the teichoic acids attached to the membrane. Peschel *et al.* showed that by deactivating the genes *dltA*, *dltB*, *dltC* and *dltD*, an increased susceptibility to cationic AMPs could be achieved [36]. These genes are responsible for the creation and transport of D-alanine to the teichoic acids, and therefore deactivating them increases the net negative charge on the membrane, promoting electrostatic interactions with cationic AMPs. Similarly, Kristian *et al.* showed that deactivation of the *mprF* gene in *S. aureus* resulted in an increased succeptibility to cationic AMPs by increasing the net negative charge on the membrane [37]. This gene plays a role in the synthesis of lysyl-phosphatidylglycerol, a phospholipid that is modified with L-lysine through the *MprF* protein to increase the positive charge on the membrane. Furthermore, resistance to Pexiganan, a synthetic analogue of Magainan, has been engineered *in vitro* which alarmingly also caused cross-resistance to the human-neutrophil-defensin-1, an important AMP found in our immune systems [38]. This raises an interesting and urgent question as to whether therapeutic use of AMPs is safe? Could resistance to specific AMPs compromise our natural ability to fight off infection as well as the immune responses in other living organisms?

Not all membrane-mediated AMP resistance mechanisms are achieved from changes in membrane surface charge. A study involving the gram-negative *Salmonella enterica* identified that the *pagP* gene plays a role in membrane permeabilisation [39]. When activated, this gene encodes the protein *PagP* that drives acylation of *lipid A*, resulting in a decreased membrane permeability and restricting the AMPs ability to penetrate into the membrane. Another study involving the gram-negative *Klebsiella pneumoniae* showed that increasing the number of capsular polysaccharides attached to the outer membrane limited the interaction of AMPs with the membrane surface [40]. Worryingly, increased levels of capsular polysaccharides in *K. pneumoniae* have been shown to be influenced by treatment with the antibiotics *ciprofloxacin* and *ceftazidime* [41], suggesting that many of our conventional antibiotic therapies may be establishing cross-resistance with AMPs.

There has also been a number of studies that have shown AMP resistance

mediated through mechanisms that do not involve changes to the membrane. One such study showed that *S. aureus* secretes a proteolytic enzyme capable of cleaving and inactivating *LL-37*, an AMP commonly found at sites of inflammation in the human body [42, 43]. Similarly, the metalloprotease enzyme *ZapA* found in *Proteus mirabilis* has been shown to cleave both LL-37 and the human beta defensin 1 (*hBD-1*), an AMP found in organs throughout the human body [44, 45]. Furthermore, the bacterial species *Porphyromonas gingivalis* has been shown to secrete digestive proteases to break down AMPs [16]. Therefore microbes are not only capable of fortifying their cell membrane against AMP attack, but can also release an array of defensive molecules as a preemptive strike to deactivate or disable approaching AMPs.

1.4 The membrane potential

The membrane potential is an electrical potential found across all biological cell membranes, achieved by the balance (or more specifically, the imbalance) of intracellular and extracellular ionic concentrations [46]. This ionic imbalance is maintained by both active and passive ion transport through the cell membrane via ion channels and pumps, capable of transporting specific ions in a given direction and rate (Figure 1.7). One example is the Na^+/K^+ -ATPase ion pump, found in abundance in all animal cell membranes [47]. This pump consumes ATP to transport three Na^+ ions out of the cell and two K^+ ions into the cell, and is the primary means by which animal cells maintain a high potassium/low sodium intracellular concentration. Through this mechanism, each cycle of the pump results in a charge imbalance of -1 within the cell, and therefore drives a negative potential gradient across the membrane. Furthermore, plasma membranes exhibit permselectivity (i.e. degrees of permeability) allowing certain ions to permeate the membrane more easily than others [48]. This provides another means for cells to drive ionic gradients between the intracellular and extracellular compartments.

The potential difference across a membrane is defined as the *transmembrane voltage* (TMV) and can be estimated using the *Nerst equation*:

$$V = -\frac{RT}{zF}\, ln\, \frac{[K]_{in}}{[K]_{out}} \tag{1.1}$$

where V is the TMV (Volts), R is the gas constant (8.31 J/(K mol)), T is the temperature (Kelvin), F is the Faraday constant (9.65 x 10^4 C/mol) and z is

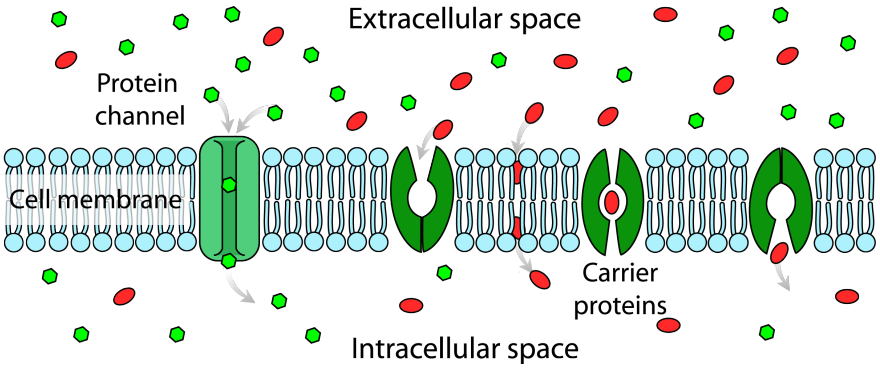

Figure 1.7 *Illustration of how a membrane potential is maintained via passive and active ion channels and pumps within the cell membrane. The membrane is also exhibits permselectivity, allowing certain ions to permeate more easily. Image adapted from [4].*

the valance of the ion (i.e. +1 for K^+). The final term is the concentration ratio of intracellular to extracellular K^+. This equation provides the measurement for a TMV across a biological membrane with ideal permselectivity. However as biological membranes are far from ideal, the Nerst equation must be modified to take into account the permselectivity of the membrane for other ions that also significantly contribute to the membrane potential (Na^+ and Cl^-). This is known as the Goldman-Hodgkin-Katz Constant Field equation:

$$V = -\frac{RT}{F}\, ln\, \frac{P_K[K]_{in} + P_{Na}[Na]_{in} + P_{Cl}[Cl]_{out}}{P_K[K]_{out} + P_{Na}[Na]_{out} + P_{Cl}[Cl]_{in}} \tag{1.2}$$

which now includes the permselectivity terms P_i (in cm/s) for each ion.

Virtually all eukaryotic and prokaryotic cells maintain a resting TMV in the order of 10-100mV [49], although higher voltages have been observed in many bacterial species such as *Escherichia coli* and *Bacillus subtilis* [50, 51]. The existence of the membrane potential plays a crucial role in a wide range of cellular processes. These include the transport of nutrients into and out of cells, biophysical signaling across cells including signaling for muscular and cognitive processes, and cell proliferation [46, 47, 52]. Many transmembrane peptides and proteins exhibit voltage sensitivity, allowing them to act as molecular devices that are activated through voltage induced conformational changes that modulate their function within the cell. One such example is the Na^+/K^+ -ATPase ion pump discussed above, which has been observed to increase its activity with higher voltages [53]. Another example is the phosphohydrolytic enzyme *phospholipase* A_2 which hydrolyses the bond connecting the second fatty acid to the glycerol molecule in phospholipids, and whose activity was shown to increase with higher voltages

[54]. In electrically excitable cells such as *myocytes* (muscle cells) and *neurons*, the membrane potential also acts as a communication relay, capable of transmitting signals between the various voltage sensitive proteins within the membrane [55]. These proteins, known as voltage-gated ion channels, open or close in response to changes in the membrane potential. Upon opening, they allow ions to flow through the channel causing a rapid change in the local membrane potential, known as an *action potential*, which is detected by neighbouring voltage-gated channels causing them to open, thus relaying the signal along the cell membrane through each ion channel. This biophysical signalling process plays an essential role in the function of the central nervous, skeletal muscular and cardiac systems.

Whilst TMVs have also been observed to play a role in the binding affinity of various peptides and proteins [56–59], cell membranes are impenetrable to many other molecules at biologically relevant voltages. For example, DNA and RNA molecules in solution cannot enter most eukaryotic cell types (apart from specialised immune cells such as macrophages). However in 1982 it was discovered that eukaryotic (and later prokaryotic) cells subjected to electric field pulses allowed the uptake of DNA and (later) other molecules into the cell [60]. This uptake is mediated by the formation of transient water pores in the cell membrane, established through a biophysical phenomenon known as *electroporation*.

1.5 Molecular dynamics

Molecular dynamics (MD) is a highly evolving computational technique that allows the dynamics and energetics of complex molecular systems to be captured with atomic resolution, and fills the spatial and temporal resolution gap that other experimental techniques cannot observe. MD allows us to solve Newton's equations of motion for a system of atoms by integrating their positions and velocities over time:

$$\bar{F}(t) = m\bar{a}(t) \tag{1.3}$$

$$\bar{a}(t) = \frac{d\bar{v}(t)}{dt} \tag{1.4}$$

$$\bar{v}(t) = \frac{d\bar{r}(t)}{dt}. \tag{1.5}$$

As many body calculations are inherently complex, the errors involved in integrating the positions and velocities of a system of atoms after a time interval (t) grow proportionately with the size of t. To solve this, the simulations are

divided into many smaller time intervals (known as a time step, Δt), typically 1-2 fs, which is small enough to reduce the integration error when dealing with typical atomic forces and velocities. The forces acting on each atom are recalculated at each time step, which not only takes into account the Coulomb and van der Waals interactions between atoms, but also the contributions from the stretching and rotation of atoms connected via covalent bonds.

The increasing CPU power of todays computing facilities along with advances in both hardware and software means MD is becoming a highly accessible technique to improve our understanding of the behaviour of molecular systems. With the creation of supercomputers such as IBM's BlueGene and the UK National Supercomputing Service HECToR/ARCHER, we can perform increasingly more complex calculations to analyse the inner workings of massive systems, such as lipid bilayers, over biologically significant timescales.

1.6 Aims and outline of this thesis

During my time at the University of Edinburgh, I have taken part in a variety of projects and collaborations, all with slightly different themes but broadly based around AMPs and lipid bilayers. As my background is in computational physics, I also set out to develop software to assist in the construction and interpretation of lipid bilayers, which have not only benefited the work presented in this thesis, but also for those in the MD community conducting similar research. The aims and outline of the projects presented in this thesis are as follows:

In **Chapter 3: Advancing software for the study of lipid bilayers through MD**, I present `Membrainy`: a unified intelligent analysis tool capable of employing a range of analytical techniques to measure the various membrane-specific properties of simulated lipid bilayers. Currently, there are very few existing tools capable of measuring and interpreting changes in lipid bilayer properties. Furthermore, these existing tools are problematic to install and operate, requiring complicated user-created configuration files and run scripts containing detailed information about each bilayer being analysed. These existing tools also have difficulties interpreting double bilayers, asymmetric bilayers, and bilayers undergoing structural changes such as lipid flip-flopping. `Membrainy` was written to solve these problems, providing a highly automated and versatile tool that interprets a wide variety of bilayer compositions and force fields without the

need for user input. `Membrainy` will also automatically interpret single, double, and asymmetric bilayers, and contains algorithms to automatically detect and compensate for structural changes such as lipid flip-flopping. This chapter also introduces several construction tools that were designed to aid in the creation and management of ion imbalances across double bilayers, and a post-analysis tool aimed at removing the fluctuations from a data set due to poor sampling of lipid bilayer trajectories.

In **Chapter 4: An investigation into antimicrobial peptide inhibitors**, I investigate a theoretical resistance mechanism to AMPs from the binding of an amphipathic antagonist peptide released by the bacterium. Such a peptide could theoretically exploit hydrophobic interactions with the AMP to form a dimer or *coiled coil*, rendering the AMP inert. This study aims to explore this mechanism by conducting simulations of coiled coil formation using a mutant of the AMP cecropin-B along with an engineered anti-AMP. These peptides are simulated under various initial orientations, and the frequency and efficiency of coiled coil formation is explored when these peptides are initiated under an ideal orientation. These simulations reveal that coiled coil formation from these peptides is possible but highly unlikely, due to the presence of a proline residue which disrupts the helical and amphipathic nature of each peptide.

In **Chapter 5: Advancing our understanding of membrane potentials**, I investigate the effect a transmembrane potential (TMV) has on the properties of lipid bilayers. I present simulations of lipid bilayers at and above biologically relevant voltages, and use `Membrainy` to determine the differences in membrane and system properties of these bilayers when compared with bilayers without a TMV. These comparisons reveal subtle changes in thickness, area per lipid and fluidity at high voltages, but no significant changes at biologically relevant voltages within these timescales. In the second half of this chapter, I explore the membrane targeting sequence of the bacterial protein MinD (MinD-MTS), which plays an important role in the cell division of *B. subtilis* and is known to show binding sensitivity to membranes under the influence of a TMV. By conducting simulations of MinD-MTS with model bacterial membranes, the insertion dynamics and energetics were captured. I also explore the theory of lipid splaying: an increased flexibility of the lipid tails in the annular shell of lipids surrounding inserted amphipathic peptides. I use `Membrainy` to analyse the annular shell of lipids surrounding inserted MinD-MTS peptides, which reveals higher levels of disorder in these lipid tails when compared to the bulk lipids,

indicating the presence of lipid splaying.

In **Chapter 6: An investigation of electroporation in lipid bilayers**, I study the electroporation phenomenon induced by an ion imbalance across a variety of lipid bilayer compositions at different temperatures. This allows for a comparison of the electroporation process in membranes with different bilayer properties, such as area per lipid, fluidity, and surface charge, with the aim to determine whether certain lipid types incur changes in the pore formation process and frequency. My results reveal that increases in membrane surface area require an increase in ion imbalance to achieve the same voltage, where the membrane surface area is determined by properties such as the temperature, bilayer composition and fluidity. Surprisingly, the electroporation threshold voltage appears identical in all fluid bilayers regardless of the temperature and composition; however, this threshold voltage is larger for bilayers in the gel phase, likely due to an increased bilayer stability from the additional van der Waals forces between ordered lipid tails. These simulations also reveal that the presence of a negatively charged lipid has no significant effect on the pore formation process; however, these charged lipids are observed to translocate through the pore in the direction of the electric field, giving rise to an asymmetrically charged bilayer. The second half of this chapter aims to answer the questions: Can AMPs, or more generally charged peptides, induce a TMV across a double bilayer? And if so, can charged peptides generate a sufficiently strong electric field to induce pore formation via electroporation mechanisms? I present simulations showing that the AMP Pexiganan induces an electrostatic potential across a double bilayer with identical shape and strength to one produced by an ion imbalance. Furthermore, I show that the peptides Pexiganan, Poly-l-lysine and Poly-glutamic acid are capable of inducing transient water pores in lipid bilayers via electroporation mechanisms. This may provide evidence for an additional step in the pore formation mechanisms and membrane disruption achieved by various AMPs and cationic peptides.

Chapter 2

Simulation methods

Section 2.1 will give a brief overview of the fundamental concepts and techniques used in MD, which are widely available in many textbooks. For a more comprehensive description of the techniques used in MD, and for the citations of the information contained within this section, see [61] and [62].

Section 2.2 will give an overview of the model lipid bilayers used in the simulations presented throughout this thesis.

2.1 Molecular dynamics

2.1.1 GROMACS

GROMACS [63] is a fast, well respected MD package maintained by a vast community of computational biophysicists and biochemists, and is available under the GNU General Public License. GROMACS has been cited in thousands of articles since first being published in 1995 and is becoming one of the most widely used open source MD packages. Originally designed for low-end scaling, such as desktops and small clusters, GROMACS has since been improved for better scaling on high-end machines. GROMACS contains some clever algorithms designed to boost performance during simulations, such as dynamic load balancing that automatically reassigns atoms to a different processor if the load imbalance is above a threshold. Recent advances in the software also allows for simulations to be conducted on GPGPU clusters, utilising a hybridisation

of CPUs and GPUs by performing non-bonded force calculations on the GPUs, while the remaining calculations are performed on the CPUs. This is highly advantageous as the non-bonded force calculations are the most computationally expensive step during the integration and can be safely calculated on the GPUs in parallel, yielding a boost in simulation speeds of 3-5x over pure CPU simulations.

GROMACS also contains a powerful suite of construction and analytical tools used throughout the simulations presented in this thesis. Many of these construction tools enable the creation of topologies for complex systems such as lipid bilayers, and allow for proteins to be solvated with water and ions. The analytical tools are capable of employing a range of techniques such as root mean square fluctuations, electrostatic potential calculations, and deviation from ideal helices.

2.1.2 Force fields

Force fields are an essential part of every MD simulation; they express how the atoms in a system interact with each other and obey the laws of Physics. Force fields explicitly define the bond strengths, angles, and torsion angles between two or more atoms, as well as an approximated mass and charge. These values are obtained from both quantum mechanical calculations and experimental data. There are many force fields to choose from, each with slightly different approximations that reflect a physically realistic system. There is no perfect force field suitable for all systems, but recent studies suggest that some force fields may be more accurate in modelling certain systems, such as protein folding and membrane interactions [64, 65]. Because of this, each MD simulation needs to carefully choose an appropriate force field to maximise the accuracy of the intended results.

Equation 2.1 denotes the potential energy function of the atomic positions ($\mathbf{r}$) of N atoms, and is incorporated into the most common force fields. The first term in the equation models the interaction between pairs of bonded atoms modelled with a harmonic potential, which allows for an increase in energy when the bond length b deviates from its resting bond length b_0. The second term sums over the valance angles (the angle formed between three bonded atoms, e.g. A−B−C), which is also modelled using a harmonic potential. The third term is the torsional potential, sometimes recognised as "improper" torsions, which models the changes in energy as groups of four bonded atoms rotate. The final term refers to the non-bonded

$$V(\mathbf{r^N}) = \sum_{bonds} \frac{k_b}{2}(b - b_0)^2 + \sum_{angles} \frac{k_\theta}{2}(\theta - \theta_0)^2 + \sum_{torsions} \frac{k_\phi}{2}[1 + cos(n\phi - \gamma)] + \sum_{i=1}^{N} \sum_{j=i+1}^{N} \left(4\varepsilon_{ij} \left[\left(\frac{\sigma_{ij}}{r_{ij}} \right)^{12} - \left(\frac{\sigma_{ij}}{r_{ij}} \right)^{6} \right] + \frac{q_i q_j}{4\pi\epsilon_0 r_{ij}} \right). \tag{2.1}$$

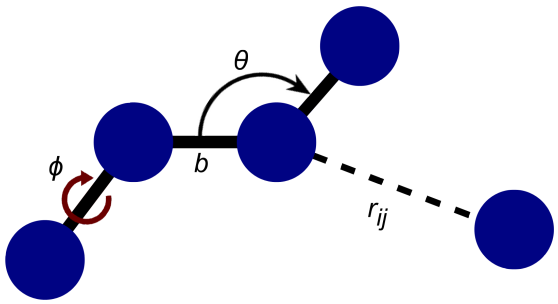

Figure 2.1 *Overview of the force field potential energy interactions. Solid lines represent covalent bonds, and dashed lines represent non-covalent interactions.*

interactions between all pairs of atoms (i and j) in the system. These pairs can be in different molecules or in the same molecule when each atom is separated by three bonds or more. This nonbonded contribution uses partial charges q_i on each atom interacting via Coulomb's Law, as well as a Lennard-Jones 6-12 potential for van der Waals interactions.

Once calculated, the potential energy function for each atom in the system can then be translated into a force using the simple relation:

$$\bar{F}(t) = \frac{d\bar{V}(\bar{r}(t))}{dt}, \tag{2.2}$$

where $\bar{F}(t)$ can then be substituted into Equation 1.3 to determine the accelerations of each atom in the system.

CHARMM

The CHARMM (Chemistry at HARvard Macromolecular Mechanics) force field is a widely used and well respected *atomistic* force field that has been in development since the early 1980s. Hydrogen bonding in proteins and peptides was the key principal behind the force field; it was designed by using quantum calculations of hydrogen bonded complexes between water and the hydrogen bond donors/acceptors of amino acids. It was found that fitting the peptide-water

interactions led rise to peptide-peptide hydrogen bonding [66, 67]. There are many different versions of the CHARMM force field available, the most popular being the CHARMM22 protein force field, CHARMM27 lipid/DNA/RNA force field, and the recent CHARMM36 all lipid + cholesterol force field. These force fields can be used in combination with each other which is often advantageous when mixing peptides with membranes. CHARMM is also the primary force field used by NAMD (NAnoscale Molecular Dynamics) [68], a widely used Molecular Dynamics package designed to scale over hundreds of computer cores and is particularly suitable to high-end systems such as IBM's BlueGene [69].

As the CHARMM force field contains parameterisation for the most common lipid types, this makes it an ideal choice for simulating membrane systems. However, for systems containing proteins and peptides (including peptides interacting with membranes), CHARMM is known to show helical bias and is therefore not the best choice when studying protein or peptide folding [70].

AMBER

The AMBER force field is another well respected and established atomistic force field that has been in development since the early 1980s. AMBER derives its atomic charges through quantum chemistry calculations via fitting of partial atomic charges to the quantum electrostatic potential [66]. The van der Waals forces were adapted from fits to amide crystals [71] and from liquid-state simulations [72]. Similarly to CHARMM, AMBER has many versions to choose from. The latest version AMBER99_SB-ILDN has been shown to be particularly accurate in protein folding simulations when compared with other force fields [73]. AMBER has recently introduced a version of its force field specifically designed for lipids, known as Lipid14 [74]. This force field looks promising but has yet to be extensively tested.

OPLS

The OPLS (Optimized Potentials for Liquid Simulations) is another widely used force field in development since the late 1980s, containing parameterisation for both united-atom and all-atom simulations. OPLS adopts the bond stretches, angle bends, and torsional terms from the AMBER force field; however the torsional potential has been improved by including a cosine expansion.

GROMOS

The GROMOS force field formed the basis for the development of GROMACS in the early 1990s [62]. The force field is a *united atom* force field; it treats small groups of atoms as a single united atom (e.g. aromatic rings are treated as a single particle or bead). Non-polar hydrogens are also paired with their bonding partners. The result is a force field that reduces the number of calculations per timestep, ideal for membrane simulations or protein folding simulations over long timescales. Although GROMOS does not contain any force field parameters for lipids, it is often paired with Berger lipids [75]: a hybrid of GROMOS atom types and OPLS partial charges. These lipids were parameterised such that the lipid bilayer properties match experimental values almost exactly.

Martini

The Martini force field is a coarse grained force field that groups clusters of atoms together into *beads*. This force field was designed to allow MD to reach timescales that would not be possible with other force fields, and as such lipid bilayer simulations can easily reach several microseconds in the time it would take an atomistic force field to achieve 100 ns. This force field is ideal for studying lipid mixing/demixing and domain formation, as these processes typically take hundreds of nanoseconds to occur. Martini requires a fixed backbone structure for proteins and is therefore not suitable to study protein folding. A lipid, which typically contains around 125 atoms can be compressed into $\sim$13 beads, which results in computationally cheaper calculations when compared with a fully atomistic force field.

2.1.3 Integrators

In order to compute the trajectory and coordinates of a system over time, the equations of motion must be integrated for each particle over a given timestep, Δt. Several integrators have been derived for this purpose, each with varying levels of accuracy and computational cost. Typically, minimising the integration error involves using more complex calculations which incur additional computational cost, and therefore one must carefully choose an appropriate integrator based on the type of simulation being conducted. Each integrator follow Newton's

equations of motion for a given particle i:

$$\frac{\partial^2 \mathbf{r}_i}{\partial t^2} = \frac{\mathbf{F}_i}{m_i} \quad i = 1...N, \tag{2.3}$$

where the force for a given particle can be calculated from its negative derivative of a potential function:

$$\mathbf{F}_i = -\frac{\partial V(r)}{\partial r_i}, \tag{2.4}$$

where $V(r)$ is explicitly defined by the force field and is likely a variant of Equation 2.1. Once the forces acting on each atom have been calculated, each integrator then applies a different approach to determining the updated positions and velocities of each atom. The two most commonly used integrators in MD simulations are as follows:

The leap frog integrator

The leap frog integrator is a commonly used integrator in MD simulations due to it being computationally cheap while maintaining a high level of accuracy. As the name suggests, this integrator uses small leaps in time to compute the new positions and velocities of each atom in the system. The leaps are divided into $1/2\ \Delta t$, where the velocity is calculated on the first leap and position on the second leap:

$$\mathbf{v}(t + \frac{1}{2}\Delta t) = \mathbf{v}(t - \frac{1}{2}\Delta t) + \frac{\Delta t}{m}\mathbf{F}(t) \tag{2.5}$$

$$\mathbf{r}(t + \Delta t) = \mathbf{r}(t) + \Delta t\, \mathbf{v}(t + \frac{1}{2}\Delta t). \tag{2.6}$$

which leads to an error in the position of order $\mathcal{O}\Delta t^2$. This should be sufficiently accurate in MD simulations if a small enough timestep is used.

The velocity verlet integrator

The velocity verlet integrator is another commonly used integrator that computes the new position and velocity at the same timestep, but computes an additional half timestep velocity in order to increase the accuracy of the full timestep calculations. The equations become:

$$\mathbf{v}(t + \frac{1}{2}\Delta t) = \mathbf{v}(t) + \frac{1}{2}\mathbf{a}(t)\Delta t \tag{2.7}$$

$$\mathbf{r}(t + \Delta t) = \mathbf{r}(t) + \Delta t\, \mathbf{v}(t + \frac{1}{2}\Delta t) \tag{2.8}$$

$$\mathbf{v}(t + \Delta t) = \mathbf{v}(t + \frac{1}{2}\Delta t) + \frac{\Delta t}{2m}\mathbf{F}(t + \Delta t) \tag{2.9}$$

This has the advantage of decreasing the error in the position to order $\mathcal{O}\Delta t^4$, but requires an additional calculation per atom making it more computationally expensive than the leap frog integrator.

2.1.4 Pressure coupling

Pressure coupling is an important part of MD that allows the running of simulations in an *NPT ensemble* (isobaric-isothermal). It works by allowing the simulation box dimensions to fluctuate thus maintaining a constant pressure by changing the box volume. This is of particular importance for membrane systems as they are known to expand/shrink with changes in temperature; therefore the simulation box must account for this. Pressure coupling can be determined isotropically, semi-isotropically or anisotropically. Systems with interfaces, such as lipid bilayers, are dealt with semi-isotropically where the x/y dimensions (bilayer plane) are coupled together, and the z dimension is independently coupled. The two most common pressure coupling schemes are as follows:

Berendsen pressure coupling

The Berendsen approach rescales the coordinates and box vectors using a matrix μ, giving a first order kinetic relaxation of the pressure towards a defined reference pressure $\mathbf{P_0}$:

$$\frac{d\mathbf{P}}{dt} = \frac{\mathbf{P_0} - \mathbf{P}}{\tau_p} \tag{2.10}$$

and the scaling matrix is defined by:

$$\mu_{ij} = \delta_{ij} - \frac{n_{PC}\Delta t}{3\tau_p}\beta_{ij}\left\{P_{0ij} - P_{ij}(t)\right\} \tag{2.11}$$

where β is the isothermal compressibility of the system and n_{PC} is the number of steps to wait before updating the box dimensions. This approach does not scale the velocities, and although it produces the correct average pressure, it fails to produce an accurate NPT ensemble. The Berendsen coupling scheme is therefore ideal for system equilibrations and simulations where maintaining a low

computational cost is important.

Parrinello-Rahman coupling

The Parrinello-Rahman approach allows the box dimensions to obey the equation of motion:

$$\frac{db^2}{dt^2} = VW^{-1}b'^{-1}(P - P_{ref}) \tag{2.12}$$

where V is the volume of the box, W is a matrix parameter that determines the strength of the coupling and b represents the matrix of box vectors. The values of W^{-1} can be calculated at the start of the simulation from the desired compressibility β and the pressure time constant τ_p:

$$\left(W^{-1}\right)_{ij} = \frac{4\pi^2\beta_{ij}}{3\tau_p^2 L} \tag{2.13}$$

where L is the largest box matrix element.

The Parrinello-Rahman approach also has the advantage of altering the equations of motion for the particles in the box:

$$\frac{d^2r_i}{dt^2} = \frac{F_i}{m_i} - M\frac{dr_i}{dt} \tag{2.14}$$

where

$$M = b^{-1}\left[b\frac{db'}{dt} + \frac{db}{dt}b'\right]b'^{-1} \tag{2.15}$$

This approach is often paired with the Nosé-Hoover thermostat (see Section 2.1.5), as both use similar modifications to the equations of motion for all particles in the box. Parrinello-Rahman coupling produces an accurate NPT ensemble and is therefore the ideal choice for most MD simulations. However as the box dimensions are constrained to equations of motion, the Parrinello-Rahman approach may produce inaccuracies in systems where the box dimensions undergo rapid changes, such as during equilibration and the lateral expansion of membranes.

2.1.5 Temperature coupling

As with the majority of MD systems, a constant temperature ensemble needs to be established for NPT and NVT (isochoric-isothermal) ensembles - but not NVE (isochoric, constant energy). The three most common coupling schemes are as follows:

Berendsen temperature coupling

Also known as the *weak coupling* scheme, the Berendsen algorithm mimics weak coupling with first-order kinetics to an external heat bath with temperature T_0. Any deviation from the system temperature is slowly corrected according to:

$$\frac{dT}{dt} = \frac{T_0 - T}{\tau} \tag{2.16}$$

causing an exponential decay with time constant τ. This means that the strength of the coupling can be varied with τ, which can be beneficial for differentiating between equilibration runs and MD runs. The Berendsen thermostat suppresses the fluctuations of the kinetic energy, meaning that a proper canonical ensemble is not generated. The error scales with $1/N$, so for large systems the ensemble averages will not be significantly affected, but properties such as the heat capacity will be affected. The heat flow within the system is affected by the scaling of velocities of each particle at every given timestep n_{TC} with a time-dependent factor λ:

$$\lambda = \left[1 + \frac{n_{TC}\Delta t}{\tau_T}\left\{\frac{T_0}{T(t - \frac{1}{2}\Delta t) - 1}\right\}\right]^{1/2} \tag{2.17}$$

The parameter τ_T is close but not equal to the time constant τ in Equation 2.16:

$$\tau = \frac{2C_V\tau_T}{N_{df}k_B} \tag{2.18}$$

where N_{df} is the total number of degrees of freedom. The kinetic energy change caused by rescaling the velocities is partly redistributed between kinetic and potential energy; therefore the change in temperature is less than the scaling energy. This is why $\tau \neq \tau_T$.

Velocity rescaling thermostat

This is an addition to the Berendsen thermostat that includes a stochastic term to ensure the correct kinetic energy distribution:

$$dK = (K_0 - K)\frac{dt}{\tau_T} + 2\sqrt{\frac{KK_0}{N_{df}}}\frac{dW}{\sqrt{\tau_T}} \tag{2.19}$$

where K is the kinetic energy and dW refers to the Brownian motion term. This thermostat produces a correct canonical ensemble and still has the advantages of the Berendsen thermostat.

Nosé-Hoover temperature coupling

The Berendsen velocity rescaling thermostat is suitable for relaxing a system to a given temperature but, for true MD, a more accurate thermostat is needed that explores a correct canonical ensemble. An extended ensemble approach was first proposed by Nosé [76] and later modified by Hoover [77] which extends the system Hamiltonian by introducing a thermal reservoir and a friction term ξ to the equations of motion. The friction parameter is a fully dynamic quantity with its own momentum p_ξ. The equations of motion for the particles becomes:

$$\frac{d^2\mathbf{r}_i}{dt^2} = \frac{\mathbf{F}_i}{m_i} - \frac{p_\xi}{Q}\frac{d\mathbf{r}_i}{dt} \tag{2.20}$$

and for the heat bath:

$$\frac{dp_\xi}{dt} = (T - T_0). \tag{2.21}$$

where T_0 is the reference temperature defined in the simulation parameters. The strength of the coupling can be determined by the mass parameter constant Q:

$$H = \sum_{i=1}^{N}\frac{p_i}{2m_i} + U(r_1, r_2, ..., r_N) + \frac{p_\xi^2}{2Q} + N_{df}k_BT\xi \tag{2.22}$$

The mass parameter can then be described in terms of the oscillation period τ_T for kinetic energy between the system and the reservoir:

$$Q = \frac{\tau_T^2 T_0}{4\pi^2} \tag{2.23}$$

which provides a much more intuitive way of selecting the coupling strength since τ_T is independent of the system size and reference temperature.

In summary, the weak coupling scheme as used by the Berendsen and the velocity rescaling thermostats provides a strongly damped exponential relaxation of the temperature deviation, ideal for equilibrating systems, whereas the Nosé-Hoover approach produces an oscillatory relaxation, which leads to more accurate MD simulations.

2.1.6 Replica exchange

Also known as *parallel tempering*, replica exchange is a technique that allows systems to overcome relatively high energy barriers and explore possible conformations that may not be achievable with a standard MD simulation. In short, we simulate or "sample" multiple replicas of the same system at different temperatures. The samples can then be randomly exchanged between two temperatures with the probability:

$$P(1 \leftrightarrow 2) = \min\left(1, \exp\left[(\frac{1}{k_B T_1} - \frac{1}{k_B T_2})(U_1 - U_2)\right]\right) \tag{2.24}$$

where U_1 and U_2 are the instantaneous potential energies of two given replicas. After two replicas have been swapped, the velocities are scaled by $(T_1/T_2)^{\pm 0.5}$ so that the correct Boltzmann sampling is achieved [78, 79].

However when using pressure coupling, the density at higher temperatures will decrease, leading to higher energy. To compensate, a modification to Equation 2.24 was proposed by Okabe *et al.* [80] to include the respective pressures:

$$P(1 \leftrightarrow 2) = \min\left(1, \exp\left[(\frac{1}{k_B T_1} - \frac{1}{k_B T_2})(U_1 - U_2) + \left(\frac{P_1}{k_B T_1} - \frac{P_2}{k_B T_2}\right)(V_1 - V_2)\right]\right) \tag{2.25}$$

where V_1 and V_2 are the respective instantaneous volumes in the simulations. In most cases the differences in volume are small enough that the last term is negligible, but when the difference between P_1 and P_2 becomes large, the last term begins to affect the probability significantly.

2.1.7 Ewald summation

The Ewald summation is a numerical approach to approximate the long range electrostatic contributions acting on each atom in a system. In general, the electrostatic contributions of N atoms, including their periodic imagines, can be determined by:

$$V = \frac{1}{2}\sum_{i=1}^{N}\sum_{j=1}^{N}\frac{q_i q_j}{4\pi\varepsilon_0 r_{ij}}, \tag{2.26}$$

where i and j are atomic indexes and r_{ij} is the minimum distance between two atoms. This can be expanded to include additional terms when treating the system and its periodic images as a lattice:

$$V = \frac{1}{2}\sum_{n_x}\sum_{n_y}\sum_{n_z}\sum_{i=1}^{N}\sum_{j=1}^{N}\frac{q_i q_j}{4\pi\varepsilon_0 \mathbf{r}_{ij,\mathbf{n}}}, \tag{2.27}$$

where $\mathbf{r}_{ij,\mathbf{n}}$ is the real distance (not the minimum-image) between two atoms and $\mathbf{n}$ represents a cell in the cubic lattice at point $\mathbf{n} = (n_x L, n_y L, n_z L)$, where n_x, n_y, n_z are integers. This method is problematic in that it converges extremely slowly and is *conditionally convergent*, meaning that the order in which the terms are considered results in different outcomes.

The solve this, the Ewald approach considers each charge to be surrounded by a neutralising Gaussian charge distribution of equal magnitude but opposite sign. This allows the electrostatic contributions to be split into a sum of the interactions between charges (direct) and their neutralising distribution (reciprocal), and includes a third term to correct for the interactions of each Gaussian with itself:

$$V = V_{dir} + V_{rec} + V_0, \tag{2.28}$$

where:

$$V_{dir} = \frac{f}{2}\sum_{i,j}^{N}\sum_{n_x}\sum_{n_y}\sum_{n_z} q_i q_j \frac{\operatorname{erfc}(\beta\, r_{ij,\mathbf{n}})}{r_{ij,\mathbf{n}}}, \tag{2.29}$$

$$V_{rec} = \frac{f}{2\pi V}\sum_{i,j}^{N} q_i q_j \sum_{m_x}\sum_{m_y}\sum_{m_z}\frac{\exp(-(\pi\mathbf{m}/\beta)^2 + 2\pi i\mathbf{m}\cdot(\mathbf{r}_i - \mathbf{r}_j))}{\mathbf{m}^2}, \tag{2.30}$$

$$V_0 = -\frac{f\beta}{\sqrt{\pi}}\sum_{i}^{N} q_i^2. \tag{2.31}$$

β is a parameter that determines the relative weight of each sum, and $\mathbf{m}$ is

the wave vector defined as $\mathbf{m} = (m_x, m_y, m_z)$. The erfc term is know as the complimentary error function, defined as:

$$\text{erfc}(x) = \frac{2}{\sqrt{\pi}} \int_x^\infty \exp(-t^2) dt. \tag{2.32}$$

As the Ewald summation considers reciprocal charges for every charge in the lattice, this approach requires a neutrally charged system for the summation to converge.

2.2 Model lipid bilayers

The simulations presented within this thesis focus on five bilayer compositions. The first is POPE/POPG (3:1): a negatively charged bilayer comprising *1-palmitoyl-2-oleoyl-sn-glycero-3-phosphoethanolamine* (POPE), a neutrally charged lipid with a mixture of saturated and unsaturated lipid tails and a zwitterionic headgroup containing an ethanolamine group (NH_3); and *1-palmitoyl-2-oleoyl-sn-glycero-3-phosphoglycerol* (POPG), a negatively charged lipid with the same lipid tails to POPE, and a glycerol group containing two oxygen atoms on the headgroup. This bilayer composition forms a model bacterial membrane and carries an overall negative charge, making it highly attractive to cationic peptides. Its transition temperature has been determined to be around 298-299 K [81].

The second bilayer composition is another model bacterial membrane containing a quaternary mixture of *1,2-dioleoyl-sn-glycero-3-phosphoethanolamine* (DOPE), *1,2-distearoyl-sn-glycero-3-phosphoethanolamine* (DSPE), *1,2-dioleoyl-sn-glycero-3-phosphoglycerol* (DOPG), and *1,2-distearoyl-sn-glycero-3-phosphoglycerol* (DSPG). The full bilayer is referred to as DOPE/DSPE/DOPG/DSPG and has a ratio of 3:3:1:1 for the respective lipids. Similarly to the POPE/POPG bilayer, this composition contains neutrally charged PE lipid headgroups and negatively charged PG lipid headgroups, and also contains a mixture of saturated and unsaturated lipid tails. The transition temperature of this mixture is not precisely known.

The third bilayer composition is *1-palmitoyl,2-oleoyl-sn-glycero-3-phosphocholine* (POPC), a neutrally charged bilayer comprising a mixture of saturated and unsaturated lipid tails and a choline headgroup (CH_3). This is a model eukaryotic bilayer with a transition temperature of 271 K [81].

The fourth bilayer composition is POPC/POPG (3:1). This bilayer was created as a direct comparison with a POPE/POPG bilayer, replacing the smaller PE headgroups with bulkier PC headgroups to result in a bilayer that displaces a larger surface area.

The fifth bilayer composition is *1,2-dipalmitoyl-sn-glycero-3-phosphocholine* (DPPC), a neutrally charged bilayer comprising two saturated tails and a choline headgroup, and has a transition temperature of 314 K [81]. This bilayer was created to represent a bilayer with a high gel content (L_β phase) at room temperature.

Each bilayer was constructed using the CHARMM-GUI membrane builder [82, 83], comprising 200 lipids per leaflet[1]. Due to incompatibilities with the CHARMM-GUI output and GROMACS, the MD software NAMD (version 2.9) was used to perform a minimisation of the membranes for 2000 steps. The water and ions were also removed prior to minimisation as NAMD encounters errors in systems containing over 100,000 atoms. After minimisation, topologies were constructed using the program `pdb2gmx` with the CHARMM36 force field, and new water and ions were added using the programs `genbox` and `BoxMod` (as described in Chapter 3). To safely solvate the membranes using genbox, the "van der Waals trick" was employed, which is described in the GROMACS tutorial by Justin A. Lemkul [84]. Following solvation, a small void existed between the water and lipid headgroups which was fixed by applying position restraints to the lipids and equilibrating the system for 50ps, allowing the water and ions to soak into the lipid headgroup region. The bilayers were further minimised in GROMACS and then equilibrated for 50-100ns using the Parrinello-Rahman and Nosé-Hoover coupling schemes. Double bilayers were then constructed by duplicating the single bilayer and placing it on top of itself, removing additional waters such that the separation between bilayers was approximately 5 nm. The double bilayers were then equilibrated for 100 ns.

[1]The POPE/POPG (3:1) bilayer comprised 192 lipids per leaflet.

Chapter 3

Advancing software for the study of lipid bilayers through MD

3.1 Background

The nature and behaviour of lipid bilayers has been widely studied with MD since the parameterisation of the first phospholipid force fields in the 1990s. The first bilayer studies comprised DPPC and DMPC bilayers with 18-50 lipids per leaflet and were simulated on timescales in the range of 100 ps to 1 ns [85–87]. As bilayer simulations were new, these studies employed "in-house scripting" to measure the various membrane-specific properties from the MD trajectories, such as fluidity, area per lipid (APL), bilayer thickness and order parameters. These measurements could then be directly compared with measurements obtained through experimental techniques to confirm their validity.

Lipid bilayer simulations conducted today are considerably more complex than those conducted 20 years ago, whereby planar bilayer simulations typically involve 100-200 lipids per leaflet conducted on timescales of tens to hundreds of nanoseconds for atomistic force fields, and up to tens of microseconds for coarse-grained force fields. Furthermore, the number of parameterised phospholipids has expanded considerably, and as such many simulations employ lipid bilayer mixtures containing two or more types of phospholipids, sterols or other molecules. In addition, various studies have simulated more complex types of bilayers such as double bilayers, vesicles, micelles and virus capsids [88–91].

As lipid bilayer simulations continue to evolve, there is a surprising lack of available analytical tools targeted for the analysis of membrane-specific properties. Many publications still employ in-house scripting, which is a highly inefficient use of time and can lead to analytical mistakes and inconsistencies between publications. Several of the existing analytical tools are reviewed in Section 3.1.1, where the abilities and limitations of each tool are discussed.

Tools specifically targeted at the construction of membrane systems are also rare; most existing construction tools are primarily designed for protein in water simulations and can be problematic when used for membrane systems. One such example is the program `genbox`, a construction tool provided with the GROMACS package used to solvate simulation boxes [63]. When solvating membranes, this program incorrectly inserts water molecules within the hydrophobic core of the membrane. Another example is the GROMACS tool `genion`, a program to set the ionic concentration of a system by replacing water molecules with ions. This program accepts an ionic concentration as an input parameter and determines the number of ions to insert based on the volume of the box. This approach is accurate for protein in water systems as the protein displaces very little volume; however, as membranes displace a much larger volume in the simulation box, this approach leads to incorrect ionic concentrations. Furthermore, as the water molecule selection is random, this approach is incompatible with membrane systems that contain compartments such as double bilayers, vesicles and capsids, as they require identical ionic concentrations in each compartment to avoid inadvertently establishing a membrane potential.

One example of a construction tool that is targeted specifically for membrane systems is CHARMM-GUI [83], a tool to construct lipid bilayers with customised lipid compositions. This is a powerful and easy to use tool that is entirely web-based, and therefore requires no installation. The main disadvantage of this tool is that the output files are primarily designed to work with the CHARMM [92] and NAMD [93] MD packages. Once the bilayer has been constructed, a selection of output files are provided which includes a trajectory file containing the atomic coordinates of the membrane; however, this membrane has not been energy minimised and encounters an error when trying to minimise in GROMACS. The membrane must first be energy minimised using CHARMM or NAMD before it can be ported to GROMACS. Furthermore, when creating a bilayer that leads to a system with 100,000+ atoms (which is typical of most modern bilayer simulations), this program produces formatting errors in the trajectory file, which

can only be corrected by removing some or all of the water molecules (to reduce the number of atoms) and adding them back at a later stage.

3.1.1 Review of existing tools

This section reviews a selection of the existing tools targeted for the analysis of membrane-specific properties. An analysis of the advantages, disadvantages and common flaws in each tool can assist in the design of a new membrane analysis tool.

g_order

The GROMACS tool `g_order` is a program to measure the order parameters of acyl chains [63] (which will be discussed further in Section 3.2.1). These measurements are often presented in studies involving lipid bilayers to quantify the level of fluidity in the bilayer. As `g_order` is contained within the GROMACS package, it requires a complete install of GROMACS to operate, which has many dependencies such as FFTW [94] and GCC [95]. `g_order` was originally designed to measure the order parameters for united-atom force fields; however, a more accurate approach is available for atomistic force fields which is currently not utilised by `g_order`. Furthermore, the approach used by `g_order` incorrectly calculates the order parameters for double-bonded carbon atoms in unsaturated lipid tails. In addition, this program requires user-created index files containing the atom types for each carbon atom in each lipid tail, which is a complicated and tedious process that must be repeated for each analysis. These index files are also static, meaning `g_order` cannot be used to generate order parameters for a dynamic region of the bilayer, such as the annular shell of lipids surrounding molecules (in which lipids are continuously entering and exiting the shell). `g_order` requires a GROMACS tpr file to operate, meaning it is restricted to a GROMACS-only analysis and as such it would be difficult (but not impossible) to analyse trajectories produced by other MD packages.

In summary, `g_order` is capable of measuring order parameters from a wide range of trajectory formats; however, it could be greatly improved by removing the dependency for a user-generated index file, which could easily be generated automatically. Furthermore, `g_order` could be greatly improved by utilising a more accurate approach to determining atomistic order parameters, which

would also allow for the correct measurement of double bond order parameters in unsaturated lipid tails.

GridMAT-MD

`GridMAT-MD` is a program to measure the APL and bilayer thickness from a trajectory file [96], and requires no installation due to the choice in language (Perl). The APL is measured by assigning each lipid to a cell in a 2D grid of polygons and then averaging the area of each polygon. `GridMAT-MD` will also subtract the area of any proteins or peptides embedded in the membrane. The coordinates of the polygons are plotted to a file which can be visualised using another program. The bilayer thickness is determined by measuring the separation between paired lipids on each leaflet using a user-specified reference atom. These lipids are paired based on their proximity to each other, where only the z-distance is used. The final bilayer thickness is averaged over each paired lipid, and `GridMAT-MD` also produces a data file containing a 2D lattice to be visualised by another program. Because APL and bilayer thickness are relatively simple calculations, this program is force field independent. `GridMAT-MD` is limited to the analysis of single planar bilayers.

As with the other tools, the analysis of a trajectory using `GridMAT-MD` requires a user-constructed parameter file that contains information about the system to be analysed. This includes the names of the lipids, water and ions, the number of frames and the number of lipid types within the trajectory, and whether the system contains any protein molecules. At first glance, many of these input parameters seem unnecessary; for example, the parameter file asks for the names of each lipid type contained within the trajectory, and therefore it is unnecessary to also ask for the number of lipid types. Furthermore, as there are only a handful of lipid types currently parameterised, it would not be overly difficult to automatically scan the trajectory to determine which lipid types exist within the membrane. It is also unnecessary to ask how many frames are in the trajectory file, as any algorithm capable of reading a trajectory file could easily detect this automatically. This may seem trivial, but these unnecessary input parameters cost additional time and effort during the analysis and may lead to analytical mistakes.

In summary, `GridMAT-MD` provides a comprehensive algorithm to determine membrane APL and thickness; however each analysis requires a user-generated

parameter file that must be configured for each system, and requires information that could easily be determined automatically. `GridMAT-MD` is also limited to gro and pdb (uncompressed) trajectory file formats, which are slow to read and utilise much larger files than compressed trajectory formats. Furthermore, as pdb and gro trajectories (containing multiple frames) are not natively produced by most MD packages, this will likely require a conversion to this format which will incur additional time and effort. This tool could be greatly improved by adding the ability to read compressed trajectory files such as GROMACS xtc and trr files.

g_lomepro

`g_lomepro` is a unified membrane analysis tool capable of measuring membrane thickness, APL, membrane curvature and order parameters [97]. This tool utilises a similar technique to that employed by `GridMAT-MD` to generate the APL and membrane thickness. The order parameters are calculated using the same approach employed by `g_order`; however a different formula is used to calculate the order parameters for double-bonded carbon atoms in unsaturated lipid tails, yielding the correct values when compared with `g_order`.

`g_lomepro` is currently the most comprehensive unified membrane analysis tool available, containing four analytical techniques for various membrane-specific measurements. This tool works with GROMACS trajectory files and is entirely dependent on a complete GROMACS installation. As this tool is written in the C language, it requires compilation which may be difficult for the inexperienced (and sometimes the experienced) user, and may be problematic on non-Linux operating systems. This also means `g_lomepro` would require a recompilation each time a new GROMACS version is installed, and may not be compatible with newer versions. Similarly to `g_order`, `g_lomepro` requires a GROMACS tpr file to operate and would likely be problematic for the analysis of trajectories produced by other MD packages.

In summary, `g_lomepro` provides a broad range of analytical techniques in one unified tool, making it ideal for many types of lipid bilayer simulations. However, due to the choice in language, `g_lomepro` is difficult to install and is therefore limited to the experienced user (n.b. I consider myself an experienced user and I could not get `g_lomepro` to install successfully). This choice of language is where tools like `GridMAT-MD` and CHARMM-GUI have an advantage over `g_lomepro` in that they do not require compilation. It is also worth noting that `g_lomepro` does

not appear in any search engine results and has not been updated since early 2014. There is also no mention of its usage with double bilayers, asymmetric bilayers and spherical bilayers, so it is assumed that its analysis is limited to single planar bilayers.

3.1.2 Aims and software design

In Section 3.1.1, several existing tools targeted at the analysis of membrane-specific properties were reviewed. The advantages of each tool were highlighted, and several common flaws were identified that greatly reduced the usability of each tool. With these in mind, any future tool targeted at the analysis of membrane-specific properties should have the following specifications:

- Employ a wide range of analytical techniques in one unified tool.
- Be written in a language that is usable across a range of operating systems and requires no compilation.
- Minimise user input, avoiding the use of parameter files and avoiding user-specified variables that could otherwise be determined automatically.
- Be compatible with as many file formats (especially compressed trajectory files) and force fields as possible.
- Be able to interpret as many bilayer types as possible (single, double, asymmetric, vesicle, etc.)

Section 3.2 presents `Membrainy`: a 'smart', unified membrane analysis tool designed and constructed using the specifications listed above. This tool was required for the analysis of the simulations presented throughout this thesis, as existing tools were insufficient for the types of analysis required, and not suitable for double bilayers. Each analytical component within `Membrainy` was tested using a variety of lipid bilayer systems, and each result was confirmed by comparing it to those produced either with existing tools, experimental data, or judged for logical consistency. This tool is also presented in Publication 1.

Section 3.3 presents the tools `BoxMod`, `MoleculeInserter` and `SmoothGraph`. `BoxMod` (Section 3.3.1) is a tool used to set the ionic concentrations of single or double bilayers, and can be used to establish ion imbalances between membrane

compartments. `MoleculeInserter` (Section 3.3.2) is a tool used to insert molecules into a lipid bilayer system. `SmoothGraph` (Section 3.3.3) is a tool to remove fluctuations in analytical plots due to poor sampling, enhancing its presentation and assisting in the interpretation of meaningful data.

3.2 Membrainy

`Membrainy` is an intelligent membrane analysis tool that endeavours to provide both the inexperienced and experienced user access to a wide range of analytical techniques to enable the measurement of various membrane-specific properties from planar bilayer trajectories [98]. `Membrainy` was designed for simplicity and ease of use, requiring no compilation and minimal user input to operate. As the range of lipid bilayer studies is broad, `Membrainy` was designed to automatically interpret a variety of bilayer compositions and force fields, and is capable of interpreting single, double and asymmetric bilayers. `Membrainy` can also interpret dynamic membranes that undergo structural changes such as lipid flip-flopping and pore formation, and employs different analytical approaches when switching between atomistic, united-atom or coarse grained force fields.

A suite of ten analytical techniques is integrated within `Membrainy`. These include the following:

1. **Acyl chain order parameters:** a measurement to quantify the degree of order in the lipid tails, which is often associated with lipid fluidity [99–101].
2. **Headgroup orientations:** a measurement of the angles observed in the lipid headgroup relative to the membrane surface, which are known to be sensitive to electric charges and dipole fields [102].
3. **Area per lipid (APL):** a measurement to quantify the average surface area consumed by each lipid within the membrane.
4. **Lipid mixing/demixing entropy:** a quantification of the level of mixing between two or more lipid types, which plays an important role in a wide variety of cellular functions including DNA fusion and phase transitions [103].
5. **Time evolution of the transmembrane voltage (TMV):** a measurement to monitor changes in the TMV, which may be of particular

importance in electrophysiology or electroporation simulations [104–106].

6. **2D surface maps:** a high resolution 2D representation of the bilayer surface, which is particularly helpful when looking at defects, undulations and gel clusters that may not be easily observable in 3D visualisation software.

7. **Gel percentage:** a quantification of the level of fluidity in the bilayer, determined by measuring the linearity of the lipid tails.

8. **Leaflet and membrane thickness:** a measurement which may be of importance in simulations where bilayers undergo electrostriction [107].

9. **Leaflet symmetry:** a measurement used to detect and quantify lipid flip-flopping, which may be useful in bilayers containing transient water pores [108].

10. **Annular shell analysis:** an ability to perform a separate analysis on the annular shell of lipids surrounding molecules, whether inserted or in close contact with the membrane surface, which may be helpful in understanding how these molecules affect the local properties of the membrane, such as changes in lipid tail flexibility [109].

`Membrainy` is written in Java, a language that is widely used in all modern architectures and operating systems. As programs written in Java are precompiled, they require no compilation or installation to operate, which is highly advantageous when compared with tools written in other languages such as C. Java also provides for the safe execution of multithreaded code, allowing much of the analytical components within `Membrainy` to be conducted in parallel. `Membrainy` also contains performance boosting multithreaded algorithms to enhance its functionality, such as algorithms for using multiple threads to load larger trajectory files, and algorithms for preloading the next frame in the trajectory while the current frame is being analysed.

To minimise user input, the algorithms within `Membrainy` automatically detect and interpret each membrane system. On loading the trajectory files, `Membrainy` constructs a system box which contains an array of atoms, where each atom stores the atomic positions, velocities, atom type, residue identification (resID) and the residue name. An algorithm then converts this array of atoms into an array of molecules, where each molecule is constructed based on its resID as

atoms containing the same resID belong to the same molecule. `Membrainy` then scans the array of molecules to determine which lipids (and sterols) exist in the system. This is done by accessing a database containing every four letter lipid and sterol name parameterised within `Membrainy`. The geometric centre of the bilayer is calculated, and then each lipid is assigned to a corresponding leaflet by comparing the height of the phosphorous atom in each lipid with the geometric centre of the bilayer. This calculation can be done once for static bilayers or can be performed on every frame for dynamic bilayers that may undergo structural changes to the leaflets such as pore formation or lipid flip-flopping. Flip-flopping occurs when the phosphorous atom crosses the geometric centre of the bilayer, causing the algorithm to assign the lipid to the opposite leaflet. `Membrainy` also contains an algorithm to automatically detect double bilayers, which is achieved by comparing the separation between the geometric centre of the lowest and highest lipid in the system. If the z-component of this separation is greater than 6 nm (which is slightly larger than a typical bilayer thickness) then a double bilayer is assumed. `Membrainy` then calculates a geometric centre for each bilayer, and applies the same algorithm to assign each lipid to one of the four leaflets.

`Membrainy` has an inbuilt force field library containing information on systems utilising the CHARMM36, Berger/GROMOS87 and Martini v2.0 lipid parameters, and other force fields will likely be implemented in the future. This library contains a list of the atom types used by each lipid tail, the bond lengths and angles for lipid tails and water molecules, and various other force field specific information. This removes the dependency for the user to provide detailed information about each membrane system being analysed, allowing each analytical component within `Membrainy` to operate efficiently and accurately, and eliminates the possibility of human error. `Membrainy` contains an algorithm to automatically detect the force field used in the trajectory files, which is achieved by comparing the lipid headgroup atom types with those stored in the library.

`Membrainy` is written in Java, a language that is compatible with all modern architectures and operating systems. `Membrainy` requires no installation, a particular benefit over existing software written in C/C++ which requires some knowledge to install and rarely compiles without a hitch. `Membrainy` is entirely object-orientated and written such that adding to or modifying the source code is easy. The core code is multithreaded and contains various performance boosting algorithms designed to optimise the workload across all processors, and additional analytical components can easily be written and implemented into `Membrainy`

without the need to modify the core code.

`Membrainy` has only been available to download for a short time and has already received interest from many scientists in the field. `Membrainy` is freely available to download at **www.membrainy.net** and contains the following analytical components:

3.2.1 Order Parameters

The measurement of acyl chain order parameters is a technique used to describe the degree of freedom and flexibility in the lipid tails and has a direct correlation with membrane fluidity [99–101]. Deuterium order parameters are typically obtained through 2H-NMR (Deuterium Nuclear Magnetic Resonance) and are plotted as an entropy (S_{CD}). In MD systems, order parameters for saturated and unsaturated lipid tails in atomistic force fields are calculated from the equation:

$$S_{CD} = \left\langle \frac{3cos^2\theta - 1}{2} \right\rangle, \tag{3.1}$$

where θ is the angle the C−H bond vectors along the lipid tails make with the membrane normal [110], taken as the z-axis for planar bilayers. This approach utilises each individual C−H bond in the lipid tails. As united-atom force fields lack non-polar hydrogen atoms, the above equation is modified to include the relation:

$$S_{CD} = \frac{2}{3}S_{xx} + \frac{1}{3}S_{yy}, \tag{3.2}$$

which is derived from the order parameter tensor [111], and achieved by defining molecular axes where the z-axis encompasses the C_{i-1}−C_{i+1} vector, the y-axis lies on the plane containing C_{i-1}−C_i−C_{i+1}, and the x-axis is orthogonal to the y and z axes. The angles that the x and y axes make with the membrane normal is then used to determine S_{xx} and S_{yy} from Eqn. 3.1. This approach is utilised by `g_order` for both atomistic and united-atom force fields. Martini order parameters are calculated from the equation:

$$P_2 = \frac{1}{2}\left(3\, cos^2\left\langle\theta\right\rangle - 1\right), \tag{3.3}$$

where θ is the angle between the lipid tail bonds and the membrane normal.

The final order parameter for each technique is averaged over all leaflets in the

system, and `Membrainy` will also produce separate order parameters for each lipid type and leaflet. For atomistic and united-atom force fields, `Membrainy` plots the values of $-S_{CD}$ for each carbon along the lipid tails. This experiences maximum order at 0.5 and disorder at -1, whereas the Martini force field experiences maximum order at $P_2 = 1$ and disorder at $P_2 = -0.5$. The resulting order parameters plot can be directly compared to other order parameter plots to reveal changes in lipid tail flexibility and membrane fluidity, or can be compared with 2H-NMR measurements. `Membrainy` can also produce histograms of the angles measured by each technique. To maximise performance, the order parameter algorithms are multithreaded, where each lipid tail type (e.g. POPE-palmitoyl, POPE-oleoyl, etc.) is assigned its own thread, allowing much of the analysis to be conducted in parallel.

To achieve these measurements, `Membrainy` constructs an index of all acyl chains in the system by determining each lipid tail type and loading the corresponding carbon atom types from its inbuilt force field library. This is a significant improvement over the existing tool `g_order`, which requires these indices to be user-constructed. As `Membrainy` contains three approaches for generating order parameters based on whether the force field is atomistic, united-atom or coarse grained, the appropriate algorithms are automatically selected based on the force field in use. If an atomistic force field is detected, `Membrainy` will also index the hydrogen atoms connected to each carbon atom, which allows for the C−H bond vectors to be calculated. The membrane normal is set to (0,0,1) for upper leaflets and (0,0,-1) for lower leaflets.

As an exemplar, a POPE/POPG (3:1) double bilayer was simulated for 50 ns in the CHARMM36 force field at 297 K using the HECToR supercomputer (1024 cores), and the saturated and unsaturated order parameters were measured using both `g_order` and `Membrainy`. Figures 3.1a-b depict a comparison of these measurements, revealing that both programs produced near identical order parameters for saturated and unsaturated lipid tails, with the exception of the double bond region in the unsaturated lipid tails (Figure 3.1b, carbon numbers 8 and 9) in which `g_order` calculates incorrectly. To produce these results, `Membrainy` was executed with a single command line which initiates the analysis without the need for user input or parameter files. In comparison, `g_order` required the use of the tool `make_ndx` to generate three lipid tail index files containing the saturated, unsaturated, and double bond indices. These require a user input of each lipid tail carbon atom type, which are located within the force

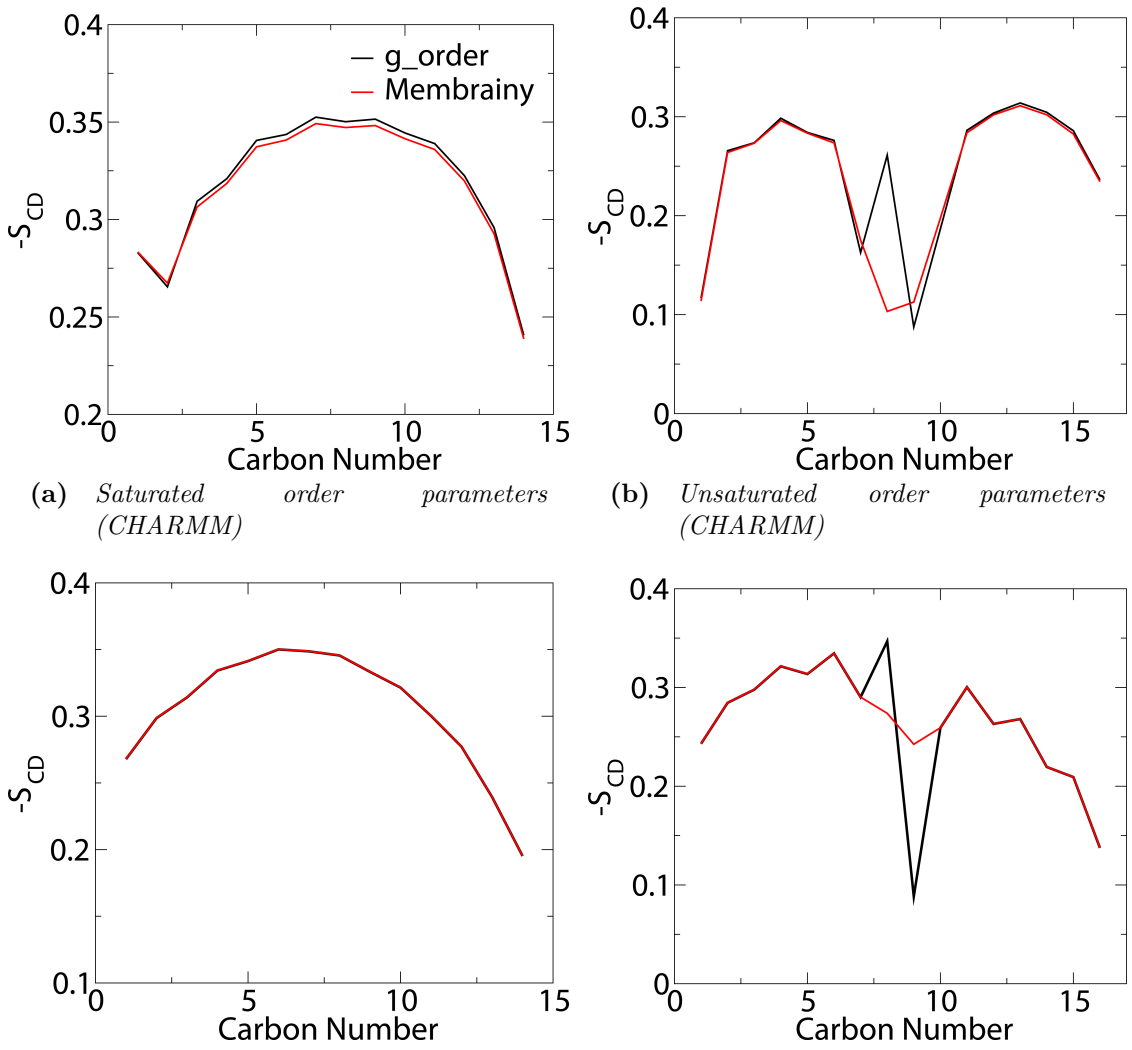

(a) *Saturated order parameters (CHARMM)*

(b) *Unsaturated order parameters (CHARMM)*

(c) *POPE saturated order parameters (Berger/GROMOS)*

(d) *POPE unsaturated order parameters (Berger/GROMOS)*

Figure 3.1 *Saturated and unsaturated order parameters for lipid tails in a POPE/POPG (3:1) double bilayer at 297 K, where (a) and (b) employ the CHARMM force field, and (c) and (d) employ the Berger/GROMOS force field. Measurements are made using the tools* `g_order` *and* `Membrainy`*. Both tools yield similar order parameters in the CHARMM force field, and identical order parameters in the Berger/GROMOS force field. However* `g_order` *incorrectly calculates the order parameters in the double bond region of unsaturated lipid tails ((b) and (d), carbon numbers 8 and 9).*

field parameter files and can be difficult to interpret (this interpretation requires the knowledge of which atom types are bonded to each other). Once interpreted, each atom type must be manually typed into `make_ndx` in the correct sequence before executing. Saturated and unsaturated order parameters must be calculated separately, and unsaturated double bonds require a third execution of `g_order`.

This entire setup process takes 15-20 minutes for an experienced user and must be repeated for each system under analysis. In comparison, there is no setup for `Membrainy` (and therefore takes 0 minutes). `g_order` executes the analysis slightly faster than `Membrainy` due to a more efficient trajectory reader; however, the additional time cost incurred from creating the index files makes `Membrainy` the overall faster tool.

Similarly, a POPE/POPG (3:1) double bilayer was simulated for 50 ns in the Berger/GROMOS force field at 297 K (512 cores), and a similar analysis was conducted on POPE lipid tails only (Figure 3.1c-d). Both `Membrainy` and `g_order` yield identical order parameters, with the exception of the double bond region in the unsaturated lipid tails (Figure 3.1d, carbon numbers 8 and 9) which `g_order` calculates incorrectly. Calculating the order parameters using `g_order` incurs additional time when using the Berger/GROMOS force field, as the atom types in POPE and POPG lipid tails are different. This means that a total of six executions of `g_order` (and `make_ndx`) is needed to produce a full average of saturated and unsaturated order parameters in this system. In comparison, `Membrainy` requires only a single execution to generate a full average of each order parameter.

These result suggests that `Membrainy` produces more accurate results than `g_order` in the CHARMM force field, and identical results in the Berger/GROMOS force field. Furthermore, `Membrainy` shows an overall speed increase over `g_order` when analysing a system, and requires no user input to operate.

3.2.2 Annular shell analysis

When a peptide, protein or other molecule comes into contact with a bilayer, whether in contact with the bilayer surface or fully inserted into the bilayer, the properties of the lipids within a given radius or *shell* of the peptide may be modified. This may be in the form of molecules changing the rotational freedom or orientation of the lipid headgroups, or molecules changing the local fluidity of the bilayer. `Membrainy` identifies those lipids within the annular shell surrounding a molecule and performs an analysis on those lipids (Figure 3.2). This analysis can then be compared with a control group comprising lipids selected from outside of the shell in the same leaflet.

`Membrainy` isolates the annular shell of lipids around a molecule by calculating a

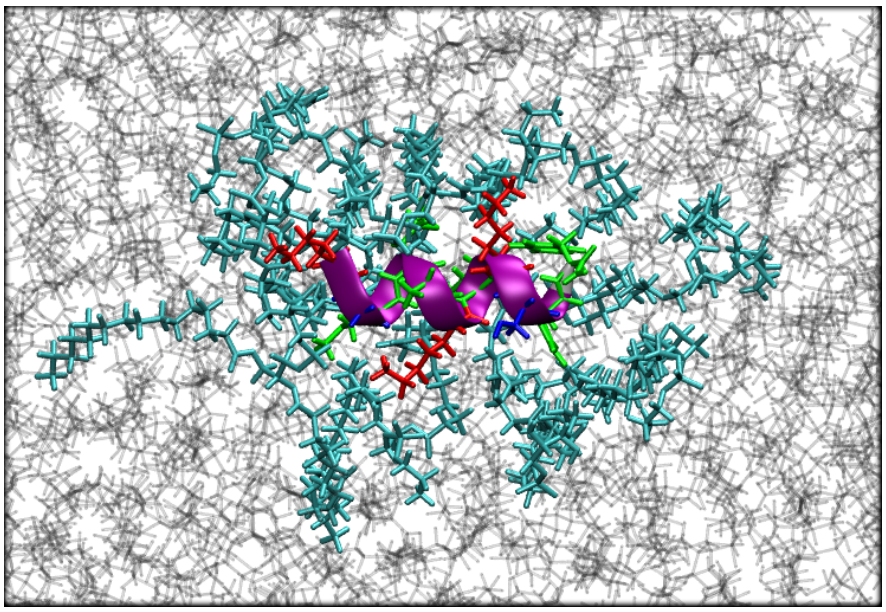

Figure 3.2 *The first annular shell of lipids (shown in turquoise) surrounding an inserted amphipathic peptide.*

distance vector between each atom in the bilayer and each atom in the molecule. If the distance between any two atoms is within a user-specified radius (the default is 4 Å), the lipid is counted as being within the shell. These lipids can then be analysed to determine their properties. A control group can also be established by selecting random lipids outside of the shell from the same leaflet, comprising either a fixed number of lipids, an identical number of lipids to those found within the shell, or all lipids outside of the shell. `Membrainy` also contains an algorithm to exclude gel lipids from the control group, as many proteins and peptides are known to show selectivity for inserting into fluid regions [112]. Gel lipids are identified using the same technique described in Section 3.2.7. If multiple molecules are present, the user may specify one, several or all molecules to construct annular shells, and `Membrainy` will assign a thread to each molecule, populating the shells in parallel. The output plots contain an average of all shells in the system. `Membrainy` is also fitted with an annular shell analysis algorithm to produce detailed records of which lipids occupy the shell at any given time and which lipids spend the longest time in the shell. In mixed bilayer compositions, `Membrainy` will plot the ratio of lipid types found within the shell over time.

The method of calculating a distance vector between the atoms in molecules with the atoms in lipids is a computationally expensive one. To improve performance, these calculations are multithreaded such that each molecule receives its own thread. Furthermore, the leaflet nearest to the molecule is identified every few

frames and only the lipids from that leaflet are used in the distance calculations. `Membrainy` is also capable of scanning only the lipid headgroups or tails when determining if a lipid lies within the shell, which may be advantageous when considering the contact between the molecules and only one part of the lipid.

An exemplar of this tool is provided in Chapter 5 (Section 5.3.3), where the amphipathic peptide MinD-MTS was inserted into a POPE/POPG (3:1) double bilayer, and `Membrainy` was used to investigate the changes in order parameters to the lipids in the first annular shell of this peptide.

3.2.3 Time evolution of the TMV

With the main focus of double bilayer simulations being aimed at the study of TMVs, the ability to monitor the time evolution of the TMV may be important in understanding changes to the TMV from various biophysical phenomenon such as electrostriction and electroporation. Specifically for electroporation simulations, pore formation can be identified by a sharp drop in TMV due to ion transport through the pore, and the gradient of this drop can determine the rate of voltage loss. Changes in the TMV may also occur when bilayers undergo the flip-flopping of charged lipids, as changes in the charge distribution between leaflets may affect the TMV. The electrostatic potential across a bilayer can be determined from a double integral of Poisson's equation:

$$\Psi(z) = -\frac{1}{\varepsilon_0}\int_0^z dz' \int_0^{z'} \rho(z'')dz'', \tag{3.4}$$

and is achieved by splitting the simulation box into "slices" along the z-axis and calculating the charge density in each slice [113]. The box is then corrected such that $\Psi(0) = 0$. `Membrainy` outsources this task to the GROMACS tool `g_potential` as the force field library within `Membrainy` lacks non-lipid parameters. The TMV against time measurements are achieved by splitting the full trajectory into smaller trajectories and calculating the electrostatic potential in each trajectory. The TMV can then be extrapolated from each smaller trajectory and recombined to produce a TMV against time measurement over the full trajectory. This extrapolation is achieved by intelligently scanning the electrostatic potential output file to measure the average voltage across the central water compartment, a task which is not easy as `Membrainy` must predict the

central compartment boundaries based on changes in the electrostatic potential gradients, which differ greatly depending on the strength of the TMV. Several checks are made within this algorithm to prevent false predictions, and `Membrainy` will also alert users to TMV calculations it thinks may be inaccurate.

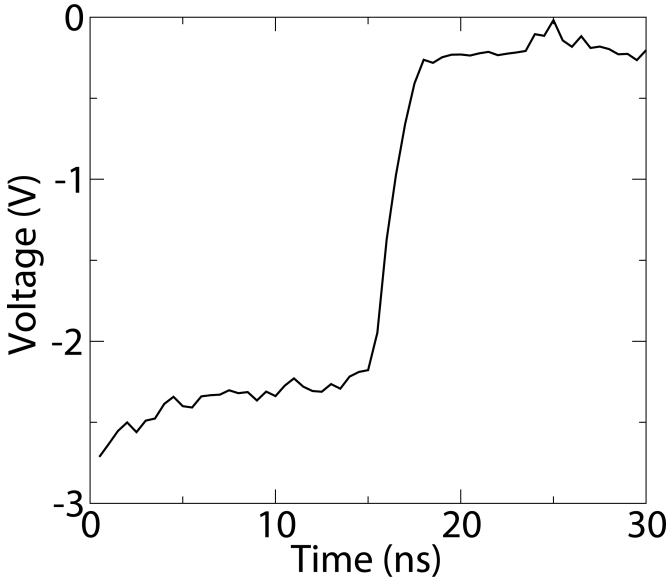

Figure 3.3 *The time evolution of the TMV across a POPE/POPG (3:1) double bilayer at 297 K with an ion imbalance of +20. The plot indicates a pore formed at ∼15 ns, followed by a sharp drop in TMV as ions were transported through the pore, resulting in a dissipation of the ion imbalance. The resulting TMV is indicative of the remaining ion imbalance (+2).*

Numerous electroporation simulations were conducted for 30 ns using POPE/POPG (3:1) double bilayers at 297 K (1024 cores). These systems were initially established with ion imbalances of +20, achieved by moving 10 cations from the inner (anodic) water compartment to the outer (cathodic) water compartment, similar to the approach taken by Sachs *et al.* [88]. Transient water pores were observed to form after a random time interval, allowing both cations and anions to travel through the pores in opposite directions, resulting in a loss of the initial ion imbalance. `Membrainy` was used to monitor the time evolution of the TMV for each simulation, one of which was chosen as an exemplar and is referred to throughout this Chapter. Figure 3.3 depicts the TMV against time measurements for this simulation, revealing an initial TMV of -2.65 V, which lowers to -2.35 V during the first 5 ns due to the lateral expansion of the bilayers undergoing electrostriction (which is discussed in Section 5.1.2). Once a pore had formed, a sharp drop in TMV is observed at a rate of 0.75 V/ns, corresponding to ion transport through the pore at a rate of 3 ions/ns. The resulting TMV is indicative

of the remaining ion imbalance (+2). These measurements provide an informative way to monitor changes to the TMV during a trajectory, and can be used in electroporation simulations to determine the time at which a pore is formed and the rate at which the TMV is dissipated.

3.2.4 Bilayer and Leaflet Thickness

As lipid tails are more linear when in the gel phase, they produce thicker bilayers. As the temperature increases, the flexibility of the lipid tails increases which results in a loss of linearity and subsequent thinning of the bilayer. Bilayer thickness measurements can be used to determine changes in fluidity and phase transitions [114, 115]. Furthermore, bilayer and leaflet thickness can be useful when looking at electrostriction effects [107, 116].

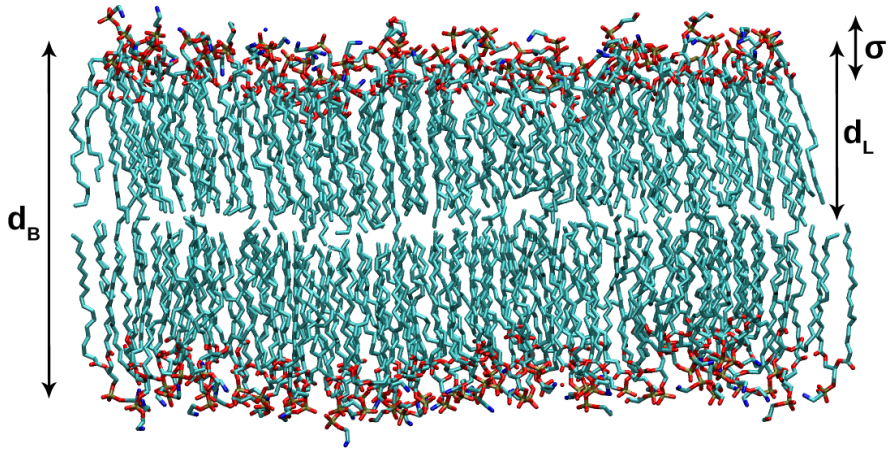

Figure 3.4 *Bilayer and leaflet thickness measurements d_B and d_L, and the standard deviation in the thickness σ.*

`Membrainy` measures bilayer and leaflet thickness (d_B and d_L) by averaging the heights of the phosphorous atoms in each leaflet (Figure 3.4). Membrane thickness is then calculated by subtracting the average phosphorous height from two opposing leaflets, and leaflet thickness is calculated by subtracting the average phosphorous height with the geometric centre of the bilayer. Standard deviations in thickness can also be calculated from the height variations of the phosphorous atoms, which is useful when determining the level of perturbations experienced by the bilayer surface.

Measurements of the bilayer and leaflet thickness were made on the previous electroporation simulation (Figure 3.5), which reveals that the bilayers and leaflets experience a thinning prior to pore formation due to electrostriction. Upon pore

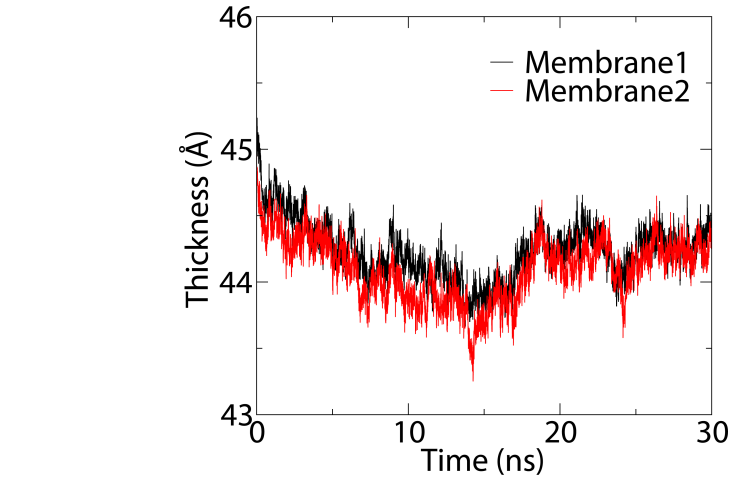

(a) *Membrane thickness*

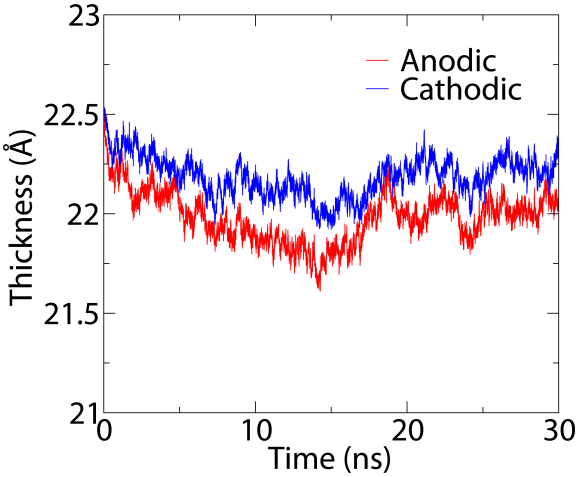

(b) *Leaflet thickness*

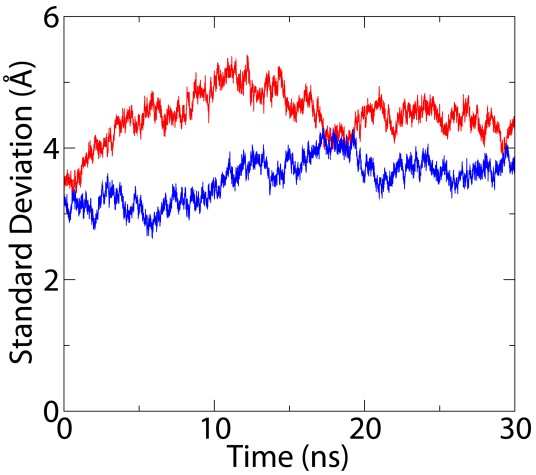

(c) *Standard deviation in leaflet thickness*

Figure 3.5 *Measurements of (a) membrane thickness, (b) leaflet thickness and (c) standard deviations in the leaflet thickness of a POPE/POPG (3:1) double bilayer undergoing electroporation at ∼15 ns. Prior to pore formation, membrane and leaflet thickness decrease due to electrostriction, and both increase immediately after pore formation. The anodic leaflets also appear slightly thinner than the cathodic leaflets, and show increased standard deviations in the leaflet thickness suggesting a more perturbed leaflet.*

formation, the bilayers and leaflets begin to expand as the TMV is reduced, allowing the bilayers to relax towards their initial thickness. Interestingly, the anodic leaflets are consistently thinner than the cathodic leaflets, which was also observed by Böckmann *et al.* [117]. Measurements of the standard deviations in leaflet thickness reveal that both leaflets become more perturbed, with greater perturbations in the anodic leaflets. These measurements show `Membrainy` to be an effective tool to monitor changes in membrane and leaflet thickness upon

environmental perturbations such as a TMV.

3.2.5 Area per lipid

Area per lipid (APL) is a measurement that describes the average surface area that lipids would occupy within the membrane, and is another structural property of the membrane that has a correlations with membrane fluidity [118]. Bilayers in the gel phase exhibit lower APLs due to a tighter packing of the lipids, and bilayers in the fluid phase exhibit larger APLs from the increased mobility of the lipids. The APL is therefore highly specific to the temperature and lipid types found in the membrane, as lipids with larger headgroups displace more surface area. As an example, POPE lipids have a small ethanolamine headgroup and both a saturated and unsaturated lipid tail, and have been measured to occupy an APL of 56.6 $Å^2$ at 30°C [119]. SOPC lipids (1-stearoyl-2-oleoyl-sn-glycero-3-phosphocholine) have a larger choline headgroup and also have a mixture of saturated and unsaturated lipid tails (with the saturated tail containing an additional two carbons compared with POPE), and they occupy an APL of 64.3 $Å^2$ at 30°C. This increase in APL is primarily due to choline headgroups displacing more surface area in the bilayer. `Membrainy` offers a simple APL calculation, achieved by dividing the box xy area with the number of lipids per leaflet, which is then plotted against time. `Membrainy` is also capable of producing multiple APLs when an asymmetric bilayer is detected.

As an exemplar, `Membrainy` was used to measure the APL from the previous electroporation simulation (Figure 3.6), revealing an initial APL of 50.75 $Å^2$ followed by a sharp increase within the first few nanoseconds corresponding to the lateral expansion of the bilayers from electrostriction, and a steady increase prior to pore formation. As pore formation occurs, the APL sharply increases to accomodate for the area consumed by the pore. The APLs between leaflets also differ during pore formation, suggesting that some lipid headgroups are sitting in the pore and occasionally cross the geometric centre of the bilayer (which may lead to lipid flip-flopping). The APL sharply drops between 15-18 ns as the TMV is dissipated and the bilayers relax, reaching a relatively constant APL of 51.7 $Å^2$ by 30 ns. The APLs between leaflets are also consistently different during the final 5 ns, suggesting that lipid flip-flopping has occurred. To determine the validity of this analytical component, the tool `g_energy` was used to output the box dimensions, which were then converted into an APL via simple scripting.

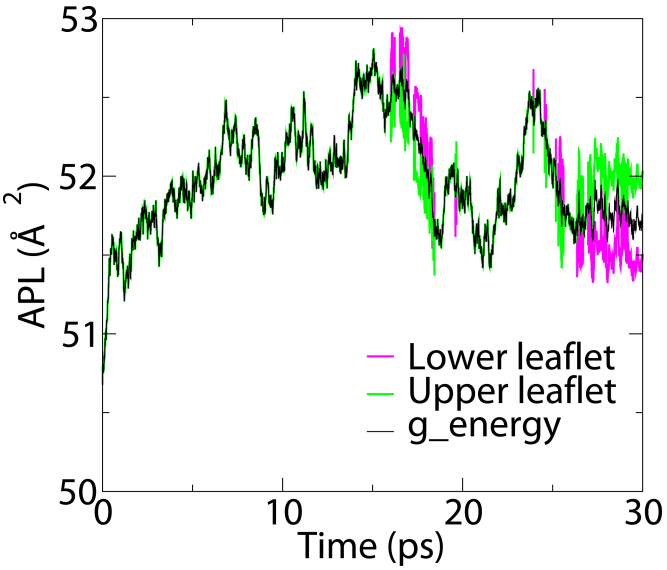

Figure 3.6 *APL measurements of a POPE/POPG (3:1) bilayer undergoing electroporation at ∼15 ns. Prior to pore formation, the APL steadily increases by ∼2 Å, after which the APL steadily decreases to a relatively stable value. This result was confirmed using the tool* `g_energy`. `Membrainy` *shows the APL to differ between leaflets after pore formation, suggesting lipid flip-flopping may have occurred.*

This plot (also depicted on Figure 3.6) confirms the validity of `Membrainy`, and correctly shows an average APL between leaflets when flip-flopping has occurred.

3.2.6 Lipid flip-flopping

Transmembrane lipid translocation, more commonly known as lipid flip-flopping, is the process in which lipids are translocated between the two opposing leaflets of a bilayer [120]. This translocation occurs from both passive and active transport mechanisms and plays a crucial role in the maintenance of asymmetric cell membranes [121]. Lipid flip-flopping has been documented in a number of studies, many of which involved pore-forming peptides suggesting a possible link between pore formation and lipid flip-flopping [122–125]. Lipid flip-flopping has also been observed in simulated DMPC bilayers through electroporation, whereby lipids translocate through transient water pores in both directions [108].

`Membrainy` automatically detects lipid flip-flopping when scanning the bilayers on each frame, and has the ability to produce a plot of leaflet symmetry over time. This symmetry is calculated by subtracting the number of lipids in the cathodic leaflets from the number of lipids in the anodic leaflets, and therefore a value of

-2 indicates a single flip-flop to the cathodic leaflet.

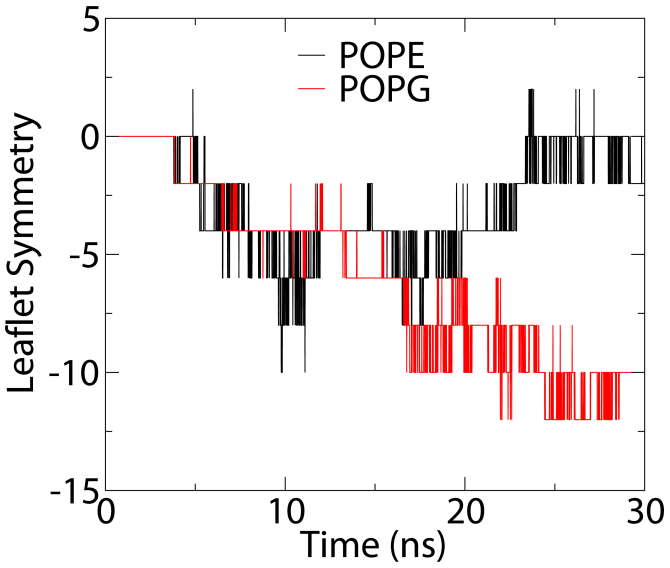

Figure 3.7 *Leaflet symmetry of a POPE/POPG (3:1) double bilayer undergoing electroporation. Pore formation occurs within ∼5 ns, where the leaflet symmetry reveals the pore is constructed with lipids from the anodic leaflet. By 30 ns, all but one POPE lipid had returned to the anodic leaflet (and one POPE lipid had translocated from the cathodic to anodic leaflet), which is shown as a leaflet symmetry of 0. POPG symmetry reveals a value of -10, suggesting five POPG lipids had flip-flopped to the cathodic leaflet. This suggests POPG lipids show an increased tendency to flip-flop towards the cathodic leaflet through transient water pores in TMV simulations.*

`Membrainy` was used to detect lipid flip-flopping during a 30 ns simulation of a POPE/POPG (3:1) double bilayer (1024 cores), in which an ion imbalance of +20 was maintained with position restraints. A pore formed within 5 ns and remained open for the duration of the simulation. Fig. 3.7 depicts leaflet symmetry measurements during the simulation revealing that, upon pore formation, both POPE and POPG plots show negative symmetry, suggesting that the toroidal structure of the pore mainly comprises POPE and POPG lipids from the anodic leaflet. This is likely due to the tendency for transient water pores to initiate formation from the anodic water compartments, as observed by Böckmann et al. [117]. After 15 ns, the POPE symmetry returns to zero, indicating that the distribution of POPE lipids across both leaflets has equalised; however, the POPG symmetry steadily decreases, indicating that POPG lipids are translocating through the pore towards the cathodic leaflet. By 30 ns, one POPE lipid in each leaflet has flip-flopped and five POPG lipids have flip-flopped to the cathodic leaflet. This suggests that POPG lipids experience a greater tendency to flip-flop

through transient water pores in bilayers subject to a high voltage TMV, in which the POPG lipids are translocated towards the cathodic leaflet, likely due to the additional forces acting on the anionic POPG headgroups from the electric field. `Membrainy` has therefore detected and interpreted lipid flip-flopping through a transient pore within this system.

3.2.7 Gel percentage

The gel content of a bilayer can be represented as a percentage by considering the distance between the first and last carbon atoms on a lipid tail for an ideal gel lipid. This distance is made up from a series of carbon-carbon bonds with a length and angle predefined by the force field. By knowing these lengths and angles, the number of carbons in the lipid tail, and the number of double bonds, simple trigonometry can be used to determine the distance between the first and last carbons for a perfectly linear lipid tail (Figure 3.8).

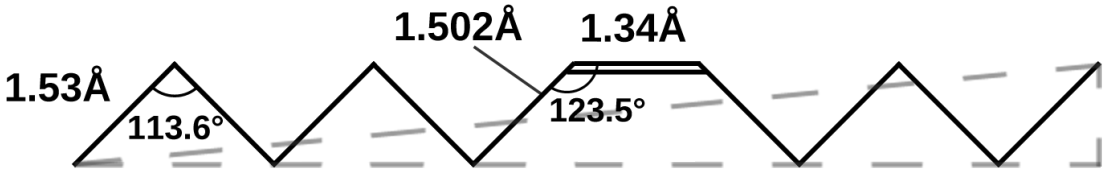

Figure 3.8 *Method of calculating the length of a perfectly linear lipid tail by using the force field bond lengths and angles with trigonometry. The lengths and angles displayed are taken from the CHARMM36 force field.*

`Membrainy` is equipped with an algorithm to calculate this length for any lipid tail, including those that are yet to be implemented. The carbon-carbon bond and double bond lengths are all hard coded into `Membrainy` from each implemented force field, as well as the carbon-carbon-carbon angles and carbon-carbon=carbon angles (the latter being the double bond angle). `Membrainy` will identify the lipid tails within the bilayer and calculate the separations between the first and last carbon atoms in the tails for each lipid. These lengths are compared to the length of an ideal lipid tail, and any lipid tail length above a user-specified tolerance is counted as a gel lipid. A final overall gel percentage is produced and plotted against time. Examples of gel percentage calculations are presented in Section 3.2.8.

3.2.8 2D Surface Maps

The membrane surface can be represented in a 2D map by binning the heights of each atom in each leaflet into a 2D lattice and applying the Gauss-Seidel method

$$\phi_{i,j}^{n+1} = -\frac{1}{4}\left[A_{i,j} - \left(\phi_{i-1,j}^{n} + \phi_{i+1,j}^{n} + \phi_{i,j-1}^{n} + \phi_{i,j+1}^{n}\right)\right] \tag{3.5}$$

where $A_{i,j}$ is the highest atom in cell i,j, $\phi_{i,j}^{n+1}$ is the resulting scalar value produced by the method, and the final term is the sum of the neighbouring cells' scalar values. Iterating over this method produces a scalar field of successive displacement, generating a series of Gaussians that can be scaled and mapped to a colour to produce a contour map of the leaflet surface. These maps also behave as density maps, producing more prominent Gaussians in regions of the lattice containing a high density of atoms, such as lipid tails in the gel phase. As the Gauss-Seidel method is one of successive displacement, the lattice must be recalculated many times ($\sim$100-200 iterations) in order to fully populate each cell. There is a "sweet spot" for the number of iterations used; too few and the lattice will not be sufficiently populated, and too many will lose the resolution of the individual lipids on the lattice and flatten the Gaussians. The resolution of the lattice also has a sweet spot which, through trial and error, is roughly 4 cells per angstrom when using 100 iterations of the Gauss-Seidel method.

Once the lattice has been populated, each cell is scaled to a number between 0 and 1, and mapped to a colour. Values of 0 are presented as blue, which represents thin or sparsely populated regions of the lattice; values of 1 are presented as red, which represents thick or densely populated regions of the lattice; and values of 0.5 are represented as green, which typically represents fluid regions. Values in the range [0,0.5] and [0.5,1] are represented as proportionate mixes of green and blue, and green and red respectively. Black areas represent a hole or pore in the leaflet, which is identified by unpopulated regions of the lattice. A map for each leaflet is displayed through an inbuilt graphical interface in real-time and can be saved as an image. `Membrainy` will also overlay the positions of molecules and ions on the maps, where the N-terminus of peptides and proteins are highlighted in dark purple. This inbuilt graphical interface is highly advantageous as it removes the dependency to require other software to visualise this analysis. As iterative approaches can be computationally expensive, each leaflet is assigned its own thread allowing the maps to be generated in parallel.

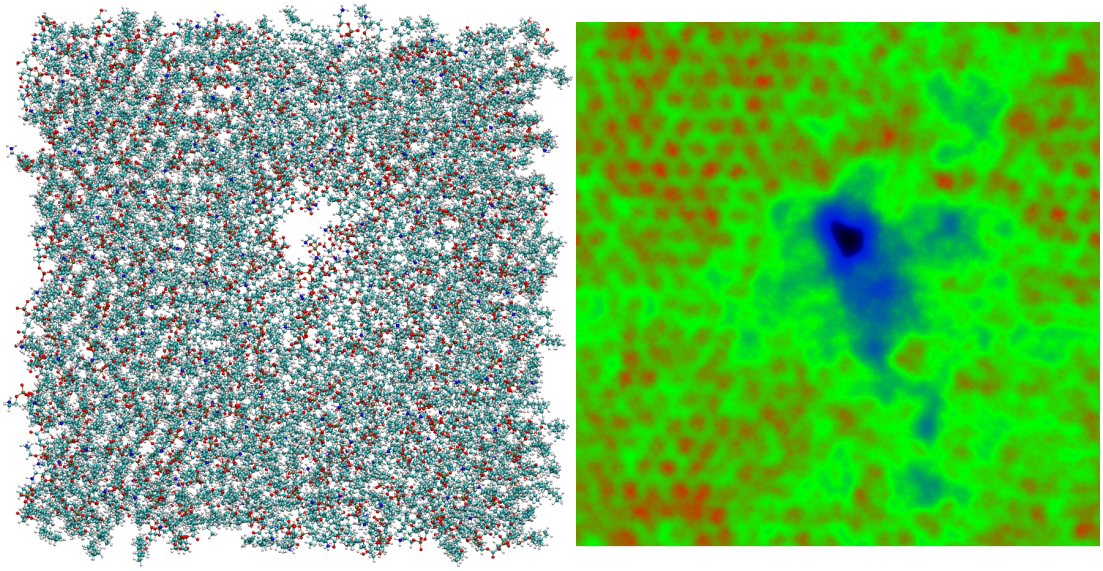

Figure 3.9 *Example of a 2D surface map (right) from a leaflet containing a pore, displayed using* `VMD` *(left). The maps are colour coded such that blue indicates thin or sparsely populated regions, red indicates thick or densely populated regions, with green in between. Hexagonally packed red dots indicate gel clusters, and black indicates a pore or hole.*

By modifying the resolution of the map and number of iterations of the method, it is possible to tune the map such that it captures the landscape of individual lipids in great detail, with visual similarities to high resolution atomic force microscopy (AFM). Lipids in the gel phase appear as hexagonally packed red dots due to the lipid tails establishing a densely populated region on the lattice (where one red dot represents one lipid tail), and the hexagonal packing is a natural property of lipid tails in a highly ordered phase [126].

There are many 3D visualisation programs, such as `VMD` [127] and `Pymol` [128], capable of visualising a lipid bilayer from all orientations; however, in these 3D representations it is often difficult to visualise thin spots, perturbations and defects in the bilayer and on the bilayer surface. As a 2D representation contains far less detail, it becomes much easier to visualise this. One such example is depicted in Figure 3.9, where the bilayer from the previous electroporation simulation was imaged immediately after pore formation using `VMD`, and compared with its corresponding 2D surface map. This map reveals the presence of gel regions throughout the bilayer (approximately 50%) and also shows a thin region of the bilayer extruding away from the pore. The green region around the pore also suggests the pore formed in a fluid region of the bilayer.

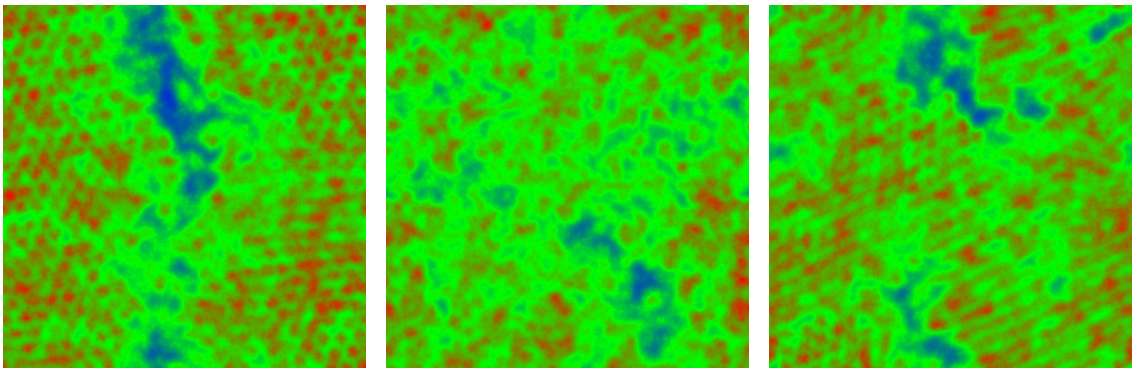

(a) *POPE/POPG 297 K* **(b)** *POPC 297 K* **(c)** *DPPC 297 K*

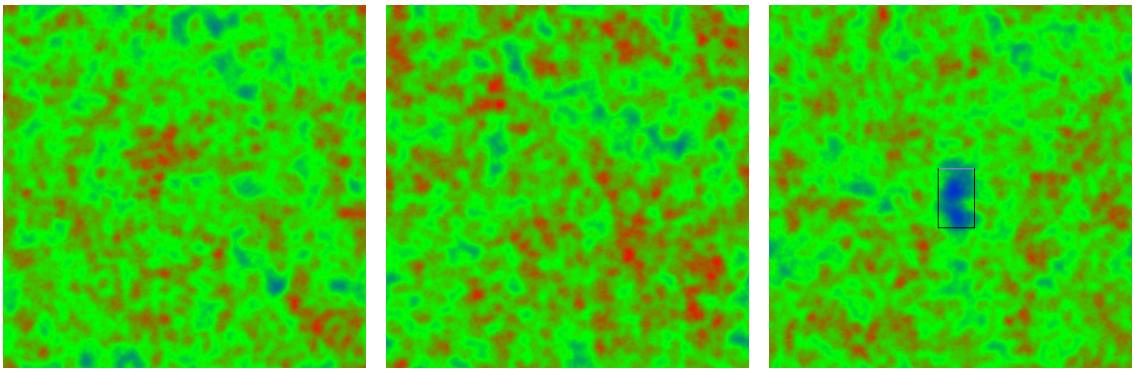

(d) *POPE/POPG 320 K* **(e)** *POPC 320 K* **(f)** *Peptide insertion*

Figure 3.10 *Measurements of (a) membrane thickness, (b) leaflet thickness and (c) standard deviations in the leaflet thickness of a POPE/POPG (3:1) double bilayer undergoing electroporation at ∼15 ns. Prior to pore formation, membrane and leaflet thickness decrease due to electrostriction, and both increase immediately after pore formation. The anodic leaflets also appear slightly thinner than the cathodic leaflets, and show increased standard deviations in the leaflet thickness suggesting a more perturbed leaflet.*

As further examples, six surface maps were generated from various bilayers conducted at different temperatures, and `Membrainy` was used to determine the gel percentages of each bilayer. Figures 3.10a and d depict a POPE/POPG (3:1) bilayer at 297 K and 320 K respectively. As the transition temperature for this bilayer composition is between 298-299 K [81], `Membrainy` detected ∼53% gel at 297 K and ∼14% gel at 320 K, which is accurately portrayed in each surface map and confirms that this bilayer composition has undergone a phase transition between the temperatures. Similarly, Figures 3.10b and e depict a POPC leaflet at 297 K and 320 K respectively, for which `Membrainy` detected ∼16% gel at 297 K and ∼14% gel at 320 K. These percentages correspond to bilayers in the fluid phase, which is in agreement with a transition temperature of 271 K for POPC bilayers [81], and is accurately portrayed in each surface map.

Figure 3.10c depicts a DPPC bilayer at 297 K, in which `Membrainy` detected ∼85% gel. This percentage is in agreement with a transition temperature of 314 K for DPPC bilayers [81], and is accurately portrayed in the surface map. Interestingly, this surface map shows gel lipids in the tilted $L_{\beta'}$ phase which is represented by the smudged appearance in the gel domains and has an orientation of ∼30 degrees to the x axis. Figure 3.10f depicts the surface map of the MinD-MTS peptide inserted into a POPE/POPG (3:1) bilayer at 300 K (where this simulation is presented in Section 5.3.3). This map shows the location of the peptide in the bilayer and reveals the size and shape of the defect within the bilayer. `Membrainy` has therefore provided an alternate means to visualise the membrane surface through the generation of 2D surface maps, which presents information about the membrane shape and structure that would otherwise be difficult to determine from a 3D representation.

3.2.9 Headgroup Orientations

The lipid headgroup is the polar interface between the membrane core and the intracellular/extracellular spaces and has been observed to exhibit sensitivity to electric charges, dipole fields, and temperature effects [129, 130]. These headgroups exhibit a degree of flexibility around their phosphorous hinge (Figure 3.11), and experimental techniques have shown the headgroup to sit roughly perpendicular to the lipid tails with a variation of around 30 degrees to the membrane surface [102, 131]. In MD simulations, measurements of lipid headgroup orientations can provide an effective means to compare bilayers undergoing environmental perturbations, such as those under the influence of a TMV.

`Membrainy` measures lateral headgroup orientations θ by establishing a vector between two reference atoms in the headgroup, one being the phosphorous atom and the other being another atom on the headgroup (which is usually polar). This vector is then projected onto the membrane normal to produce an angle. `Membrainy` then bins these angles into a histogram in the range -90 to 90 degrees, where a value of 0 indicates the headgroup is parallel to the membrane surface and positive angles indicate the headgroup is pointing away from the membrane. Axial headgroup orientations ϕ are calculated by projecting the headgroup vector onto the membrane surface, taken as the xy plane, to produce a radial angle between 0 and 360 degrees. Each axial angle is plotted for each lipid over time.

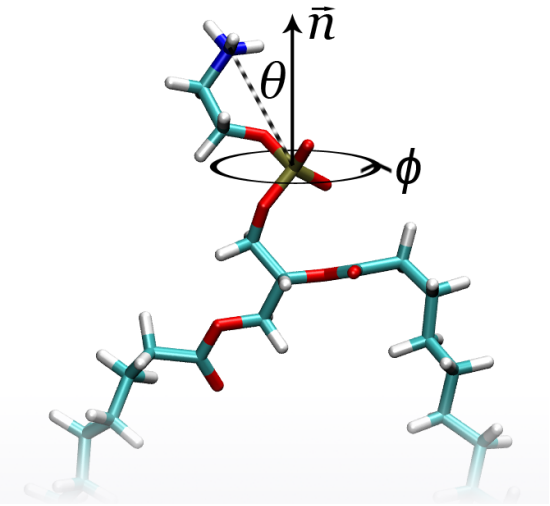

Figure 3.11 *Method of calculating headgroup orientations for lipids. A vector is established between two reference atoms, one being the phosphorous atom and the other being the polar atom. Lateral headgroup angles θ are produced by projecting this vector onto the membrane normal, and axial angles ϕ are produced by projecting this vector onto the XY plane and calculating its angle to the x-axis.*

This algorithm is multithreaded, where each lipid type is assigned its own thread and run in parallel.

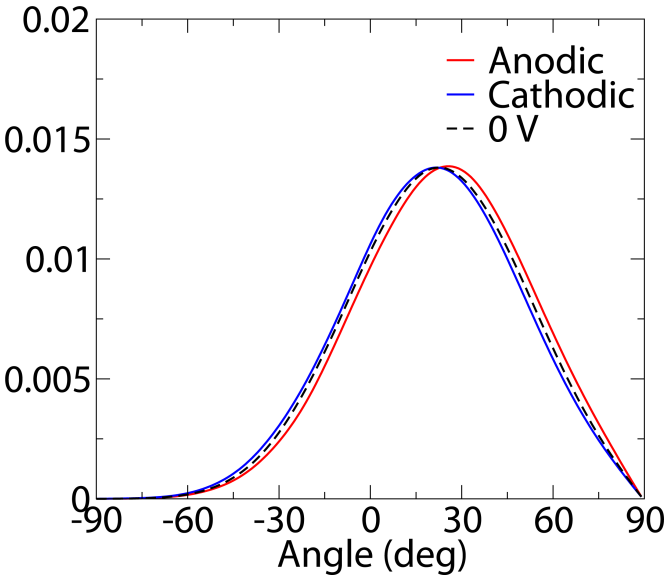

Figure 3.12 *Headgroup orientations of a POPC double bilayer subject to a TMV of -1.95 V. The anodic and cathodic leaflets are compared with a no-TMV (0V) double bilayer, which reveals a shift of +2.5 degrees for anodic leaflets and -1.5 degrees for cathodic leaflets. This shift suggests the headgroups are tending to align with the electric field.*

As an exemplar, a POPC double bilayer was equilibrated for 100 ns without a

TMV, after which a 30 ns simulation was conducted using an ion imbalance of +28, achieving a TMV of -1.95 V. `Membrainy` was used to measure the headgroup orientations before and after applying a TMV, which were then smoothed with the program `SmoothGraph` (see Section 3.3.3) and depicted in Figure 3.12. These measurements yield a mean angle of 23 degrees in both leaflets without a TMV, and mean angles of 25.5 and 21.5 degrees in the anodic and cathodic leaflets respectively after applying a TMV. This reveals a shift of +2.5 degrees in the anodic leaflets and -1.5 degrees in the cathodic leaflets, suggesting that the headgroups in both leaflets are tending to align with the electric field. These measurements are comparable to those found by Böckmann *et al.* [117], who conducted simulations of POPC bilayers subject to an applied electric field. This study also saw a positive shift for anodic leaflets and a negative shift for cathodic leaflets, with roughly the same magnitude.

3.2.10 Lipid Mixing/Demixing Entropy

As all known eukaryotic and prokaryotic membranes contain more than one type of lipid, many model lipid bilayer simulations are conducted using phospholipid and sterol mixtures. These mixtures are not always ideally mixed; many studies have reported the presence of *lipid demixing* where individual lipid types cluster together to form domains [132–134]. Various MD studies have also observed demixing effects in lipid bilayers [135–137].

`Membrainy` has the ability to quantify the level of lipid mixing/demixing as an entropy, which provides a measure of the two-dimensional spatial heterogeneity of any lipid bilayer system, and a means to study changes following an environmental perturbation. This entropy follows the formula:

$$S(x_1,..,x_N) = N \sum_{x_i,nb_i} p(x_i, nb_i)\, log\, p(x_i \mid nb_i), \tag{3.6}$$

as provided by Brandani *et al.* [138], where $p(x_i, nb_i)$ is the probability of finding a lipid of type x_i neighboured to a lipid of type nb_i, and $p(x_i \mid nb_i)$ indicates the conditional probability that a lipid is of type x_i given that its neighbour is of type nb_i. `Membrainy` calculates this entropy by running a distance calculation between two reference atoms (usually the phosphorous) for each lipid in a leaflet in order to determine the nearest neighbouring lipid and its type. This information is then binned into a probability matrix and is normalised such that the total probability

is always 1. This can then be used with Equation 3.6 to calculate an entropy. A theoretical maximum entropy can be calculated from:

$$S_{max} = -\sum \rho_{x_i} \, log \, \rho_{x_i}, \tag{3.7}$$

where ρ_{x_i} is the density of a lipid of type x_i. `Membrainy` also produces a scaled entropy such that $S_{max} = 1$.

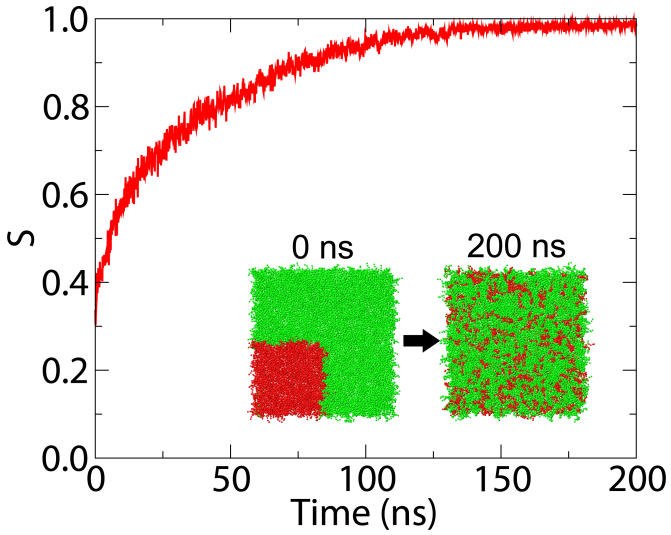

Figure 3.13 *Lipid mixing entropy of a POPE/POPC (3:1) bilayer over 200 ns, scaled such that $S_{max} = 1$. The bilayer was initially constructed such that the POPC lipids (red) are clustered together in the lower left quadrant. Both lipid types mix together during the simulation, achieving a scaled entropy just below the theoretical maximum for a perfectly mixed system.*

As an exemplar, a bilayer was constructed containing 1512 POPE and 504 POPC Martini lipids, where the POPC lipids were initially clustered together in a quadrant of the bilayer creating a perfectly demixed system. This bilayer was simulated for 200 ns on a quad core linux machine, and its trajectory was analysed by `Membrainy` to produce a scaled mixing entropy over time (Figure 3.13). These measurements reveal an initial entropy of 0.3, which immediately increases as the system began to mix. By ∼150 ns the entropy settles just below the theoretical maximum entropy, indicating the bilayer is fully mixed. `Membrainy` therefore quantifies the level of mixing/demixing in this system.

3.2.11 Conclusion

`Membrainy` is an intelligent membrane analysis tool that not only supplements or replaces existing analytical tools, but also contains a range of analytical techniques to measure membrane-specific properties that have no comparable tool. As lipid bilayer studies continue to evolve, many existing analytical tools fail to interpret newer approaches to simulating bilayers, such as the use of double bilayers and asymmetric bilayers. Furthermore, many existing tools require a considerable amount of user input to install and operate, often requesting information on the trajectory file that could easily be determined automatically. This additional user input can lead to human error and inconsistencies between each analysis. `Membrainy` provides an easy to use tool targeted for both the inexperienced and experienced user, which requires no installation and is compatible with all modern operating systems. `Membrainy` operates with minimal user input, requesting only the user-specified variables required for each analysis (e.g. probe radius, surface map resolution etc.). This is a considerable improvement over existing tools and allows for an overall faster analysis.

Each analytical component within `Membrainy` was tested on a variety of lipid bilayer systems and was found to be either comparable to or an improvement upon existing software. For the analytical techniques that have no comparable software, the results were confirmed using experimental data or judged for logical consistency.

`Membrainy` has now been published in the journal *Source Code for Biology and Medicine* (Publication 1) and is already in use within the MD community.

3.3 Other Tools

The construction and parameterisation of membrane systems, especially double bilayer systems, is often problematic with existing construction tools. There is no convenient method to establish an ion imbalance across a double bilayer, or to assign the correct salt concentration around a bilayer, which includes assigning equal salt concentrations for each membrane compartment. These parameters are usually achieved manually by "copying and pasting" atoms into the trajectory file, which can easily lead to human error and inconsistencies between simulations, as well as being time consuming.

With this in mind, I developed tools to assist in the construction and parameterisation of membrane systems, and are compatible with double bilayers. These include `BoxMod` (Section 3.3.1), a tool designed to manage the salt concentrations in membrane systems, and `MoleculeInserter` (Section 3.3.2), a tool to insert peptides, proteins, and other molecules into a membrane system. These tools not only remove the human error component but also contain safety and sanity checks to remove further human error from incorrect parameterisation of each system.

In addition, I have created the post-analysis tool `SmoothGraph` (Section 3.3.3) that uses progressive and iterative averaging to remove the fluctuations from a data set caused by poor sampling, which is common to many analytical approaches applied to membrane systems. This tool can be used in combination with several analytical tools from `Membrainy`.

I have also created many other tools that are not presented in this thesis. These include:

1. `DoubleBilayerBuilder:` a tool to duplicate and transform a single bilayer into a double bilayer, specifying the exact separation between the bilayers and removing or adding waters if necessary. This tool can also be used to shrink or expand existing double bilayers.

2. `ShrinkBilayer:` a tool to reduce the number of lipids per leaflet by removing lipids, waters and ions from the edges of the simulation box while maintaining equal x and y box dimensions.

3. `PDBtoGro:` a tool to safely convert a membrane pdb file to a gro file, normally done incorrectly by the GROMACS tool `editconf` which changes four letter lipid names to three letter names, thus rendering the file unusable.

4. `PeptideSequencer:` a program to scan a pdb/gro file and list the sequences of any peptides or proteins, which are not easy to obtain from the trajectory or topology.

5. `PeptideMonitor:` a program to monitor a peptide's tilt and height, which may be useful for peptides inserted into a membrane. This also includes the orientation of the hydrophobic face for amphipathic peptides.

6. `ConcentrationChecker:` a program to determine the salt concentration in a system, including those with membrane compartments.

7. `CompartmentScanner:` a program to determine the ion and water imbalance between membrane compartments.

8. `TopologyScanner:` a program to scan a system and generate a GROMACS topology file.

9. `Indexer:` a program to generate a GROMACS index file that contains the indices for each leaflet.

10. `AverageDataSets:` a program to average or merge data sets, which is extremely useful when used in combination with analytical data produced by `Membrainy`.

Finally, I have written an interface to the `Grace` software that allows axis labels, titles, subtitles, and plot legends to be predefined in my tools. This interface is also used extensively within `Membrainy`.

3.3.1 BoxMod

`BoxMod` is a construction tool designed to optimise ionic concentrations, ion placement, and ion imbalances across single and double bilayers. This tool was a necessary and essential development for the management of double bilayer systems as they require the number of ions in each water compartment to be identical, unless intentionally establishing a TMV.

`BoxMod` scans double bilayer systems to determine the number of ions in each compartment. `BoxMod` will then add or remove ions such that each compartment matches a user specified salt concentration. This concentration is defined by the equation:

$$C = \frac{55.5 \times \frac{n_a+n_c}{2}}{n_w}, \tag{3.8}$$

where n_a,n_c and n_w are the number of anions, cations and water molecules in each compartment. If the salt concentration requested is greater than the original salt concentration, `BoxMod` will randomly select water molecules from each compartment and replace them with ions, where the ion takes the atomic coordinates of the oxygen atom in the water molecule. If a lower salt

concentration is selected, `BoxMod` will remove the ions closest to the centre of the water compartments to ensure the ions that have been soaked up by the lipid headgroups are left untouched. These ions are then replaced with water molecules, where the oxygen atom from the water molecule takes the atomic coordinates from the ion, and two hydrogen atoms are generated with a random orientation to the oxygen atom such that they lie on the same plane. `BoxMod` will also issue warnings if the salt concentration requested is very different to the initial salt concentration, as this may be unintentional and would require additional equilibration of the bilayers.

If an ion imbalance is requested for the purpose of establishing a TMV, then cations from the inner water compartment are replaced with water molecules, and water molecules from the outer compartment are replaced with cations. Moving a single cation achieves an ion imbalance of +2 (as one cation is removed and one is added from opposing compartments); therefore it is only possible to achieve an even ion imbalance with this method.

`BoxMod` also completely reorders the molecules in the output file and topology such that they are more readable and informative. This means that a quick glance at the topology file can inform the user of the exact number of ions and water molecules in each compartment, and the number of lipids in each leaflet. This was developed as a safety check for double bilayer systems that may involve TMVs to ensure the correct ion imbalance is used, which normally cannot be determined from the topology file.

3.3.2 MoleculeInserter

`MoleculeInserter` is a program designed to insert peptides into the water compartments around a membrane. This program allows the user to specify the exact separation and orientation of the peptide from the membrane surface. `MoleculeInserter` loads a membrane system and peptides from separate input files and then runs a distance calculation between each atom in the peptide with each atom in the bilayers. If the separation between peptide and bilayer is below a user-specified distance, then the peptide is moved away from the membrane surface until it reaches that distance. The program then removes all waters and ions within a given radius of the peptide (the default is 2.5 Å) and merges the peptides and bilayers into a single output file, generating a new topology.

`MoleculeInserter` allows the user to specify amphipathic helical peptide orientations to the bilayer; the peptide can be rotated such that the hydrophobic face points towards or away from the membrane surface. This may be beneficial in assisting the insertion of that peptide into the membrane, as specific orientations of the hydrophobic face may lead to faster insertion times. The hydrophobic face is located by averaging the geometric centres of each hydrophobic residue. A vector is then established by projecting this average onto a backbone vector, which runs directly through the centre of the helix. The resulting vector produces an orientation for the hydrophobic face in amphipathic peptides, which then allows for the peptide to be rotated around the backbone vector until the hydrophobic face is aligned with the membrane normal.

3.3.3 SmoothGraph

Many of the analytical tools within `Membrainy` use histograms to represent certain data, such as the headgroup orientations and the C−H bond angles in the lipid tails. This is a highly efficient means to present this data in a format that can be easily understood and interpreted. However, histograms rely on a high level of sampling to produce meaningful results, which is sometimes difficult to achieve from simulations of lipid bilayers. As these simulations are typically quite large (100,000+ atoms), the simulationist must carefully choose a trajectory output frequency that is small enough to ensure good data sampling, but large enough to meet the limited storage requirements imposed on the simulationist. This is often a delicate balance which considers the purpose of the simulation, the length of the simulation, and the size of the simulation (or specifically, the number of lipids to be sampled). However, many spontaneous events, such as pore formations, may further limit the window of sampling. Additionally, bilayers with mixed lipid compositions contain fewer lipids of each type, and therefore will also suffer reduced sampling for each lipid type when compared with a bilayer composed of a single lipid type. Poor sampling in a histogram often results in large fluctuations between the data points, producing a plot that lacks visual finesse and increases the difficulty in interpreting any meaningful data.

As an exemplar, `Membrainy` was used to produce a histogram of the anodic and cathodic headgroup orientations from a POPE/POPG (3:1) double bilayer undergoing electroporation, where only 10 ns of sampling was obtained which produces a heavily fluctuating plot (Figure 3.14a). One approach to removing

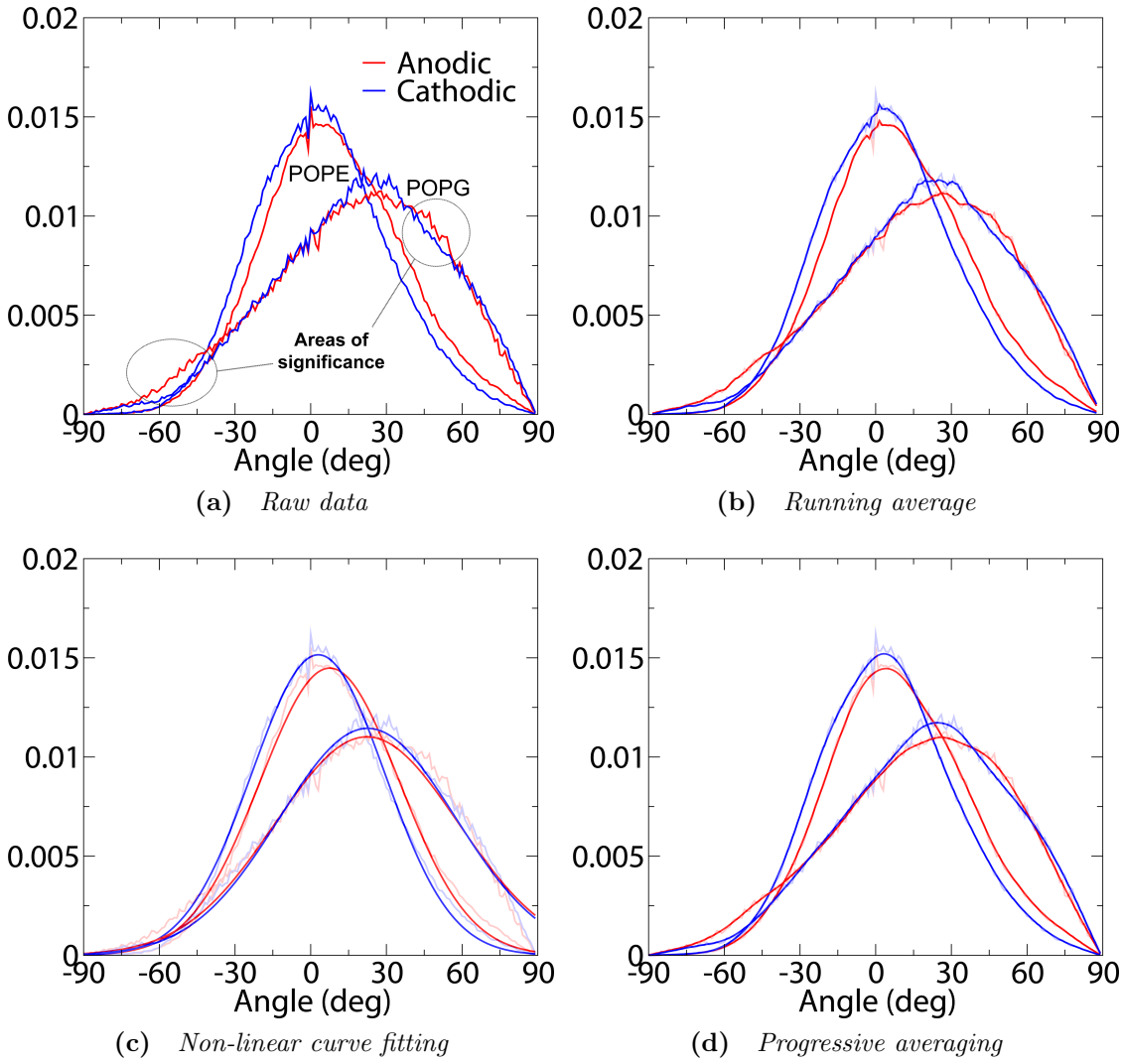

(a) *Raw data* **(b)** *Running average*

(c) *Non-linear curve fitting* **(d)** *Progressive averaging*

Figure 3.14 *Three approaches to smoothing a heavily fluctuating histogram, where (a) is the raw data produced by* `Membrainy`*, (b) uses the tool* `Xmgrace` *to produce a running average, (c) uses the tool* `Xmgrace` *to impose non-linear curve fitting, and (d) uses the tool* `SmoothGraph` *to produce a progressive averaging, resulting in smooth but highly accurate plots.*

these fluctuations is known as a *running average*, employed by the software `Xmgrace`. Although there is no documentation to explain the exact methods used by `Xmgrace`, it is likely that this approach approximates each data point by taking a simple average over N-points either side of the central data point. This approach is unable to calculate averages at the boundaries and, as such, the resulting plots lose the data points at the boundaries. `Xmgrace` was used to smooth the headgroup orientations histogram, specifying a length of average $N = 4$ (Figure 3.14b). From the figure, some of the larger fluctuations have been

removed and the plot remains accurate, encompassing a path close to the original data; however, much of the plot remains unsmooth, and the first and last four data points have been lost. The smoothing can be enhanced by increasing the size of N; however, larger values of N result in a loss of accuracy through changes to the shape of the plot, and also incur a flattening of the peaks (and troughs) and lose even more data points at the boundaries.

As a second approach to smoothing these plots, `Xmgrace` also has the ability to apply non-linear curve fitting to a data set. This was applied to the headgroup orientations histogram using the formula:

$$y = \frac{1}{A_0\sqrt{2\pi}} \; exp\left[-\frac{1}{2}\left(\frac{x - A_1}{A_0}\right)^2\right], \tag{3.9}$$

where A_0 and A_1 are variables automatically determined by `Xmgrace`. The resulting plot shows perfectly smoothed curves that approximately trace the outline of the raw data (Figure 3.14c). However, a closer inspection of these plots reveals that the mean orientations have shifted by a significant amount, which is most noticeable in the anodic POPE plot which shifts by +4 degrees. Furthermore, the plots are inaccurate around the boundaries and completely fail to capture areas of significance highlighted in Figure 3.14a, where an increased number of anodic POPG headgroup orientations were observed between -90 and -30 degrees, and between 40 and 60 degrees.

As neither of these approaches using `Xmgrace` have produced an accurate and visually correct smoothed plot, an additional tool was constructed to host a new approach specifically designed for this type of histogram. `SmoothGraph` is a program to smooth the data of any plot or graph that may suffer visible fluctuations from poor sampling. This program uses progressive averaging of a data set which not only enhances the visual presentation of the plot, but also maintains a high level of accuracy without losing the shape of the original plot. The resulting plot is a prediction of what the original plot would look like should it receive additional sampling. This tool is ideally suited for plots that follow a non-linear and non-Gaussian pattern.

`SmoothGraph` uses an iterative and progressive algorithm to calculate averages between groups of adjacent data points:

$$x_{i_{(n+1)}} = \frac{1}{2(n+1)} \sum_{j=-n}^{+n} x_{i_n+j} \quad (i \neq j), \tag{3.10}$$

where x_{i_n} is the data point at position i on the iteration n, and $2n$ is also the number of data points averaged on iteration n. This equation is iterated N times, where the value of n grows by one on each iteration to a maximum size of N such that $\{n \in \mathbb{Z} \mid 0 \leq n \leq N\}$. This allows each iteration to expand the number of data points used in the average by two (one either side of x_i), causing a slower convergence on the averaged data point when compared to taking a single average over $2N$ data points, as employed in the running averages. This leads to a less fluctuated, more accurate plot when using smaller values of N. At the boundary conditions, the value of n shrinks accordingly such that x_{i_n+j} never samples through the boundary.

`SmoothGraph` was used to smooth out the fluctuations from the headgroup orientation histograms, specifying an identical length of average used by the running averages ($N = 4$, Figure 3.14d). This plot reveals the same level of accuracy when compared with the running averages (Figure 3.14b), where both approaches captured the areas of significance in the anodoic POPG headgroup orientations; however, `SmoothGraph` considerably enhanced the appearance of the histograms without the need for a larger averaging size, thus maintaining a high level of accuracy when smoothing the plots.

Chapter 4

An investigation into antimicrobial peptide inhibitors

The majority of my first year was spent working in collaboration with the National Physical Laboratory (NPL) in Teddington, London; the department of biochemistry at the University of Oxford; and the IBM T.J. Watson Research Centre in Yorktown Heights, New York. The aim of the collaboration was to advance our understanding of antimicrobial peptides (AMPs) by exploring their mode of action, with the goal of ultimately designing better, more efficient AMPs.

In this chapter, the AMP Cecropin-B was chosen as a model system to investigate the regulation of antimicrobial activity through the formation of a *coiled-coil* between AMPs and AMP inhibitors. These inhibitors exploit the hydrophobic effect between amphipathic peptides by binding with the AMP, thus restricting its ability to adopt new confirmations. This proposed mechanism could be used to exploit other known coiled-coils for the treatment of human disease.

4.1 Background

4.1.1 Cecropin-B

Cecropins are a family of AMPs found across a variety of species ranging from the hemolymph of insects to pig intestines [139–141], and have been suggested

to exploit both the carpet mechanism and formation of ion channels [28, 142]. They are highly cationic, contain between 35 and 39 residues, and are strongly active against both gram-positive and gram-negative bacteria [143]. Circular dichroism (CD) and 1H-NMR experiments have shown the cecropins to adopt helical conformations when in contact with lipid bilayers and to be random coils in solution [144, 145]. Cecropin-B comprises 35 residues with several cationic

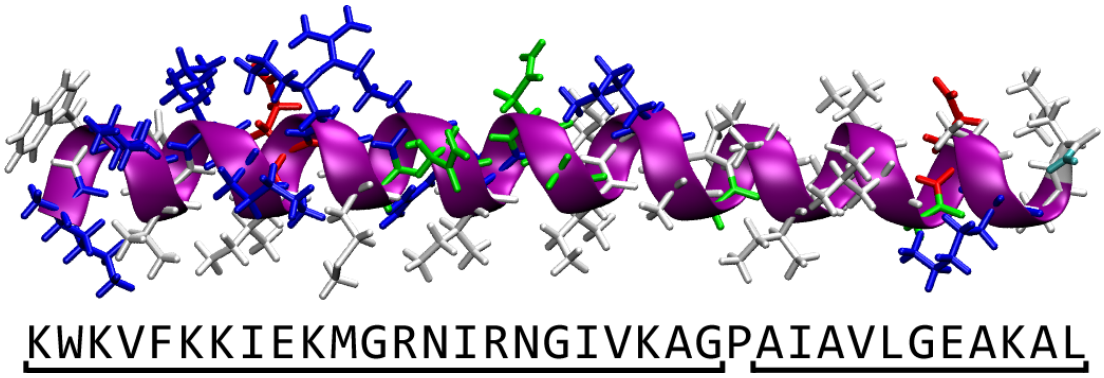

Figure 4.1 *Cecropin-B in helical form. This peptide shows amphipathic properties as the majority of the hydrophobic residues (white) align on one face of the helix. However the proline residue (24th residue) normally disrupts the helix, allowing two helical regions to coexist. When inserted into the membrane, the 23 residue N-terminus spans the bilayer while the 10 residue C-terminus spans the lipid headgroups.*

lysines and arginines spread over the full peptide, and a sequence that is highly amphipathic when in helical form (Figure 4.1). Cecropin-B contains a proline residue which is known to act as a backbone 'hinge' by lacking the ability to form hydrogen bonds in the backbone, thus disrupting the helix [146]. Interestingly, proline is the 24th residue in Cecropin-B, which divides the peptide into a 23 residue and 10 residue section, where 23 residues is the same number of residues found in the magainin family (as well as other short AMPs). Studies have shown this 23 residue section likely inserts into and spans the lipid bilayer while the remaining 10 residues interface with the headgroup region [147]. Cecropin-B also contains a tryptophan residue at position 2 which plays an important role in membrane fusion [148].

4.1.2 Coiled coils

Whilst the amphipathic helices of AMPs such as Cecropin-B and Magainin have the property of binding to microbial membranes as part of their activities, these

AMPs have sequence similarities to 'coiled coils'. These are common structures in biology, found in a wide range of proteins such as: *keratins*, a structural protein found in human skin; *myosins*, a family of motor proteins found in muscle cells; and *kinesins* (Figure 4.2), another family of motor proteins designed to transport cargo around the cell [149–151]. They consist of two or more α-helices in a superhelical configuration with their hydrophobic residues meshed together in a zip-like manner [152], and have been described as having 'Velcro'-like properties [153].

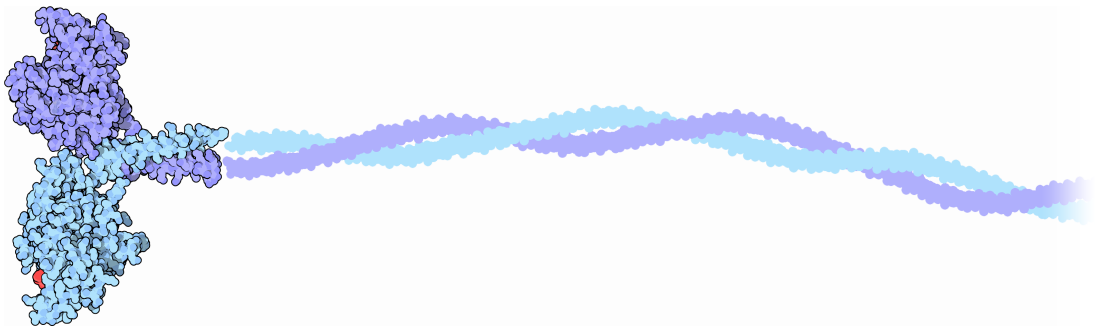

Figure 4.2 *Motor protein Kinesin containing the motor domains (left) that are connected by a long coiled coil. Kinesins are powered through ATP conversion to 'walk' along the microtubules within various eukaryotic cells, transporting cargo around the cell [151].*

Coiled coils are a unique super structure to α-helices and require a level of amphipathicity to establish formation, driven by the hydrophobic effect between non-polar residues of amphipathic molecules. The individual helices comprise a heptad repeat of residues with the empirical sequence *hpphcpc*, where *p* represents a polar residue, *c* represents a charged residue, and *h* represents a hydrophobic residue, typically leucine, isoleucine, valine or alanine [154]. As α-helical peptides exhibit 3.6 residues per turn, placing the hydrophobic side chains every three and four residues results in an amphipathic peptide. However, this achieves an average spacing of 3.5 hydrophobic residues per turn, causing a slight rotation of the hydrophobic face that spirals around the helix at around 10 degrees per turn [152]. It is this spiral that allows two helical peptides following the heptad sequence to wrap around each other and form a coiled coil.

Coiled coil design and function has been explored computationally in several studies. These include a study by Woolfson and Alber whereby an algorithm was presented to predict the oligomerisation states of coiled coils [155]. This algorithm specifically determines whether an amino acid sequence will favour a dimeric or trimeric oligomerisation state. A similar study by Lupas et al. presented an

algorithm to determine coiled coil regions in protein sequences [156], and was used to identify over 200 proteins in the GenBank database [157] that contained coiled coil domains.

4.1.3 Designing a Cecropin-B mutant and inhibitor

The possibility of interactions between AMPs and inhibitor peptides, or 'anti-AMPs', may provide a platform to facilitate the regulation of antimicrobial activity through coiled coil formations [158]. Upon binding of an anti-AMP, the structural properties of the AMP are modified, which may limit their ability to adopt certain conformations and disrupt their antimicrobial action [159]. Nevertheless, despite the sequence similarity of AMPs to coiled coils, a feature of many AMPs is the inclusion in their sequences of helix-disrupting motifs [160]. In the case of Cecropin-B for example, three $G(X)_nG$ (glycine zipper) motifs form a continuous stretch starting in the second heptad from the N-terminus, which potentially disrupts the ability to form coiled coils. Therefore, in order to facilitate coiled coil formation with Cecropin-B, selective mutations were necessary to incorporate the heptad repeat sequence.

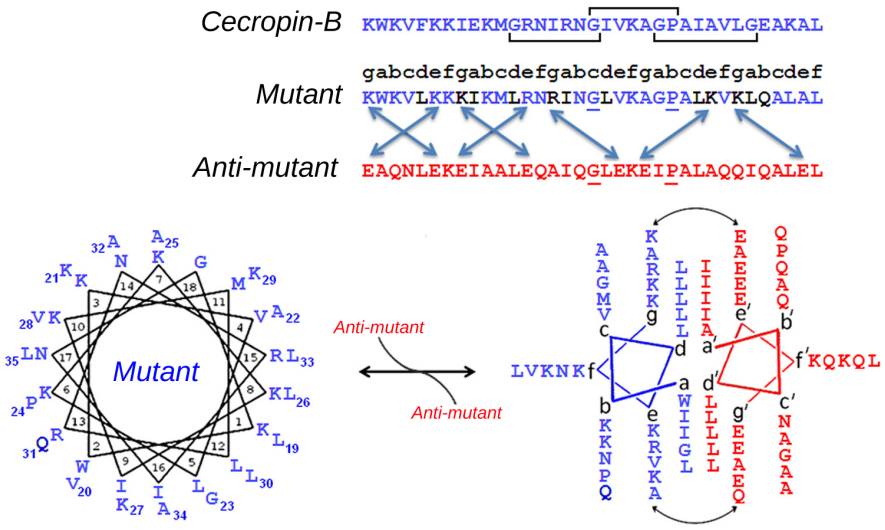

Figure 4.3 *Designing the Cecropin-B mutant and anti-mutant [160].*

Figure 4.3 represents the design process in creating a Cecropin-B 'mutant' along with its inhibitor counterpart, the 'anti-mutant'. The tryptophan residue at position 2 and the proline residue at position 24 were left untouched in the mutant as they have been shown to be important for antimicrobial activity [147]. The anti-mutant was designed to be the direct counterpart to the mutant by following

a similar heptad repeat using oppositely charged residues.

Stain-dead assays using *Staphylococcus aureus* were conducted at NPL and confirmed that the Cecropin-B mutant retained antibacterial activity, albeit slightly less potently than the native sequence (Publication 2). As expected, the anti-mutant alone showed no antibacterial activity. Assays were conducted containing the mutant and anti-mutant at ratios of 1:5-10 respectively, which revealed a significant reduction in the cell killing rates compared to the mutant alone. At ratios lower than 1:5, there was no difference in killing rates compared to the mutant alone. These results indicate that there is some anti-antimicrobial effect from the anti-mutant at high concentrations. CD measurements of the mutant and anti-mutant provided quantitative information of coiled coil interactions.

4.1.4 Simulation methods

All peptides were generated *in silico* using the Xplor-NIH program [161, 162], which generates alpha helical peptides with a short 1 ps equilibration using the CHARMM19 force field. A stepsize of 1 fs was used, and hydrogen bonding between backbone atoms was constrained to helical distances during the equilibration. The resulting peptides were near linear alpha helical structures.

All experiments were conducted using the AMBER99_SB-ILDN force field with a stepsize of 2 fs, unless otherwise stated. This force field has been identified in a number of studies to be optimal in determining protein/peptide secondary structures with a significant improvement on side chain torsion potentials [163–165]. For all peptide-water systems, the peptides were added into a box with dimensions 7x7x7 nm and periodic boundary conditions, and solvated with the TIP3P water model. The number of water molecules in each system varied between 11000 and 11100. All production runs used an NPT ensemble with the pressure maintained by an isotropic Parrinello-Rahman coupling scheme with a time constant of 2 ps, reference pressure of 1 bar and isothermal compressibility of 4.5 $\times 10^{-5}$ bar^{-1}. The temperature was maintained by a Nosé-Hoover coupling scheme with a time constant of 0.5 ps, and the peptides and water/ions were coupled separately to a heat bath at 300 K. Nonbonded interactions were evaluated with a 1 nm range and updated every 10 fs. Bond lengths and angles were constrained using the LINCS algorithm. The equations of motion were integrated using the leapfrog method. All systems were minimised using the

steep algorithm, and then equilibrated in an NVT ensemble for 100 ps, followed by an NPT ensemble for 100 ps, and all production runs were 20 ns.

All secondary structure timelines have their x-axis as time and y-axis as residue number. The timeline legend is:

Color	Type
Pink	Alpha Helix
Blue	3-10 Helix
Turquoise	Turn
Red	Pi Helix
Yellow	Extended Conformation
White	Coil

4.2 Investigating coiled coil formation with a model AMP and inhibitor

4.2.1 Secondary structures in solution

CD spectra produced at NPL suggested that the native Cecropin-B, mutant and anti-mutant are all random coils in solution. A molecular picture of this secondary structure can be obtained through short MD runs, which will also determine the validity and accuracy of the AMBER99_SB-ILDN force field for these systems. The three peptides were placed in water boxes with counter ions, equilibrated and simulated for 20 ns. Figure 4.4b reveals the native Cecropin-B peptide begins to unfold within the first nanosecond and continues to unfold for the remaining simulation time. A short alpha helical section remains between residues 6-15 (`KKIEKMGRNI`); however this may disappear at longer timescales. The resulting secondary structure suggests that Cecropin-B prefers a random coil conformation in solution, with ∼25% helicity after 20 ns (Figure 4.4a). Figure 4.5b reveals the mutant is more helical than its native counterpart, with a persistent break in the helix between residues 16-24 (`INGLVKAGP`) due to the proline residue. The resulting structure comprised two helical sections folded over each other, with ∼50% helical content (Figure 4.5a). Figure 4.6b reveals the anti-mutant remained slightly more helical than the mutant with a similar break in the secondary structure around residues 16-24 (`IQGLEKEIP`). This break appears less persistent than in the mutant, with an overall helical content of ∼65%, where most of the

helicity loss is located at the terminals (Figure 4.6a).

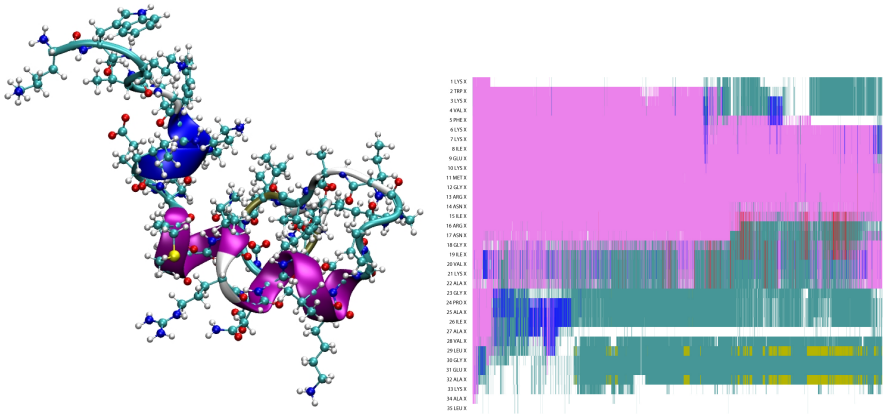

(a) *Cecropin-B* **(b)** *Timeline*

Figure 4.4 *(a) Cecropin-B structure after 20ns in solution. (b) Secondary structure timeline for Cecropin-B over 20ns.*

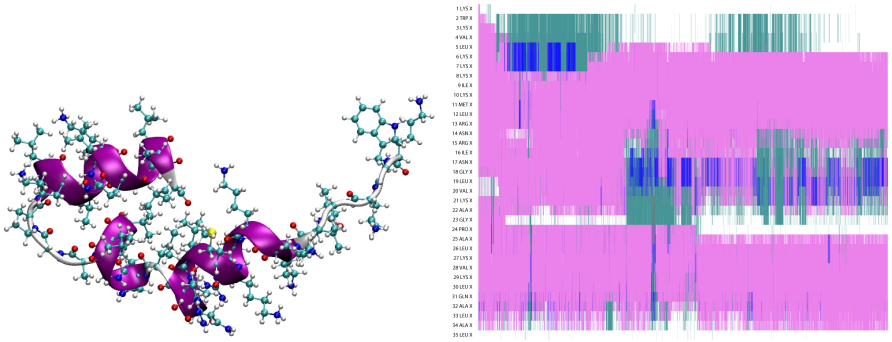

(a) *Cecropin-B mutant* **(b)** *Timeline*

Figure 4.5 *(a) Cecropin-B mutant after 20ns in solution. (b) Secondary structure timeline for the Cecropin-B mutant over 20ns.*

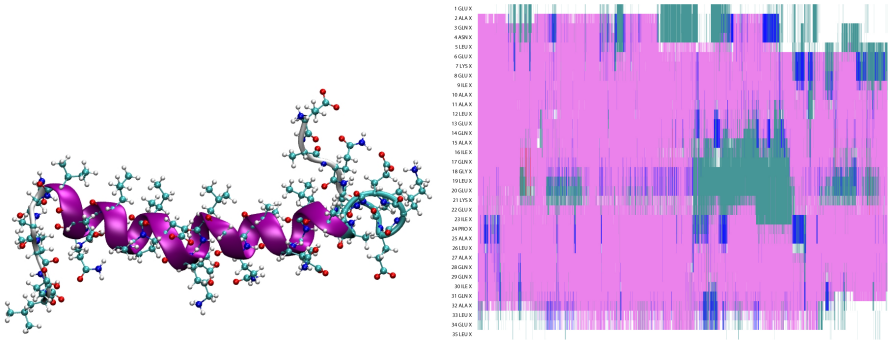

(a) *Anti-mutant* **(b)** *Timeline*

Figure 4.6 *(a) Anti-mutant after 20ns in solution (b) Secondary structure timeline for the anti-mutant over 20ns.*

4.2.2 Secondary structure of Cecropin-B with an anionic bilayer

In order to observe how the secondary structure of Cecropin-B is affected by contact with the surface of an anionic lipid bilayer, a simulation was conducted containing two Cecropin-B peptides (cB1 and cB2) placed either side of a *1,2-dilauroyl-sn-glycero-3-phosphocholine / 1,2-dilauroyl-sn-glycero-3-phosphoglycerol* (DLPC/DLPG (3:1)) bilayer, pre-equilibrated for 20 ns at 300 K. Only counter ions were used as similar experiments were conducted at NPL using the same bilayer composition without salt. The peptides were initially α-helical and placed within a few angstroms of the bilayer surface using the program `MoleculeInserter`, where the hydrophobic faces of each peptide were directed away from the membrane to maximise initial electrostatic interactions. A short equilibration run was conducted before simulating the system for 20 ns. The CHARMM36 force field was used, and the secondary structure of each peptide was mapped over the full trajectory (Figures 4.7a-b).

Having started in a helical conformation, both peptides show a strong preference to remain helical while in contact with an anionic lipid bilayer. This may be due to the electrostatic interactions between the charged residues and the lipid headgroups increasing the backbone stability and preventing unfolding. Interestingly, cB2 experienced folding around the hinge at 2.5 ns and established an "L" shaped peptide. At 7 ns, the two helical sections folded on top of each other to form a "U" shape, merging their hydrophobic faces. This suggests that the proline hinge may be active even when the peptide is in contact with a lipid bilayer. cB1 remained almost perfectly helical through the simulation, with slight unfolding around the proline hinge (Figure 4.7c). There was no sign of peptide insertion on this timescale. A radial distribution function (RDF) between the nitrogen atom on the lysines and the phosphorous atom on both DLPC and DLPG lipids is shown in Figure 4.7d, revealing a strong preference for the peptides to interact with the anionic DLPG lipids.

The CHARMM force field has previously been found to show a bias for helical conformations [165, 166], and it is therefore difficult to assess the accuracy of the peptide secondary structure from these simulations. To further investigate this bias, a separate simulation was conducted where Cecropin-B was placed in a water box and allowed to unfold over 20 ns using the CHARMM36 force field. The resulting peptide comprised $\sim$91% helical content and even remained

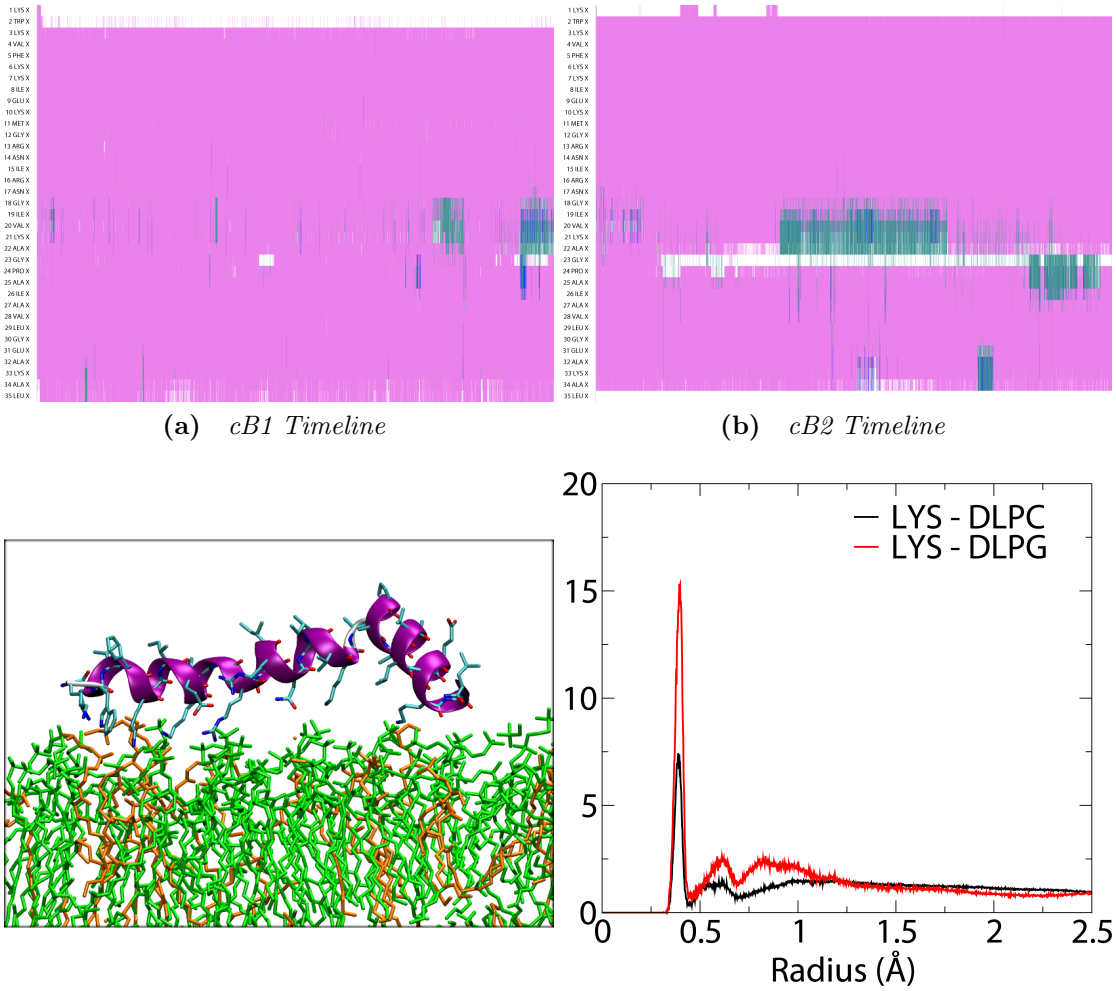

(a) *cB1 Timeline* **(b)** *cB2 Timeline*

(c) *cB1 after 20ns* **(d)** *Radial distribution function*

Figure 4.7 *(a),(b) Secondary structure timelines for two Cecropin-B peptides over a DLPC/DLPG (3:1) bilayer at 300K over 20 ns. (c) Image of cB1 after 20ns, with a break in the backbone by the proline residue. (d) Radial distribution function (RDF) of the lysines from both peptides interacting with the DLPC and DLPG headgroups.*

helical around the proline residue, confirming the helical bias in this force field. Future experiments involving Cecropin-B with anionic membranes could utilise the AMBER or Berger lipid force field to achieve a more accurate analysis of the secondary structure when in contact with anionic bilayers.

4.2.3 Formation of an ideal coiled coil

To investigate whether the mutant and anti-mutant are capable of forming a coiled coil under ideal conditions, a simulation was devised to maximise the likelihood of

spontaneous coiled coil formation in water. Both peptides were placed in a water box and orientated in the z direction such that their hydrophobic faces were pointing towards each other, with a separation of 1.4 nm between the peptide geometric centres (Figure 4.8a). The anti-mutant was given a 30 degree incline in the x and y directions to match the spiral of the hydrophobic face in the mutant. The system was subject to a short equilibration followed by a 25 ns simulation.

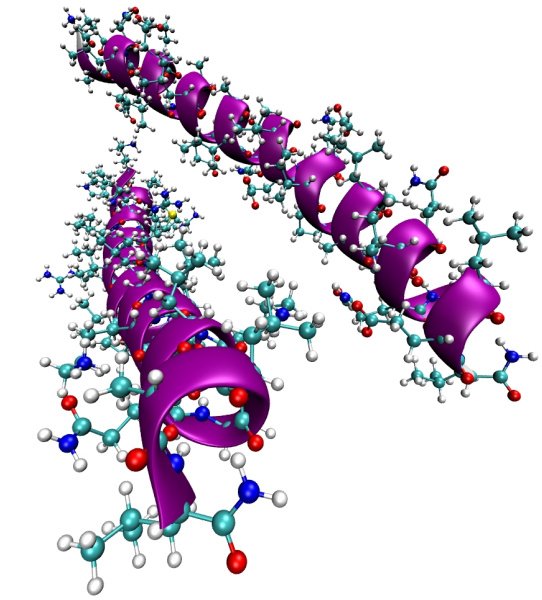

(a) *Initial Configuration*

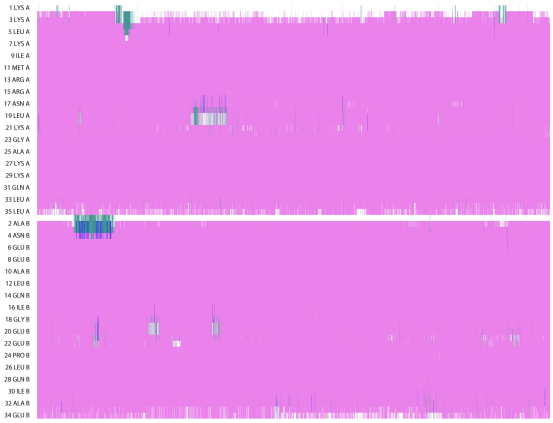

(b) *Timeline*

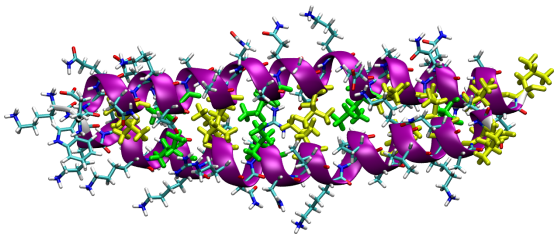

(c) *The resulting coiled coil structure*

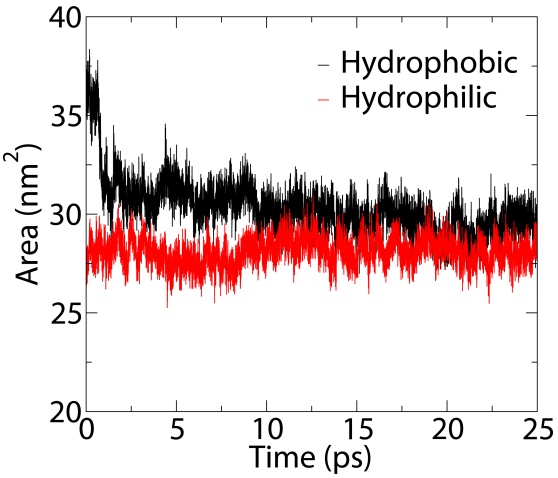

(d) *Solvent accessible surface area*

Figure 4.8 *(a) The initial orientations between the mutant (left) and anti-mutant (right) in optimal position to form a coiled coil. (b) Secondary structure timeline for both peptides over 25 ns shows very little deviation from alpha helices. (c) The resulting coiled coil after 25 ns, with the leucine (yellow) and isoleucine (green) residues highlighted. (d) The solvent accessible surface area of the coiled coil.*

Both peptides fused at their N-termini within the first nanosecond, followed by fusion of the remaining hydrophobic residues along the peptides in a zip-like manner. By 10 ns, the peptides had formed an optimal coiled coil and maintained their structure for the remaining simulation time. The dimerisation of the peptides was observed to prevent them from unfolding in solution, as both peptides maintained a high helical content during and after coiled coil formation (Figure 4.8b); however, there was slight unfolding at the mutant N-terminus, and the proline residues in both peptides caused a slight disruption to the helix throughout the simulation. The resulting coiled coil structure can be seen in Figure 4.8c.

One measurement that can be obtained from the coiled coil formation is the solvent accessible surface (SAS), a measurement used to describe the amount of hydrophobic/hydrophilic surfaces on molecules that are exposed to water/solvent. Figure 4.8d depicts the SAS over the full trajectory. A sharp drop in hydrophobic SAS is observed within the first 1-2 ns as the peptides fuse their hydrophobic faces together, removing some contact with the water. Interestingly, the hydrophobic SAS area continued to descend slightly for the first $\sim$20 ns, suggesting that the hydrophobic residues require this time to optimise their packing. There was relatively little change in hydrophilic SAS area, which is to be expected for an ideal coiled coil formation as there should be no packing of hydrophilic residues.

This simulation reveals that the mutant and anti-mutant are capable of spontaneous coiled coil formation given ideal starting conditions, and will remain as a coiled coil for the duration of the simulation. The interactions between both peptides enhances the stability of the secondary structure and prevents loss of helicity. However it is apparent from the secondary structure timeline that there is a persistent instability at the N-terminus of the mutant. Visual inspection of the trajectory showed this instability to be caused by the tryptophan residue, which is too large to sit comfortably in the hydrophobic zip between peptides. Tryptophan is also found in the coiled coil C-terminus of the HIV-1 protein gp41 and has been noted to establish a cavity in the coiled coil due to its size [167]. Instabilities in the secondary structure also exist around the proline hinge in both helices while in coiled coil formation. Prolines are found in other coiled coil forming proteins but are almost always found in the first turn of the helix [168, 169]. It would be interesting to observe the likelihood of spontaneous coiled coil formation in non-ideal conditions, given the tendencies for the proline to rapidly destabilise the helix and disrupt the amphipathicity in both peptides.

4.2.4 Investigating parallel coiled coil formation

Spontaneous coiled coil formation has previously been simulated using MD by Piñeiro *et al.* [170]. In their study, two peptides utilising the heptad repeats were placed in parallel in water boxes with four different initial orientations and run for 10 ns. A total of 8 simulations were conducted with the goal of observing coiled coil formation under a variety of initial orientations. With this study in mind, a similar study was devised to explore coiled coil formation with the mutant and anti-mutant peptides, applying a similar technique to the one used in the Piñeiro *et al.* study but increasing the number of simulations performed and orientations used to explore coiled coil formation from many starting trajectories.

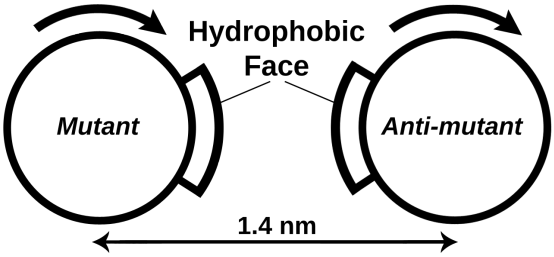

Figure 4.9 *Initial setup of the simulations, where each peptide was rotated individually through 90 degrees to expose all faces.*

A series of 48 simulations were conducted with the mutant and anti-mutant peptides, exploring 16 possible orientations. Both peptides were placed in parallel in a water box separated by 1.4 nm between the peptide geometric centres (Figure 4.9). Each peptide was individually rotated by 90 degrees along the backbone vector to establish 16 orientations and expose all faces of the peptides to each other. Each orientation was duplicated three times and simulated for 20 ns using randomised starting velocities.

From the 48 simulations, only one simulation resulted in a successful coiled coil formation (Figure 4.10). This formation took slightly longer than the coiled coil previously formed under ideal conditions; however, the resulting structure was very similar. Interestingly, but not surprisingly, the simulation that resulted in a coiled coil started from a conformation where the hydrophobic faces were aligned. The two duplicate simulations with identical initial orientations failed to form a coiled coil, suggesting that coiled coil formation from these peptides is highly sensitive to the initial conditions. This may also suggest that a coiled coil formation with these peptides is non-favourable, where other dimerisation states are preferred.

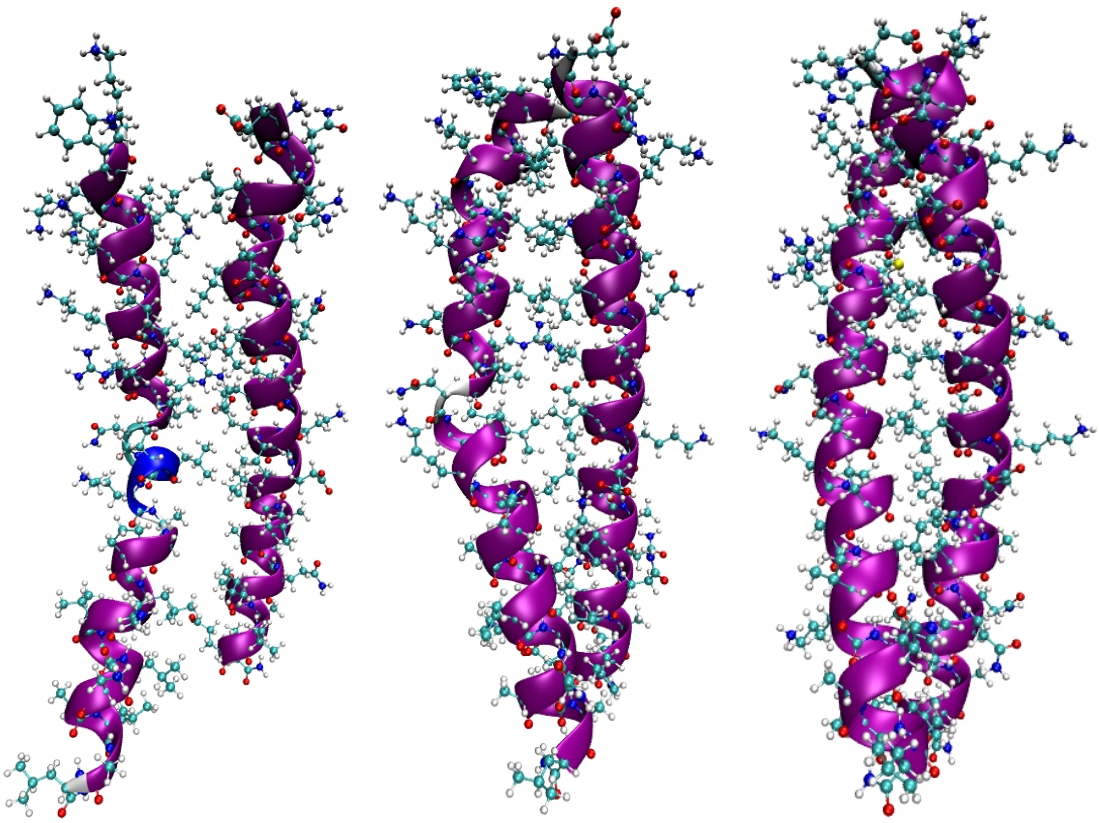

(a) *0ns* **(b)** *5ns* **(c)** *10ns*

Figure 4.10 *Evolution of the coiled coil formation over 10ns. The initial configuration had the hydrophobic faces aligned and took ∼10ns to develop into a coiled coil.*

The study conducted by Piñeiro *et al.* also resulted in only one parallel coiled coil formation from an initial orientation that saw the hydrophobic faces aligned. They concluded that coiled coil formation may be a two-stage process, firstly forming an initial complex which then slowly rearranges to form a coiled coil. However they also extended simulations of two failed coiled coil complexes for an additional 100 ns and saw no rearrangement and coiled coil formation, suggesting that their peptides had fallen into a long-lived energy trap. Their result, along with the result of this experiment suggest that coiled coil formation will only occur within a timescale of 20ns under ideal initial conditions.

Figure 4.11a shows the SAS of the hydrophobic residues for the three systems with identical starting configuration and randomised initial velocities, one of which resulted in successful coiled coil formation while the other two formed linear dimers. Interestingly, there is very little difference in the SAS between each system. This can likely be explained by the dimers having a similar configuration

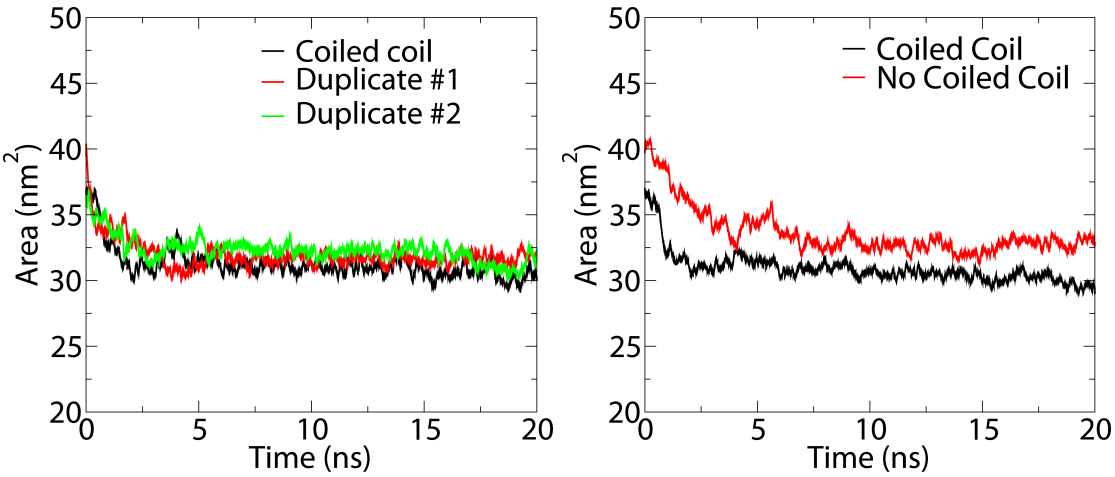

(a) *SAS of the three duplicates*

(b) *SAS of coiled coils with failed coiled coils*

Figure 4.11 *Solvent accessible surface area (SAS) of the hydrophobic residues for (a) The three simulations with identical starting configuration and randomised velocities, one of which resulted in a coiled coil and the others as perfect dimers. (b) Successful and unsuccessful coiled coil formation from different starting configurations.*

to a coiled coil, where many of the hydrophobic residues are buried together but lack the optimal packing achieved from a coiled coil, resulting in a slightly higher SAS. It is therefore possible that extending these simulations may allow the peptides additional time to optimise their packing by adopting the coiled coil conformation.

Figure 4.11b shows the averaged SAS of both successfully formed coiled coils (from Section 4.2.3 and from this section) compared with two randomly selected configurations (failed coiled coils) from the 48 simulations. This reveals a clear difference in SAS between both averages, indicating that the two failed coiled coils lack optimum packing of the hydrophobic residues. As both failed coiled coils had lost some helicity and amphipathicity due to unfolding around the proline residue and at the terminals, it is highly unlikely that extending these simulations would result in a coiled coil conformation. This likely suggests that the helix-disrupting motifs within these peptide sequences make coiled coil formation highly unfavourable.

4.2.5 Investigating antiparallel coiled coil formation

Although each simulation so far has utilised the mutant and anti-mutant with a parallel helix alignment, coiled coils are also capable of antiparallel formations due to the symmetry in the heptad sequence [171]. The majority of coiled coils observed in nature appear to associate with parallel helix alignment; however, a growing number of antiparallel coiled coils have been documented [172]. Piñeiro *et al.* also observe antiparallel coiled coils with their peptides, which interestingly show preference for antiparallel conformations even though their peptides were designed to dimerise in parallel. They reported that the positioning of charged residues, the favourable interactions between the helix dipoles, and the packing of the lysines and leucines at the hydrophobic interface all resulted in increased stability in antiparallel confirmations. This suggests that preference for parallel or antiparallel conformations may be sequence dependent.

As Figure 4.3 previously indicated, the mutant and anti-mutant sequences were designed to form parallel coiled coils. The mutant is highly cationic with a charge of +12, and the anti-mutant contains a mix of two cationic and seven anionic residues and has a resulting charge of -4. Therefore it is likely that electrostatic attraction will persist when antiparallel.

A further series of 48 simulations were conducted with the mutant and anti-mutant placed antiparallel in water, exploring 16 orientations. Surprisingly, none of the 48 simulations resulted in a coiled coil, including those with ideal starting configurations. This may simply reflect the low frequency of successful coiled coil formations observed in the parallel experiments, and therefore no conclusion can be drawn as to whether antiparallel coiled coil formation is possible using these peptides.

4.2.6 Further investigations of coiled coil formation under ideal conditions

To further investigate the likelihood of coiled coil formation given an ideal starting orientation, a series of 50 simulations were conducted using an identical starting configuration of the mutant and anti-mutant, allowing only the initial velocities to be randomised for each simulation. The peptides were orientated in parallel such that their hydrophobic faces were aligned.

Out of the 50 simulations, only one coiled coil was observed, with the remaining simulations forming a range of non-specific configurations similar to those observed previously. To quantify the amount of coiled coil in each simulation, a program was constructed to calculate the percentage of coiled coil observed in the final frames of each system. This percentage is achieved by calculating the separation between the geometric centres of paired hydrophobic residues; an ideal coiled coil with optimum hydrophobic packing should see each hydrophobic residue on both peptides in close contact to each other. A separation of 5 Å or less was designated 100%, whereas 10 Å or more was designated 0%, with the percentage scaled linearly inbetween. The percentages for each paired residue are averaged to give the overall percentage of coiled coil in the system. The resulting percentages were then binned into a histogram (Figure 4.12).

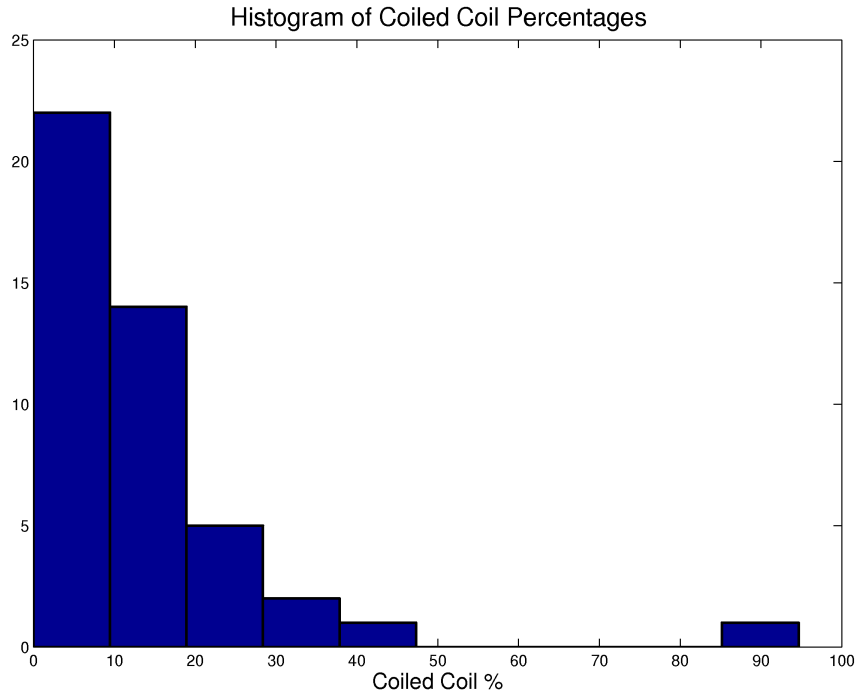

Figure 4.12 *Histogram of the distribution of coiled coil percentages from 50 identical simulations with randomised initial velocities.*

Only one system resulted in a coiled coil and achieved percentage of 94.65%, where the last 5% was lost due to unfolding at the C-terminus on both peptides. The remaining systems scored below 50%, with the majority scoring $0 - 10\%$. This analysis demonstrates that the formation of a coiled coil with the mutant and anti-mutant in solution, given an ideal starting conformation, is possible but infrequent. It is worth noting that Piñeiro *et al.* conducted a total of 6 simulations using an ideal starting conformation, which resulted in four successful coiled

coils. This differs greatly from the 57 simulations I have conducted using an ideal starting configuration, which resulted in only three coiled coils. This strongly suggests that coiled coil formation with these peptides is highly unfavourable. It is likely that the presence of helix-disrupting motifs, particularly the proline residue which was required for antimicrobial action in the mutant, elicits strong peptide unfolding which may seriously hinder coiled coil formation in both parallel and antiparallel conformations when simulated in water.

4.2.7 Investigation of a coiled coil in various ionic concentrations

Ions are known to influence the stability of various biological systems, including proteins and lipid bilayers, by modifying the electrostatics of the system [173, 174]. As an example, changing the ionic concentration around a lipid bilayer can modify the properties of the bilayer such as its area per lipid or lipid mobility. The effect of ions on coiled coil formation has previously been studied by Jelesarov *et al.* [175]. Their findings suggest that coiled coil formation is only promoted in the presence of *kosmotropic* ions (e.g. sulfate, phosphate, carbonate) which are known to promote protein folding and the burial of hydrophobic residues. The simulations conducted throughout this chapter, and those conducted by Piñeiro *et al.*, were all done so in the presence of counter ions (sodium) only.

As the mutant and anti-mutant are highly charged peptides, the presence of various ionic concentrations surrounding a preformed coiled coil may disrupt the electrostatics between the peptides and modify the stability of a preformed coiled coil. To explore this, a range of ionic concentrations was introduced to the preformed coiled coil established in section 4.2.3. This coiled coil was placed in water boxes containing ionic concentrations of 0.01, 0.1, 0.15, 0.5, 1.0, 5.0 and 10.0 Mol/l of Na^+Cl^-. The simulations were subject to a brief equilibration before being conducted for 20 ns. The RMS deviations from an ideal helix, a measure used to determine changes in helicity, are show for 0.01 and 10 Mol/l in Figure 4.13.

The RMS deviations show no significant deviations from an ideal helix between using 0.01 and 10 Mol/l of Na^+Cl^-, suggesting that modifying the ionic concentration has no effect on the stability or structure of a preformed coiled coil. Visual inspection of each final frame showed the coiled coil to remain

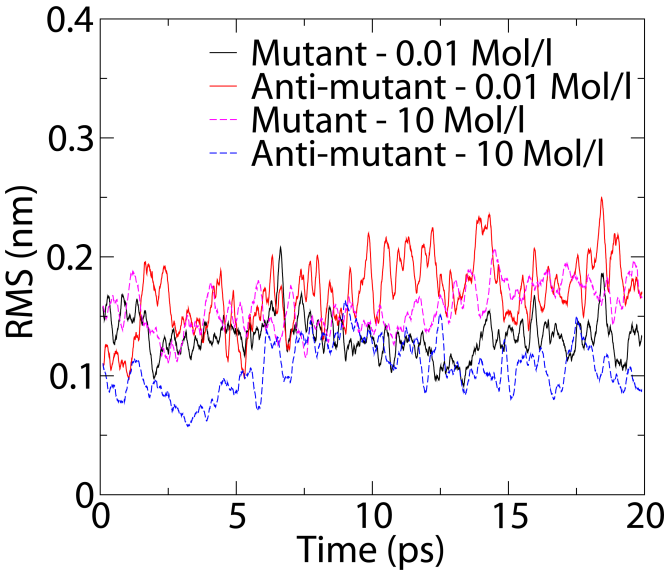

Figure 4.13 *RMS deviation from an ideal helix for a 20ns run of a coiled coil in 0.01 and 10 Mol/l of Na+Cl-. The plot shows no significant difference in RMSD of the helices at low and high salt concentrations.*

intact in each simulation. This suggests that the stability of the coiled coil is primarily driven by the hydrophobic interface between peptides, and changes to the electrostatic interactions around the coiled coil are insufficient to disrupt the hydrophobic interface.

4.2.8 Conclusion

The possibility of interactions with AMPs and an inhibitor peptide, an 'anti-AMP', may provide a means to regulate the antimicrobial activity of certain AMPs through the formation of a coiled coil. This coiled coil formation restricts the ability for AMPs to adopt new conformations, an important step in their mechanism of action. However, susceptibility to coiled coil formation is not native to AMPs and, as such, their sequences must be mutated to facilitate this.

In this chapter, I have explored the formation of a coiled coil using a model system of two designed peptides, which have their sequences derived from the AMP Cecropin-B. As the native Cecropin-B is incapable of exploiting coiled coil formation, its sequence was mutated to include the heptad repeat motif commonly found in coiled coil forming peptides; however, several residues were left untouched as they are known to be vital for antimicrobial action. Similarly, an inhibitor peptide was designed to be the counterpart to this mutant. Stain-

dead assays conducted at NPL revealed that the mutant Cecropin-B retained antimicrobial properties, albeit slightly less potent than the native Cecropin-B (Publication 2). Furthermore, circular dichroism (CD) measurements of the mutant and anti-mutant provided quantitative information of coiled coil interactions.

An investigation of the secondary structures of Cecropin-B, Cecropin-B mutant and the anti-mutant indicated each peptide has a tendency to unfold in water, which is in agreement with CD measurements. The unfolding was most noticeable around the terminals and residues 16-24 due to a disruption in the backbone caused by a proline residue. The native Cecropin-B was by far the most unstructured, achieving a helicity of $\sim$25% after 20 ns after unfolding from a pure helix. From similar simulations, the mutant and anti-mutant peptides appeared much more helical than the native sequence, achieving helicities of $\sim$50% and $\sim$65% under the same conditions. The secondary structure of Cecropin-B in contact with the surface of an anionic lipid bilayer was also explored through simulation, showing high levels of helicity; however, the simulations indicated unfolding at the proline hinge, suggesting that this helix-disrupting motif persists when in contact with anionic bilayers.

The spontaneous formation of a coiled coil with the mutant and anti-mutant in water was explored through simulation using a variety of initial configurations. In total, 147 simulations were conducted of which 48 were parallel and 48 were antiparallel, exploring 16 initial orientations of the mutant and anti-mutant. A further 50 simulations were conducted using an ideal initial configuration, achieved by aligning the hydrophobic faces of both peptides. A final simulation was conducted from an ideal configuration that also saw a 30 degree incline in the x and y directions to the anti-mutant in order to match the spiral of the hydrophobic faces on both peptides.

Of the 147 simulations, only three captured the dimerisation process of a successfully formed coiled coil, each of which began from a parallel ideal initial configuration. In these simulations, both peptides initially fused at their N-termini, followed by burial of each hydrophobic residue in a zip-like manner. Measurements of the solvent accessible surface (SAS) yielded an initial sharp drop in hydrophobic area followed by a slight decrease over 20 ns, suggesting that the hydrophobic residues require this time to optimise their packing. The tryptophan residue was observed to protrude from the hydrophobic core of the coiled coil due to its size, and the proline residues in both peptides elicited instabilities in the

secondary structure which persisted during and after coiled coil formation. The helical percentages of both peptides remained high throughout the simulations, suggesting that coiled coil formation enhances the stability of the helices and prevents them from unfolding.

Of the 144 simulations that failed to produce a coiled coil, 54 were conducted using an ideal initial configuration. From this, at least two possible conclusions can be drawn: either spontaneous coiled coil formation is highly infrequent from simulations conducted in water over short timescales, or that spontaneous coiled coil formation between the mutant and anti-mutant is unfavourable. A study conducted by Piñeiro *et al.* using different peptide sequences saw four spontaneous coiled coil formations from six simulations initialised with an ideal configuration, suggesting that the second conclusion is more likely. However, their study also noted that spontaneous coiled coil formation is highly dependent on the initial configuration, indicating that the first conclusion may also be true. No definitive conclusions can be drawn as to whether the mutant and anti-mutant are capable of antiparallel coiled coil formation, as only three antiparallel simulations were conducted using an ideal initial configuration. Additional experiments are sought to further explore the possibility of antiparallel coiled coils with these peptides.

A preformed formed coiled coil was subjected to varying ionic concentrations in the range of 0.01-10 Mol/l of Na^+Cl^- to study its effect on coiled coil stability. Visual inspection and RMS deviations from an ideal helix revealed no change to the overall structure of the coiled coil, which remained intact at all concentrations. Future experiments could explore the effect of kosmotropic ions on coiled coil formation, as these ions are known to promote protein folding and the burial of hydrophobic residues. In addition, umbrella sampling or pulling simulations could be used to determine the strength of the hydrophobic interactions in the coiled coil in order to determine the amount of energy required to separate the two peptides.

As both the mutant and anti-mutant retain many of the helix-disrupting motifs from the native Cecropin-B sequence, it is likely that the formation of a coiled coil in a physical system is infrequent, given the need for high helicity and amphipathicity to propagate coiled coil formation. Unless additional interactions occur that promotes folding, the mutant is only in its folded helical conformation when in contact with lipid bilayers; however, this is a short-lived state as the mutant likely inserts into the bilayer, allowing the hydrophobic residues to interface with the bilayer core, removing its susceptibility to coiled coil formation.

Nonetheless, there is experimental evidence suggesting that the addition of the anti-mutant into *Staphylococcus aureus* cultures treated with the mutant results in anti-antimicrobial activity, albeit at molar ratios of 5-10 times more that of the mutant. Should this not be due to coiled coil formations, I speculate that this may be achieved through partial dimerisation of the two peptides in solution which, upon contact with the lipid bilayer, would restrict the mutant's ability to fold into an amphipathic helix. Another possible explanation for the anti-antimicrobial activity is that the anti-mutant may be attracted to the cationic ion channels established by the mutant, lodging themselves within the channel and disrupting their function.

The MD analysis of coiled coils is not restricted to AMPs and may have important practical applications for development of new treatments for disease. The results for the model system of a Cecropin-B mutant shows that it may be possible to inhibit its function through the binding of an inhibitor peptide via the formation of a coiled coil structure, which restricts the ability of the mutant to adopt the conformations required to exhibit antimicrobial activity. Whilst it has been speculated that bacterial resistance to AMPs could develop through host-produced inhibitor peptides, there is no evidence for this phenomenon, especially as AMPs such as Cecropin-B typically incorporate helix-disrupting motifs and lack the necessary motifs that incur susceptibility to coiled coil formation. However, artificially designed inhibitors which form coiled coil structures with target peptides and proteins may have applications as new therapies for human disease. This potential has already been demonstrated in at least three diseases where the causative proteins have coiled coil motifs. In Alzheimers disease, a synthetic inhibitory peptide was shown to block formation of amyloid aggregates which are responsible for brain plaque formation [176]. In HIV-1, a synthetic inhibitory peptide was shown to block viral fusion with cells by blocking the gp41 coiled coil protein [177]. In cancer, a synthetic inhibitory peptide was shown to block the function of an envelope protein of the human T-cell leukemia virus and bovine leukemia virus [178]. The design and development of inhibitors which form coiled coil structures represents a very exciting possibility for future therapies, which can be greatly assisted by the MD approaches developed in this chapter.

Chapter 5

Advancing our understanding of membrane potentials

5.1 Background

5.1.1 The MinCDE system

One application of the membrane potential that has recently been identified is its role in bacterial cell division. Cell division is a highly complex process involving many transmembrane proteins that play key roles in the division process. Division is ultimately achieved by the formation of the *Z-ring* at the midcell (Figure 5.1) [179]. Its formation at the midcell maximises the survival probability of each new bacterium by allowing an even distribution of cellular contents and genetic material in the newly formed compartments. The Z-ring is formed by the protein FtsZ, a GDPase which is present in almost all types of bacteria and Archae [180]. FtsZ binds with other proteins such as ZipA and FtsA to form microtubules, acting as a scaffold and allowing the formation of a new cell wall at the midcell. The localisation of FtsZ is modulated by another group of proteins known as the MinCDE system, encoded by the *minB* operon and comprising three proteins: MinC, MinD and MinE [181].

The MinCDE system inhibits FtsZ binding at the poles and restricts its localisation to the midcell. MinD, a transmembrane ATPase, oscillates from pole to pole, anchoring itself to the headgroup region of the membrane and forming

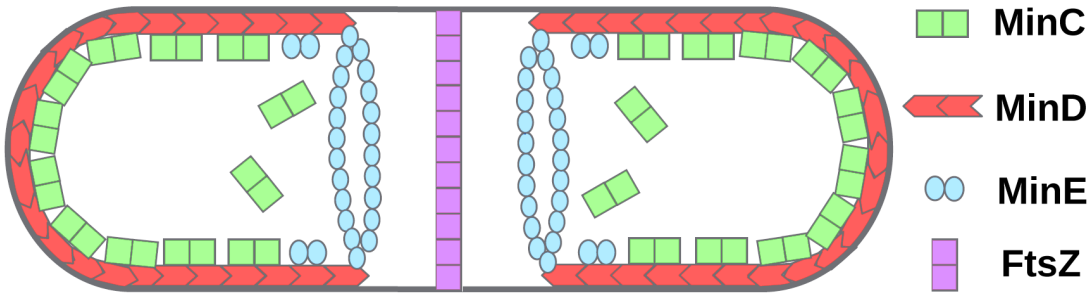

Figure 5.1 *Diagram of the MinCDE system. MinD binds to the cell membrane at the poles, assisted by MinE, and recruits the binding of MinC. MinC inhibits the binding of FtsZ (which forms the Z-ring) at the poles thus restricting its localisation to the midcell. This allows the division process to begin at the midcell, allowing an even distribution of cellular contents in both compartments to maximise the survival probability of each newly formed bacterium. Image adapted from [179].*

a polar zone that extends towards the midcell. MinD localisation is assisted by MinE, which forms a ring at the edge of the MinD polar zone. MinC is then free to bind to MinD, stimulating its ATPase ∼10-fold and inhibiting the binding of FtsZ at the poles, thus restricting its localisation to the midcell.

A recent study by Strahl and Hamoen [182] found that the localisation of MinD in *B. subtilis* is disrupted on dissipation of the membrane potential via poly-lysine coated slides. These slides are used to hold the bacteria in place, but are also known to dissipate the membrane potentials of cells [183]. They further explored this dissipation with the addition of the ionophore *carbonyl cyanide m-chlorophenylhydrazone* (CCCP), which exhibits a similar dissipation effect to poly-lysine [184]. On addition of CCCP to *B. subtilis*, over 20 proteins had their localisation disrupted as many of these proteins rely on an anchor protein such as MinD for their localisation. To investigate this further, Strahl and Hamoen synthesised the 21-residue amphipathic helix found at the C-terminus of MinD, responsible for anchoring MinD to the membrane. They introduced this peptide to bacterial liposomes and observed that its binding affinity to the membrane increased five to sixfold on induction of a membrane potential. Additional experiments using a mutated version of the C-terminus peptide identified its amphipathicity to be essential for the binding process. Strahl and Hamoen proposed two possibilities as to why this peptide exhibits sensitivity to membrane potentials. Firstly, they proposed that a membrane potential may result in a subtle conformational change of the amphipathic helix that enhances MinD

binding to bacterial membranes. Secondly, they proposed that the membrane potential may affect the fluidity of the membrane and enhance MinD binding, as it has previously been observed that MinD binding affinity is increased when membrane fluidity is increased [185]. This second hypothesis forms the basis for the experiments conducted in Section 5.4.

5.1.2 Electrostriction

Electrostriction is an effect observed in all dielectric materials when subject to an electric field. The result is a slight thinning of the material, caused by the charges within the dielectric experiencing a slight displacement in the direction of the electric field. For lipid bilayers, which are dielectrics, the mechanical force acting on the bilayer from the electrostatic attraction of the charges located on the two bilayer surfaces may also induce a reduction in bilayer thickness.

A study by Heimburg focused on the theory of electrostriction in lipid bilayers which treats the bilayer as a capacitor and investigates its association with changes in membrane thickness and fluidity [107]. By considering a membrane of fixed thickness D, capacitance C_m and a TMV V_m, the force acting on the membrane can be calculated from:

$$F = \frac{1}{2}E \cdot q = \frac{1}{2}\frac{V_m}{D} \cdot q = \frac{1}{2}\frac{C_m V_m^2}{D} \tag{5.1}$$

where $E = V_m/D$ if the membrane is assumed to have a uniform dielectric constant. By assuming biologically relevant values for the capacitance and thickness, this electrostrictive force roughly equates to 0.1 bar at 100 mV, and 10 bar at 1 V. As the hydrostatic pressure between the two leaflets is significantly weaker than this force, this implies that the bilayer will undergo a thickness reduction and an increase in surface area. This is significant because both these changes are characteristic of a phase change from gel to fluid, suggesting that a TMV across a membrane could "melt" the bilayer, effectively lowering its transition temperature.

5.1.3 Disruption of the membrane potential in bacteria

As mentioned previously, the membrane potential is an electrical potential found across all biological cells and plays a crucial role in many cellular processes

such as biophysical signaling, conformational changes in transmembrane proteins, transport of ions and molecules into and out of the cell, and cell proliferation. The dissipation of the membrane potential in *B. subtilis* was observed to result in antimicrobial activity, and therefore may be an area of interest in the development of new antimicrobial therapies.

Most antibiotic drugs in use today target and disrupt five key biosynthetic pathways relating to the synthesis of proteins, folic acid, peptidoglycans, DNA and RNA [186]. Whilst targeting these pathways has been hugely successful in treating bacterial infection since their discovery, there is an obvious need for new antimicrobial drugs to combat the growing number of drug-resistant strains. Most antibiotics are largely ineffective at treating persistent infections in which bacteria are *quiescent* (meaning slow-growing or dormant). These species of bacteria, such as *Mycobacterium tuberculosis* (TB) or *Pseudomonas aeruginosa*, are capable of becoming recalcitrant to antibiotic attack by undergoing physiological adaptations to render themselves quiescent, establishing a level of immunity (or indifference) to antimicrobials without the need for genetic resistance. Once antimicrobial attack has ceased, these bacterial species will often regain normal function. They are thought to achieve this indifference by downregulating their biosynthetic processes to baseline levels, maintaining a metabolically inactive state without compromising their survival [186]. Importantly, during this period of inactivity these bacterial species still rely on normal membrane function for survival, exposing a weakness that could be exploited through the treatment of membrane-targeting antimicrobials such as AMPs.

In addition to the many membrane-targeting AMPs that exhibit their antimicrobial action via membrane disruption and permeabilisation, several AMPs have been discovered that behave as TMV-disruptors, exhibiting their antimicrobial action through the dissipation of the membrane potential. One such AMP that exploits this mechanism is *lactoferrin*, a member of the transferrin family found in the secreted fluids of mammals (milk, saliva, mucus etc.) that has broad antimicrobial activity in many species of bacteria, viruses, fungi, and parasites [187]. Unlike the vast majority of AMPs, lactoferrin causes no significant disruption to the membrane integrity. Instead, it has been associated with changes to the membrane permeability, allowing the transport of small ions through the membrane and resulting in the loss of membrane potential. Its exact mechanism is still unclear; however it is thought to act intracellularly by causing perturbations in metabolic pathways.

Another AMP that behaves as a TMV-disruptor is *daptomycin*, a lipopeptide antibiotic produced by *Streptomyces roseosporus* that has shown potent antimicrobial action against multiple drug-resistant gram-positive organisms [188]. This AMP inserts into the plasma membrane and is thought to trigger oligomerisation of membrane proteins to form ion channels, transmembrane pores or other aggregate structures. The result is a loss of intracellular potassium. Interestingly, it has been reported that daptomycin requires an initial TMV in order to exhibit its AMP action. One study found that lowering the initial TMV of *S. aureus* from -165 mV to -100 mV before the addition of daptomycin severely impaired its lethal effects [51].

The exact reason why the loss of a TMV results in antimicrobial action is still unclear. A study by Schäffer and Thiele looked at the association between changes in membrane fluidity induced by imposing an electric field across the membrane [189]. They stated that a change in membrane thickness can lower the free energy contributions of the electrostatic and long-range forces acting across the membrane, which in turn can induce a phase separation in the membrane resulting in the formation of domains. In combination with Heimburg's theory of electrostriction which suggests an electric field across a membrane can induce changes in thickness, these two studies imply that a TMV may result in an increase in membrane fluidity that may assist the insertion of amphipathic helices such as in the C-terminus of MinD.

5.1.4 Establishing a TMV in simulation

Almost every biological simulation conducted with MD uses periodic boundary conditions. This imposes a problem on establishing a TMV across a lipid bilayer, as any ions situated above or below the bilayer are easily transported through the boundaries and will exert forces through the boundaries. Therefore it is not possible to create an ionic gradient across a bilayer with a traditional simulation.

There are two documented approaches to establishing a TMV in lipid bilayer simulations. The first approach uses an applied uniform electric field, which can be specified as an input parameter in the configuration file of the simulation. This adds an additional force parameter experienced by every atom to include the electric field force, defined by $F = qE$. This method has the advantages of being relatively computationally cheap and easy to set up, and can be performed with any bilayer type, size and force field. The second approach was developed

by Sachs *et al.* [88], who showed that a TMV can be established by creating an ionic gradient between the membrane or water compartments of a double bilayer, which consists of two planar bilayers on top of each other separated by several nanometres of water and ions. This establishes two distinct water compartments between the bilayers, restricting the movement of water and ions to their assigned compartment. A TMV can then be established by transplanting an ion imbalance between the water compartments, creating an *anodic* and *cathodic* compartment with corresponding anodic and cathodic leaflets (Figure 5.2). This method is considerably slower than using an applied electric field as there are effectively twice as many atoms in the system compared with using a single bilayer. This method can also cause some of the bilayer properties to become coupled as they experience the same semi-isotropic pressure coupling, and as such will always have identical area per lipid and similar bilayer thickness. However, this method is the most biologically relevant as it generates its electric field in the same way to the electric field found across cell membranes. Therefore this method was employed to establish TMVs in each simulation throughout this chapter.

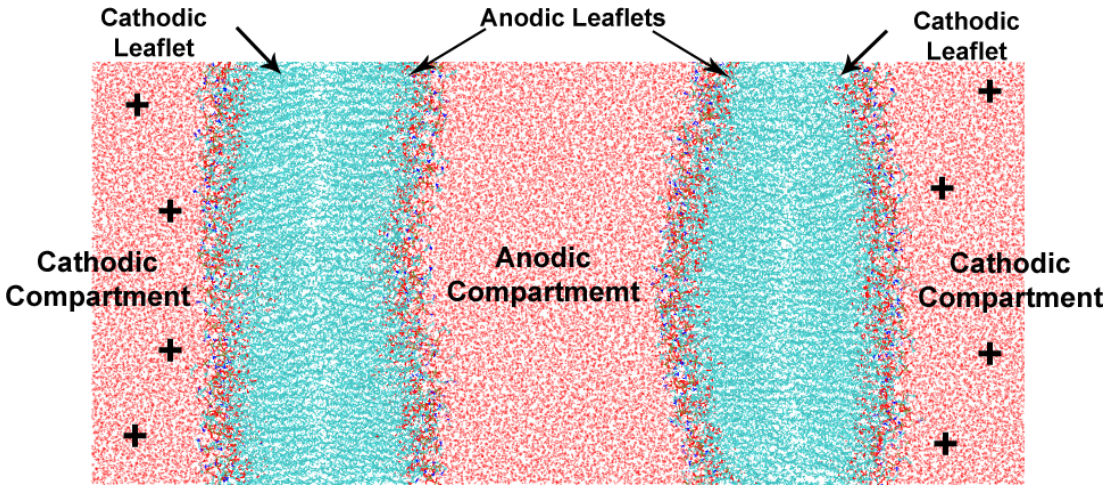

Figure 5.2 *Illustration of a double bilayer with an established membrane potential. Cations are removed from the inner water compartment and placed in the outer compartment, establishing an anodic and cathodic compartment with corresponding leaflets.*

To achieve accurate ion imbalances and ionic concentrations with a double bilayer, the tool `BoxMod` is required (see Section 3.3.1 for a full description of its function). This tool is capable of achieving identical ionic concentrations in each water compartment, and is capable of establishing an ion imbalance between the compartments by removing cations from the central (inner) compartment and distributing them throughout the outer compartment.

The resting TMV for *E. coli* has been measured to be in the range of -85 mV to -142 mV [50]. However, achieving a voltage this small across a double bilayer proved to be difficult. The smallest possible voltage can be achieved by moving a single cation from the inner to outer compartment, which establishes an ion imbalance of +2 (one compartment experiences a change in charge of +1, while the other experiences -1). However, measurements revealed that moving a single cation across bilayers with a surface area of ∼10x10 nm induces a TMV in the range of -210 mV to -275 mV, higher than the voltages found in both eukaryotic and prokaryotic cells. Lower voltages can only be achieved by constructing larger bilayers; however, this would make an already computationally expensive system even more so. Therefore it was decided to retain these bilayers and conduct simulations with slightly higher voltages than found in *E. coli*.

Interestingly, one outcome of the research in this thesis was the observation that the electric field within the bilayers is not uniform, with the anodic leaflets experiencing a larger electric field strength than the cathodic leaflets (which is detailed in Section 6.2.3). For this reason, analysis of the bilayers must treat each leaflet separately, producing an average for the anodic and cathodic leaflets. As the field strength is greatest in the anodic leaflets, any effect achieved from a TMV on the membrane properties will be most noticeable in these leaflets.

5.2 Aims

Section 5.3 aims to investigate the insertion and inclusion of the MinD-MTS peptide into a model bacterial membrane, where its binding affinity to bacterial membranes is altered when under the influence of a membrane potential. The energetics and dynamics of the insertion process are studied in detail, and changes in lipid properties in the annular shell of lipids surrounding inserted MinD-MTS peptides are identified.

Section 5.4 aims to investigate why the membrane potential plays a crucial role in the localisation of MinD and therefore bacterial cell division. This is done by investigating a possible link between membrane potentials and changes in membrane properties, such as the thickness, area per lipid and fluidity.

5.3 Investigation into the insertion and inclusion of MinD-MTS

The MinD-MTS (membrane targeting sequence) is an 11-residue peptide taken from the C-terminus of the MinD protein found in *B. subtilis*. The full C-terminus includes an alpha helical region that extends outwards from the main protein structure and acts as a molecular "hook", partially inserting into the headgroup region of the membrane to anchor the full protein. Interestingly, the full C-terminus is not amphipathic, with only residues 7-17 exhibiting an amphipathic region [181]. These residues were extracted from the full terminus and assigned an acyl cap at the new N-terminus and an amide cap at the new C-terminus. The acyl cap was not parameterised in the GROMACS version of the CHARMM36 force field and had to be added manually. The resulting sequence contained an α-helical amphipathic peptide (Figure 5.3).

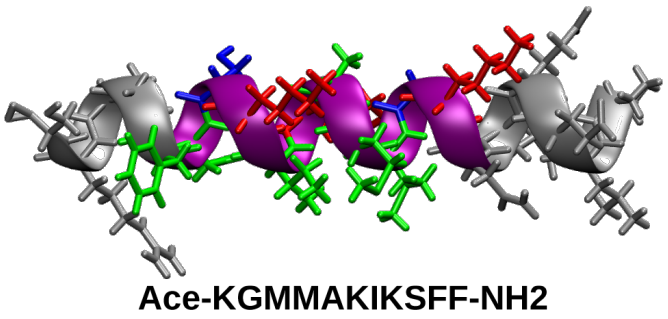

Figure 5.3 *The 21-residue MinD C-terminus, where the region displayed in colour is the 11-residue MinD-MTS containing a total charge of +3. Green side chains represent hydrophobic residues and red side chains indicate charged lysines.*

As the MinD C-terminus has shown an increase in binding affinity with bacterial membranes under the influence of a membrane potential, a series of simulations were conducted to investigate the spontaneous insertion of MinD-MTS with and without membrane potentials in POPE/POPG (3:1) double bilayers above and below the transition temperature, which is at 298-299 K for this composition [81]. In total there were fourteen systems constructed: two systems at 293K without a TMV, two systems at 293K with a TMV of -260mV (achieved from an ion imbalance of +2), three systems at 300K without a TMV, and four systems at 300K with a TMV of -210mV (+2). There were also three single bilayer systems at 300K. The differences in TMV between both temperatures are explained in Section 6.2.6. Each system contained four α-helical MinD-MTS peptides placed

1.4 nm away from the surface of each leaflet using the program `MoleculeInserter` (Figure 5.4). Each simulation was conducted for 100 ns using the HECToR super computer, where single and double bilayer systems utilised 512 and 1024 cores respectively (16 and 32 nodes), and each simulation took approximately 36 hours of runtime to complete. The resulting trajectories were then analysed visually to determine peptide insertions.

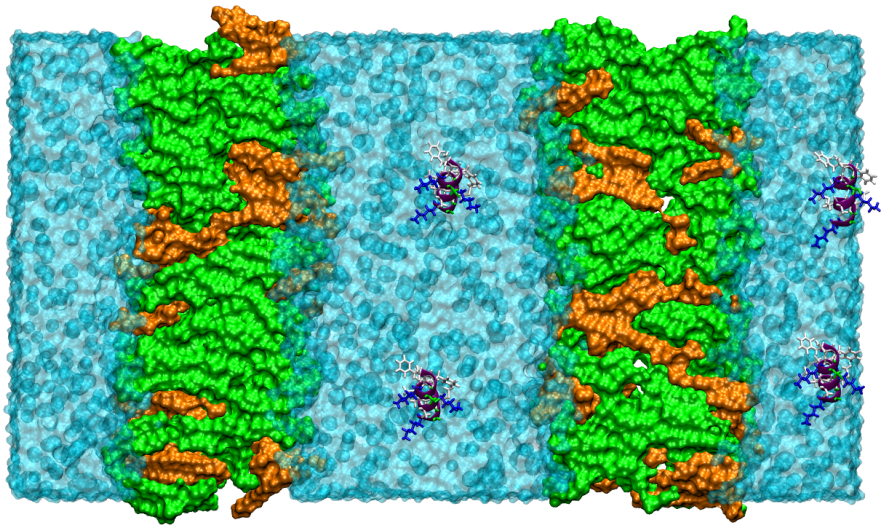

Figure 5.4 *Initial setup of four MinD-MTS peptides with a POPE (green)/POPG (orange) double bilayer. The peptides were positioned at 1.4 nm from the bilayer surface using the program* `MoleculeInserter`*. Four peptides were used to increase the probability of spontaneous insertion.*

In total, four fully inserted MinD-MTS peptides were observed within the simulation time in four separate simulations, with several more peptides showing the early stages of insertion and several peptides that had fused their hydrophobic faces together. The simulations containing inserted peptides were extended for an additional 50 ns to increase the post-insertion trajectories and allow for the analysis of the annular shell of lipids surrounding the inserted peptides. Interestingly, no peptides were observed to insert at 293 K, with all four insertions occurring in regions of high fluidity at 300 K. Insertions occurred in both TMV and no-TMV systems, including a single bilayer system.

5.3.1 Insertion process

The MinD-MTS insertion process was observed to follow a common pathway in all four insertions, and can be characterised into five stages:

1. Firstly, an initial electrostatic attraction between the lysine side-chains and the negatively charged phosphate groups on the lipids brought the peptides into contact with the bilayer surface within a few nanoseconds.

2. The peptides underwent a rotation to reorientate their hydrophobic face towards the bilayer.

3. All four insertions were N-terminus driven, with lys1 holding the terminus in place while met3 and met4 inserted into the headgroup region (Figure 5.5b). This sometimes (but not always) caused the peptides to tilt away from the bilayer.

4. The remaining hydrophobic residues inserted one by one into the headgroup region, with the bulkier phe10 and phe11 inserting last (Figure 5.5c).

5. The peptides sat in the lower headgroup region parallel to the membrane surface with their hydrophobic residues in contact with the lipid tails (Figure 5.5d). The peptides had a mean tilt of 6.6° to the membrane surface and a mean depth of 17.2 Å from the bilayer centre.

During the initial contact phase, the electrostatic interactions between the charged residues in MinD-MTS and the phosphate groups in the lipids drive the attraction of the peptide to the bilayer surface. Figure 5.6a shows the radial distribution function (RDF) of the MinD-MTS lysine N^+ atoms with the P^- atoms on both POPE and POPG lipids, where the RDF depicted is an average of all four MinD-MTS peptides. The RDF reveals that these lysine side chains have almost double the interactions with POPG lipids than with POPE lipids while in the contact phase. This translates to almost a sixfold increase in contact with PG lipids over PE lipids when taking into account the lipid ratios for this bilayer composition.

Figure 5.6b depicts the headgroup orientations for the lipids in the annular shells of all MinD-MTS peptides during the contact phase, which has been smoothed with the program `SmoothGraph` (see Section 3.3.3). A significant shift in the headgroup orientations is observed, where PE headgroups within the shells reveal a mean orientation of -4° compared with a mean of +4° for the control group, comprising randomly selected lipids from outside of the shells. This is likely explained by the electrostatic repulsion from the cationic lysines with the cationic PE ethanolamine group ($NH3^+$). This repulsion may also result in MinD-MTS driving the POPE lipids out of the shell, which may explain the low RDF values

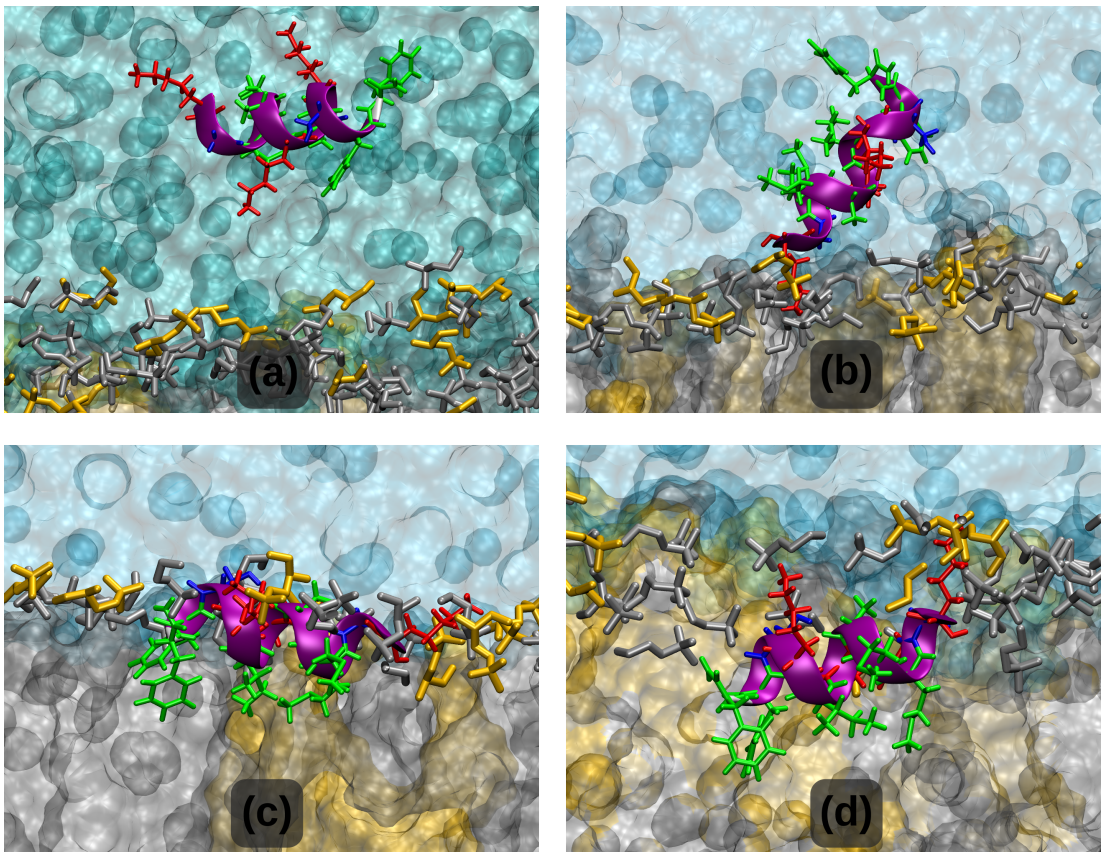

Figure 5.5 *The insertion process of MinD-MTS, with the hydrophobic and charged residues highlighted in green and red respectively. (a) Initial attraction is governed by electrostatics. (b) Insertion is N-terminus driven which can cause a tilt in the peptide. (c) The remaining hydrophobic residues inserted one by one until the full peptide was included into the headgroup region. (d) The final peptide sat at a mean depth of 17.2 Å.*

for POPE lipids. The PG headgroups within the annular shell also reveal a significant shift in orientation with a mean angle of 27°, higher than the control mean of 18°. This is likely due to the slight negative charge (-0.65 in the CHARMM force field) assigned to both oxygen atoms on the PG glycerol group, causing their orientation to raise slightly through electrostatic attraction with the lysines on MinD-MTS.

Figure 5.6c depicts the Coulomb and Lennard-Jones (LJ) energies for a single MinD-MTS peptide that inserted into the bilayer. The initial contact phase lasted ∼50 ns, during which MinD-MTS rotated its hydrophobic face towards the bilayer and inserted its N-terminus into the headgroup region, causing a tilt in the peptide (Figure 5.5b). This tilt resulted in a sharp reduction of Coulomb energy between 35 and 50 ns as two of the lysines situated near the C-terminus had

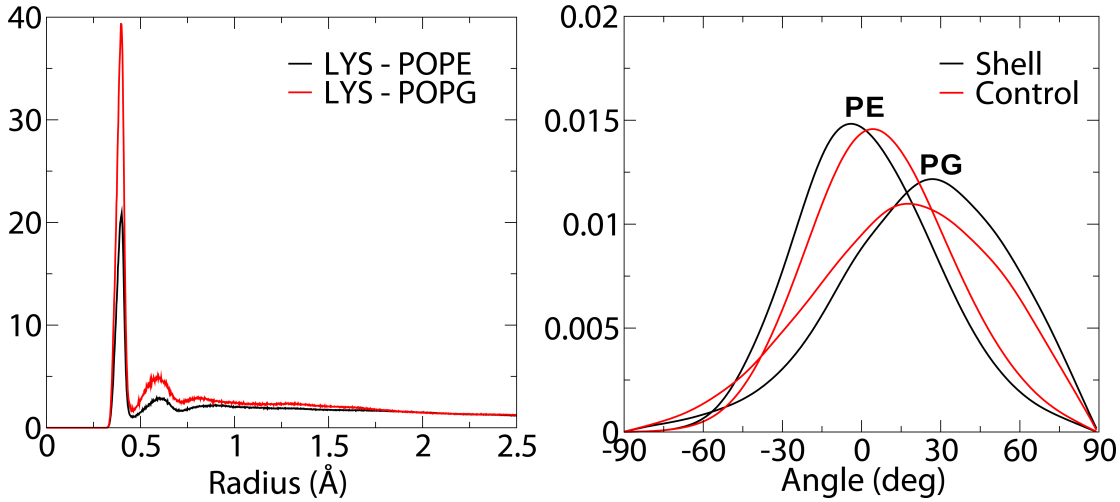

(a) *Radial distribution function* **(b)** *Headgroup orientation*

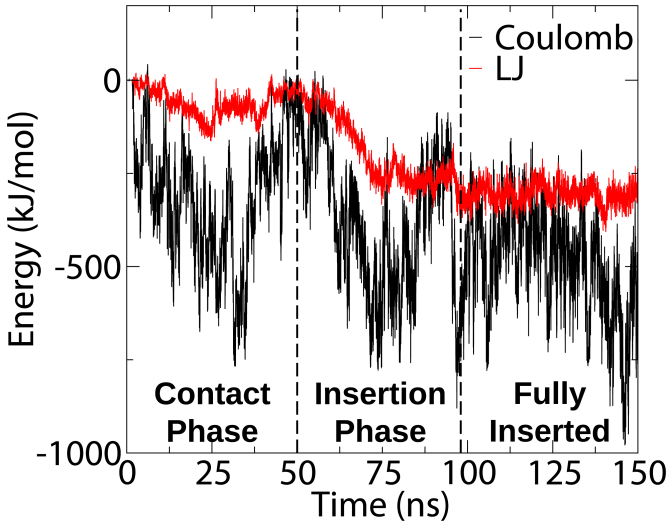

(c) *Insertion energies*

Figure 5.6 *(a) Radial distribution function of the cationic lysine side chains on all MinD-MTS peptides with the phosphate groups on both POPE and POPG headgroups during the contact phase. (b) Headgroup orientations of the annular shell of lipids surrounding all MinD-MTS peptides during the contact phase (c) The Coulomb and Lennard-Jones energies of the insertion and inclusion of a single MinD-MTS peptide with the bilayer.*

lost contact with the lipids. A steady increase in LJ energy is observed during the insertion phase as the hydrophobic residues are inserted one by one until the peptide is fully included into the headgroup region by ∼100 ns. Once fully inserted, MinD-MTS maintains a moderately constant LJ energy. Fluctuations are observed in the Coulomb energy as lipids move in and out of the annular shell.

Each MinD-MTS insertion energy plot shares similarities to that of Figure 5.6c; however, some insertions saw less or no tilt in MinD-MTS prior to insertion, resulting in a higher Coulomb energy throughout the insertion. The LJ energy was also observed to slightly increase post-insertion in some of the simulations as MinD-MTS descended deeper into the headgroup region until reaching its optimum depth.

5.3.2 Peptide depth and orientation

The program `PeptideMonitor` was constructed to monitor the relative depths of the peptides within the bilayers and the tilt on the peptides with respect to the bilayer surface. The relative peptide height is calculated by subtracting the geometric centre of the peptide backbone atoms with the geometric centre of the bilayer, and the peptide tilt is calculated by finding the angle the peptide backbone vector (that travels along the centre of the helix) makes with the xy plane (or membrane surface). Each inserted peptide was analysed for 50 ns after insertion and the average depths and tilts can be found in Table 5.1.

	Peptide depth	Peptide tilt
Insertion 1	16.9 Å ± 1.8 Å	7.3° ± 10.7°
Insertion 2	16.2 Å ± 1.7 Å	-0.8° ± 9.1°
Insertion 3	20.0 Å ± 1.9 Å	16.8° ± 9.8°
Insertion 4	15.6 Å ± 2.2 Å	3.3° ± 12.7°

Table 5.1 *The mean peptide insertion depth, relative to the bilayer centre, and the peptide tilt with respect to the bilayer surface. Positive tilt angles indicate the C-terminus is pointing downwards.*

The POPE/POPG bilayers have a typical leaflet thickness of 20-25 Å at 300 K, with a mean phosphorous atom height of ∼21.6 Å from the geometric centre of the bilayer. From visual inspection, these peptide depths are consistent with the insertion of MinD-MTS into the lower headgroup region, extending its hydrophobic residues to the first 2-3 carbons on the lipid tails and its charged residues remain in contact with the headgroup region (Figure 5.7). The peptides sit roughly parallel to the membrane surface with a slight tilt in all but one insertion, suggesting that the C-terminus sits slightly deeper within the bilayer. The resulting mean peptide depth and tilt is 17.2 Å ± 1.932 Å and 6.6° ± 10.7°.

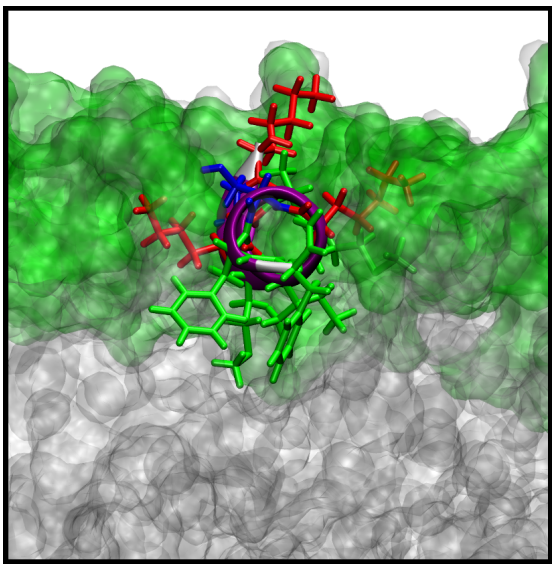

Figure 5.7 *Image depicting the final insertion depth of MinD-MTS. The bilayer is highlighted by the headgroups (green) and tails (white). MinD-MTS sits in the headgroup region with a mean depth of 17.2 Å from the bilayer centre. At this depth, the hydrophobic residues extend to the first 2-3 carbons on the lipid tails.*

5.3.3 Lipid splaying effect

Amphipathic helices exhibit some unique properties when interacting with lipid bilayers. They have been observed to sense membrane curvature and even induce curvature once inserted [190–192]. The direction of the curvature is related to the peptide's structural properties, the depth at which it resides in the membrane, and the type of lipids within the bilayer. It has been suggested that this curvature is induced as a result of changes to the lipid tails, or lipid 'splaying', in the lipids within the annular shell of an inserted amphipathic helix (Figure 5.8). The splaying effect is achieved from the inherent tendencies of amphipathic helices to reside in the headgroup region and upper lipid tail region, creating an excess of negative lateral pressure in the lower lipid tail region. This disrupts the normal van der Waals forces in the lipid tails surrounding the amphipathic helix and allows them to become more flexible, which in turn disrupts the interactions with neighbouring lipids and thus changes the local properties of the membrane, inducing positive curvature. If an amphipathic helix resides deeper in the membrane, the excess negative lateral pressure occurs in the upper lipid tail and headgroup regions, inducing negative curvature.

The presence of lipid splaying can be detected by looking at the order param-

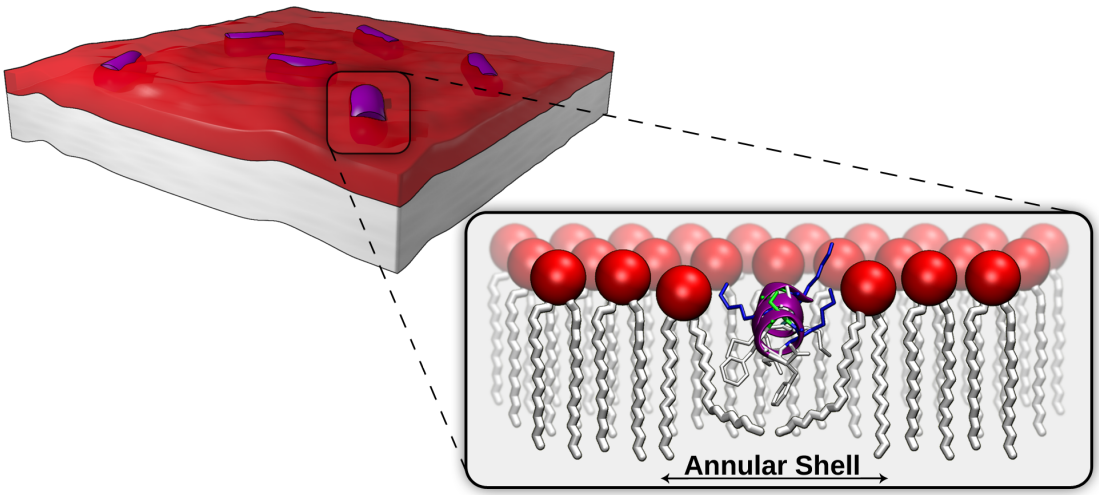

Figure 5.8 *Illustration of how amphipathic helices reside in the headgroup region of lipid bilayers and induce lipid splaying, allowing extra flexibility in the annular shell lipid tails of the peptide.*

eters in the annular shell of lipids surrounding inserted MinD-MTS peptides. `Membrainy` (see Section 3.2.2) was used to measure the order parameters in the annular shell of lipids surrounding each inserted MinD-MTS peptide, where 50 ns of sampling was measured using a probe radius of 4 Å around each peptide. Two control groups were established, both randomly selecting lipids outside of the shell in equal numbers to those found within the shell, with one control group using the option built into `Membrainy` to ignore lipids considered in the gel phase, which were identified using a tail length tolerance of 80%. This control group is of particular importance in these simulations as MinD-MTS was observed to insert only into fluid regions of the membrane, and as such would require a fluid control group for an accurate comparison.

The analysis of the annular shell of lipids surrounding the inserted MinD-MTS peptides yields clear evidence of lipid splaying (Figure 5.9a). An increase in disorder along the central carbon atoms of the acyl chains in the lipids surrounding MinD-MTS is observed. This highlights an increase in lipid tail flexibility, which is indicative of lipid splaying. The similarities in order parameters for the first few carbon atoms in the lipid tails of the shell and no-gel control group highlight the region in which the hydrophobic residues of MinD-MTS reside, which restricts the lipid tails from splaying until further down the acyl chain. Interestingly, the order parameters towards the end of the acyl chains are also very similar, suggesting that the splaying may not translate down the entire acyl chain.

It is also important to highlight the significance of the *no-gel* option implemented

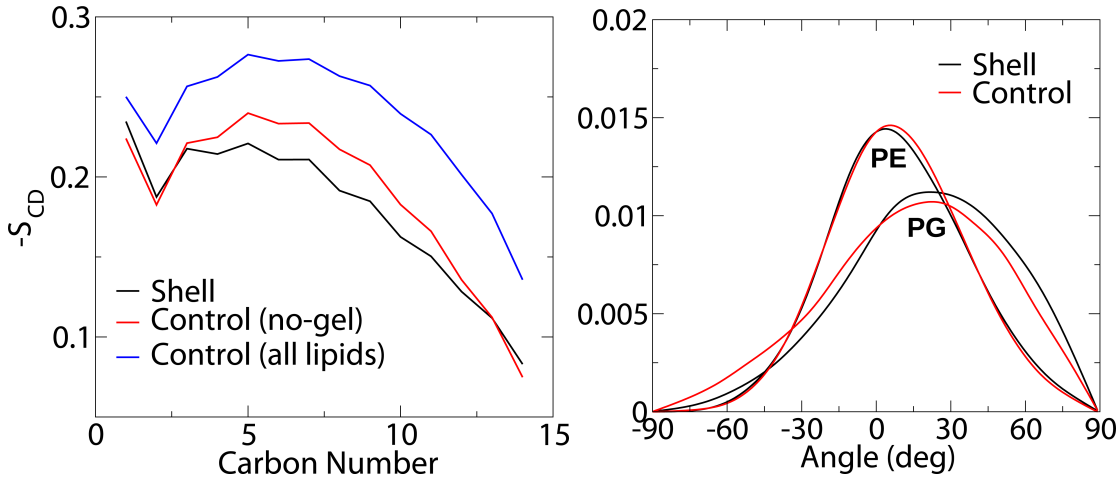

(a) *Deuterium order parameters* **(b)** *Headgroup orientations*

Figure 5.9 *(a) Deuterium order parameters, and (b) headgroup orientations, averaged from the annular shell analysis of four inserted MinD-MTS peptides with control groups. There is a clear shift in order around the centre of the lipid tail between the lipids surrounding MinD-MTS (black) and the control group (red) containing only fluid lipids. The increased disorder in the shell lipids suggests increased flexibility in the middle of the lipid tails. The effect on the headgroup orientations was significantly less than observed during the contact phase (Figure 5.6b).*

into `Membrainy`. The control group containing both gel and fluid lipids shows an increase in order for each carbon atom along the acyl chain, suggesting that this control group is sampling an entirely different phase of lipids compared with the lipids surrounding MinD-MTS. The similarities in order parameters for the shell lipids and no-gel control lipids suggest they are sampling the same phase.

Figure 5.9b depicts the headgroup orientations for the annular shell of lipids surrounding inserted MinD-MTS peptides compared with a fully fluid control group, revealing considerably less deviations from the control group when compared with the headgroup orientations during the contact phase (Figure 5.6b). This smaller deviation was investigated further by generating RDFs between the lysines and either the phosphate or ethanolamine/glycerol groups (i.e. the base or tip of the headgroup) (Figure 5.10). This revealed considerably more interactions with the phosphate groups, which is as expected due to the negative charge on the phosphate group in both POPE and POPG lipids, and is unlikely to alter the headgroup orientation. There is ∼20 times more contact with the PE phosphate group than with the ethanolamine group, and ∼3.5 times more contact with the PG phosphate group than with the glycerol group, which likely explains the

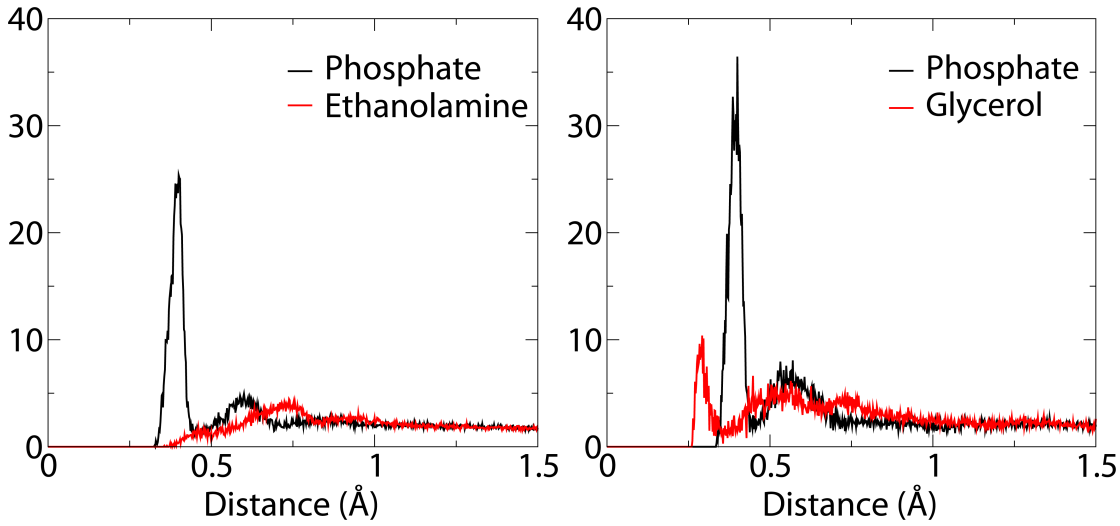

(a) *RDF (LYS - POPE)* **(b)** *RDF (LYS - POPG)*

Figure 5.10 *RDF of MinD-MTS interacting with POPE and POPG headgroups, where the headgroup phosphate base and ethanolamine/glycerol tip are calculated separately.*

larger shift in PG headgroup orientation observed in Figure 5.6b. This shift is likely achieved by the negative charges on the glycerol group. These RDFs also reveal more interactions with the phosphate group on POPG lipids than POPE lipids, indicating an enrichment of POPG lipids within the shell. The MinD-MTS insertion depth will also play a role in the headgroup orientations, as greater depths will result in less contact with the headgroup tips. The sequence of residues may also affect the headgroup orientation by defining the relative positions of each lysine residue when in helical form. Figure 5.7 depicts two lysines (shown in red) residing on the sides of the peptide that are interacting with the lower headgroup region, while the third lysine is located on the top of the peptide and is interacting with the headgroup tips. This is in agreement with the RDF data and further explains the slight shift in PG headgroup orientation.

5.3.4 Conclusion

The insertion process of the MinD-MTS peptide (residues 7-17 of the C-terminus of MinD) was investigated through MD simulations with POPE/POPG (3:1) double bilayers at 293 K and 300 K, where this bilayer composition has a transition temperature of 298-299 K [81]. These simulations saw four spontaneous insertions within 100 ns at 300 K, and no insertions at 293 K, likely due to the higher levels of gel domains increasing the difficulty of insertion. These

peptides came into contact with the bilayer surface within a few nanoseconds due to the electrostatic attraction between the cationic lysines and anionic POPG headgroups. During this contact phase, the RDFs between the lysine side chains on MinD-MTS and the phosphate groups on the lipids showed twice as many interactions with POPG lipids. The lipid headgroup orientations in the annular shells of all MinD-MTS peptides were analysed using `Membrainy` and compared with a control group comprising an equal number of lipids to those found in the shells. PE angles were observed to decrease by 8° and PG angles increased by 9°. These changes in orientation correspond with the electrostatic attraction/repulsion on the headgroups from the cationic lysines on MinD-MTS, suggesting the cationic PE headgroups experience a decrease in angle as they are repelled into the membrane, and the anionic PG headgroups experience an increase in angle as they are attracted away from the membrane. The attractive forces between the lysines and PG headgroups is indicative of the additional interactions with POPG lipids indicated by the RDFs.

Insertion of MinD-MTS began with a rotation of its hydrophobic face to reorientate it towards the lipids. In each of the four complete insertions, MinD-MTS first inserted its N-terminus hydrophobic residues, followed by the remaining hydrophobic residues until the phenylalanines at the C-terminus had inserted. MinD-MTS then sank deeper into the headgroup region until reaching a mean depth of 17.2 Å from the bilayer centre. This depth places MinD-MTS in the lower headgroup region, with the hydrophobic residues penetrating the first 2-3 carbon atoms in the lipid tails and the charged residues interacting with both the lower and upper headgroup region. MinD-MTS also exhibits a slight tilt of 6.6° leaving the C-terminus slightly deeper than the N-terminus.

The order parameters were measured in the first annular shells surrounding the four inserted MinD-MTS peptides and compared with a control group comprising fluid lipids randomly selected from outside of the shell. The order parameters yielded clear evidence of lipid splaying, shown as an decrease in lipid tail order in the shelled lipids, which implies an increase in lipid tail flexibility. The first few carbon atoms in the lipid tails surrounding MinD-MTS showed no significant change in order parameters, suggesting that the hydrophobic residues in MinD-MTS (which are located in this region) restrict the splaying effect to further down the tails. This may have implications in understanding how amphipathic helices give rise to membrane curvature, which has been shown by Zemel et. al to be highly dependent on the insertion depth [192].

The headgroup orientations were also measured in the first annular shells surrounding each inserted MinD-MTS and compared with a control group. Although a slight shift in orientation was observed, this shift is significantly less than observed during the contact phase, suggesting the inserted MinD-MTS peptides have very little influence on headgroup orientation once inserted. RDFs of the inserted peptides show the lysines are mostly interacting with the phosphate groups, with some interaction with the glycerol groups on the POPG headgroups. It is likely that these headgroup orientations are dependent on the insertion depth and the sequence of the peptide. Peptides residing deeper in the membrane will interact more with the phosphate groups and less with the headgroup tips, which exerts less influence on the headgroup orientations. The sequence of the peptide will define the positioning of charged residues on the helix, where lysines located on top of the helix are more likely to interact with the headgroup tips that residues located elsewhere.

The initial investigation covered in this chapter sought to explain why MinD exhibits an increase in binding affinity with membranes under the influence of a membrane potential. However, the simulations revealed insertions of MinD-MTS in both TMV and no-TMV simulations, highlighting that insertion is still possible without a TMV. The study conducted by Strahl and Hamoen also observed MinD-MTS binding in bacterial liposomes with and without a TMV, with an increase in binding affinity in TMV liposomes. This therefore suggests that a membrane potential merely enhances the insertion process of amphipathic helices. However, the experiments conducted by Strahl and Hamoen with *B. subtilis* showed that MinD was delocalised when the membrane potential was dissipated, suggesting that the membrane potential also plays a role in the ability of MinD to sense the bacterial poles. As these polar regions are highly curved (which is also true for liposomes), it is plausible that a membrane potential may assist in the ability of amphipathic helices to sense membrane curvature. It is also plausable that a membrane potential across a curved membrane could behave differently than with a planar membrane, as curved membranes will have one surface slightly larger than the other which may influence the strength and shape of the electric field across the bilayers (and is discussed further in Chapter 6). Additional simulations are required to specifically look for changes that may occur in the lipids under the influence of a TMV. This forms the basis for the next series of experiments in this chapter.

The MD analysis of MinD-MTS with model bacterial membranes provides a

high level of detail of the dynamics and energetics associated with its insertion. Whilst the MinD-MTS peptide is specialised for strong anchoring of the MinD protein into the interior cell membrane of certain bacteria, its ability to rapidly bind to and insert into bacterial membranes makes it a promising target for the development of drug delivery systems into cells. Sequences with similar properties to the MinD-MTS have already shown promise in several studies as an effective drug delivery methods, where these sequences are transplanted onto larger molecules to facilitate cell penetration. Roshihiko *et al.* showed that the highly hydrophobic 11-polyarginine peptide can be used to efficiently transport the cancer suppressing protein p53 into cancer cells [193]. Morris *et al.* showed that the peptide Pep-1 facilitates rapid cell uptake of various peptides, proteins, and even full-length antibodies into mammalian cells [194]. The MD analytical tools developed and applied in this research may be of value in designing peptide sequences to optimise membrane insertion and delivery of a wide range of molecules into cells for a range of medical applications such as treatment of cancers.

5.4 Investigation into the effects of TMVs on lipid bilayers

As discussed in Section 5.1.1, a study conducted by Strahl and Hamoen found that the binding affinity for the amphipathic C-terminus of MinD increased five to sixfold when a membrane potential was introduced to bacterial liposomes [182]. They concluded that the membrane potential may be modifying the properties of the membrane, such as its fluidity, to promote the binding of amphipathic helices to the membrane.

The simulations presented in this section explore possible changes in the membrane properties of model bacterial membranes with and without a membrane potential. By using `Membrainy`, these membrane properties could be analysed to detect any changes experienced by the lipids that may alter the fluidity of the membrane, or other effects that could contribute to an increase in binding affinity of MinD.

5.4.1 Simulations at biologically relevant voltages

Two model bacterial lipid bilayers were chosen for this study. These were a POPE/POPG (3:1) double bilayer containing 192 lipids per leaflet, and a DOPE/DSPE/DOPG/DSPG (3:3:1:1) double bilayer containing 200 lipids per leaflet (a full description of both bilayers can be found in Section 2.2). Both bilayers had approximate dimensions of 10x10x20 nm, and all simulations were conducted on the HECToR super computer using 1024 cores (32 nodes) requiring approximately 36 hours of runtime to complete.

POPE/POPG bilayers

The POPE/POPG double bilayer had received 50 ns of equilibration at 300 K prior to establishing an ion imbalance of +2 and corresponding TMV of -225 mV. The system was energy minimised and subjected to a brief equilibration before conducting the simulation for 200 ns. The original (no-TMV) double bilayer simulation was also extended for 200 ns to provide a direct comparison for the analysis of the TMV system.

`Membrainy` was used to analyse the final 100 ns of each simulation (Figure 5.11). Surprisingly, there was no significant change between the TMV bilayers (red) and the no-TMV bilayers (black) for each membrane property. Figures 5.11a-b depict the area per lipid (APL) and bilayer thickness for both simulations. Should there be an increase in fluidity, we might expect to see an increase in APL and decrease in bilayer thickness. However, both plots fluctuate considerably during the simulation but show no significant difference between the TMV and no-TMV systems. Figures 5.11c-d depict the order parameters and headgroup orientations for both simulations, where the headgroup orientations have been smoothed with the program `SmoothGraph`. Again, should there be an increase in fluidity, we might expect to see lower numbers in the order parameters for the TMV system; however, both order parameter plots are virtually identical. As the lipid headgroups for POPE are zwitterionic, we might expect to see some form of alignment of the headgroup with the electric field established by the TMV; however, the plots show no significant change in headgroup orientation for both PE and PG lipid headgroups when compared with the no-TMV system.

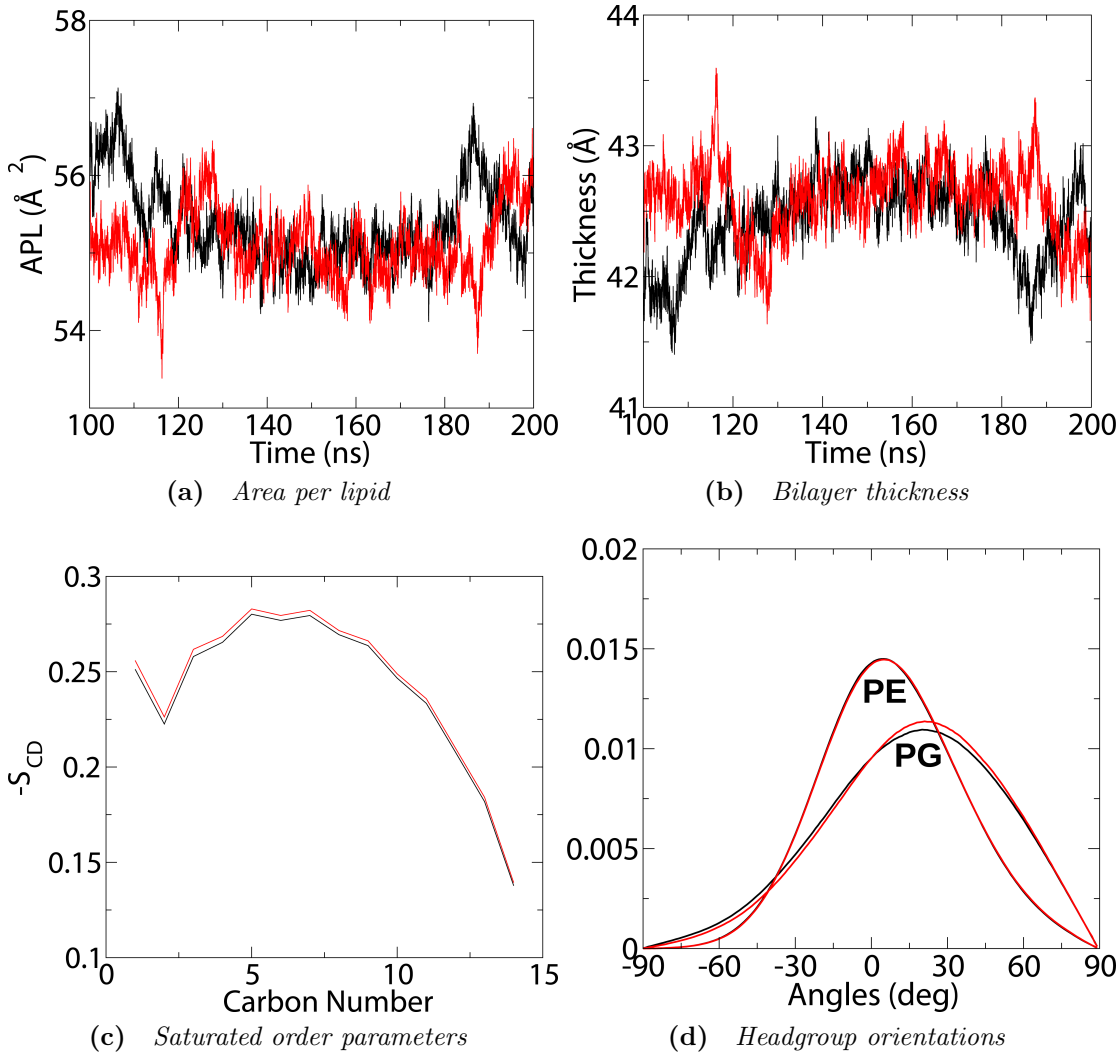

(a) *Area per lipid* **(b)** *Bilayer thickness*

(c) *Saturated order parameters* **(d)** *Headgroup orientations*

Figure 5.11 *Comparison of 0V (black) and -225mV (red) simulations for (a) area per lipid, (b) bilayer thickness, (c) saturated order parameters and (d) headgroup orientations in a POPE/POPG (3:1) double bilayer at 300 K for 100 ns. There is no significant difference between the plots, suggesting there is no observable effect from the TMV on the bilayer properties on this timescale and temperature.*

DOPE/DSPE/DOPG/DSPG bilayers

The DOPE/DSPE/DOPG/DSPG (3:3:1:1) double bilayer had received 50 ns of equilibration at 310 K. As this bilayer is a mix of 4 lipid types, its exact transition temperature is unknown and difficult to approximate. Pure DOPE, DSPE, DOPG and DSPG bilayers have respective transition temperatures of -16 °C, 74 °C, -18 °C and 55 °C [81]. It was therefore decided to conduct simulations of this bilayer at two temperatures: 310 K and 330 K, in order to determine the most appropriate temperature to explore possible changes in membrane fluidity.

The simulation of the 310 K double bilayer was extended for 200 ns. Additionally, the 310 K double bilayer was annealed to 330 K over 50 ns at a rate of 1 K/ns, and conducted for 200 ns.

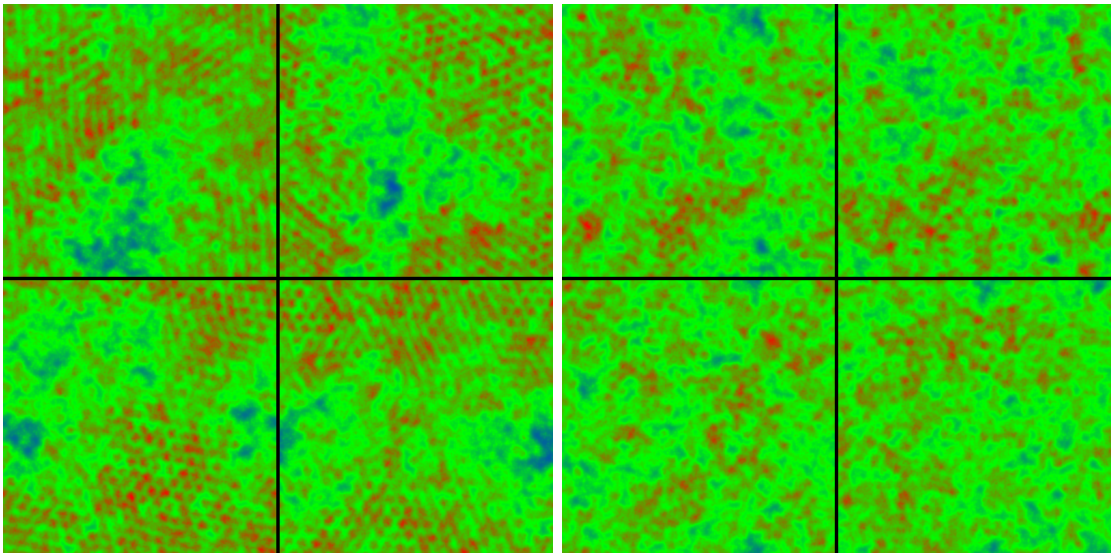

(a) *310K* **(b)** *330K*

Figure 5.12 *2D surface maps of a 310 K and 330 K simulation of DOPE/DSPE/DOPG/DSPG (3:3:1:1). Red hexagonally packed dots indicate the presence of gel clusters. The 310 K and 330 K simulations had final gel percentages of 62.4% and 16.3% respectively.*

`Membrainy` was used to calculate gel percentages and 2D surface maps for the final frames of both simulations (Figure 5.12). The bilayers at 310 K indicated a gel percentage of 62.4% (Figure 5.12a), whereas the bilayers at 330 K indicated a gel percentage of 16.3% (Figure 5.12b). We can therefore deduce that the transition temperature is somewhere between the two temperatures. As it has been suggested that TMVs should lower the transition temperature, the 310 K simulation would be more applicable to detect possible changes in fluidity than a bilayer above the transition temperature.

A TMV of -275 mV was established with an ion imbalance of +2 using the initial frame of the 310 K system, and the simulation was conducted for 200 ns. This was then compared to the existing 200 ns of the no-TMV simulation at 310 K.

Figure 5.13 depicts the results from the final 100 ns of the TMV and no-TMV simulations. Again, there is no significant difference between the TMV and no-TMV bilayer properties. Figures 5.13a and 5.13b depict the APL and bilayer thickness, which again show fluctuations in both simulations and no significant

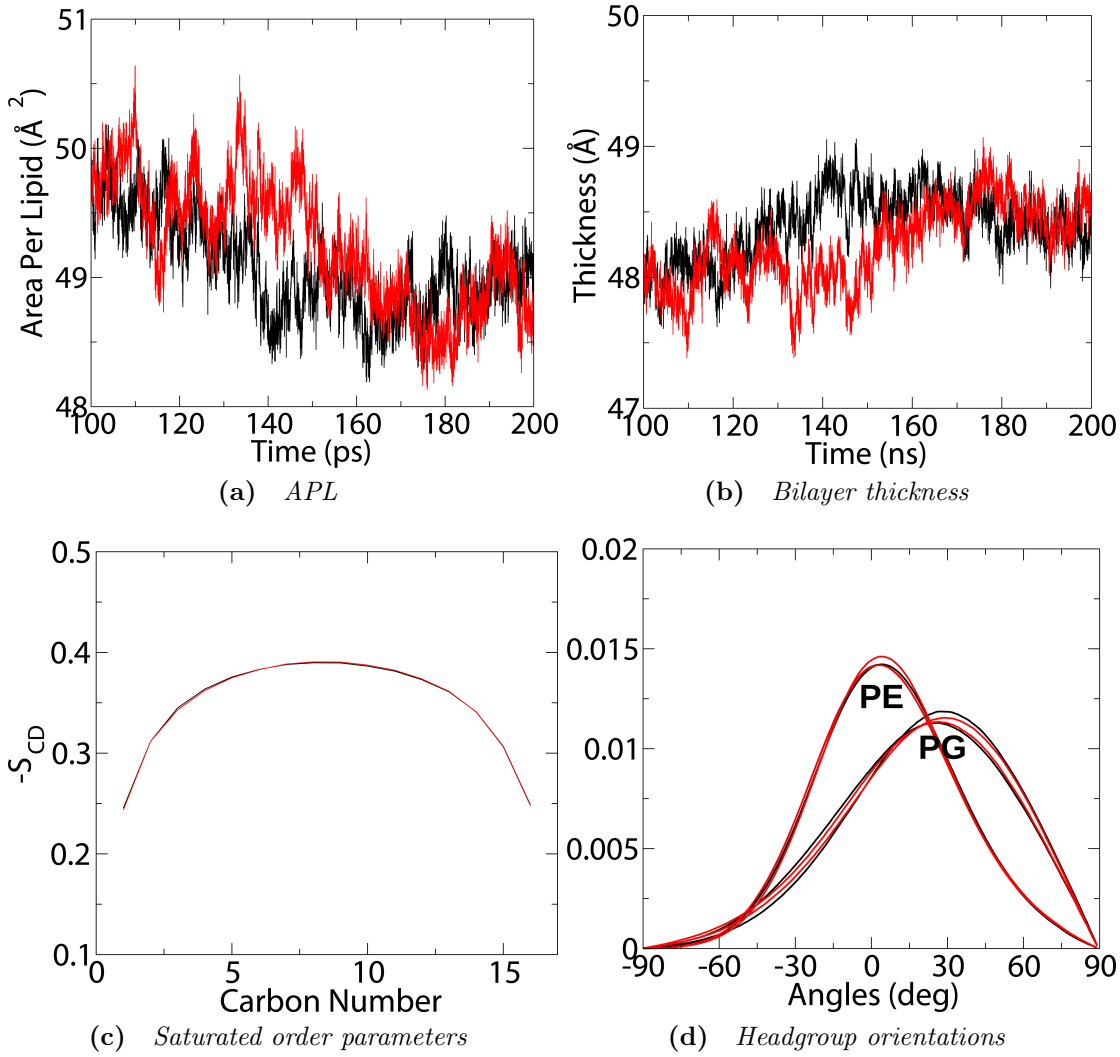

(a) *APL* **(b)** *Bilayer thickness*

(c) *Saturated order parameters* **(d)** *Headgroup orientations*

Figure 5.13 *Comparison of 0V (black) and -275mV (red) simulations for (a) APL, (b) bilayer thickness, (c) saturated order parameters and (d) headgroup orientations in DOPE/DSPE/DOPG/DSPG (3:3:1:1) double bilayers at 310 K for 100ns. There is no significant difference between the plots, suggesting there is no observable effect from the TMV on the bilayer properties on this timescale and temperature.*

difference between the plots. Figure 5.13c depicts the order parameters for saturated lipids, showing virtually identical values in both plots. Finally, Figure 5.13d depicts the headgroup orientations for all four lipid types, which have been smoothed with `SmoothGraph` and show no significant shift in headgroup orientation.

The result from both the POPE/POPG and DOPE/DSPE/DOPG/DSPG TMV simulations was surprising; the studies highlighted in Section 5.1 imply that the

influence of a membrane potential will induce changes in membrane fluidity, yet these simulations show no significant changes to the membrane properties when compared with bilayers without a membrane potential, implying there is no change in fluidity. However, as Heimburg has suggested that membrane potentials may lower the transition temperature and 'melt' the bilayer [107], a temperature of 300 K in the POPE/POPG bilayer may be too high to show any changes in fluidity when under the influence of a membrane potential, as this lipid composition has a transition temperature of 298-299 K [195]. Furthermore, Heimburg's models of electrostriction in lipid bilayers suggest that a TMV of 1 V would lower the transition temperature of a DPPC membrane by around 1.5 degrees, which is likely to be of similar order for POPE/POPG and DOPE/DSPE/DOPG/DSPG bilayers. Therefore we can deduce that it would be highly unlikely to see any changes in fluidity in these bilayers at biologically relevant voltages. Even if the appropriate temperatures were to be chosen, it seems unlikely that any measurements made over 100 ns of simulation time would reflect any significant changes in membrane properties.

5.4.2 Simulations above biologically relevant voltages

As the previous study has failed to capture any changes in membrane properties in bilayers under the influence of a membrane potential, one possible option to further investigate this would be to use higher voltages. Any changes to the membrane properties would likely be intensified from a high voltage TMV and may be observable within the timescale of 100-200 ns. However, care needs to be taken in choosing an appropriate voltage as too high a voltage would result in electroporation effects in the bilayers (which is presented in Chapter 6).

Multiple voltages of DOPE/DSPE/DOPG/DSPG at 310K

Additional simulations were constructed of the DOPE/DSPE/DOPG/DSPG mixture at 310 K with TMVs of -865 mV, -1.17 V, -1.4 V and -1.63 V. These voltages were achieved using ion imbalances of +6, +8, +10 and +12, and each simulation was conducted for 100 ns. `Membrainy` was used to analyse the final 50 ns, allowing some time for the bilayers to equilibrate to the TMV. Figure 5.14 depicts the order parameters for saturated lipid tails in the anodic leaflets for all voltages. In this figure, there is no clear trend in the ordering of the lipid

tails. The maximum separation in order is ∼0.03 between the -275 mV and -1.17 V simulations, which is considerably less than the shift in order observed in the MinD-MTS simulations when comparing gel and fluid lipids (∼0.5). This suggests that the differences in order are likely due to normal fluctuations between each system, and shows no sign of fluidity changes between each voltage.

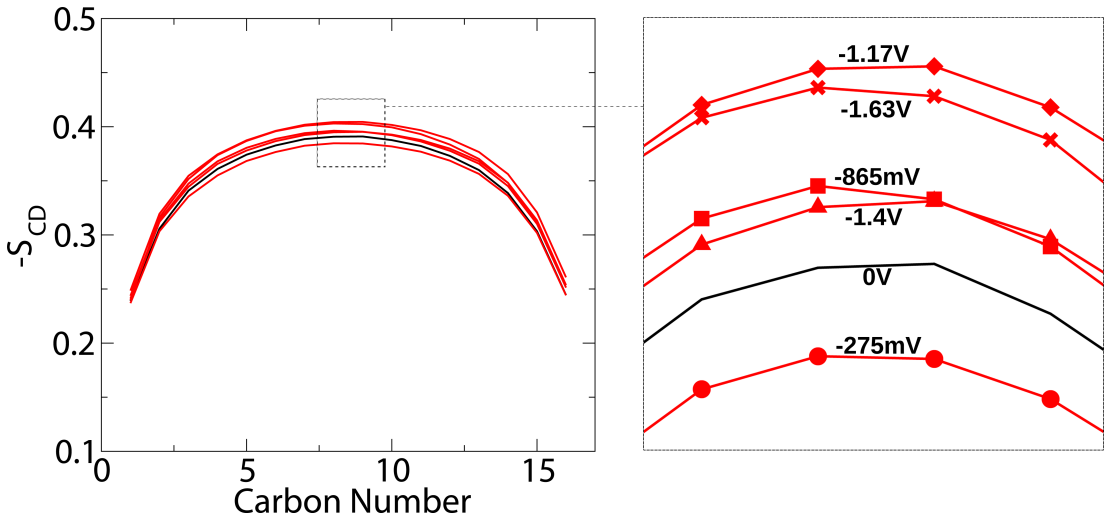

Figure 5.14 *Saturated order parameters for multiple voltages of DOPE/DSPE/-DOPG/DSPG double bilayers at 310K. There is no trend in the direction of order parameter shift between the plots, suggesting the differences are due to normal fluctuations between simulations.*

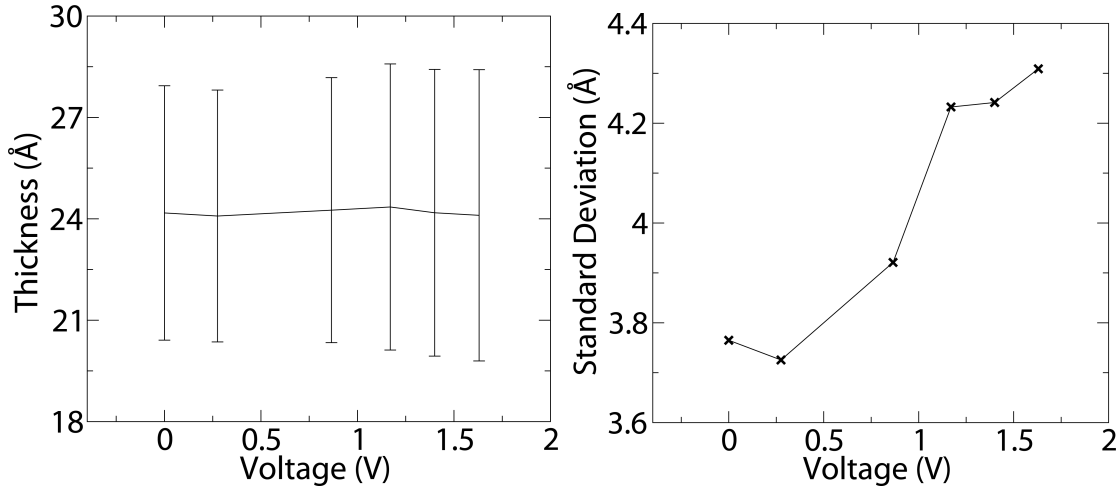

(a) *Leaflet thickness* **(b)** *Standard deviation*

Figure 5.15 *(a) Leaflet thickness for the inner leaflets only across all voltages, and (b) the standard deviations taken from (a). There is relatively no change in leaflet thickness, however we do observe an increase in standard deviation suggesting the leaflet is becoming more perturbed.*

Similarly, measurements of the average bilayer thickness over the trajectory

showed no significant differences between the voltages (data not shown). Anodic leaflet thickness also showed very little deviation across all voltages (Figure 5.15a). However an increase in standard deviation of the anodic leaflet thickness is observed as the voltages increases (seen as the error bars in Figure 5.15a, which are plotted in Figure 5.15b). Leaflet thickness is measured by subtracting the average height of the phosphorous atoms in a leaflet with the geometric centre of the bilayer, and therefore the standard deviation of this thickness portrays the height variations in the phosphorous atoms. This suggests that the leaflet surface is becoming more perturbed as the voltage increases.

This is the first observation from these simulations of a change in membrane properties induced by a membrane potential. However it is surprising that there is no significant change in leaflet or bilayer thickness, showing no evidence of electrostriction effects. This may be due to the temperature selected for this simulation, which may be too far below the transition temperature to fully explore the influences of a membrane potential on the bilayer properties.

Multiple temperatures of POPE/POPG at 1V

As the exact transition temperature for the DOPE/DSPE/DOPG/DSPG mixture cannot be determined without additional simulations or experimental data, the POPE/POPG (3:1) double bilayer provides the best means to investigate membrane potential effects around the transition temperature which, as mentioned previously, is around 298-299 K. To provide a quantitative study, three temperatures were chosen to simulate bilayers above and below the transition temperature for this lipid composition: 295 K, 297 K and 300 K. As Heimburg's model of electrostriction has predicted a $\sim$1.5 degree decrease in transition temperature for a TMV of 1 V, the 297 K bilayer falls within this window and therefore should be the most relevant temperature to observe any changes in the membrane properties.

The previous double bilayer at 300 K was annealed to 295 K and 297 K at a rate of 1 K/ns, and equilibrated for 50 ns each. Simulations were conducted at both 0 V and -1 V (using an ion imbalance of +8) over 100 ns, and each simulation was duplicated and conducted using different starting velocities. An analysis of the membrane properties of both duplicates was conducted and averaged using `Membrainy`, and the analysis of the order parameters and headgroup orientations was taken from the final 50 ns.

Figure 5.16 depicts the order parameters for the anodic leaflets, area per lipid, anodic leaflet thickness and anodic headgroup orientation across the three temperatures. The saturated order parameters (Figures 5.16a-c) show a significant increase in disorder in the TMV systems below the transition temperature (295 K and 297 K), with the largest increase observed in the systems closest to the transition temperature (297 K). There is also an increase in disorder observed in the cathodic leaflets in systems below the transition temperature, but to a lesser extent (data not shown). Above the transition temperature (300 K), there is no significant difference between the plots. This measurement suggests that the bilayers experience an increased level of fluidity in the TMV systems below the transition temperature when compared to the no-TMV simulations, expressed as an increase in flexibility/disorder throughout the entire lipid tail. The levels of fluidity remain unchanged above the transition temperature.

Similarly, the areas per lipid (Figure 5.16d-f) show a slight increase in APL below the transition temperature, with the greatest difference (about 1 $Å^2$) between the 297 K systems. This increase in APL indicates that the membrane is expanding laterally, which is representative of an increase in fluidity and may be caused by electrostriction. The was no significant difference in APL in the 300 K systems. Figures 5.16g-i depict the anodic leaflet thicknesses, which shows thinning of the leaflets below the transition temperature, with a decrease in thickness of around 0.25 - 0.5 Å in the 297 K systems. This may also be representative of electrostriction, and agrees with the increase in APL and increase in disorder to suggest higher levels of fluidity. There was no significant difference in anodic leaflet thickness at 300 K.

The effect of a TMV on the lipid headgroups is inconclusive (Figures 5.16j-l). Although there is some shift between the TMV and no-TMV systems, the mean angles are roughly identical (Table 5.2). The POPE orientations are 1-2 degrees higher and the POPG orientations are 0-3 degrees lower in the TMV simulations when compared to the no-TMV simulation. These shifts in mean angles are well within standard deviations, and could be explained by normal fluctuations across the systems. Nonetheless, it is interesting that the headgroup orientation is affected considerably less (if at all) by the TMV compared with other membrane properties. The effect of a TMV on headgroup orientation is investigated further in Chapter 6.

These results show conclusive evidence that a TMV of 1 V is capable of altering the properties of a POPE/POPG double bilayer below its transition temperature

	Mean PE angle		Mean PG angle	
	noTMV	TMV	noTMV	TMV
295 K	3°	4°	24°	24°
297 K	3°	5°	27°	24°
300 K	3°	5°	24°	21°

Table 5.2 *The mean headgroup orientations for POPE and POPG lipids in TMV/no-TMV simulations conducted at three temperatures. Each orientation is averaged from two systems.*

(295 K and 297 K) within 100 ns, suggesting that the bilayers undergo an increase in fluidity and experience a lowering of the transition temperature. It is surprising that a slight effect from the TMV exists at 295 K which is 3-4 degrees below the transition temperature, slightly more than the shift of ∼1.5 degrees predicted by Heimburg. However that prediction is based on a DPPC bilayer at 314 K, and therefore the shift in transition temperature for POPE/POPG bilayers will be different. It is also interesting that there is no observable effect at 300 K, which is only 3 degrees higher than the systems showing the greatest change in membrane properties, and only 1-2 degrees higher than the transition temperature.

5.4.3 Conclusion

The aim of research in this chapter was to elucidate the mechanism in which MinD-MTS binding affinity is increased when interacting with bacterial membranes under the influence of a membrane potential. Evidence from the various studies highlighted in this chapter suggests that membrane potentials may alter the fluidity of the membrane by lowering the transition temperature. This may be achieved from electrostriction effects that cause a decrease in membrane thickness, lowering the free energy contributions of the electrostatic and long-range forces acting across the membrane which in turn can induce a phase change. This finding lead to an investigation into possible changes to the membrane properties by comparing TMV systems with no-TMV systems. This also required the construction of analytical tools, compatible with double bilayers, to monitor any changes occurring in the membrane properties that may affect its fluidity. This was a major factor in the development of `Membrainy`.

Two lipid bilayer compositions were studied: POPE/POPG (3:1) and DOPE/DSPE/DOPG/DSPG (3:3:1:1). These bilayers were simulated with a variety of voltages and temperatures. To achieve biologically relevant voltages, a

single cation was moved across the bilayers achieving a voltage of -225 mV for POPE/POPG bilayers at 300 K, and -275 mV for the DOPE/DSPE/-DOPG/DSPG bilayers at 310 K. These voltages are more than double that of the voltage found across *E. coli*; however, smaller voltages cannot be achieved without substantially compromising simulation speed and computational cost. At these voltages, no changes to the membrane properties (order parameters, APL, membrane thickness and headgroup orientation) were observed in either bilayer composition when compared with no-TMV systems. This was a surprising result as the literature clearly describes changes in fluidity in membranes under the influence of a TMV. The lack of any change to the membrane properties in these simulations may be explained by using the incorrect temperature, incorrect timescale, or a combination of the two. It was therefore decided to further explore TMVs using a variety of temperatures in the region of the transition temperature for each composition. The voltages were also increased to intensify any TMV effect on the lipids so that it may be observed within the timescales achievable through atomistic MD.

Additional voltages of the DOPE/DSPE/DOPG/DSPG bilayers were explored, ranging from -865 mV to -1.63 V. The order parameters for all voltages showed a maximum deviation of around 0.03, which is considerably smaller than those observed in previous measurements of gel and fluid ($\sim$0.075) suggesting that these deviations may be representative of normal fluctuations between each system. An analysis of the anodic leaflet thickness showed very little deviation across each voltage; however, the standard deviation in leaflet thickness showed a consistent increase as voltage increased, suggesting that the leaflets were more perturbed at higher voltages. The exact transition temperature for this bilayer composition is unknown, and it is likely that 310 K is too far below the transition temperature to observe the full effect from a TMV.

A further experiment was conducted using three temperatures of the POPE/POPG bilayers: 295 K, 297 K and 300 K. As the transition temperature for this bilayer composition is roughly 298-299 K, these temperatures were chosen to model this composition above and below the transition temperature. Four simulations were conducted at each temperature for 100 ns using randomised initial velocities, two of which exhibited a TMV of -1 V. `Membrainy` was used to analyse the membrane properties of each system, yielding a clear increase in disorder in the order parameters for the simulations below the transition temperature (295 K and 297 K) but not above the transition temperature (300

K). Similarly, an increase in APL and a decrease in anodic leaflet thickness was observed in the TMV simulations below the transition temperature but not above. These changes in bilayer properties strongly suggest that the bilayers below the transition temperature are experiencing electrostriction, which incurs an increase in fluidity due to the lateral expansion of the bilayers. These changes in bilayer properties are intensified just below the transition temperature (297 K). An increase in fluidity implies that the TMV may be capable of lowering the transition temperature, which explains why there is no effect at 300 K. Surprisingly, there was very little deviation in headgroup orientations across all temperatures when comparing TMV and no-TMV systems. An analysis of the electric field strength in the headgroup and lipid tail region may provide further information as to why the lipid tail flexibility is more strongly influenced by the TMV than the headgroup orientations.

Although these results suggest that the bilayers are experiencing an increase in fluidity in the presence of a TMV, there are still many unanswered questions as to how this might apply to the binding affinity of MinD-MTS. Firstly, no effect was observed at biologically relevant voltages; the changes in membrane properties were only observable at -1 V. This may simply highlight an issue with the MD timescales, where an effect might be observable at biologically relevant voltages on timescales outwith those achievable through atomistic MD. Secondly, a shift in transition temperature of 1.5 degrees at -1 V is highly unlikely to have any significant shift in transition temperature at biologically relevant voltages. This shift would translate to 0.1-0.3 degrees at -150 mV, and would fail to see any changes to the MinD localisation in fluid bacterial membranes. The changes in fluidity may play a role in the MinD localisation, but it is likely that there are other pieces of the puzzle yet to be discovered. This investigation warrants additional studies to further elucidate the mechanisms behind the increase in binding affinity observed with MinD-MTS, in which I would be very interested to see how the membrane potential differs around regions of curved membranes (i.e. bacterial poles) compared with planar membranes.

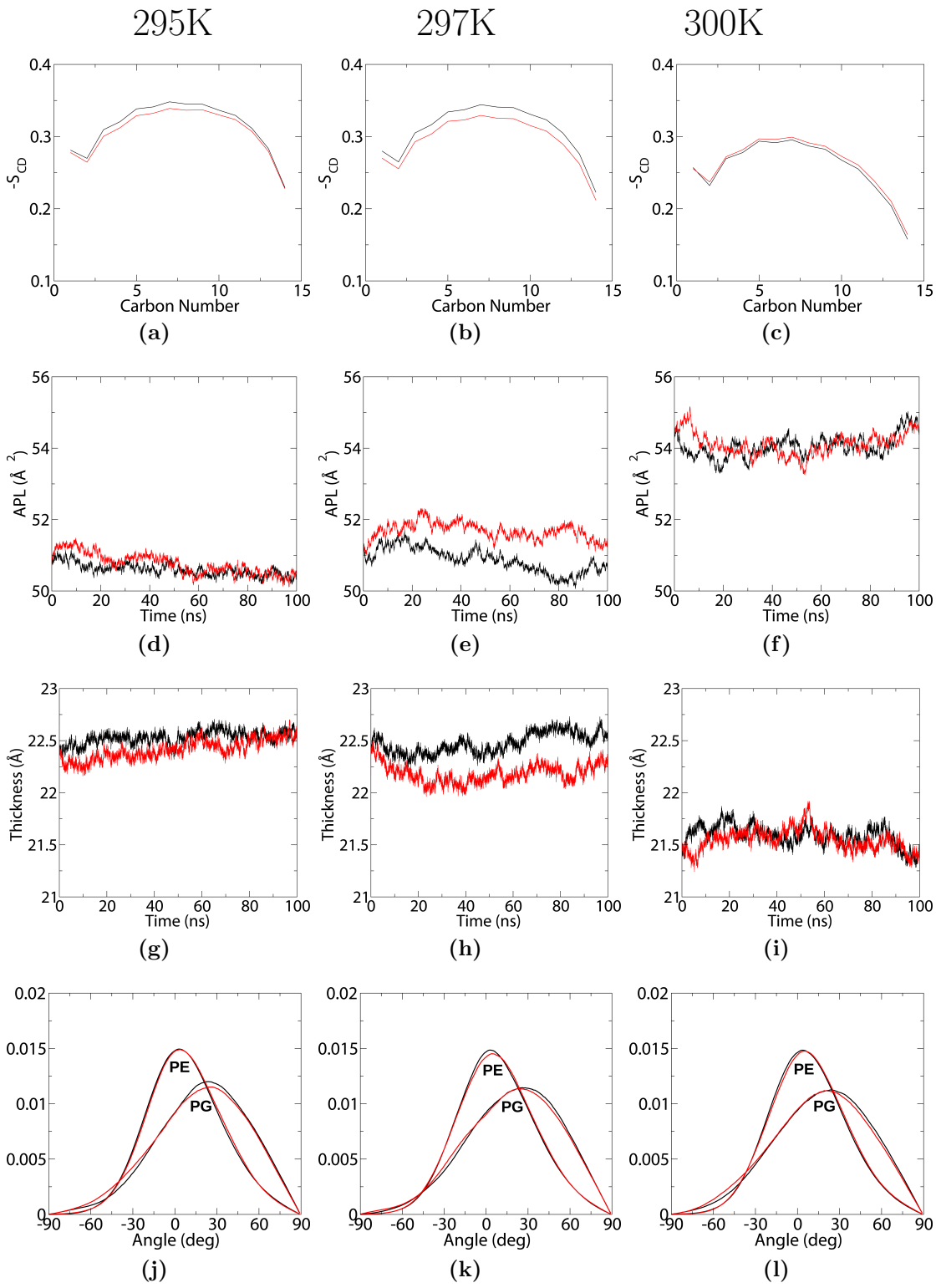

Figure 5.16 *Black = 0V, Red = 1V. Analysis from POPE/POPG double bilayers at 295K, 297K and 300K, with each plot averaged from two simulations. (a-c) Saturated order parameters for the anodic leaflets. (d-f) Area per lipid. (g-i) Leaflet thickness for the anodic leaflets. (j-l) Headgroup orientations. The plots show changes in membrane properties in the 295K and 297K simulations, but not the 300K simulations. Headgroup orientations appear unaffected in all temperatures.*

Chapter 6

An investigation of electroporation in lipid bilayers

6.1 Background

6.1.1 Electroporation

Electroporation is the term given to the induction of transient pores or holes within biological membranes through the use of electric fields. This biophysical phenomenon has been documented and utilised *in vivo* for several decades as a technique to introduce molecules (e.g. antibiotics, dyes, DNA) into a cell through electropermeabilisation of the cell membrane [196]. These transient pores are established by applying electric field pulses on a microsecond to millisecond timescale, which typically generate transmembrane voltages (TMVs) in the range of 200 mV to 1 V with a corresponding electric field strength of the order of 10^8 V/m [197]. The use of electric field pulses allows the membrane to heal between each pulse, enabling the entry of extracellular molecules into the cell while preserving the overall structure and function of the cell. Because of this, electroporation is seen as a highly attractive means for many biomedical and biotechnological applications. These include electrogenetherapy, whereby utilising electric field pulses after injection of genetic materials *in vivo* has been observed to enhance DNA transfection into host cells, which may have applications for immunisation and treatment of human disease [198, 199].

Another application is that of electrochemotherapy, in which electric field pulses targeted at permeation nodules have been observed to improve chemotherapy responses by boosting the uptake of antitumor drugs into cancer cells [200, 201]. The same electric field pulses can also give rise to electrofusion, a phenomenon which utilises the electroporation of cell membranes to merge two adjacent cells [202].

On a molecular level, the enhanced permeabilisation of the cell membrane is achieved through the formation of transient toroidal water pores, in which the size and frequency of pore formation is proportional to the strength of the electric field [203]. These pores can also occur naturally and serve an important role in the maintenance of the ionic electrochemical gradient involved in many cellular processes, as discussed in Section 5.1. As these pores exist on such short timescales, the mechanisms and dynamics behind their formation and lifespan had proven difficult to capture with existing experimental techniques and remained elusive for many years. However, recent advances in lipid force field parameters allowed several MD studies to elucidate the kinetics and energetics behind electroporation, providing a clear picture of the step-by-step process involved in pore formation [117, 203–205]. The mechanisms behind pore formation induced by an applied electric field can be categorised into five stages:

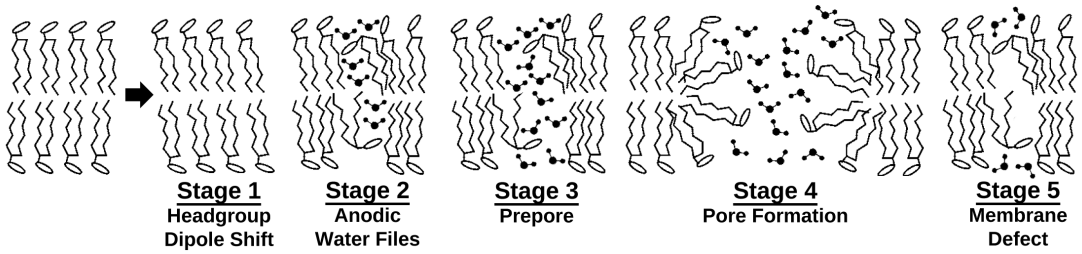

- **Stage 1:** The lipid headgroups, which are typically charged and/or zwitterionic, experience a shift in dipole orientation as the charges attempt to align the headgroup with the electric field. This shift strongly perturbs the orientation of the lipid tails, which incurs a thinning of the hydrophobic bilayer core [117].

- **Stage 2:** Water molecules on either side of the bilayer experience an alignment of their dipole to the electric field, which enhances the probability of water molecules inserting into the anodic leaflets (the leaflets in contact with the cellular compartment containing a negative electrostatic potential).

This enhanced probability, along with the changes in headgroup orientation and bilayer thinning, allows for the intrusion of *water files* into the bilayer.

- **Stage 3:** These water files drag the lipid headgroups deeper into the bilayer, causing defects or perturbations on the bilayer surface. Under the right conditions, water files can connect with the cathodic water compartment to form a *prepore*.
- **Stage 4:** Pore formation immediately follows from a prepore, which sees additional water molecules pulled into the bilayer through a dielectric avalanche. This pulls additional lipid headgroups into the hydrophobic region of the bilayer, giving rise to the toroidal shape of the pore. The pore remains open for the duration of the pulse and sees cations and anions flow through the pore in opposite directions.
- **Stage 5:** Once the pulse is terminated, the membrane slowly heals by closing the pore; however, a defect is left within the bilayer comprising a thin, highly perturbed region in both leaflets.

Although the pore formation mechanisms have been elucidated, the implications of electroporation with certain bilayer compositions are still unknown, with only a handful of MD studies being published in the past few years. One such study by Casciola *et al.* looked into the relation between the electroporation process and bilayers containing cholesterol [206]. Their findings suggest that increasing the levels of cholesterol in simulated POPC bilayers increased the electroporation threshold voltage, i.e. the minimum voltage required to induce pore formation within the simulation time. As cholesterol is known to modify the fluidity of bilayers, this may suggest that electroporation of membranes in the gel phase will also require higher threshold voltages. Gurtovenko and Lyulina conducted electroporation simulations using an asymmetric neutrally charged bilayer [207], where one leaflet was composed entirely of POPE lipids and the other of POPC. Their findings suggest that pore formation is initiated from the POPC leaflet regardless of the direction of the electric field, suggesting that the POPE leaflet is considerably more robust due to increased intermolecular hydrogen bonding between the lipids, leading to a denser packed water-lipid interface and increased ordering in the lipid tails. They found that this water-lipid interface prevents the formation of water files, an essential stage in the pore formation mechanisms.

Another study by Reigada looked into the electroporation of heterogeneous membranes containing lipid rafts, in which lipids in a highly ordered phase were

surrounded by lipids in a disordered phase [208]. This study saw minimal changes in the properties of those lipids in an ordered phase, whereas the lipids in a disordered phase experienced significant changes in order parameters, area per lipid and bilayer thickness. Furthermore, pore formation was exclusive to regions of disordered lipids.

Polak *et al.* investigated the electroporation effect using bilayers constructed from DPhPC (diphytanoyl-phosphocholine) esters and ethers [209]. These lipids differ from DPPC lipids by having additional branched chains connected throughout the lipid tails. When compared with pure DPPC bilayers, DPhPC bilayers exhibited a higher electroporation threshold voltage, likely explained by the increased stability in the bilayers from a slower conformational motion of the lipid tails. In addition, a study by Wang and Larson found that electroporation in DPhPC bilayers favoured barrel-stave pore formation, also due to the increased stability in the bilayers [106]. On terminating the electric field, barrel-stave pores were observed to close within 2 ns, whereas toroidal pores remain open after 40 ns, further highlighting the increased stability in DPhPC bilayers.

Most MD studies of electroporation in lipid bilayers follow the technique of applying a uniform electric field to the simulation box, achieved by adding an additional component $\vec{F} = q\vec{E}$ to the force acting on each atom, where $\vec{E}$ is the desired electric field strength defined in the simulation parameters. Sachs *et al.* adopted an alternate approach of inducing electroporation in lipid bilayers by replacing the applied electric field with an ion imbalance across a double bilayer [88]. This approach, which is discussed and used throughout Chapter 5, simulates the natural ionic gradient found across biological cell membranes. However, as this approach is considerably more computationally expensive than simulating a single bilayer, only a handful of studies have utilised this approach [106, 108, 205]; as such, the specific properties of bilayers undergoing electroporation induced by ion imbalances have yet to be fully explored. Studies utilising both approaches have described similar pore formation mechanisms but different pore lifetimes: an applied electric field allows pores to remain open indefinitely, whereas an ion imbalance achieves short-lived pores. This is because the electric field across the bilayers causes ions to flow through the pore in the direction that results in a dissipation of the ion imbalance. Once dissipated, the electric field strength is greatly reduced and unable to sustain the pore, allowing the membrane to slowly heal.

One area of electroporation that has yet to be explored through MD is a proposed

mechanism whereby charged molecules, such as AMPs, are capable of inducing a sufficient electric field across the membrane to induce pore formation. This possibility was first proposed by Miteva et al. [210], who conducted non-MD electrostatic potential calculations with NK-lysin and found that this protein has sufficient charge to induce electroporation in membranes. Gurtovenko and Vattulainen also briefly mentioned that charged peptides may be capable of inducing electroporation in double bilayers when substituting an ion imbalance [205].

6.1.2 Aims

The work in Section 6.2 aims to improve our understanding of the electroporation process when induced by ion imbalances using a range of bilayer compositions and temperatures. These include simulations of POPE/POPG (3:1), POPC/POPG (3:1), POPC and DPPC bilayers at 297 K and 320 K[1]. A comparison of each composition and temperature may help elucidate the relationship between the electroporation threshold voltage and the bilayer fluidity. Also, by conducting simulations with POPE/POPG (3:1) and POPC/POPG (3:1) bilayers, the implications of electroporation on negatively charged bilayers can be explored. Furthermore, the shape of the electric field and the role of electroporation induced lipid flip-flopping in POPE/POPG (3:1) bilayers is explored.

The work in Section 6.3 merges the topics discussed in Chapters 4 and 5 (AMPs and TMVs) to answer the question: Can an AMP generate a TMV across a double bilayer? And if so, can AMPs achieve pore formation in double bilayers via electroporation? How does this differ from using an ion imbalance, and what implications will this have on cell membranes? This section also raises the interesting question as to whether certain AMPs utilise membrane electroporation as a stage in their mechanism of action.

6.1.3 Simulation methods

All peptides were synthesised using the Xplor-NIH program [161, 162] as α-helices with a short 1 ps run using the CHARMM19 force field. A stepsize of 1 fs was used, and hydrogen bonding between backbone atoms was constrained

[1]Due to time constraints and insufficient computational resources, DPPC bilayers were conducted at 297 K only.

to helical distances during the dynamics run. POPC, POPC/POPG (3:1) and DPPC bilayers were constructed using the CHARMM-GUI bilayer builder [82] with 200 lipids per leaflet and a water thickness of 15 Å to each leaflet. Additional waters were then added to achieve a box height of approximately 10 nm. The single bilayers were energy minimised using the steep algorithm and equilibrated for 50 ns at 297 K in the CHARMM36 force field. Afterwards, each single bilayer was duplicated and placed on top of the original bilayer to form a double bilayer. Waters and ions were added/removed such that the box height was approximately 20 nm, and each water compartment was assigned a salt concentration of 150 mM K^+Cl^- using the program `BoxMod` (see Section 3.3.1). The bilayers were then equilibrated for 150 ns at 297K, and duplicates were created and annealed to 320 K at a rate of 1 K/ns and equilibrated for 150 ns. The equilibrated POPE/POPG (3:1) double bilayer from Chapter 5 was reused.

A velocity rescale thermostat was used with a time constant of 0.2 ps, which saw the bilayers and solution coupled separately. A Berendsen semi-isotropic pressure coupling scheme was used with a time constant of 2 ps, reference pressure of 1 bar and a compressibility of 4.5 x10^{-5} bar^{-1}, which saw the xy and z box vectors coupled separately. Bond lengths and angles were constrained using the LINCS algorithm and were limited to all bonds with hydrogen atoms. Nonbonded interactions were evaluated with a cutoff of 1.4 nm and updated every 10 fs, with the exception of van der Waals interactions which were evaluated with a cutoff a 1.2 nm and experienced an exponential decay from 0.8 nm. The equations of motion were integrated using the leapfrog method with a stepsize of 2 fs. All simulations were conducted using the GROMACS v4.5.5 package [63].

All simulations were conducted on the HECToR super computer using 1024 cores (32 nodes), which is capable of simulating 30 ns of these double bilayer systems in approximately 12 hours.

6.2 Electroporation of model membranes using ion imbalances

6.2.1 Electroporation of POPE/POPG bilayers

MD simulations were conducted to investigate electroporation of a POPE/POPG (3:1) double bilayer induced by an ion imbalance. The program `BoxMod` was used to establish an ion imbalance of +20, which moves 10 cations from the inner water compartment to the outer compartment to create a negative potential in the inner (anodic) compartment. The resulting simulation was energy minimised and conducted for 30 ns.

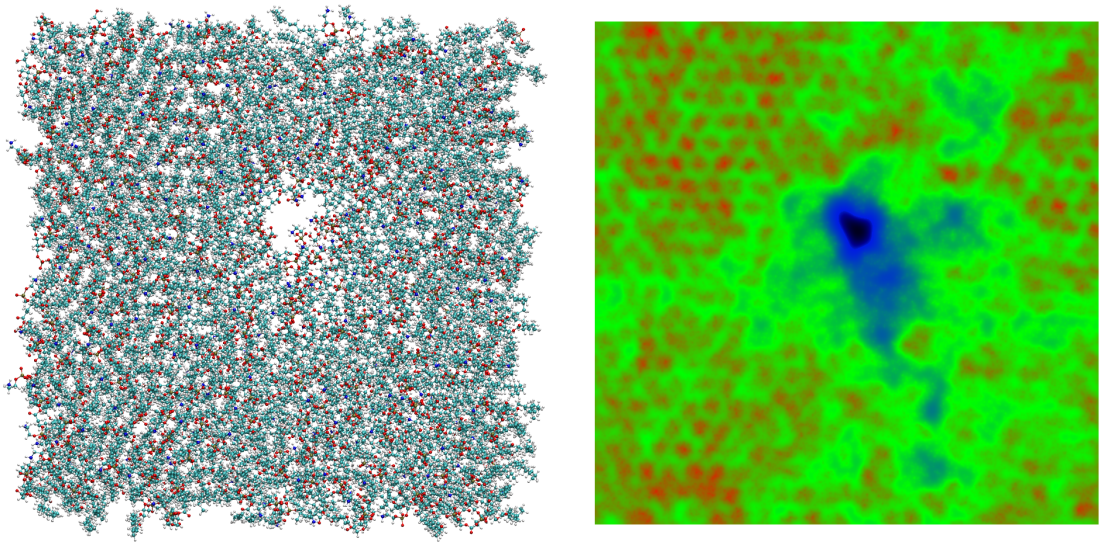

(a) *Membrane image* **(b)** *2D surface map*

Figure 6.1 *(a) Image of a pore in the POPE/POPG (3:1) bilayer at 16 ns, obtained with the program VMD [127]. (b) 2D surface map of the pore at 16 ns, obtained with* `Membrainy`*. The surface map indicates the pore formed in a region of high fluidity on a thin, highly perturbed spot on the membrane.*

Through visual inspection of the trajectory, a single pore formed at ∼15 ns and remained open for the remaining simulation time (Figure 6.1a). Whilst open, cations were transported through the pore from the cathodic to anodic compartment, corresponding to the direction of the electric field. Having been initialised with an ion imbalance of +20, the final imbalance of the system after 30 ns was +2, suggesting that the existence or purpose of the pore was to return equilibrium to the ionic concentrations in each compartment and lower

the TMV across the bilayers. A 2D surface map of the pore was generated using `Membrainy` and shows the pore occurring in a thin or weak spot in the membrane with a high level of fluidity (Figure 6.1b). Prior to pore formation, the trajectory showed the formation of various water files in the anodic leaflet which were subsequently dissipated in less than a nanosecond. These water files have also been observed in the anodic leaflets when using an applied electric field [117], suggesting that the mechanisms of pore formation between both approaches are similar. Pore formation was established after a water file from the anodic compartment connected with the cathodic compartment, which then rapidly increased in size to a maximum diameter of approximately 10.8 Å.

Figure 6.2 depicts various membrane and system properties analysed from the simulation. Figure 6.2a depicts the evolution of the TMV over the trajectory, revealing an initial TMV of -2.7 V which decreases over 5 ns to -2.35 V. During these 5 ns, Figure 6.2b reveals that the box is expanding laterally and shrinking in height, likely due to electrostriction effects causing a compression of the bilayers and subsequent lateral expansion. There may also be thinning of the bilayers from a headgroup dipole shift as highlighted in stage 1 of the pore formation mechanism. The lateral expansion incurred a small increase in membrane surface area, resulting in a slight drop in TMV as the ion imbalance is spread over a larger area. At 15 ns, a sharp drop in TMV is observed as pore formation occurred. Cations flowed through the pore at a rate of 3 ions/ns (Figure 6.2c), resulting in a rapid loss of TMV at a rate of 650 mV/ns. By 18 ns, the ion imbalance drops to +4 and the TMV lowers to -250 mV, which is likely well below the electroporation threshold; however, the pore remained open for the remainder of the simulation time. This is likely due to its hydrophilic toroidal shape which held ions and water molecules within the pore, restricting or slowing the bilayer's ability to close the pore. The pore diameter decreased in size over the remainder of the simulation and saw an additional cation enter the pore and briefly become stuck at ∼24 ns, taking approximately 2 ns to pass through the pore. After 30 ns, the resulting pore diameter was 3.5 Å and the TMV was approximately -225 mV from an ion imbalance of +2.

Figures 6.2d-e depict the saturated and unsaturated lipid tail order parameters taken between 5-15 ns (i.e. after equilibration and before pore formation) and are compared with a no-TMV system sampled over 10 ns. A significant increase in disorder is observed in both saturated and unsaturated lipids, which also reveals slightly more disorder in the anodic leaflets than the cathodic leaflets. Figure

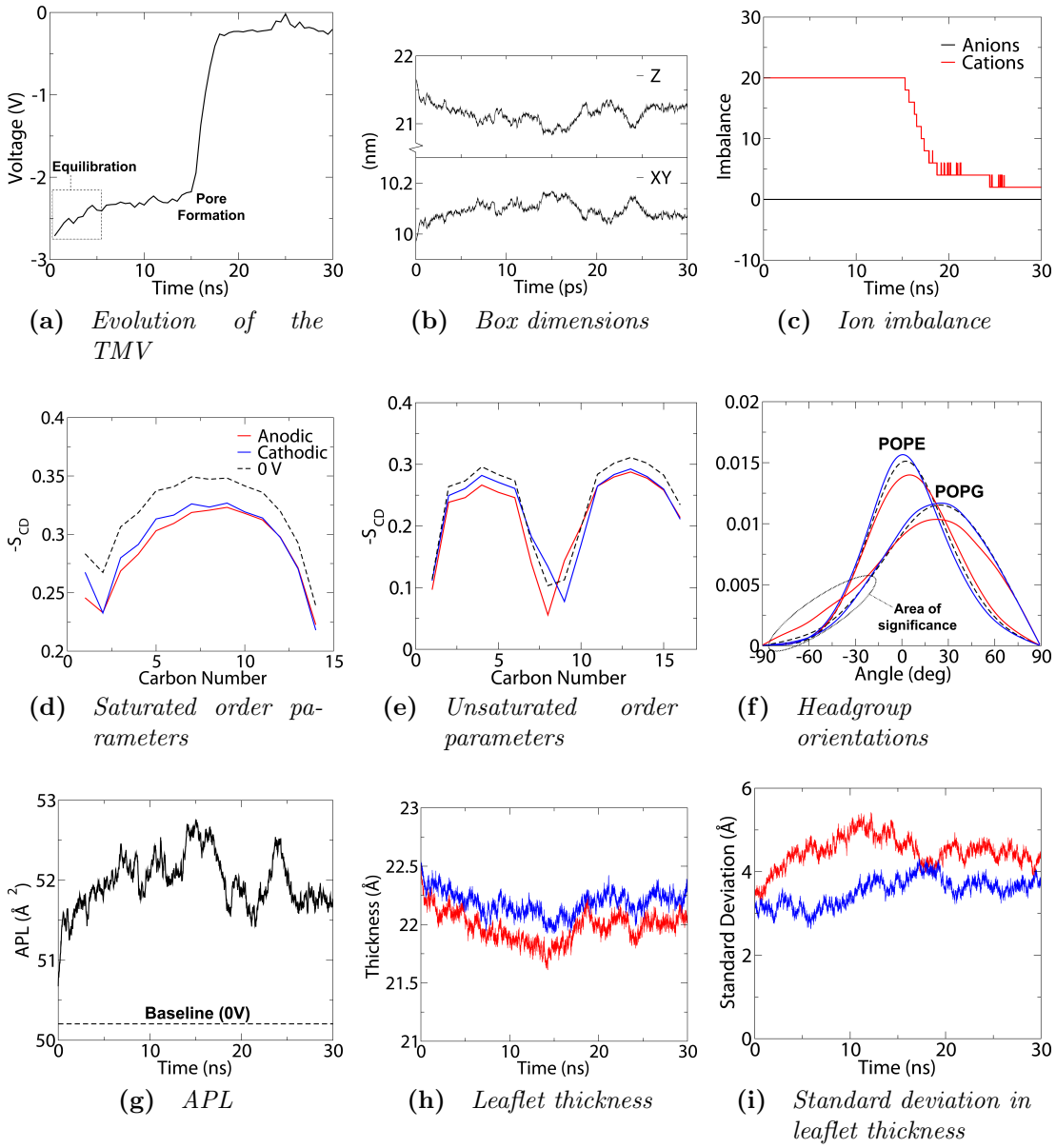

(a) *Evolution of the TMV*

(b) *Box dimensions*

(c) *Ion imbalance*

(d) *Saturated order parameters*

(e) *Unsaturated order parameters*

(f) *Headgroup orientations*

(g) *APL*

(h) *Leaflet thickness*

(i) *Standard deviation in leaflet thickness*

Figure 6.2 *Analysis of a POPE/POPG (3:1) double bilayer undergoing electroporation from an ion imbalance of +20 (-2.35 V). Pore formation occurred at ∼15 ns, which incurs a drop in TMV to -225 mV as cations flowed through the pore towards the anodic leaflet, resulting in a dissipation of the ion imbalance. Order parameters and headgroup orientations were measured between 5-15 ns, revealing an increase in disorder when compared to a no-TMV simulation, and a small shift in mean headgroup orientation which suggests that the headgroups are tending to align with the electric field. An increase in APL and a reduction in thickness is observed in both leaflets prior to pore formation, which is reversed after pore formation. The plots reveal that anodic leaflets incur greater changes to the lipid properties over cathodic leaflets.*

6.2f depicts the headgroup orientations for the anodic and cathodic leaflets taken between 5-15 ns and smoothed with the program `SmoothGraph` (see Section 3.3.3). A slight shift in orientation is observed in both anodic and cathodic leaflets, which show mean POPE orientations of 5 and 0.5 degrees respectively, and mean POPG orientations of 22.5 and 25.5 degrees. The same bilayer without a TMV shows mean orientations of 2.5 degrees for POPE headgroups and 24.5 degrees for POPG headgroups. This indicates a mean anodic and cathodic POPE headgroup shift of +2.5 and -2 degrees respectively, and a POPG headgroup shift of -2 and +1 degrees, suggesting that the headgroups are tending to align with the electric field; however, this alignment is extremely subtle which may indicate that the electric field within the headgroup region is relatively weak. The anodic leaflets appear to experience a greater shift in orientation than cathodic leaflets, and anodic POPG headgroups reveal an area of significance between -90 and -15 degrees, indicating an increased number of headgroup orientations within this region which suggests that POPG headgroups are being pulled into the bilayer.

Figures 6.2g-i depict the area per lipid (APL), leaflet thickness and standard deviations in the leaflet thickness. The APL shows a steady increase of $\sim$2 Å^2 within the first 15 ns (Figure 6.2g), corresponding to the lateral expansion of the bilayers. Once the pore is formed, a sharp drop in APL is observed while cations flowed through the pore (15-18 ns) which corresponds with the lateral shrinking of the bilayers as the TMV is lowered. Once the ion flow slows, the APL fluctuates but remains relatively constant for the remainder of the simulation at around 1 Å^2 higher than the initial APL. Prior to pore formation, both the anodic and cathodic leaflets decrease in thickness by around 0.5-0.8 Å (Figure 6.2h), where the anodic leaflets are consistently thinner than the cathodic leaflets. Once the pore is formed, both leaflets rapidly expand and then maintain a relatively constant thickness for the remainder of the simulation, which is 0.25-0.5 Å thinner than the initial thickness. The standard deviations in the leaflet thickness reveal an increase for both leaflets, with slightly larger deviations in the anodic leaflets (Figure 6.2i), suggesting that the anodic leaflets are more perturbed than the cathodic leaflets.

Figure 6.2c reveals that no anions were observed to travel through the pore during the simulation. This is likely explained by the overall lack of anions in the system, as each compartment contained only 9 anions (compared with 97 or 117 cations). This vast difference in ion ratios is due to the requirement imposed by the Ewald summation (see Section 2.1.7) to maintain a neutrally

charged system, which required a significantly larger amount of cations given that POPE/POPG (3:1) bilayers are highly anionic. Previous electroporation studies (discussed throughout Section 6.1.1) have shown both anions and cations to flow through the pore in opposite directions, suggesting that this is an artifact from simulating charged bilayers.

To determine the validity and consistency of these results, and the frequency of pore formation at this TMV, six additional simulations were carried out using four initial frames taken from the equilibrated no-TMV POPE/POPG (3:1) trajectory (the frames chosen were after 50 ns, 80 ns, 90 ns and 100 ns of equilibration[2]). Simulations containing duplicates of the initial frames were given randomised initial velocities, and each simulation was conducted for 30 ns.

`Membrainy` was used to measure the time evolution of the TMV for each simulation, which is depicted in Figure 6.3a along with the TMV measurements from the previous simulation. In total, five pore formations (from seven simulations) were observed to occur within the simulation time. Interestingly, each simulation starting from the 50 ns frame experienced pore formation at roughly the same time even though randomised initial velocities were used. An analysis of the lipids involved in these pores indicated that two of the pores formed in exactly the same spot on the same bilayer (in the double bilayer system), and the third pore formed on the opposite bilayer. This suggests that their formation at similar times is coincidental. The pores that formed from the two simulations starting from the 100 ns frame occurred on opposite bilayers, but formed at the same weak spots observed in the pore formations that occurred in the 50 ns frames. These results suggest that pore formation occurs at a random point in time on either bilayer, but shows a high probability to form at the same thin or weak spot on the bilayer containing a high level of fluidity. The resulting TMVs ranged between -0.4 V and -0.1 V.

Of the two simulations that failed to form a pore (80 ns and 90 ns), Figures 6.3b and 6.3c depict a comparison of the APL and TMV measurements over the trajectories. This reveals that in simulations where the ion imbalance remains constant, the APL and TMV are partially coupled. Any change in APL incurs a similar change in TMV, which is also true for each pore formation simulation prior to the pore opening. This partial coupling is likely achieved because both the APL and electrostatic potential calculations are heavily influenced by the box

[2]Note that the POPE/POPG (3:1) bilayer had received approximately 200 ns of equilibration prior to the numbers stated in this section.

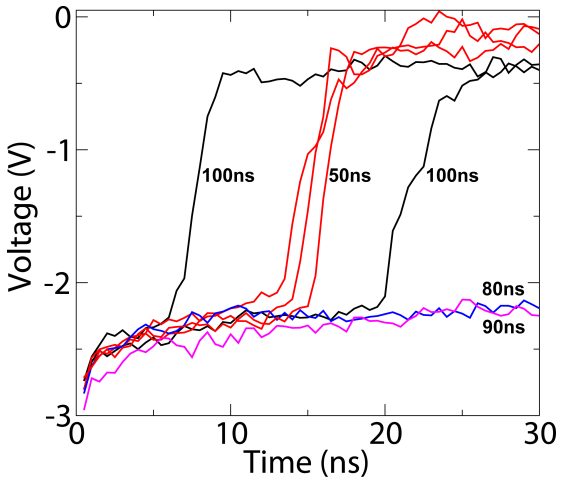

(a) *TMVs of all simulations*

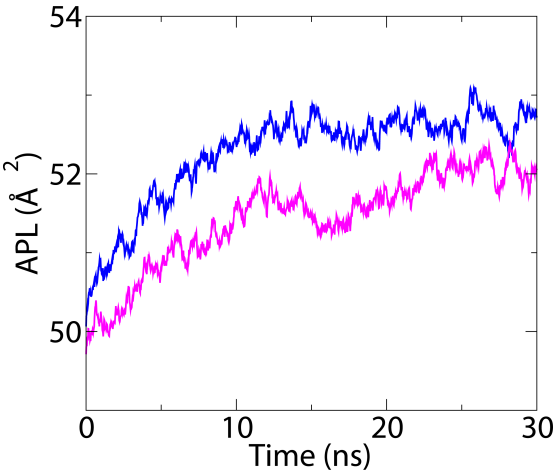

(b) *APLs of failed pores*

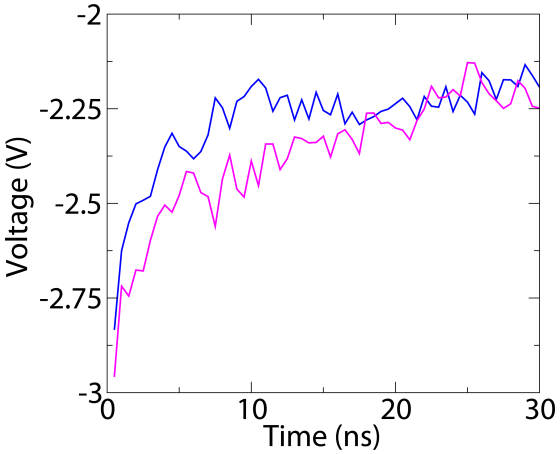

(c) *TMVs of failed pores*

Figure 6.3 *(a) Time evolution of the TMV for seven simulations of POPE/POPG (3:1) double bilayers with ion imbalances of +20 (-2.35V). The initial frames used were taken after 50 ns (red), 80 ns (blue), 90 ns (purple), and 100 ns (black) of equilibration. Five out of seven simulations resulted in pore formations. (b) and (c) depict the APL and TMV measurements for the two simulations (80 ns and 90 ns) that failed to produce a pore, revealing partial coupling between the APL and TMV.*

x and y dimensions, and may have some interesting applications when studying bilayer compositions that undergo changes in APL such as upon transitioning from gel to fluid phases.

6.2.2 Investigating the unsaturated order parameters shift

The order parameters of the double bond (carbons 8-9 in Figure 6.2e) reveal an unusual shift between the anodic and cathodic leaflets, showing the first carbon in the anodic leaflets to be considerably more disordered than the second carbon, and vice-versa for the cathodic leaflets. This differs greatly from the no-TMV simulation which shows roughly equal order parameters for both carbons.

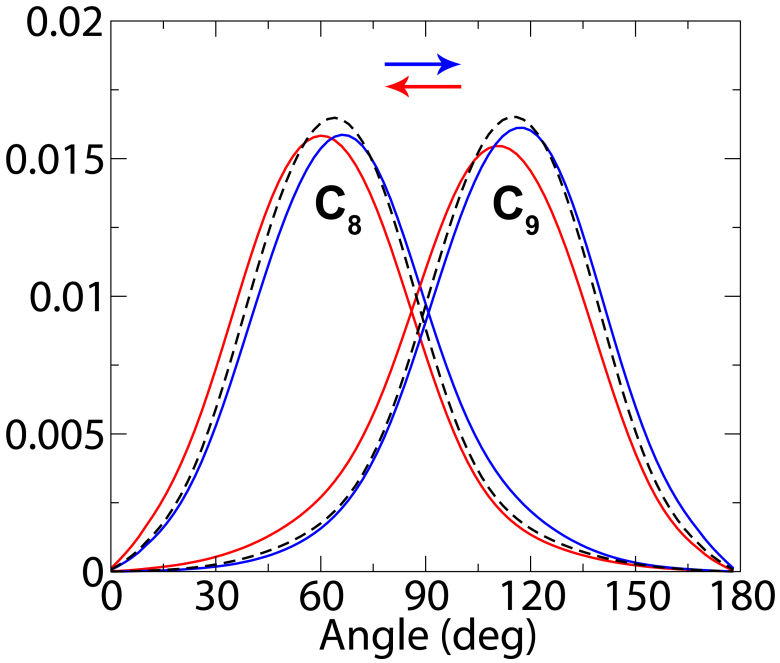

Figure 6.4 *The distribution of C-H bond angles for the C_8 and C_9 double bond carbon atoms in the unsaturated lipid tails of a POPE/POPG (3:1) double bilayer with a TMV of -2.35 V. The anodic (red) and cathodic (blue) leaflets are compared with a no-TMV (dashed black) system. The shift in angles suggest the C−H bonds are tending to align with the electric field.*

To investigate this shift in order parameters, `Membrainy` was modified to produce histograms of the C−H bond angles for each carbon in the lipid tails. Figure 6.4 depicts the histograms produced for the C_8 and C_9 carbon atoms in the unsaturated lipid tails, which have been smoothed with the program `SmoothGraph`. A shift in bond angle is observed when compared with a no-TMV system, revealing that the anodic leaflets experience a decrease in mean C−H bond angle in both carbon atoms, whereas the cathodic leaflets experience an increase in mean angle in both carbon atoms. This corresponds with the C−H bond tending to align with the electric field in both leaflets, since the CHARMM force field assigns a charge of -0.15 to the carbon atom and +0.15 to the hydrogen

atom. This alignment accounts for the unusual shift in order parameters because bond angles tending towards 90 degrees are more ordered; therefore, the C_8 atom in anodic leaflets would appear more disordered while the C_9 atom would appear more ordered, and vice-versa for the cathodic leaflets.

It is interesting to note that this shift in mean C−H bond angle, including those in other carbon atoms in the lipid tails, is more substantial than the shift observed in the mean headgroup orientations in Figure 6.2f, which one would expect to be more perturbed by an electric field due to the headgroups holding considerably more charge and flexibility than these C−H bonds. This may suggest that the electric field is stronger in the lipid tail region than in the headgroup region, and is investigated further below.

6.2.3 Analysis of the electric field

The simulations conducted in Section 6.2.1 produced some interesting results that shed light on the shape and strength of the electric field within the bilayer. Firstly, the anodic leaflets exhibit slightly larger changes to their properties than the cathodic leaflets, suggesting that the electric field may be stronger in the anodic leaflets. Secondly, on applying a TMV, the shift in mean headgroup orientations for both zwitterionic POPE and anionic POPG headgroups is smaller than the shift in mean orientation of the lipid tail C−H bonds, which hold considerably less charge and are less flexible than the lipid headgroups. This suggests that the electric field may be weaker in the headgroup region than in the lipid tail region. Finally, the formation of water files occurs mostly in the anodic leaflets, and each pore formation is visibly initiated by the anodic leaflet/compartment. This has been suggested to be a result of the water dipole alignment in the anodic compartment [117], but may also be explained by the increased perturbations observed in the anodic leaflet properties.

To investigate this, the electric field across the bilayers in the previous simulation was calculated by taking the negative derivative of the electrostatic potential, since $E = -\nabla\phi$. The electrostatic potential from the original electroporation simulation was measured between 5-15 ns using the program `g_potential`, and then the program `Xmgrace` was used to calculate the negative derivative of this potential.

Figure 6.5 depicts the electric field across the lower bilayer from the -2.35 V

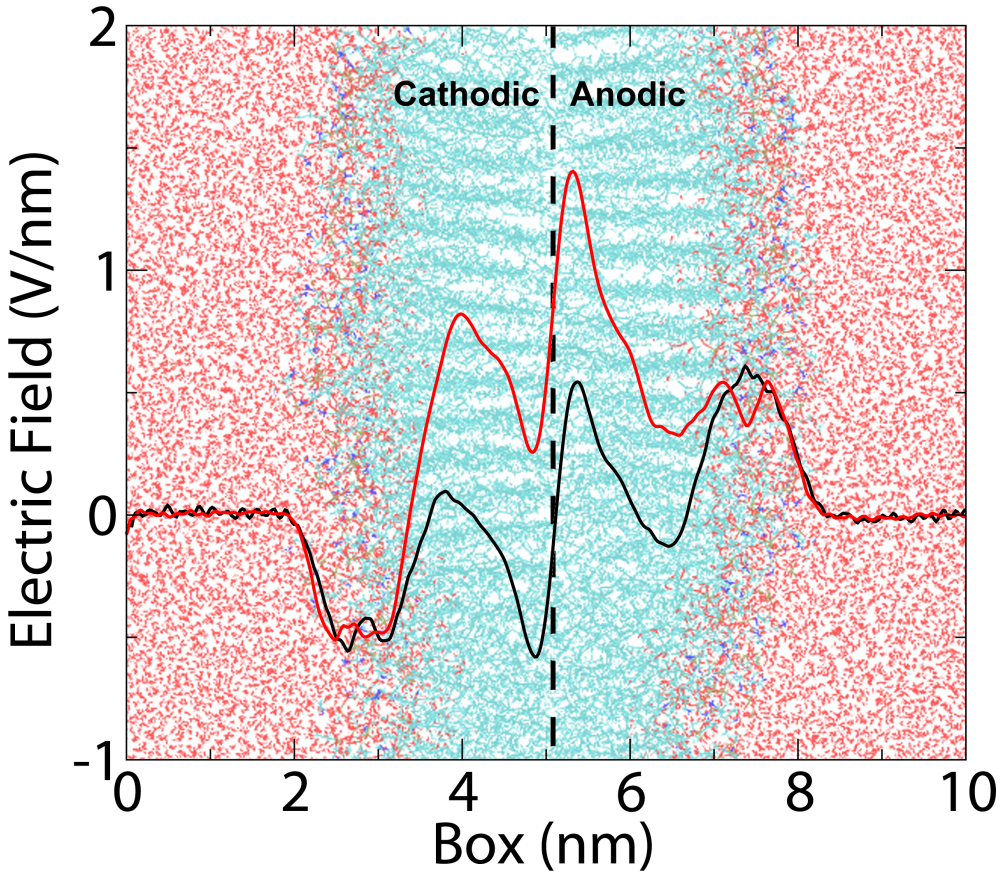

Figure 6.5 *The electric field across a POPE/POPG (3:1) bilayer with a TMV of -2.35 V (red) and 0 V (black). The 0 V system exhibits glide reflection symmetry with a mean electric field strength of 0 V/nm across the bilayer. The -2.35 V system shows positive electric field values throughout the bilayer, with a greater field strength in the anodic leaflets and a mean field strength of 0.37 V/nm.*

POPE/POPG (3:1) system (red) compared with a no-TMV system (black). The no-TMV plot shows a non-zero electric field within the bilayer, revealing glide reflection symmetry around the bilayer centre (i.e. the electric field values are equal and opposite across both leaflets). This electric field peaks with a value of ∼0.5 V/nm in both headgroup regions and at the end of the lipid tails. The -2.35 V system shows a similarly shaped electric field that is skewed in the positive direction in both leaflets, peaking in the lipid tails with a value of 0.8 V/nm in the cathodic leaflet and 1.4 V/nm in the anodic leaflet. The average electric field strength over the bilayer (taken between 2 and 8 nm) is 0.37 V/nm. This electric field strength is slightly larger than the electroporation threshold field strength reported by various electroporation studies using applied electric fields, which is 0.29 V/nm for POPC bilayers and 0.3 V/nm for DMPC bilayers, both of which were approximated from simulations using the Berger lipid force field

[117, 205]. This may suggest that electroporation in POPE/POPG bilayers may occur within 30 ns at voltages lower than -2.35 V. To confirm this, an additional simulation was conducted using an ion imbalance of +16 (-1.9 V) which revealed a pore formation at 29 ns. This voltage corresponds to an electric field strength of 0.29 V/nm averaged over the bilayers.

The shift in electric field at -2.35 V provides clear evidence that the anodic leaflets experience a greater field strength than the cathodic leaflets, and may explain the stronger changes in anodic leaflet properties observed in Figure 6.2, as well as the low voltage TMV simulations conducted in Chapter 5. This is an interesting finding which was also observed by Böckmann *et al.* when using an applied electric field with POPC bilayers [117]; however, the shape of the electric field within the bilayers is different to their observations, possibly due to the differences between the two approaches of generating a TMV. Interestingly, Gurtovenko and Lyulina saw no preference for the creation of water files in a specific direction while applying an electric field to pure POPE and POPC bilayers [207]. Clearly there is a conflict in results which requires a detailed comparison of the experimental procedures employed by each study to further elucidate this.

Another significant finding from this analysis is that the electric field strength in the headgroup regions of both leaflets is almost identical to those of a no-TMV system, which may explain why there is very little change in mean headgroup orientation between TMV and no-TMV systems. As the previous headgroup orientation analysis reveals some shift in headgroup orientation above and below the mean, this may be due to lipid headgroups sitting deeper within the bilayer and are subject to the stronger electric fields observed in the tail region. This is clearly evident with the presence of water files which drag the lipid headgroups into the lipid tail region, and may also explain the increase in anodic POPG headgroup orientations observed between -90 and -15 degrees.

6.2.4 Electrostatic potential for bilayers of different dimensions

As observed in the previous experiments, an increase in the bilayer surface area results in a drop in TMV due to the ion imbalance being spread over a larger surface. This can be further explained by looking at Equation 3.4 in Section 3.2.3, which calculates the electrostatic potential by taking a double integral of

Poisson's equation and utilises the charge density of a slice in the z-dimension [211]. Calculating this charge density requires dividing by the volume of these slices, which is mainly dependent on the box xy area as the height of the slices are typically very small (about 0.18 Å for these simulations).

As the TMV is highly sensitive to changes in the box x and y dimensions, to what extent will the TMV be affected when the z-dimension is increased to allow for a greater separation between the bilayers? To investigate this, three simulations of POPE/POPG (3:1) double bilayers with different dimensions and lipids per leaflet were constructed. An ion imbalance of +20 was established across each double bilayer, which were then simulated for 30 ns.

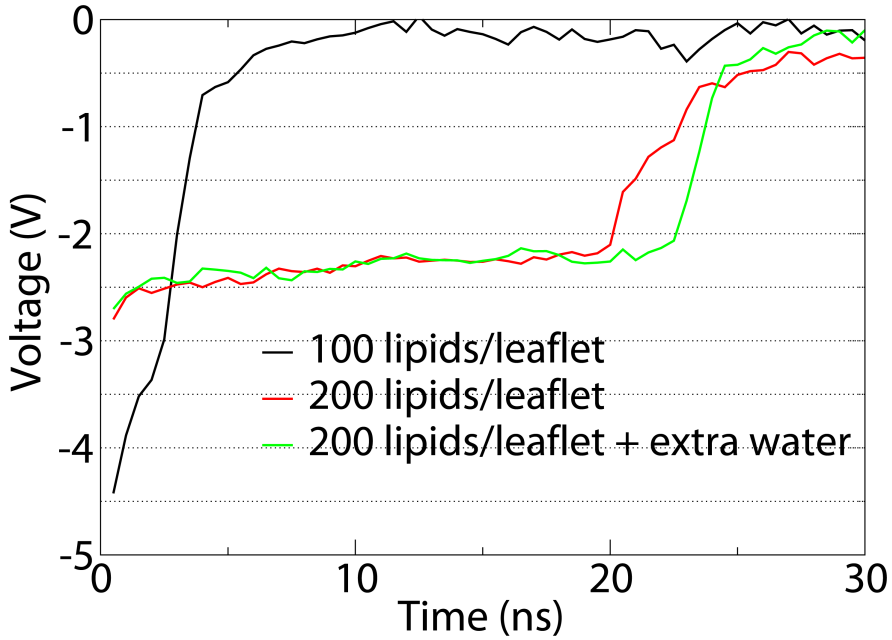

(a) *Evolution of the TMV*

	Waters	Start Size	End Size
100 lipids/leaflet	23804	7.4 x 7.4 x 21.3 nm	7.5 x 7.5 x 20.7 nm
200 lipids/leaflet	42810	10.8 x 10.8 x 18.9 nm	11.1 x 11.1 x 17.9 nm
200 lipids/leaflet	77970	9.97 x 9.97 x 32.05 nm	10.03 x 10.03 x 31.67 nm

(b) *Simulation dimensions*

Figure 6.6 *(a) Time evolution of the TMV for 3 double bilayers of different dimensions and lipids per leaflet. (b) The dimensions of each system before and after electroporation.*

Figure 6.6a and Table 6.6b depict the time evolution of the TMV and box dimensions for each system. As expected, halving the number of lipids per leaflet results in a vastly increased TMV, which incurred pore formation within the first nanosecond. Surprisingly, an increased separation between the bilayers has no

significant effect on the TMV as both plots show near identical TMVs and pore formation times.

This result is quite puzzling as one would expect the TMV to lower when increasing the separation between bilayers, since the ion imbalance is spread out over a greater distance. However, as both simulations experience pore formation on a similar timescale, this implies that these TMV measurements are accurate. As an additional check, the height of the slices used in the electrostatic potential calculations was varied in the analysis of each system in order to determine whether this variable has an effect on the TMV; however, each analysis produced similar electrostatic potentials and TMVs.

6.2.5 Electroporation in various bilayer compositions

The electroporation of POPE/POPG (3:1) bilayers discussed in Section 6.2.1 has yielded some interesting observations on the changes in lipid and system properties before and after pore formation. These simulations have also suggested that POPE/POPG (3:1) bilayers experience an electroporation threshold voltage of around -1.9 V within the 30 ns simulation time, with a corresponding ion imbalance of +16.

As membrane compositions of different lipid types result in bilayers with very different membrane properties, such as differences in their APL, fluidity and surface charge, the implications of electroporation with various lipid bilayer compositions at 297 K was investigated. Firstly, a POPC bilayer was selected to represent a neutrally charged bilayer. This composition has a transition temperature of 271 K [81], and therefore will be highly fluid at 297 K. POPC lipids also exhibit larger APL values than POPE lipids and will therefore result in an increased surface area for a similar number of lipids per leaflet. The second bilayer composition was POPC/POPG (3:1), which combines the differences observed between POPC and POPE lipids with the negatively charged POPG lipids. This composition should give a good indication of whether a charged lipid has any effect on the pore formation process by directly comparing it to pure POPC bilayers undergoing electroporation. The final composition was a DPPC bilayer, which has a transition temperature of 314 K and therefore should contain a high gel content at 297 K. As the various studies mentioned in Section 6.1.1 suggest that the electroporation threshold voltage is higher in highly ordered bilayers, a DPPC bilayer should provide an interesting comparison to observe the pore

formation process within gel domains and explore the differences in threshold voltage between each bilayer composition.

POPC

Three initial frames of an equilibrated POPC double bilayer at 297 K were subject to an ion imbalance of +24, which achieved a TMV of approximately -1.75 V after equilibration[3]. This bilayer composition contained a similar number of lipids per leaflet to the POPE/POPG bilayers. Each simulation was conducted for 30 ns and saw no pore formations within that time. Three more simulations were constructed containing an ion imbalance of +28, which achieved a TMV of -1.95 V after equilibration. This TMV is roughly identical to the threshold voltage of POPE/POPG bilayers when using an ion imbalance of +16.

Two of the three simulations (at -1.95 V) resulted in pore formations at ∼20 ns. Figure 6.7 depicts various membrane and system properties from one of the electroporation systems analysed by `Membrainy`. The APL (Figure 6.7a) reveals a large increase from ∼62 Å^2 to ∼68 Å^2 prior to pore formation, which is a significantly greater increase in APL than observed in the POPE/POPG simulations prior to pore formation (∼2 Å^2). A sharp drop in APL is observed upon pore formation, which coincides with a sharp drop in TMV (Figure 6.7b) and an ion transfer rate of 3 cations/ns and 3.2 anions/ns (Figure 6.7c), which saw roughly equal numbers of anions and cations pass through the pore in opposite directions. The sharp drop in APL while the pore is open suggests that the bilayers are relaxing as the electric field strength is reduced, which alleviates the compression on the bilayers from electrostriction. Figure 6.7d depicts the headgroup orientations measured between 5-30 ns from the +28 ion imbalance simulation that failed to produce a pore within the simulation time, which allowed for greater sampling of the headgroup orientations. This figure reveals a slight shift in orientation for both anodic and cathodic leaflets, which indicate mean orientations of 25.5 and 21.5 degrees respectively. This differs slightly from a mean orientation of 23 degrees measured from a no-TMV system, revealing a 2.5 degree increase in orientation for the anodic leaflets and 1.5 degree decrease for the cathodic leaflets. This shift in orientation is indicative of the headgroups tending to align with the electric field and further signifies the additional electric field strength within the anodic leaflets. These shifts in mean angles are in

[3]The equilibration is defined as the first 5 ns of the dynamics run, where the TMV stated is not the initial TMV but the TMV achieved after the bilayers had laterally expanded.

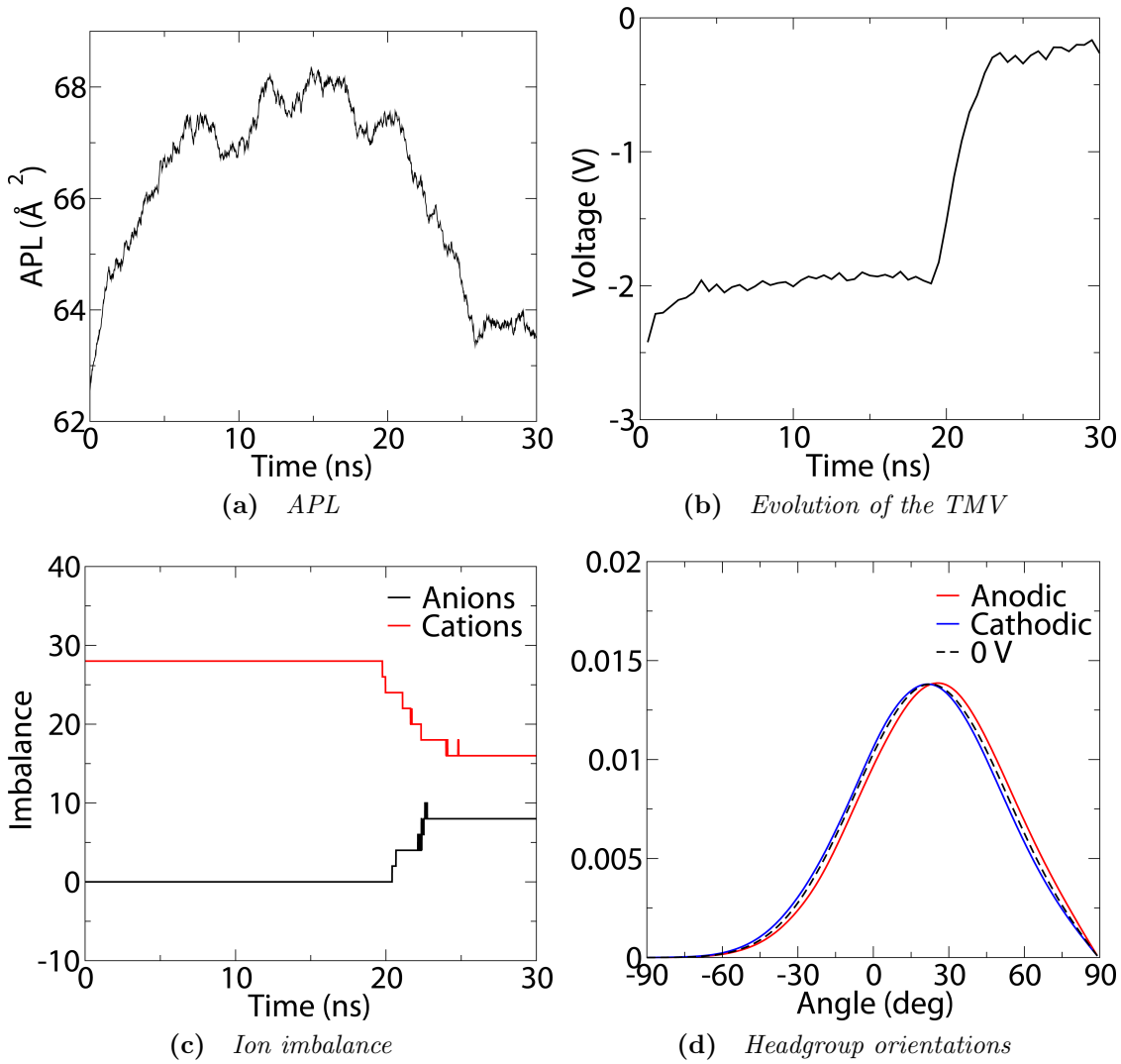

(a) *APL* **(b)** *Evolution of the TMV*

(c) *Ion imbalance* **(d)** *Headgroup orientations*

Figure 6.7 *Electroporation of a POPC bilayer with an ion imbalance of +28.* `Membrainy` *was used to analyse various membrane and system properties during the simulation, which saw pore formation occur at ∼20 ns.*

agreement with the angles measured by Böckmann *et al.* [117], who also conducted electroporation simulations of POPC bilayers.

It is interesting to note that this bilayer composition requires an additional ion imbalance of +12 to induce the same TMV observed in POPE/POPG bilayers. This is likely due to the larger APL exhibited by POPC lipids, and suggests that larger ion imbalances are required to induce electroporation in membranes containing lipids that displace more surface area. This may provide a basis to design antimicrobial agents or therapies that discriminate against membranes of different compositions by exploiting this voltage-shift, whereby certain membrane

compositions would be more susceptible to electroporation than others when the ionic gradient or electric field strength across the membrane is precisely calibrated.

POPC/POPG

Ion imbalances of +24 and +28 were established in six initial frames (three at each ion imbalance) of an equilibrated POPC/POPG (3:1) double bilayer at 297 K, which achieved TMVs of -1.7 V and -1.9 V respectively. These values are 0.05 V lower than those achieved by a pure POPC bilayer, which likely suggests that POPG lipids displace slightly less surface area than POPC lipids.

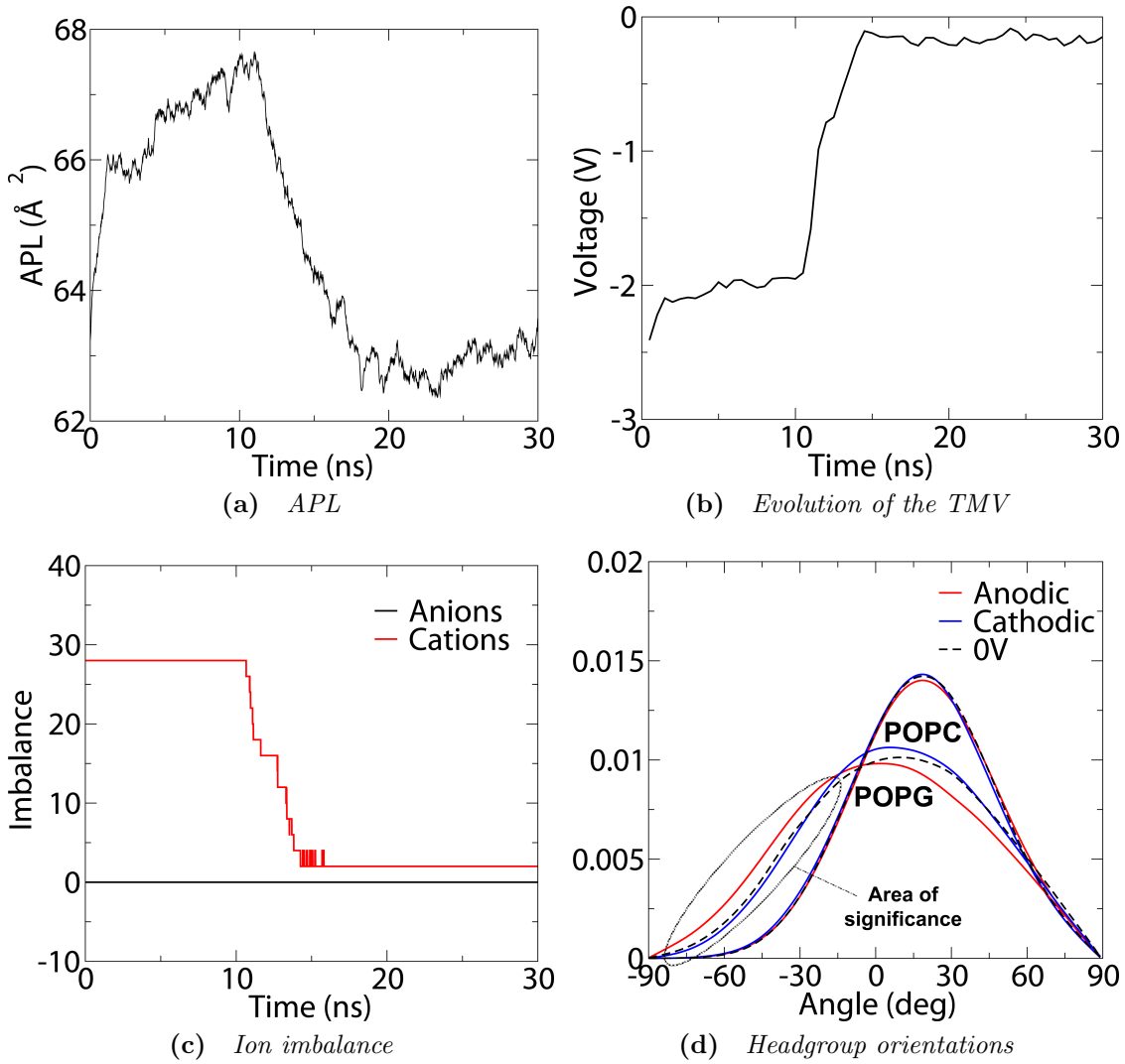

(a) *APL* **(b)** *Evolution of the TMV*

(c) *Ion imbalance* **(d)** *Headgroup orientations*

Figure 6.8 *Electroporation of a POPC/POPG (3:1) bilayer with an ion imbalance of +28.* `Membrainy` *was used to analyse various membrane and system properties during the simulation, which saw pore formation occur at ∼10 ns.*

Only one pore was observed in a system containing an ion imbalance of +28 which saw pore formation occurring at ∼10 ns (Figure 6.8). The changes in APL are very similar to those observed in the POPC bilayers (Figure 6.8a). In addition, ions travelled through the pore at a rate of 3.25 cations/ns (Figure 6.8c), similar to the rate observed in both POPC and POPE/POPG (3:1) simulations. No anions passed through the pore, however this system had a similar setup to the POPE/POPG (3:1) bilayers and saw only 30 anions per compartment (and 116-144 cations per compartment). Figure 6.8d depicts the headgroup orientations measured between 5-30 ns from a +28 simulation that failed to produce a pore within the simulation time. These measurements reveal that POPC lipids experience very little shift from their mean orientation of 19 degrees, which is 4 degrees lower than those found in a pure POPC bilayer. POPG lipids in the anodic and cathodic leaflets experience mean orientations of 1.5 and 5.5 degrees respectively, a significant decrease from their mean orientation of 10 degrees obtained from a no-TMV simulation. This no-TMV mean orientation is also substantially lower than the mean orientation of 24.5 degrees observed from POPE/POPG simulations, suggesting that replacing POPE lipids with POPC lipids has a significant effect on the POPG headgroup orientations. Although the cathodic leaflet sees a slight change in mean POPG orientation, the histogram reveals very little difference when compared with the no-TMV POPG orientation histogram; however, POPG lipids in the anodic leaflets experience a similar increase in headgroup orientations between -90 and -15 degrees as observed from the POPE/POPG (3:1) simulations, suggesting that anodic POPG headgroups are being pulled into the bilayer.

When comparing these simulations to pure POPC bilayers, these results suggest that the presence of negatively charged lipids in the bilayer composition has little consequence on the electroporation process and the voltage required to induce pore formation; however, both POPE/POPG (3:1) and POPC/POPG (3:1) simulations display increased sensitivity in anodic POPG headgroup orientations from the electric field, which may incur changes to the membrane properties and electroporation threshold voltage by increasing the instability of the membrane. Additional simulations are required to fully explore the consequences of a negatively charged lipid on the electroporation process. It is also possible that negatively charged lipids may restrict the flow of anions through the pore from electrostatic repulsion, which cannot be determined from these simulations due to the limitations imposed by the Ewald summation. One possible solution to bypass this limitation would be to construct a double bilayer where each bilayer contained

an equal and opposite charge, e.g. a POPE/POPG bilayer and a POPE/DOTAP bilayer. This would allow for the monitoring of both anions and cations travelling through transient water pores in anionic and cationic membranes.

DPPC

Ion imbalances of +16 and +20 were established in six initial frames (three at each ion imbalance) of an equilibrated DPPC double bilayer at 297 K. `Membrainy` determined that these bilayers contained ∼85% gel, and ion imbalances of +16 and +20 achieved TMVs of approximately -1.95 V and -2.4 V respectively, which is 0.05 V higher than those observed across POPE/POPG bilayers.

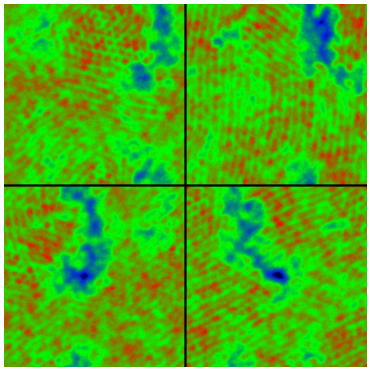

(a) *2D surface map*

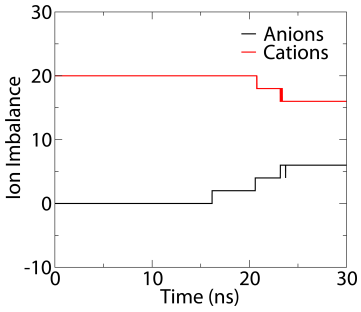

(b) *Ion imbalance*

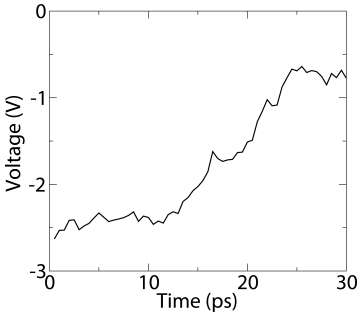

(c) *Evolution of the TMV*

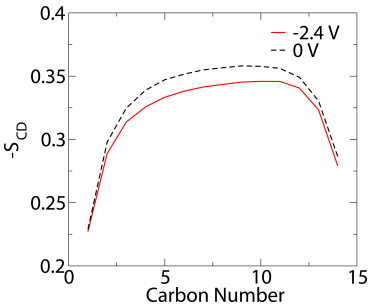

(d) *Saturated order parameters*

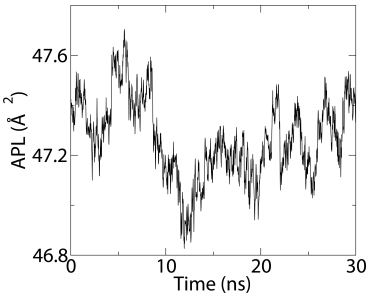

(e) *APL*

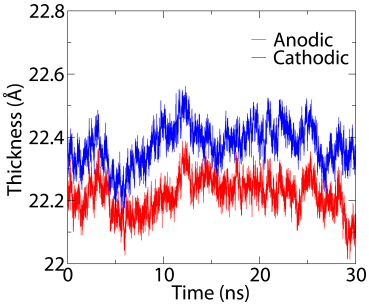

(f) *Leaflet thickness*

Figure 6.9 *Electroporation of a DPPC bilayer with an ion imbalance of +28 and gel content of ∼85%.* `Membrainy` *was used to analyse various membrane and system properties during the simulation. These plots reveal that electroporation of a DPPC bilayer in the gel phase is very different to those previously observed in other bilayer compositions. A small, slow functioning pore is formed at ∼13 ns and is highly restrictive to ion transfer through the pore.*

The three simulations at -1.95 V failed to achieve pore formation within the

simulation time; however, two pore formations occurred in the simulations at -2.4 V, one of which is depicted in Figure 6.9. Visual inspection of the trajectory showed a toroidal pore which was considerably smaller than those observed previously. A 2D surface map taken at 15 ns reveals this pore to occur in a thin spot of the membrane with a diameter of ∼6.3 Å (Figure 6.9a). The small size of the pore is likely due to the additional van der Waals forces between lipid tails in the gel phase, which was observed by Polak *et al.* to bring extra stability to the bilayer and restrict pore formation and duration [209]. The result is a very slow passage of ions through the pore (Figure 6.9b), which achieves an ion imbalance of +10 after 13 ns of activity, and an ion transfer rate of 0.33 ions/ns through the pore, which is ∼9 times slower than pores observed in fluid bilayers. A resulting TMV of -750 mV is observed (Figure 6.9c), which appears to be insufficient to drive additional ions through the pore beyond 25 ns. An analysis of the order parameters for saturated lipid tails between 5-10 ns reveals increased disorder in both leaflets when compared to a no-TMV simulation (Figure 6.9d). Both the APL (Figure 6.9e) and leaflet thickness (Figure 6.9f) reveal very little change in each plot throughout the simulation when compared to similar plots from fluid bilayer simulations. The fluctuations in both plots appear to have no correlation with the changes observed in TMV, suggesting that both plots depict normal fluctuations experienced by lipid bilayers. The other simulation that experienced pore formation saw the pore form within the first few nanoseconds and remained active for 14 ns, transferring ions at a rate of 0.5 ions/ns to yield a final imbalance of +6 and a corresponding TMV of -400 mV.

The electroporation threshold voltage in this bilayer composition appears to be higher than those of fluid bilayers, which all saw pore formation occur at around -1.9 V within 30 ns. This strengthens the observations made by Reigada, Polak *et al.*, and Wang and Larson, which suggests that highly ordered membranes require higher TMVs to induce electroporation [106, 208, 209]. This may provide another basis for designing antimicrobial agents or therapies that discriminate between different bilayer compositions.

6.2.6 Electroporation at different temperatures

Changing the temperature of a membrane can result in vastly different membrane properties, especially when exploring bilayer compositions at, below and above the transition temperature. Higher temperatures give rise to more energy within

the lipids, which not only modify the membrane properties but may induce changes to the pore formation process through differences in lipid dynamics. The previous bilayer compositions were conducted at 297 K and found pore formation in fluid bilayers to occur within 30 ns at a threshold TMV of approximately -1.9 V, whereas DPPC bilayers in the gel phase exhibited a threshold TMV of -2.4 V and produced a smaller, less stable toroidal pore with a slower passage of ions through the pore.

To investigate the effects of temperature changes on pore formation, simulations were constructed containing POPE/POPG (3:1), POPC/POPG (3:1) and POPC double bilayers at 320 K. These simulations were then compared with the existing simulations at 297 K to observe any differences in membrane or system properties.

POPE/POPG

As POPE/POPG bilayers have a transition temperature of 298-299 K [81], a temperature of 320 K will give rise to higher levels of fluidity than previously observed at 297 K. `Membrainy` was used to measure gel percentages from no-TMV simulations for this bilayer composition at each temperature, which yielded ∼55.5% gel at 297 K and ∼19% gel at 320 K.

An ion imbalance of +20 was established across six simulations of a POPE/POPG double bilayer at 320 K using six different initial frames. Each simulation was conducted for 30 ns and saw TMVs of approximately -1.7 V. The same ion imbalance at 297 K achieved a TMV of -2.35 V, indicating that an increase in temperature of 23 degrees lowers the TMV by 650 mV. No pores were observed to form within 30 ns in any of the six simulations.

Six additional simulations were constructed, three of which used an ion imbalance of +24 and three with +26, achieving TMVs of -1.95 V and -2.05 V respectively. One pore was observed to form at 29 ns with an ion imbalance of +24, and another at 12 ns with an ion imbalance of +26.

Figure 6.10 depicts a comparison between POPE/POPG bilayers at 297 K (+20) and 320 K (+26) which both resulted in pore formation at roughly identical times. Figure 6.10a reveals that the 320 K simulation has an initial APL that is ∼8 Å^2 higher than that of the 297 K simulation, and appears to experience a greater increase in APL prior to pore formation, suggesting that either fluid bilayers or higher temperatures may allow the bilayers to be more responsive to

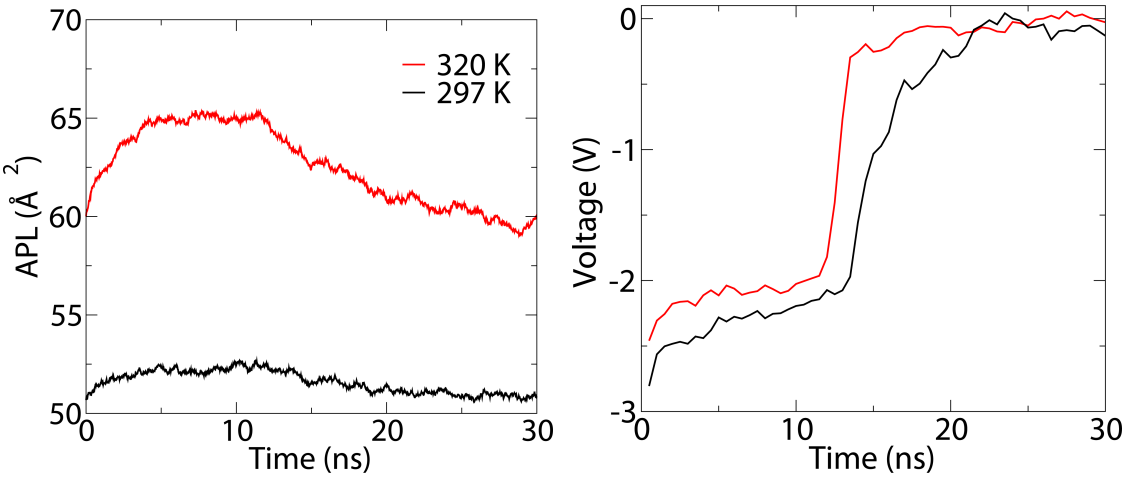

(a) *APL* **(b)** *Evolution of the TMV*

Figure 6.10 *(a) APL and (b) Evolution of the TMV measurements from two POPE/POPG bilayers, one at 297 K with an ion imbalance of +20 and the other at 320 K with an ion imbalance of +26.*

electrostriction effects. Figure 6.10b reveals that the pore formation process is almost identical between both simulations, which sees ion transfer through the pores occur at roughly the same rate and result in similar TMVs.

This experiment suggests that the pore formation process in POPE/POPG bilayers is identical at both temperatures, which occurs at the same threshold TMV of approximately -1.95 V. However, to achieve this TMV required using an ion imbalance of +16 at 297 K and +24 at 320 K, revealing an increase of +8 (a 50% increase) for simulations at 320 K. This is likely due to the larger bilayer surface area from the increased fluidity incurred by POPE/POPG bilayers well above the transition temperature.

POPC

Three initial frames of a POPC double bilayer at 320 K were subject to ion imbalances of +28, which achieved TMVs of approximately -1.9 V. Each simulation was conducted for 30 ns and saw two pore formations at 2.5 ns and 9 ns.

Figure 6.11 depicts a comparison between POPC bilayers at 297 K (+28) and 320 K (+28). The 320 K simulation sees an initial APL increase of $\sim$2 Å^2 when compared with the 297 K simulation. This is a much smaller difference than observed between the POPE/POPG bilayers at 297 K and 320 K, which is likely

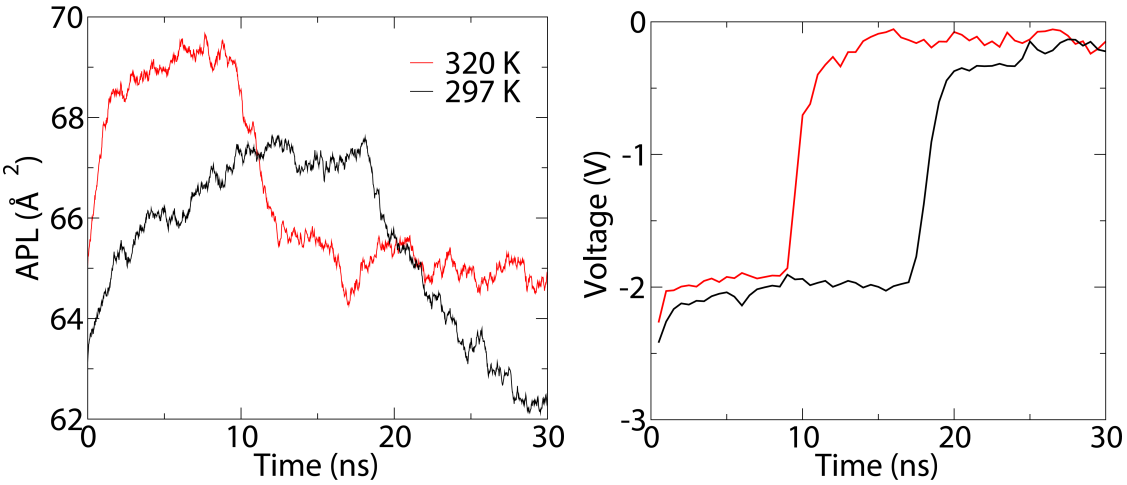

(a) *APL* **(b)** *Evolution of the TMV*

Figure 6.11 *(a) Area per lipid and (b) Evolution of the TMV measurements from two POPC bilayers with ion imbalances of +28 and temperatures of 297 K and 320 K.*

due to both temperatures being well above the transition temperature for POPC bilayers. Both systems see an initial TMV difference of ∼0.1 V and similar ion transfer rates through the pores. These results suggest that an increase in temperature from 297 K to 320 K in POPC bilayers has very little effect on the pore formation process. This may also be true for any bilayer composition sampling different temperatures in the same phase.

POPC/POPG

Three initial frames of a POPC/POPG double bilayer at 320 K were subject to ion imbalances of +28, which achieved TMVs of approximately -1.85 V and is 0.05 V lower than that of a pure POPC double bilayer. Three pores were formed at 4 ns, 11 ns and 27 ns.

Figure 6.12 depicts a comparison between POPC/POPG bilayers at 297 K (+28) and 320 K (+28). Similarly to the POPC simulations, these plots show that both temperatures, which are above the transition temperature, result in similar TMVs, changes in APL, and ion transfer rates through the pores. The presence of a charged lipid has no observable effect on the pore formation process when comparing both temperatures to a pure POPC bilayer.

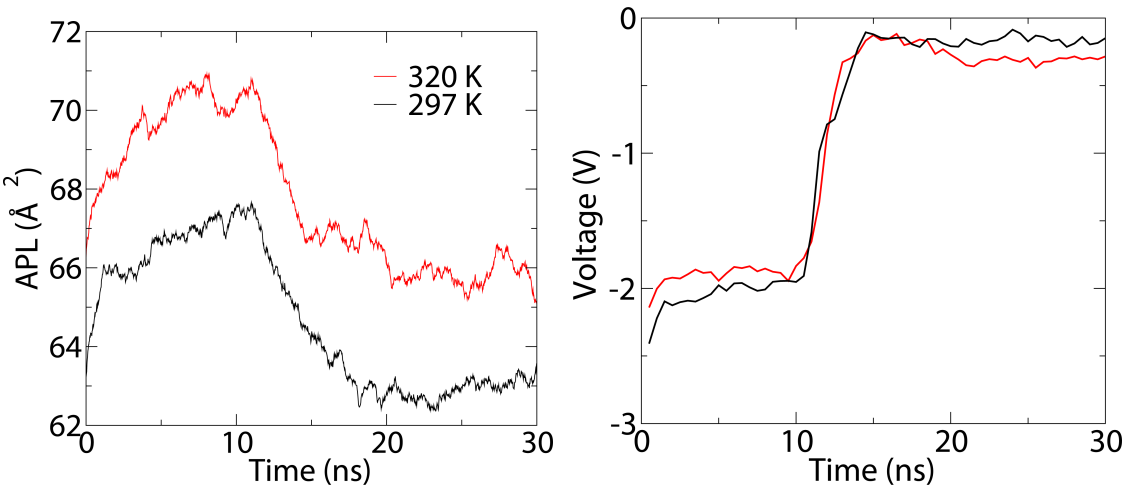

(a) *APL* **(b)** *Evolution of the TMV*

Figure 6.12 *(a) Area per lipid and (b) Evolution of the TMV measurements of two POPC/POPG bilayers with ion imbalances of +28 and temperatures of 297 K and 320 K.*

6.2.7 Electroporation induced lipid flip-flopping

Transmembrane lipid translocation, more commonly known as lipid flip-flopping, is the process in which lipids are translocated between the two opposing leaflets of a bilayer [120]. This translocation occurs from both passive and active transport mechanisms and plays a crucial role in the maintenance of asymmetric cell membranes [121]. Gurtovenko and Vattulainen previously observed lipid flip-flopping in simulated DMPC bilayers under the influence of an applied electric field, whereby lipids translocate through transient water pores in both directions [108].

To investigate the possibility of lipid flip-flopping through transient pores established by an ion imbalance, a POPE/POPG (3:1) double bilayer was constructed in which an ion imbalance of +20 was maintained with position restraints using a force constant of 1000 kJ/mol nm^2. `Membrainy` was modified to monitor for lipid flip-flopping during the trajectory.

Figure 6.13 depicts the analysis of various membrane and system properties from the simulation, which saw pore formation occur within the first few nanoseconds and remain open for the duration of the simulation. Surprisingly, after the initial equilibration, an immediate drop in TMV is observed (Figure 6.13a). This was highly unexpected as the fixed ion imbalance was expected to maintain a constant electric field strength, and therefore the TMV should only respond to changes in

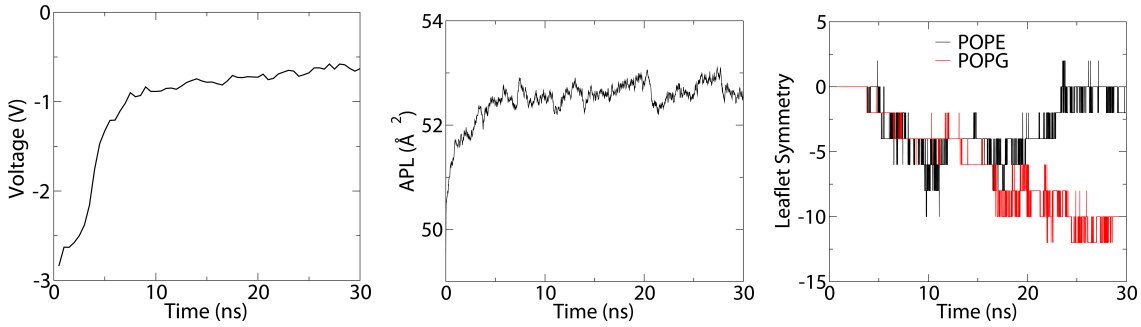

(a) *Evolution of the TMV* **(b)** *Area per lipid* **(c)** *Leaflet symmetry*

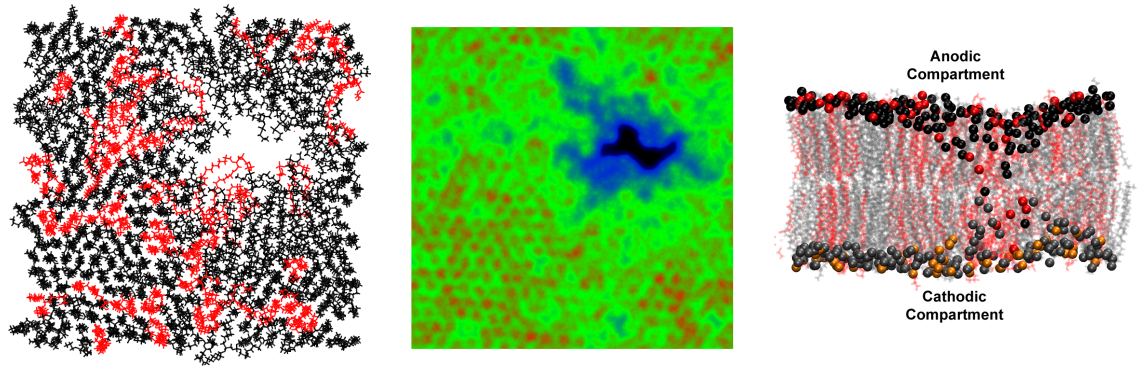

(d) *Pore at 30 ns* **(e)** *2D surface map at 30 ns* **(f)** *Pore at 30 ns*

Figure 6.13 *Analysis of the POPE/POPG double bilayer with a fixed ion imbalance of +20. (c) The leaflet symmetry defines the lipid imbalance between leaflets, where a value of zero represents a symmetrical bilayer and negative numbers represent lipid flip-flopping from the anodic to cathodic leaflet. (d) and (e) reveal that the pore formation is much larger than previously observed. (f) A side-on image of the pore after 30 ns, where the phosphorous atoms on POPE and POPG lipids are represented as black and red (respectively) in the anodic compartment, and grey and orange (respectively) in the cathodic compartment. Five POPG lipids had flip-flopped from the anodic to cathodic leaflet via the pore.*

APL. However, a comparison of the TMV and APL (Figures 6.13a and 6.13b) reveals that the sharp drop in TMV occurred after the initial expansion of the bilayers, suggesting that the TMV is being lowered through another mechanism.

One possible mechanism that may affect the TMV is the creation of an asymmetrically charged bilayer through the flip-flopping of POPG lipids. Asymmetrically charged membranes were shown by Gurtovenko and Vattulainen to be capable of modifying the TMV [212]. Figure 6.13c depicts the leaflet symmetry in the bilayer, where a value of 0 indicates a symmetric bilayer and -2 indicates a single flip-flop from the anodic to the cathodic leaflet. Upon pore formation,

the leaflet symmetry shows both POPE and POPG lipids translocating from the anodic to the cathodic leaflet. When visually inspected, these lipids formed the toroidal structure of the pore, which further signifies that pore formation is driven from the anodic leaflets. After 15 ns, the POPE lipids initially involved in the pore structure return to the anodic leaflet whereas the number of POPG lipids translocating to the cathodic leaflet increases. By 30 ns, one POPE lipid has flip-flopped between both leaflets (achieving a leaflet symmetry of 0) and five POPG lipids have flip-flopped from the anodic to the cathodic leaflet (achieving a leaflet symmetry of -10). This suggests that the negatively charged POPG lipids experience an increased tendency to flip-flop through transient pores towards the cathodic leaflet, establishing an asymmetrically charged bilayer. The POPG lipids within this simulation establish a charge imbalance of -10 within the bilayer, which may play a role in lowering the TMV by countering the ion imbalance.

Figures 6.13d, 6.13e and 6.13f depict images of the pore shape and structure at 30 ns, where the pore appears significantly larger than those observed previously. The side-on view in Figure 6.13f depicts the toroidal structure of the pore, where the phosphorous atoms for POPE and POPG lipids in the anodic leaflet are represented by black and red respectively, and grey and orange in the cathodic leaflet. By 30 ns, five POPG phosphorous atoms from the anodic leaflet are clearly visible in the cathodic leaflet, and one POPE phosphorous atom from each leaflet has swapped. It should also be noted that the lipid flip-flopping in this simulation is intermediate; most of the lipids that flip-flopped still reside in both leaflets simultaneously by having one lipid tail in each leaflet. This suggests that it would take longer than 30 ns for a lipid to completely translocate from one leaflet to the other, which is in agreement with the study by Gurtovenko and Vattulainen who found an average translocation time of 60 ns [108]. It is also interesting to note that lipid flip-flopping was only observed to occur in the lipids involved in the formation of the toroidal pore, and therefore the number of POPG lipids observed to flip-flop is dependent on those lipids located at the site of pore formation. It would be interesting to extend this simulation to observe if the toroidal pore would allow other POPG lipids in the vicinity of the pore to flip-flop.

Although the creation of an asymmetrically charged bilayer via the flip-flopping of POPG lipids may provide an explanation for the TMV loss, a comparison of Figures 6.13a and 6.13c reveals that the changes in the POPG symmetry occur at different times to the changes in TMV. The sharp drop in TMV occurred

between ∼2.5 ns and ∼8 ns, which corresponds to a leaflet symmetry value of -8 for both POPE and POPG lipids. However, after 8 ns the leaflet symmetry is reduced to -4 for both lipid types, but the TMV exhibits a slight decline which is not reflective of the changes in leaflet symmetry. This suggests that changes in the leaflet symmetry may not be solely responsible for the observed changes in TMV. Furthermore, the study by Gurtovenko and Vattulainen saw TMVs in the range of 198 - 238 mV when simulating asymmetrically charged bilayers with a charge imbalance in the range of 62 - 64. This is obviously a much greater charge imbalance than that produced by five POPG lipids, suggesting that the TMV change would be even smaller. Interestingly, the TMV lowers by ∼300 mV between 10 and 30 ns whereas the APL remains relatively constant during this time. Therefore, it is likely that a combination of effects play a role in determining the TMV, such as the APL, bilayer surface area and the surface charge distribution, which changes significantly upon pore formation. Further experiments are required to fully elucidate the role of each membrane and system property on the TMV.

6.2.8 Conclusion

The electroporation of various bilayer compositions using different TMVs and temperatures has been investigated, with the aim to broaden our understanding of the electroporation process induced by an ion imbalance. Analytical techniques were implemented into `Membrainy` that were specifically designed to analyse systems of this nature. These include measurements of the TMV over time, detection of lipid flip-flopping, and a separate analysis of the anodic and cathodic leaflet properties.

A detailed analysis of electroporation induced by an ion imbalance across a POPE/POPG (3:1) double bilayer at 297 K was made. A simulation was conducted containing an ion imbalance of +20, which achieved an initial TMV of -2.7 V. This TMV dropped to -2.35 V within the first 5 ns as the bilayers were compressed through electrostriction, resulting in a lateral expansion of the bilayers with a corresponding decrease in TMV due to the ion imbalance being spread over a greater surface area. The bilayers remained intact for approximately 10 ns, in which measurements of the order parameters and headgroup orientations were made. The order parameters for both saturated and unsaturated lipids showed a significant increase in disorder when compared with a no-TMV system,

and the anodic leaflets showed a further increase in disorder when compared with the cathodic leaflets. The headgroups revealed a slight shift in mean orientations where both POPE and POPG headgroups were observed to shift in order to align with the electric field, which was also observed by Böckmann *et al.* in simulations of POPC bilayers with applied electric fields [117]. An increase in anodic POPG lipids with headgroup orientations between -90 and -15 degrees was observed, suggesting that anodic POPG lipids were being pulled into the bilayer. Pore formation was driven by the anodic leaflet upon which a sharp drop in TMV was observed, corresponding to the flow of cations through the pore from the cathodic to anodic compartment, resulting in a dissipation of the ion imbalance. `Membrainy` showed this dissipation to occur at a rate of 3 cations/ns with a corresponding drop in TMV at a rate of 650 mV/ns. The APL sharply increased prior to pore formation, after which it lowered slightly but remained higher than the starting APL. This is likely due to the pore remaining open for the remainder of the simulation time due to its hydrophilic toroidal shape, which holds water molecules within the bilayer. The leaflet thickness continuously decreased prior to pore formation, after which it increased and settled to a thickness slightly below the initial thickness. The standard deviations in leaflet thickness increased prior to pore formation, suggesting that the leaflets were becoming more perturbed. The anodic leaflets were consistently thinner than the cathodic leaflets and exhibited greater deviations in thickness. These results were duplicated and confirmed using different initial frames and randomised initial velocities.

An unusual shift in double bond order parameters was observed in unsaturated lipid tails, which saw anodic leaflets experience an decrease in order in the first carbon of the double bond, and an increase in order for the second carbon when compared with a no-TMV double bond. Cathodic leaflets saw the exact opposite of this. To fully elucidate this, `Membrainy` was modified to produce histograms of the anodic and cathodic C−H double bond angles, which revealed a shift in mean orientation of 2-4 degrees and suggested that these bonds were tending to align with the electric field. This is an interesting result as these C−H bonds carry a slight charge of -0.15 and 0.15 respectively, yet they show a comparable shift in mean orientation when compared with the lipid headgroups, which carry considerably more charge and are more flexible than the C−H bonds. This suggests that the electric field across the bilayers may be much larger in the lipid tail region than in the headgroup region.

To elucidate this difference in electric field strength and to understand why the anodic leaflets experience greater changes in lipid properties than the cathodic leaflets, the electric field strength across each double bilayer was analysed. This was found to show glide reflection symmetry across a no-TMV system, with the electric field peaking at 0.5 V/nm in both the headgroup region and the last few carbons along the lipid tails. In each TMV system prior to pore formation, a field strength of 0.5 V/nm was also observed in the headgroup region, suggesting that the TMV has minimal influence on the headgroups. The lipid tail region showed cathodic and anodic leaflets to experience peak field strengths of around 0.8 V/nm and 1.4 V/nm respectively, which likely explains why the TMV exerts a greater influence on the anodic lipid properties over the cathodic lipids. The shape of the electric field strength within the bilayer differs to those depicted in the Böckmann et al. study, which shows a uniform field strength within the lipid tails of both leaflets. This may be due to differences between using an ion imbalance and an applied electric field. The Böckmann *et al.* study also saw pore formation initiate from the anodic leaflets; however, they attributed this to the dipole orientation of water molecules showing preference for inserting into anodic leaflets. Interestingly, the study conducted by Gurtovenko and Lyulina used an identical bilayer composition and force field to those used in the Böckmann *et al.* study, and saw no preference for pore formation to occur in a specific leaflet. A more detailed analysis and comparison of each simulation technique would be required to fully elucidate each finding.

Additional double bilayers at 297 K were constructed comprising POPC, POPC/POPG (3:1) and DPPC lipids. Each bilayer was tested using a variety of ion imbalances to determine an approximate threshold TMV in which electroporation would occur within 30 ns. This TMV was found to be approximately -1.9 V for each bilayer composition at or above its transition temperature, which corresponds to an electric field strength of ∼0.29 V/nm and is of comparable strength to the threshold electric field strengths reported in previous studies [117, 205]. A TMV of -2.4 V was required to induce pores in DPPC bilayers at 297 K, which is well below the transition temperature and comprised ∼85% gel. This suggests that bilayers in the gel phase may exhibit a higher threshold TMV to induce pore formation than those in the fluid phase, and is in agreement with a previous study by Reigada which saw preference for pore formation in disordered regions of the bilayer over ordered regions [208]. Interestingly, to achieve a TMV of -1.9 V required an ion imbalance of +16 in POPE/POPG bilayers and +28 in POPC and POPC/POPG bilayers. This

additional imbalance was needed because POPC lipids exhibit a larger APL than POPE lipids, resulting in a lower TMV as the ion imbalance is spread over a larger membrane surface area. This difference in ion imbalance may provide a basis to design antimicrobial agents and therapies that discriminate between bilayer compositions, and as such may be calibrated to electropermeabilise membranes which exhibit smaller APLs while leaving those with larger APLs intact. There were minimal differences observed when comparing POPC and POPC/POPG, suggesting that the presence of a negatively charged lipid has no effect on the electroporation process. However, both POPE/POPG and POPC/POPG simulations observed a increase in POPG headgroups orientated towards the bilayer centre, which may have consequences on the bilayer stability and pore formation process. It is also unclear whether the presence of negatively charged lipids would restrict the flow of anions through the pores, which could not be determined from these simulations due to a lack of anions in the system to satisfy the Ewald summation. One approach to explore the effects charged lipids may have on ion transport through the pore is to construct a double bilayer where one bilayer is cationic and the other is anionic, thus producing a neutrally charged system and allowing for an equal number of anions and cations.

Pore formation was also studied at 320 K for POPE/POPG (3:1), POPC/POPG (3:1) and POPC bilayers. The pore formation process was identical at each temperature, which saw similar rates of ion transport through the pore and a similar pore formation frequency. No change in ion imbalance was required in POPC and POPC/POPG bilayers as an imbalance of +28 yielded similar TMVs at both temperatures; however, POPE/POPG bilayers at 320 K required an ion imbalance of +24 to achieve the same TMV observed with an ion imbalance of +16 at 297 K. This is because the transition temperature for POPE/POPG is 298-299 K and therefore undergoes a phase change between the temperatures. This phase change incurs an increase in APL, which lowers the TMV by around 650 mV at 320 K. Exploiting this TMV gap for membranes at or around the transition temperature may provide another means to design antimicrobial agents and therapies that discriminate between membrane compositions at certain temperatures, and as such may allow for the electropermeabilisation of certain bilayer compositions while others are left intact.

Gurtovenko and Vattulainen observed that transient pore formation allowed lipids to translocate or *flip-flop* between leaflets in both directions while simulating DMPC bilayers with applied electric fields. To further investigate this effect, a

simulation of a POPE/POPG (3:1) double bilayer was conducted in which an ion imbalance of +20 was maintained using position restraints, which allowed the pore to remain active throughout the simulation. `Membrainy` was modified to detect and monitor lipid flip-flopping during the simulation, which was conducted for 30 ns. Upon pore formation, both POPE and POPG lipids from the anodic leaflet formed the toroidal structure of the pore, further signifying that pore formation is initiated by the anodic leaflets. Approximately 10 ns after pore formation, the POPE lipids within the pore moved back to the anodic leaflet, creating an even distribution of POPE lipids between leaflets. Interestingly, POPG lipids continued to translocate from the anodic leaflet to the cathodic leaflet. After 30 ns, one POPE lipid had flip-flopped between both leaflets and five POPG lipids had flip-flopped to the cathodic leaflet. This suggests that POPG lipids experience an increased tendency to flip-flop through transient pores towards the cathodic leaflet, which corresponds to the anionic POPG headgroup moving in the direction of the electric field. This system saw a drop in TMV from -2.35 V to -650 mV immediately after pore formation, which was initially thought to be due to the creation of an asymmetrically charged bilayer from the flip-flopping of POPG lipids. However, the analysis of the simulation revealed that the POPG lipids flip-flopped after this TMV drop, which implies that factors other than the ion imbalance, APL and charged lipid distribution can contribute to changes in the TMV. Further experiments are required to fully elucidate the influences on the TMV from each membrane and system property.

6.3 Electroporation of model membranes using charged peptides

In Section 6.2, the electroporation of a selection of lipid bilayer compositions, temperatures, lipid phases and TMVs was explored using ion imbalances across double bilayers. This use of an ion imbalance was originally presented in a study by Sachs *et al.* [88], which showed this as an alternate means of establishing a TMV across lipid bilayers without the need for an applied electric field. A year later, Gurtovenko and Vattulainen showed that establishing a high voltage TMV with an ion imbalance is capable of inducing electroporation [105]. In their publication, they suggest the possibility of exchanging the ion imbalance for charged peptides, such as cationic AMPs, which may induce the same electroporation effects as observed when using an ion imbalance.

The possibility of cationic peptides inducing electroporation in lipid bilayers has yet to be explored through MD, but has been suggested in many experimental studies. Binder and Lindblom saw an electroporation-like mechanism in the binding of the cell-penetrating peptide penetratin which, at a threshold concentration, allows the internalisation of penetratin within lipid vesicles [213]. Wadia and Dowdy investigated several cell penetrating peptides for cancer-specific therapies and found that increasing the number of charged residues in the peptides improved the efficiency of peptide uptake into the cell [214]. Wender *et al.* found that removing certain cationic residues in the HIV-1 tat protein dramatically reduced its ability to translocate across the cell membrane [215]. A more recent study by Kennedy *et al.* showed that treating cells with cationic peptides prior to applying an electric field enhanced membrane disruption [216].

These studies all suggest that many cell-penetrating peptides, which often contain regions densely populated with cationic residues, may increase the local permeability of the cell membrane to allow for the translocation of these peptides into the cell. This may also be an additional step in the mechanisms that allow AMPs to penetrate and disrupt cell membranes.

This section will use MD to explore the effects on lipid bilayers upon replacing the ion imbalance with charged peptides. These simulations can then be compared with the ion imbalance simulations conducted in Section 6.2 to observe any differences.

6.3.1 Pexiganan

Pexiganan, which is sometimes referred to as MSI-78, is a synthetic amphipathic cationic AMP derived from the magainin peptides that are isolated from the skin of the African clawed frog [217]. Pexiganan is structurally similar to both Magainin 1 and 2, containing many of the original residues and maintaining a similar length. Various studies investigated the significance of each residue in the magainin sequences in an attempt to understand its mechanism of action and found that substituting specific residues, including increasing the number of cationic residues, enhanced its potency [218–222]. Each enhancement was combined to create Pexiganan, which holds a total charge of +10 achieved from nine lysine residues and a positively charged N-terminus. Its mechanism of action was probed through solid-state NMR which captured the formation of toroidal pores in POPC bilayers [223].

As the previous electroporation experiments with POPE/POPG bilayers utilised an ion imbalance of +20, two Pexiganan peptides (containing a total charge of +20) were inserted into the outer water compartment of a POPE/POPG (3:1) double bilayer at 297 K using the program `MoleculeInserter`, in which the peptides were positioned equidistant to each other and each bilayer (Figure 6.14a). The simulation was energy minimised, equilibrated, and conducted for 30 ns.

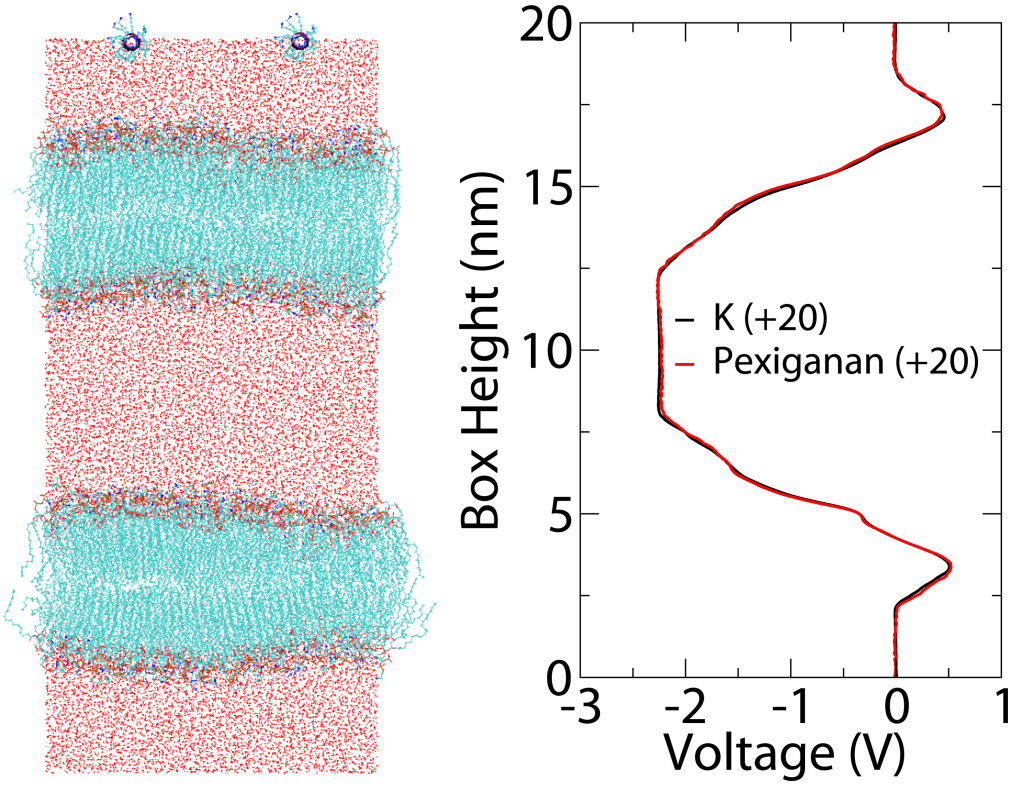

(a) *System setup* **(b)** *Electrostatic Potential*

Figure 6.14 *(a) The initial setup of a POPE/POPG (3:1) double bilayer containing two Pexiganan peptides placed in the outer compartment equidistant to each other and each bilayer, creating a charge imbalance of +20. (b) The electrostatic potential of the pexiganan system between 5-15 ns, which is compared with a system containing an ion imbalance of +20.*

Both peptides came into contact with the upper bilayer within a few nanoseconds; however, by 5 ns one peptide had switched to the lower bilayer and remained there for the remainder of the simulation. The electrostatic potential was measured between 5-15 ns and compared with the electrostatic potential from the original ion imbalance simulation discussed in Section 6.2.1 (Figure 6.14b). This comparison reveals that the simulation containing two Pexiganan peptides achieves an identical electrostatic potential across the bilayers when compared

with an ion imbalance of +20, in which both approaches achieve a TMV of -2.35 V. This implies that Pexiganan, or more generally charged peptides, are capable of generating a TMV across lipid bilayers to a similar extent as when using an ion imbalance.

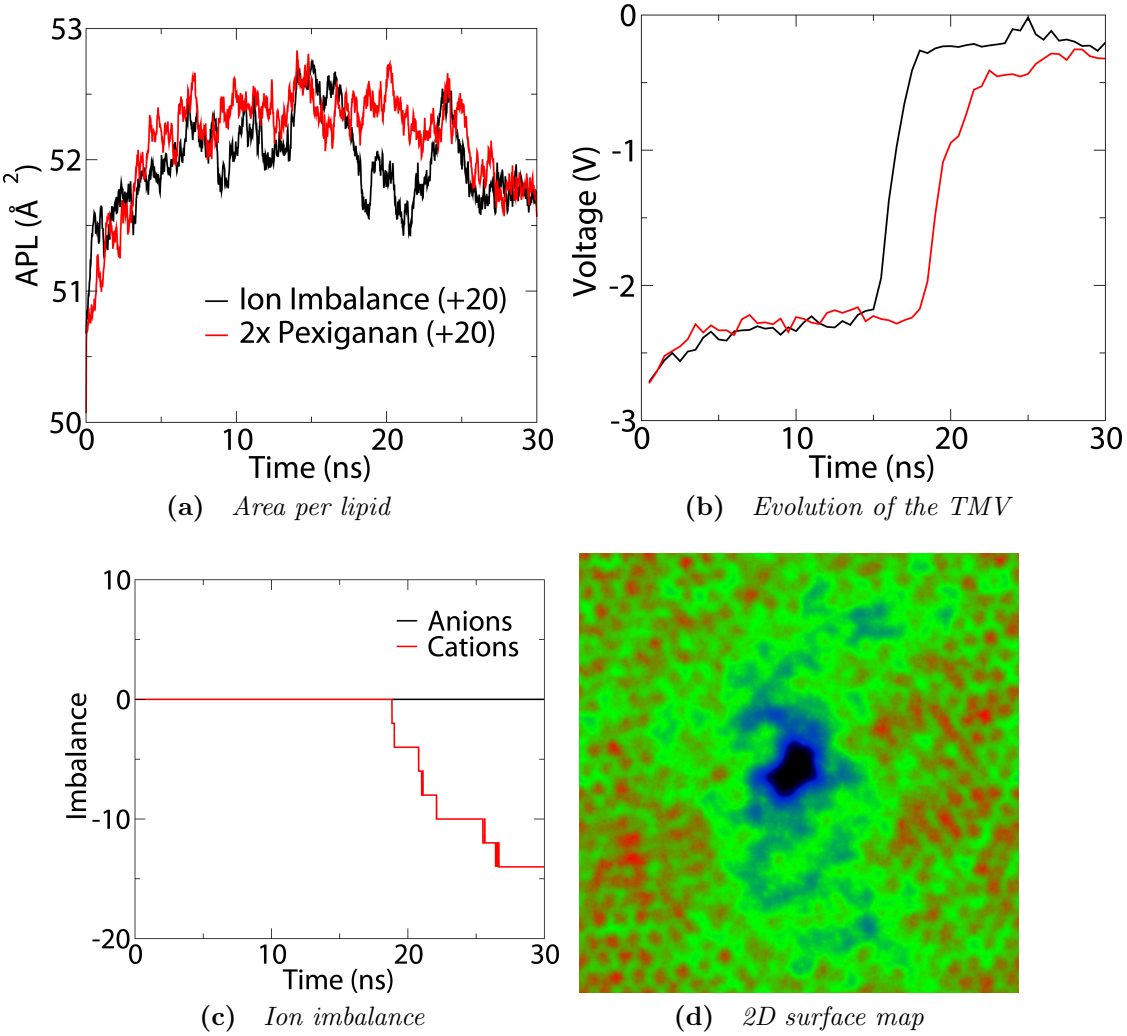

(a) *Area per lipid* **(b)** *Evolution of the TMV*

(c) *Ion imbalance* **(d)** *2D surface map*

Figure 6.15 *Analysis of the POPE/POPG (3:1) double bilayer undergoing pore formation induced by 2x Pexiganan. The (a) APL and (b) TMV measurements compared with an ion imbalance simulation reveal that both approaches achieve similar mechanisms of pore formation. (c) Cations were observed to flow through the pore, establishing an ion imbalance that counteracts with the charge imbalance from Pexiganan. (d) A 2D surface map taken from 19 ns, which shows the pore to be ∼9.8 Å in diameter.*

The Pexiganan simulation also saw pore formation to occur at ∼18 ns, which appears to follow the same pore formation mechanisms as those induced by an ion imbalance. Figures 6.15a-b reveal similar changes in APL and TMV when compared to the original ion imbalance simulation conducted in Section 6.2.1.

The rate of ion transfer through the pore is slightly slower, which saw 7 cations travel from the cathodic to the anodic compartment at a rate of 1 cation/ns (Figure 6.15c), compared to 3 cations/ns for the ion imbalance simulations. A 2D surface map was taken at 19 ns and indicates a pore diameter of ∼9.8 Å, which is comparable in size to those formed by an ion imbalance (Figure 6.15d). After 30 ns, an ion imbalance of -14 is established across the bilayers, yielding a TMV of -300 mV. This suggests that the established ion imbalance, which in this simulation is a surplus of cations in the central (anodic) compartment, is capable of counteracting the charge imbalance established from the Pexiganan peptides, resulting in a drop in TMV.

This experiment yields some interesting observations. Firstly, two Pexiganan peptides are capable of inducing a TMV across a double bilayer, achieving a virtually identical electrostatic potential along the simulation box when compared with an electrostatic potential achieved by an ion imbalance of equal magnitude. Secondly, these Pexiganan peptides are capable of inducing transient toroidal pore formation in POPE/POPG (3:1) bilayers via electroporation mechanisms, and are likely capable of inducing pores in other membrane compositions. Thirdly, pore formation results in a loss of the TMV due to the transport of cations through the pore into the anodic compartment, which drives an ionic gradient between the membrane compartments and counters the charge imbalance established by the peptides. This differs from pore formation induced by an ion imbalance which drives an equilibrium of the ionic gradient between compartments. In physical terms, this suggests that Pexiganan induced pore formation in cell membranes would increase the number of cations within the cell, which may have implications on the TMV and intracellular function. Finally, as Pexiganan is known to disrupt the cell membrane and establish toroidal pores, could this use of the electroporation phenomenon play a role in its mechanism?

To further investigate pore formation using Pexiganan, four duplicate simulations were conducted with randomised initial velocities, three of which saw pore formation within 30 ns (Figure 6.16a). Each pore formation was similar to that of the previous simulation and saw cations flow through the pore into the anodic compartment, resulting in a loss of TMV through partially neutralising the charge imbalance from the peptides. No Pexiganan peptides were observed to insert into the bilayers within the simulation time, and there was no observable correlation between the bilayer containing the pore and the bilayer in which the peptides interacted with.

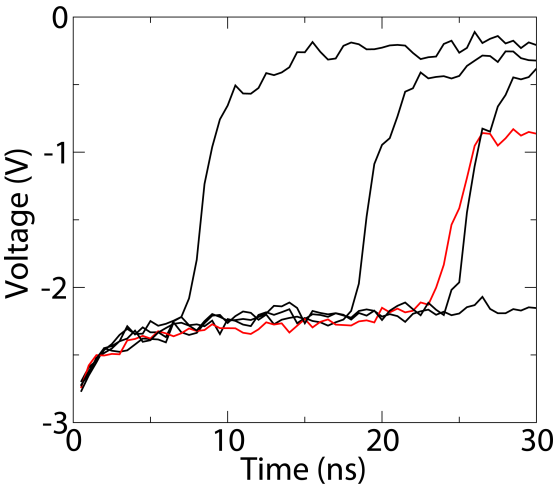

(a) *Evolution of the TMV*

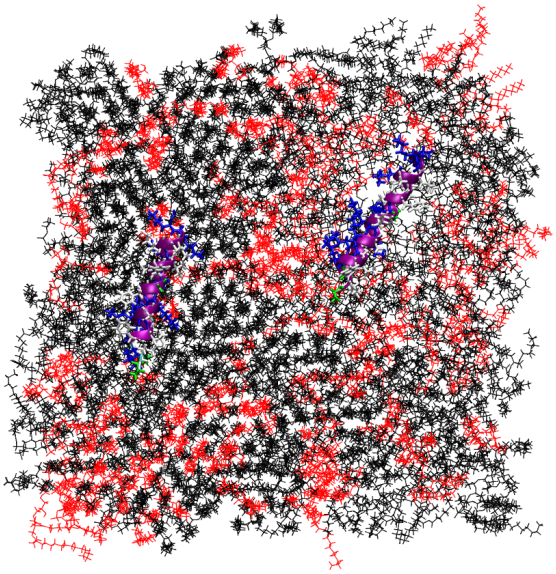

(b) *Image of Pexiganan blocking the pore*

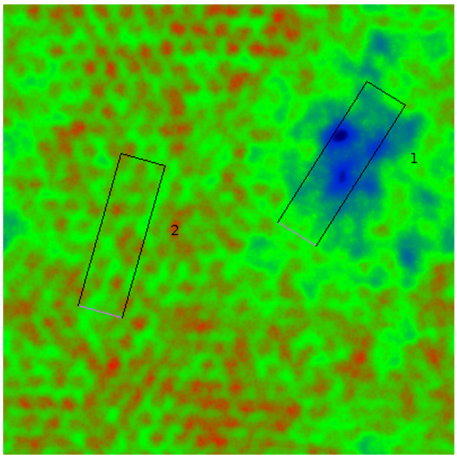

(c) *2D surface map of Pexiganan blocking the pore*

Figure 6.16 *(a) TMV measurements from multiple simulations of electroporation of POPE/POPG (3:1) double bilayers induced by two Pexiganan peptides. The red plot saw pore formation directly underneath a Pexiganan peptide, which obstructs the pore and restricts the flow of ions through the pore, resulting in a resting TMV of -900 mV. (b) Image of the simulation that saw a Pexiganan peptide blocking the pore, taken at 30 ns. (c) 2D surface map of the image displayed in (b).*

One simulation (shown in red in Figure 6.16a) yields a resting TMV of -900 mV after pore formation, which is significantly higher than the resting TMVs observed in the other simulations. A visual inspection of this trajectory showed that the pore formed directly underneath one of the Pexiganan peptides (Figure 6.16b-c), which allowed the peptide to behave as a plug and obstruct the usual

flow of cations through the pore. Two cations were observed to travel through the pore at roughly 24 ns and 26 ns by passage through a small gap between the peptide and the pore. The peptide, which has a helical length greater than the diameter of the pore, showed no signs of travelling through the pore within the simulation time.

Surprisingly, Figure 6.16a reveals that the TMV drops by more than double, yet only two cations were transported through the pore. This would leave an overall charge imbalance of +16 across the bilayers which was observed in previous ion imbalance simulations to achieve a TMV of -1.9 V, a 1 V difference to this simulation. Along with the observations made in Section 6.2, this further suggests that the TMV cannot be entirely quantified by the APL and charge imbalance, and is likely influenced by other factors such as the shape and charge distribution of the bilayer.

6.3.2 Poly-l-lysine

Poly-l-lysine (PLL) is a simplistic cationic peptide containing n-repeats of the residue lysine. Shima *et al.* showed PLL to be a potent antimicrobial agent against gram-positive and gram-negative bacteria *in vitro* when $n >= 10$ residues [224]. When synthesised to a maximum of n = 25-30, the study found that increasing the number of lysine residues increased the potency of PLL. When added to *E. coli*, PLL was observed to strip the outer membrane followed by an abnormal distribution of the cytoplasm, causing physiological damage to the cell.

In MD simulations, PLL can be synthesised to any value of n, allowing for a precise calibration of the charge imbalance across double bilayers using one or several peptides. To investigate the electroporation properties of PLL, seven simulations of PLL^{+20} were constructed in which the peptide was synthesised as alpha helical containing 20 lysine residues. PLL^{+20} was placed in the centre of the outer water compartment of four initial frames of a POPE/POPG double bilayer, taken after 50 ns, 80 ns, 90 ns and 100 ns of equilibration. Three of the simulations saw position restraints placed on the peptide backbone atoms using a force constant of 1000 kJ/mol nm^2, which held the peptide in the centre of the water compartment to restrict its contact with the bilayer surfaces. Each simulation was energy minimised, equilibrated and conducted for 30 ns.

Figure 6.17a depicts the time evolution of the TMV for each simulation, which

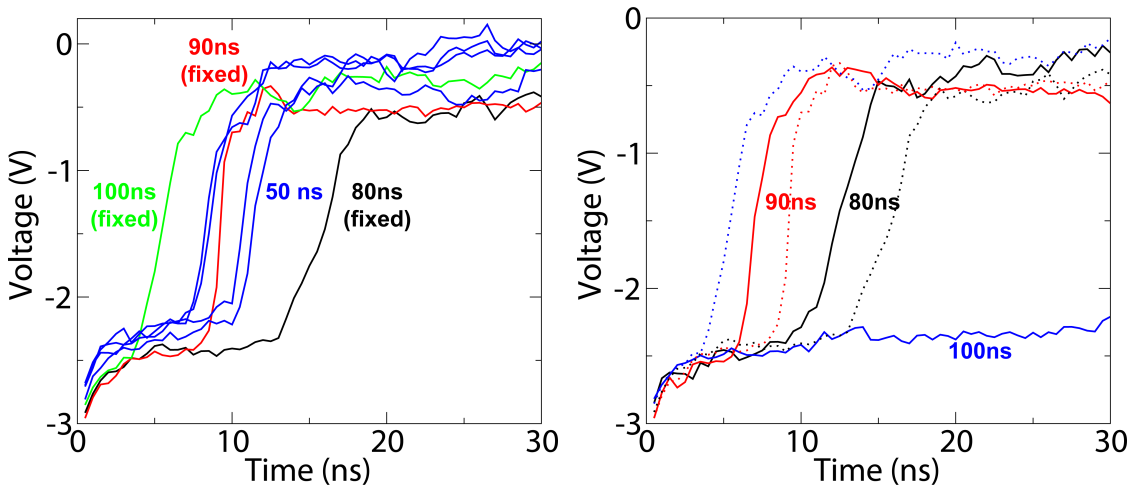

(a) *TMVs of PLL^{+20}* **(b)** *TMVs of 2x PLL^{+10}*

Figure 6.17 *TMV measurements for PLL^{+20} and two PLL^{+10} peptides. (a) A pore was formed in each PLL^{+20} simulation. (b) The TMVs of each PLL^{+10} simulation are depicted as solid lines, and their corresponding PLL^{+20} simulations using the same initial frame are depicted as dotted lines.*

all saw pore formation between 3 and 13 ns and result in TMVs in the range of 0-500 mV. Interestingly, the two simulations that saw TMVs of 0 mV both had final ion imbalances of -18, implying that a charge imbalance of +2 remained in the system. The previous chapter (Section 5.4) showed that an ion imbalance of +2 was capable of inducing a TMV of roughly -225 mV for this bilayer, which further suggests that additional factors may play a role in determining the TMV. These simulations also reveal that fixing the peptides in the centre of the box still allows pore formation to occur, implying that the peptides do not need to be in direct contact with the bilayers to induce electroporation.

Three more simulations were conducted using two PLL^{+10} peptides (containing 10 lysines each), which were inserted in the outer compartment of three initial frames of the same POPE/POPG (3:1) double bilayer (80 ns, 90 ns and 100 ns) and positioned equidistant to each other and to each bilayer. The peptides were held in place using position restraints, and each simulation was equilibrated and conducted for 30 ns. Two pore formations were observed, in which their TMV measurements are depicted in Figure 6.17b along with those of the fixed PLL^{+20} simulations. The pore formation times in the 80 ns and 90 ns simulations were roughly identical to those of PLL^{+20}; however, the 100 ns simulation failed to produce a pore within the simulation time.

This provides an interesting comparison of the pore formation times (and perhaps pore formation efficiency/frequency) between two systems with identical charge imbalance, one having the imbalance localised in a single peptide and the other having the imbalance spread between two peptides. This result suggests that a single PLL^{+20} peptide and two PLL^{+10} peptides behave in a similar way, achieving similar TMVs and pore formation times. However, based on a comparison of only three initial frames, it is still unclear as to whether using two PLL^{+10} peptides over one PLL^{+20} peptide would produce differences in the pore formation process in this bilayer composition. This would make a very interesting experiment, either *in vitro* or *in vivo*, to compare the use of double the concentration of PLL^{+10} with PLL^{+20}, which may elucidate any variations in efficiency when inducing pore formation and in exhibiting antimicrobial action.

6.3.3 Poly-glutamic acid

Poly-glutamic acid (PGLU) is another simplistic peptide which contains n-repeats of the residue glutamic acid making the peptide highly anionic. PGLU has been investigated as a drug and antigen delivery system for the treatment of cancerous tumours and HIV-1 infection [225, 226].

To investigate the effects of a negatively charged peptide on a negatively charged lipid bilayer, four simulations were conducted in which $PGLU^{-20}$ was inserted into the outer compartment of four initial frames of a POPE/POPG (3:1) double bilayer, taken after 100 ns, 110 ns, 130 ns and 150 ns of equilibration. Position restraints were placed on the backbone atoms of each peptide to prevent bilayer contact, and the simulations were equilibrated and conducted for 30 ns. Each simulation resulted in pore formation at approximately 10 ns, 15 ns and 28 ns, where the latter simulation was extended for an additional 5 ns to capture the resting TMV.

Figure 6.18 depicts the TMV measurements for each simulation. As this is a negatively charged peptide, the TMV across the bilayers is now positive, experiencing TMVs of approximately +2.35 V after the initial equilibration. Pore formation occurred in a similar manner to those previously observed with cationic peptides, with the exception that the anodic and cathodic leaflets/compartments swap positions and cations are now observed to flow into the outer (anodic) compartment where the $PGLU^{-20}$ is situated. The order parameters and leaflet thickness also confirm that the anodic and cathodic leaflets swap positions (data

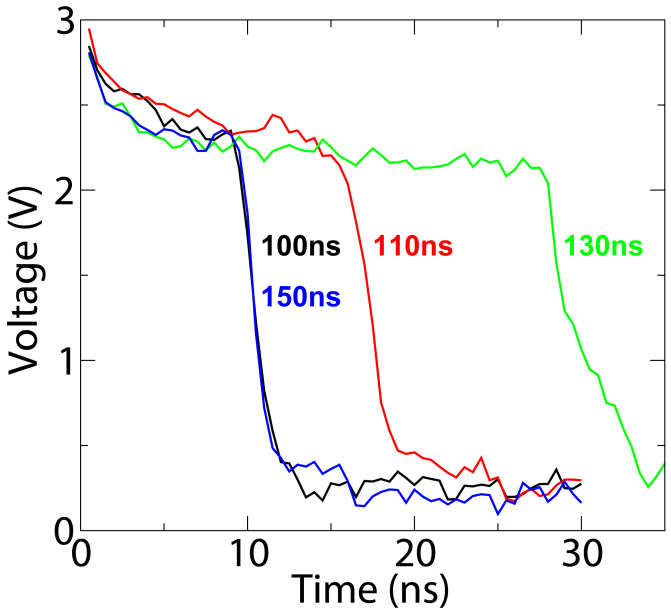

Figure 6.18 *TMV measurements of four simulations containing poly-glutamic acid ($PGLU^{-20}$) with a POPE/POPG (3:1) double bilayer. Each system started from a unique initial frame and resulted in pore formation within 10-28 ns.*

not shown) by showing that the outer leaflets experience a greater increase in disorder and decrease in thickness when compared to the inner leaflets.

These results suggest that the sign of the charge imbalance (positive or negative) appears to be irrelevant for electroporation to occur, which saw pore formation induced by $PGLU^{-20}$ peptides to occur on similar timescales to pore formations induced by PLL^{+20} peptides. However, the flow of cations (and presumably anions) has reversed, which suggests that cells may experience a surplus of anions within the cell when treated with anionic peptides.

6.3.4 Comparison of electroporation induced by charged peptides and ion imbalances

When inducing electroporation from an ion imbalance, the imbalance is spread out over the entire water compartment, whereas when inducing electroporation from charged peptides, the imbalance is highly localised over a single spot on the membrane. This difference in charge distribution may have implications on the pore formation time and frequency, and can be checked by comparing all previous peptide and ion imbalance simulations that were initiated from the same initial frame.

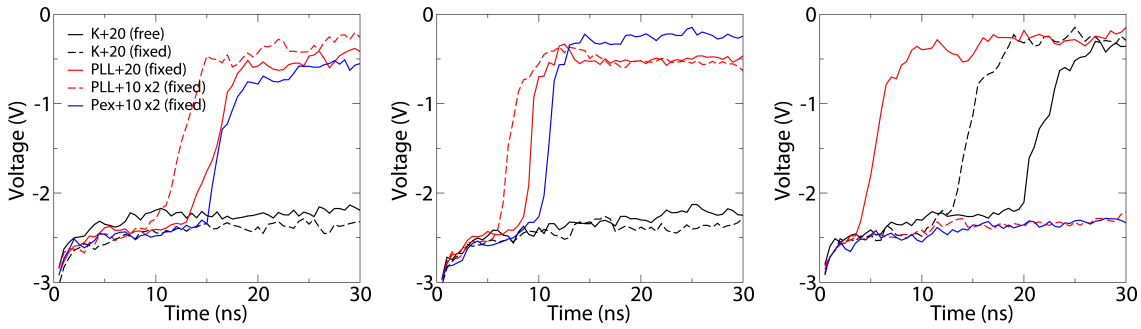

(a) *System 1* **(b)** *System 2* **(c)** *System 3*

Figure 6.19 *Comparison of TMV measurements from simulations of ion imbalances and charged peptides conducted from three initial frames.*

Figure 6.19 depicts the TMV measurements from simulations of two Pexiganan, PLL^{+20}, two PLL^{+10}, K^{+20} (free) and K^{+20} (fixed), which began from the 80 ns, 90 ns and 100 ns initial frames. All peptides in these simulations were fixed in the centre of the outer compartment, and the fixed ion simulations were constructed by removing ten cations from the inner compartment and placing them in a linear wire-like distribution in the centre of the outer compartment, which were then fixed in place with position restraints using a force constant of 1000 kJ/mol nm^2.

Both the 80 ns and 90 ns frames saw pore formation occur in all peptide simulations at similar times; however, no pores were observed in any of the ion imbalance simulations. The 100 ns frame saw pore formation occur in both the ion imbalance and PLL^{+20} simulations, but no pore formations occurred with two PLL^{+10} or two Pexiganan peptides. From this result, no general conclusions can be drawn on the differences between the pore formation time and frequency between using charged peptides and ion imbalances. A more in-depth study would be required to further elucidate any possible differences between each approach. This may also require the use of a larger membrane to distinguish between a localised electric field from a charged peptide and an evenly distributed electric field from an ion imbalance.

6.3.5 Conclusion

In this section, I have investigated a new approach of generating a TMV across a double bilayer by substituting an ion imbalance with one or several charged peptides. These peptides were shown to generate an electrostatic potential

across the bilayers with similar shape and strength to the electrostatic potential generated by an ion imbalance of equal magnitude. Furthermore, charged peptides were shown to induce electroporation in double bilayers, where the pore formation frequency, TMV, and ion transfer rate through the pore appears indistinguishable to those induced with an ion imbalance. However, whilst electroporation induced by an ion imbalance results in an equilibrium of the ionic concentrations between membrane compartments, inducing electroporation with charged peptides establishes a negative ion imbalance that counters the charge imbalance of the peptides. This negative ion imbalance may have implications for biological cells as cationic peptides would incur a surplus of cations within the cell, whereas anionic peptides would incur a surplus of anions within the cell. Furthermore, as many membrane-targeting AMPs are known to permeabilise the cell membrane through the formation of toroidal pores, it is conceivable that AMPs could utilise the electroporation phenomenon to assist in their mechanism of action and to gain entry to the intracellular compartment.

Pexiganan, a synthetic cationic amphipathic helix, is one such AMP known to permeabilise the membrane through the formation of toroidal pores in anionic membranes [223]. To investigate whether Pexiganan can utilise the electroporation phenomenon, simulations were conducted in which two Pexiganan peptides were placed over a POPE/POPG (3:1) double bilayer, yielding a charge imbalance of +20. These simulations yielded TMVs of approximately -2.35 V, an identical TMV to those observed when using ion imbalances of +20. Pore formation was also observed, and revealed no correlation between the bilayer containing the pore and the bilayer in which the peptides interacted with. Additional simulations were conducted in which the Pexiganan peptides were fixed in the centre of the water compartment using position restraints, restricting their contact with the bilayer surface. These simulations revealed that pore formation can still occur without direct bilayer contact.

Similarly, simulations were conducted with the AMP Poly-l-lysine (PLL), a simplistic cationic peptide comprising n-repeats of the residue lysine. This peptide is known to strip the outer membrane of *E. coli* followed by an abnormal distribution of the cytoplasm [224]. Simulations of PLL^{+20} and two PLL^{+10} were conducted in which these peptides were placed over POPE/POPG (3:1) double bilayers and fixed with position restraints. Pore formation was observed to occur from both peptides with no observable differences in pore formation frequency between each peptide. This could further be investigated by conducting *in vitro*

experiments to ascertain whether one peptide is more effective than the other at achieving antimicrobial action, where PLL^{+10} is used at double the concentration of PLL^{+20}. This may also determine whether electroporation plays a significant role in the antimicrobial mechanisms of these peptides.

Electroporation was also induced by Poly-glutamic acid (PGLU), another simplistic peptide containing n-repeats of the negatively charged residue glutamic acid, and has been investigated as a drug and antigen delivery system for the treatment of cancerous tumours and HIV-1 infection [225, 226]. $PGLU^{-20}$ was observed to induce pore formation in a similar manner to PLL^{+20}, with the exception that these simulations saw the anodic and cathodic leaflets and compartments swap places, and ions were observed to flow through the pore in the opposite direction when compared with electroporation from cationic peptides.

As it appears that charged peptides and ions induce electroporation with similar mechanisms, the question was asked as to whether the localisation of the charge imbalance has an effect on the pore formation frequency, i.e. does having the charge imbalance localised above a single spot on the membrane incur pore formation faster or slower than when the charge imbalance is spread out over the entire membrane surface? To investigate this, each existing peptide simulation was compared to its corresponding ion imbalance simulation. Three frames were chosen in which simulations of K^{+20} were compared with two Pexiganan (+20) peptides, one PLL^{+20} peptide and two PLL^{+10} peptides. Additional simulations were also conducted in which an ion imbalance was positioned in a wire-like structure at the top of the simulation box and fixed with position restraints. From the analysis, no conclusion could be drawn from the pore formation frequency when differentiating between different charge imbalance distributions. Further studies would be required to fully elucidate this, which may require the use of larger membranes to distinguish between localised and evenly distributed charge imbalances. Nevertheless, the results to date suggest that charged peptides induce pore formation with similar mechanisms to those observed when using an ion imbalance. This suggests that charged peptides, such as AMPs, may be capable of utilise pore formation via electroporation to gain entry into the cell or assist in their antimicrobial action.

Chapter 7

Summary, discussion and future work

In this thesis, I have presented several MD studies aimed at advancing our understanding of various biological systems and phenomena, focusing on the study of antimicrobial peptides, transmembrane potentials and electroporation of lipid bilayers. I have also presented new software to analyse and interpret the properties of lipid bilayers explored through MD simulations, allowing for a greater understanding of the changes undergone by lipid bilayers in response to environmental perturbations. To summarise, a brief outline of each project, its conclusions and potential applications, including future work, are discussed below.

Chapter 3 presents and discusses the development and implementation of the software `Membrainy`: a 'smart', unified membrane analysis tool that provides researchers with an integrated suite of analytical techniques targeted at the measurement lipid bilayer properties. These properties often change in response to various biological phenomena and environmental perturbations, including interactions with AMPs and other charged peptides (Chapters 4,5 and 6), changes in response to membrane potentials established via ionic gradients (Chapters 5 and 6), and changes in response to transient pore formation due to electroporation (Chapter 6). Existing tools were studied to identify their advantages and disadvantages, and certain key elements were identified and used in the design process of `Membrainy`. This includes the elimination of complicated index files employed by tools such as `g_order`, which can take 15-20 minutes to

construct, and parameter files used by tools such as `GridMAT-MD`, which contain parameters that could easily be determined automatically through intelligent detection algorithms. `Membrainy` automatically detects each membrane system to analyse, including automatic force field detection, automatic double bilayer detection, automatic lipid composition detection etc., allowing the user to focus his or her efforts on the interpretation of the data rather than the operation of the tool. `Membrainy` also eliminates the need to be compiled, in which existing tools written in C require complicated compilations and have many dependencies on existing libraries or software. It is these features that allow `Membrainy` to provide a safer and more convenient alternative to existing tools. Furthermore, `Membrainy` contains analytical techniques that are not available in existing tools, further advancing its usefulness as a unified membrane analysis tool. `Membrainy` has been published in the journal *Source Code for Biology and Medicine* and has already contributed to the analysis of several studies outwith this thesis.

In addition to `Membrainy`, Chapter 3 also presents two lipid bilayer construction tools, aimed at assisting the creation of single and double bilayer systems. The tool `BoxMod` allows for a precise calibration of the ionic concentrations across lipid bilayers and membrane compartments, a necessary process in the construction of any lipid bilayer system. The tool `MoleculeInserter` allows molecules to be positioned at a user-specified distance and orientation from the bilayer surface, allowing for consistency when conducting multiple simulations involving molecules and lipid bilayers. In addition, the post-analysis tool `SmoothGraph` is presented, which allows the removal of fluctuations from data sets due to poor sampling, thereby enhancing the visual finesse of the data set and assisting in the interpretation of meaningful data.

Chapter 4 introduces the concept of regulating AMP activity through the formation of a coiled coil structure upon binding with an inhibitor peptide, whereby the coiled coil formation restricts the AMP from adopting new confirmations required to exhibit antimicrobial action. This concept may also be applicable to non-AMPs, as any disease or biological process that utilises coiled coils may also allow this vulnerability to be exploited. In this chapter, the AMP Cecropin-B is used as a model system to explore the formation of coiled coils through MD simulations. Despite sequence similarity to coiled coils, AMPs such as Cecropin-B are incapable of coiled coil formation and therefore Cecropin-B was mutated to incorporate the heptad repeats commonly associated with coiled coils. This *mutant* peptide was used in the design of an inhibitor peptide,

the *anti-mutant*, which incorporates sequence similarities but with oppositely charged residues. Stain-dead assays conducted at NPL revealed the mutant to retain antimicrobial activity, albeit at a reduced potency to the native Cecropin-B. Assays containing the mutant and anti-mutant revealed anti-antimicrobial activity at molar ratios of 1:5-10 respectively, and CD measurements provided quantitative information of coiled coil interactions. The simulations presented within this chapter reveal the Cecropin-B, Cecropin-B mutant and anti-mutant to be partially unstructured in solution with approximately 25%, 50% and 65% of helicity respectively. Simulations also reveal that coiled coil formation between the mutant and anti-mutant is possible, but highly infrequent. This infrequency is likely mediated by the strong tendency for these peptides to unfold in water, where the unfolding is primarily driven by a proline residue in all three peptides, disrupting the hydrogen bonds required to stabilise the helix.

This approach of using inhibitors to target peptides and proteins susceptible to coiled coil formation is not limited to AMPs, and may have important practical applications for development of new treatments for disease. A study by Brandenburg *et al.* used a synthetic inhibitory peptide to block formation of coiled coil susceptible amyloid aggregates, which are responsible for brain plaque formation in Alzheimer's and Parkinson's disease [176]. Bianchi *et al.* used a synthetic inhibitory peptide to block HIV-1 fusion with host cells by blocking the gp41 protein via coiled coil mechanisms [177]. Lamb *et al.* used a synthetic inhibitory peptide to block the function of an envelope protein in the human T-cell leukemia virus and bovine leukemia virus [178]. The design and development of inhibitors which form coiled coil structures therefore represents a very exciting possibility for future therapies.

Chapter 5 presents an investigation into the insertion process of the MinD membrane targeting sequence (MinD-MTS) into a model bacterial membrane. This 11-residue peptide has its sequence taken from the C-terminus of the MinD protein that plays a crucial role in the cell division of *B. subtilis*. *In vitro* experiments by Strahl and Hamoen have shown MinD-MTS to increase its binding affinity to bacterial liposomes upon establishing a TMV and, upon removal of the TMV in *B. subtilis*, the MinD protein becomes delocalised [182]. MD simulations showed the MinD-MTS to be an amphipathic helix that rapidly inserts into POPE/POPG (3:1) bilayers within 50-100 ns. Prior to insertion, the MinD-MTS was shown to perturb the lipid headgroups by causing an increase in mean POPG headgroup orientation and a decrease in POPE headgroup orientation. Upon

insertion, the hydrophobic face was observed to interface with the hydrophobic core of the bilayer, extending 2-3 carbons down the lipid tails with a mean peptide depth of 17.2 Å from the centre of the bilayer. At this point, `Membrainy` was used to calculate the order parameters of the lipids in the annular shell of MinD-MTS, revealing the presence of splayed lipid tails. This is a significant finding as splayed lipid tails have been suggested to lead to membrane curvature, where the depth of the peptide plays a role in assigning the shape of the curvature [192]. This type of analysis therefore has potential applications in studying or designing peptides capable of sensing or inducing membrane curvature.

Surprisingly, the insertions of the MinD-MTS peptides occurred in simulations with and without a TMV. This lead to a further investigation to detect changes in membrane properties using a variety of bilayer compositions, temperatures and voltages. These simulations found that the transition temperature of POPE/POPG (3:1) bilayers is slightly lowered (by 1-2 degrees) when subjected to a 1 V TMV, where bilayers at 295 K and 297 K experienced an increase in fluidity (more so at 297 K) and bilayers at 300 K saw no significant changes. These results provide conclusive evidence of changes in membrane properties in POPE/POPG (3:1) bilayers when under the influence of a TMV, but only at temperatures slightly below the transition temperature.

Many of the questions regarding the MinD-MTS experiments conducted by Strahl and Hamoen remain unanswered. It is still unclear how this small shift in transition temperature could play a role, if at all, in modifying the binding affinity of MinD-MTS and the localisation of MinD. This is particularly evident when considering that this small shift in transition temperature is achieved with a TMV $\sim$5 times higher than those found in bacterial cells. Furthermore, this shift in transition temperature would only affect the MinD binding affinity and localisation in membranes slightly below their transition temperature. Nonetheless, the results from this chapter provide insight into the workings of lipid bilayers and the changes undergone when influenced by a TMV. However, additional experiments are sought to further elucidate the mechanisms behind the MinD binding affinity and localisation with bacterial membranes. Given that MinD binding to *B. subtilis* is localised at the bacterial poles when influenced by a TMV, future MD studies could focus on exploring the effects of TMVs around curved membranes, such as those found at the bacterial poles, for which the differences in surface areas on both sides of the membrane may incur local changes to the TMV, or changes to the membrane properties that differ

from those of planar bilayers to facilitate MinD binding.

The results from this study have been shared with Strahl and Hamoen, who are conducting further research to investigate the link between TMVs, MinD localisation, and the MinD-MTS binding affinity. It is likely that our research collaboration will result in a publication in the near future. Additionally, the research behind the MinD-MTS insertion process, which was conducted in collaboration with the Department of Biochemistry at the University of Oxford, is currently in submission.

Chapter 6 presents an investigation into the electroporation phenomenon, whereby applied electric fields induce transient water pores in cell membranes. The mechanisms behind the pore formation process have been captured using MD [117, 203–205], and various studies have explored the implications of electroporation with certain bilayer types [106, 206–209]. The research in this chapter continues this exploration by investigating electroporation using a variety of bilayer compositions and temperatures, allowing for a comparison of bilayers with varying levels of fluidity, area per lipid, surface charge, and electric field strength. The simulations within this chapter employ a ionic gradient approach whereby electroporation is induced by an ion imbalance across a double bilayer. This differs from the majority of electroporation studies which employ a uniform electric field approach by adding an additional force component experienced by each atom in the simulation box and, as such, the implications of electroporation induced by an ion imbalance is largely unexplored.

The simulations presented in this chapter reveal that the pore formation process appears identical to those induced by an applied electric field, with the exception that pores formed through ion imbalances are short-lived: the pore allows the equilisation of ionic concentrations between membrane compartments, resulting in a dissipation of the ion imbalance and a lowering of the TMV. Prior to pore formation, these simulations reveal a significant increase in disorder in the lipid tails, with additional disorder in the anodic leaflets. Headgroup orientations were observed to tend to align with the electric field; however, the shift in mean orientation is only 1.5-2.5 degrees (in POPC and POPE/POPG (3:1) bilayers) with TMVs of -2.35 V, with the greatest shift in the anodic leaflets. This observation is consistent with those made by Böckmann *et al.* [117], who saw similar shifts in headgroup orientations when using an applied electric field with POPC bilayers. A shift in the lipid tails C−H bond angles was also observed, which was noticeably more significant than the shift observed in the

headgroup orientations. This was a surprising observation since the headgroup is considerably more charged and flexible than the lipid tail C−H bonds. This lead to an analysis of the electric field strength throughout the bilayer, revealing an identical field strength in the headgroup region when compared to a no-TMV bilayer. This analysis also saw a significantly greater field strength in the lipid tail region, which peaks in the anodic lipid tails. This may provide an explanation as to why the anodic leaflets experience greater perturbations in membrane properties when compared to those of the cathodic leaflets.

In addition, the simulations within Chapter 6 also reveal a partial coupling between the APL and TMV, suggesting that bilayer compositions with larger APLs, or those transitioning from gel to fluid phases, will experience smaller TMVs with the same ion imbalance. The threshold voltage to induce pore formation within 30 ns appears to be roughly identical in all fluid bilayers ($\sim$1.9 V), whereas DPPC bilayers in the gel phase exhibit a higher threshold voltage ($\sim$2.4 V). This higher threshold voltage agrees with the observations made by Polak *et al.*, and Wang and Larson, who observed that highly ordered bilayers prevent the formation of water files within the bilayer due to increased stability in the lipid tail region [106, 209]. Lipid flip-flopping was also observed to occur via transient water pores, whereby neutrally charged lipids translocate through the pore in both directions. A simulation utilising a constant ion imbalance across POPE/POPG (3:1) bilayers revealed that the electric field drives POPG lipids to flip-flop towards the cathodic leaflet, which gives rise to an asymmetric bilayer. This may have potential applications in driving bilayer asymmetry via electroporation mechanisms, and future simulations could explore the effect an asymmetrically charged bilayer poses on the TMV.

This chapter also presents simulations to investigate the possibility of electroporation induced by charged peptides, a concept that has been suggested in several studies but has remained unexplored with MD [213–216]. Simulations of charged peptides (Pexiganan, Poly-l-lysine and Poly-glutamic acid) with POPE/POPG (3:1) double bilayers revealed electroporation mechanisms whereby charged peptides, which do not need to be in direct contact with the bilayer surface, achieved identical TMVs and a pore formation process when compared to using an ion imbalance of equal magnitude. One observed difference between each approach is that electroporation via charged peptides drives an ionic gradient between cellular compartments, whereas electroporation via ion imbalances results in an equilisation of ionic concentrations. However, both approaches

result in a dissipation of the TMV upon pore formation, suggesting that the ionic gradient driven by electroporation from charged peptides results in a neutralisation of the charge imbalance established by the peptides. This may have implications for cells treated with cationic AMPs, which may experience a flux of anions in the intracellular compartment prior to cell death. Furthermore, as many AMPs are known to permeabilise the membrane through the formation of pores, these simulations provide evidence to suggest that AMPs could utilise the electroporation phenomenon to assist in their mechanism of action.

The research described in this thesis may have a number of practical applications especially for the treatment of human diseases and infection. To better our understanding of the interactions of peptides with both prokaryotic and eukaryotic cells, the MD methods developed and presented in this thesis could be used to optimise peptide interactions with cell membranes. This may involve studying the insertion of amphipathic peptides to determine their effects on the local membrane properties, and investigating how changes in lipid tail flexibility may give rise to membrane curvature; or to increase peptide uptake into cells through the induction of TMVs and pore formation via electroporation mechanisms, where peptides can be designed to achieve optimal interactions with pores to achieve efficient transport into the cytoplasm of cells. Depending on the application, peptides could be designed to exploit differences in membrane properties between different species; for example, to discriminate between bacterial, human and cancer cells by designing peptides that specifically target properties unique to each type of cell.

In addition to exploiting differences in membrane properties between different cells, the observations from Chapter 6 suggest that temperature can significantly effect the TMV of different bilayer compositions, resulting in different efficiencies of pore formation which could be exploited for specific applications. In cancer, for example, the site of the cancerous cells could be heated or cooled to promote higher poration efficiencies and increased uptake of therapeutic drugs, while limiting uptake to healthy cells. Alternatively, the cancer site could be injected with ionic solutions or charged molecules, with the aim of modifying the TMV for increased membrane permeabilisation via electroporation mechanisms.

In conjunction with optimised peptide design, further functionalities could be achieved by the addition of membrane targeting sequences, such as the MinD-MTS, into the sequences of peptides or proteins in order to facilitate efficient binding and insertion into cell membranes. These additions may have potential

applications for improved drug delivery into bacteria or cancer cells by improving their interactions with cell membranes. For the treatment of cancer, there is significant interest in inhibiting or blocking certain intracellular proteins which are known to be key drivers of the cancer. A major example is peptide inhibitors of the proteins hDM2 and hDMX, which down regulate the cancer-suppressing protein p53 in a wide range of different cancers and for which peptide inhibitors have been developed using classical methods without the availability of advanced MD methods [227].

Aside from using MD to design better peptides for the treatment of disease and infection, other applications of the research described in this thesis can be envisaged. For example, the preservation of food stored at room temperature or fridge temperature could be enhanced by utilising AMPs which are specifically designed to kill bacteria at these temperatures. Creams for the treatment of topical infections such as bacterial, fungal and parasitic infections, could include charged peptides or molecules which increase the uptake of the active ingredient via electroporation mechanisms, improving the efficiency of these treatments. The same approach could be applied to antiseptics and antimicrobial wipes, whereby antimicrobials are utilised along with charged molecules or charged surfaces to more efficiently kill microbes than simple alcohols or antiseptic chemicals. AMPs could also be utilised in agriculture, whereby crops could have their genetic sequences modified to include the genes for such AMPs to inhibit growth of microbes, thus improving food yield and quality.

Whilst the above applications of MD are broad and varied, it is important to understand that living cell membranes are a fluid mixture of lipid bilayers and numerous other surface molecules, such as sugars and glycoproteins. As a result, the MD study of peptides optimised for binding to and transportation into cells should be integrated with biological studies with live cells in order to measure actual biological effects on cells. Such biological studies are likely to uncover unexpected actions of certain peptides which can then be further optimised with the assistance of MD. In addition, biological studies with live organisms would provide a further screening step for the evolution of peptides for therapeutic uses. Thus it is envisaged that the next stage in the development and application of the MD tools developed in this research would be integration into multidisciplinary research projects to achieve a powerful combination of *in silico*, *in vitro* and *in vivo* research towards fulfilling the potential of AMPs, especially for the treatment of human diseases.

Bibliography

[1] Geoffrey M Cooper and Robert E Hausman. *The cell*. Sinauer Associates Sunderland, 2000.

[2] CM O'Connor and Jill U Adams. Essentials of cell biology. *Cambridge, MA: NPG Education*, pages 71–82, 2010.

[3] Mario Schelhaas. Come in and take your coat off–how host cells provide endocytosis for virus entry. *Cellular microbiology*, 12(10):1378–1388, 2010.

[4] Mariana Ruiz Villarreal. Various scientific figures. http://en.wikipedia.org/wiki/user:ladyofhats.

[5] Emilio Montserrat, Juan Sanchez-Bisono, Nuria Viñolas, and Ciril Rozman. Lymphocyte doubling time in chronic lymphocytic leukaemia: analysis of its prognostic significance. *British journal of haematology*, 62(3):567–575, 1986.

[6] Peng Ji, Senthil Raja Jayapal, and Harvey F Lodish. Enucleation of cultured mouse fetal erythroblasts requires rac gtpases and mdia2. *Nature cell biology*, 10(3):314–321, 2008.

[7] Heide N Schulz. Thiomargarita namibiensis: giant microbe holding its breath. *Asm News*, (68):122–+, 2002.

[8] Gerrit van Meer, Dennis R. Voelker, and Gerald W. Feigenson. Membrane lipids: where they are and how they behave. *Nat Rev Mol Cell Biol*, 9(2):112–124, February 2008.

[9] Howard C Berg. *Random walks in biology*. Princeton University Press, 1993.

[10] Stephanie Tristram-Nagle and John F Nagle. Lipid bilayers: thermodynamics, structure, fluctuations, and interactions. *Chemistry and physics of lipids*, 127(1):3–14, 2004.

[11] Margus R Vist and James H Davis. Phase equilibria of cholesterol/dipalmitoylphosphatidylcholine mixtures: deuterium nuclear magnetic resonance and differential scanning calorimetry. *Biochemistry*, 29(2):451–464, 1990.

[12] Sean Munro. Lipid rafts: elusive or illusive? *Cell*, 115(4):377–388, 2003.

[13] Christian Dietrich, Zoya N Volovyk, Moshe Levi, Nancy L Thompson, and Ken Jacobson. Partitioning of thy-1, gm1, and cross-linked phospholipid analogs into lipid rafts reconstituted in supported model membrane monolayers. *Proceedings of the National Academy of Sciences*, 98(19):10642–10647, 2001.

[14] Michael Wachinger, Andrea Kleinschmidt, David Winder, Naciye von Pechmann, Alexandra Ludvigsen, Markus Neumann, Rolf Holle, Brian Salmons, Volker Erfle, and Ruth Brack-Werner. Antimicrobial peptides melittin and cecropin inhibit replication of human immunodeficiency virus 1 by suppressing viral gene expression. *Journal of General Virology*, 79(4):731–740, 1998.

[15] WEea Robinson, Brenda McDougall, Dat Tran, and Michael E Selsted. Anti-hiv-1 activity of indolicidin, an antimicrobial peptide from neutrophils. *Journal of leukocyte biology*, 63(1):94–100, 1998.

[16] Michael Zasloff. Antimicrobial peptides of multicellular organisms. *Nature*, 415(6870):389–395, 2002.

[17] Bruno Lemaitre, Jean-Marc Reichhart, and Jules A Hoffmann. Drosophila host defense: differential induction of antimicrobial peptide genes after infection by various classes of microorganisms. *Proceedings of the National Academy of Sciences*, 94(26):14614–14619, 1997.

[18] Jeffrey W Cary, Kanniah Rajasekaran, Jesse M Jaynes, and Thomas E Cleveland. Transgenic expression of a gene encoding a synthetic antimicrobial peptide results in inhibition of fungal growth in vitro and in planta. *Plant Science*, 154(2):171–181, 2000.

[19] Yoshinobu Ohsaki, Adi F Gazdar, Hao-Chia Chen, and Bruce E Johnson. Antitumor activity of magainin analogues against human lung cancer cell lines. *Cancer research*, 52(13):3534–3538, 1992.

[20] Margaret A Baker, Walter Lee Maloy, Michael Zasloff, and Leonard S Jacob. Anticancer efficacy of magainin2 and analogue peptides. *Cancer research*, 53(13):3052–3057, 1993.

[21] Peter W Sloballe, W Lee Maloy, Michelle L Myrga, Leonard S Jacob, and Meenhard Herlyn. Experimental local therapy of human melanoma with lytic magainin peptides. *International journal of cancer*, 60(2):280–284, 1995.

[22] Yoonkyung Park, Dong Gun Lee, and Kyung-Soo Hahm. Antibiotic activity of leu-lys rich model peptides. *Biotechnology letters*, 25(16):1305–1310, 2003.

[23] Michael Zasloff. Magainins, a class of antimicrobial peptides from xenopus skin: isolation, characterization of two active forms, and partial cdna sequence of a precursor. *Proceedings of the National Academy of Sciences*, 84(15):5449–5453, 1987.

[24] Dan HULTMARK, Håkan STEINER, Torgny RASMUSON, and Hans G BOMAN. Insect immunity. purification and properties of three inducible bactericidal proteins from hemolymph of immunized pupae of hyalophora cecropia. *European Journal of Biochemistry*, 106(1):7–16, 1980.

[25] Birgit Schittek, Rainer Hipfel, Birgit Sauer, Jürgen Bauer, Hubert Kalbacher, Stefan Stevanovic, Markus Schirle, Kristina Schroeder, Nikolaus Blin, Friedegund Meier, et al. Dermcidin: a novel human antibiotic peptide secreted by sweat glands. *Nature immunology*, 2(12):1133–1137, 2001.

[26] John E Cronan. Bacterial membrane lipids: where do we stand? *Annual reviews in microbiology*, 57(1):203–224, 2003.

[27] Jeremy P Bradshaw. Cationic antimicrobial peptides. *BioDrugs*, 17(4):233–240, 2003.

[28] Kim A Brogden. Antimicrobial peptides: pore formers or metabolic inhibitors in bacteria? *Nature Reviews Microbiology*, 3(3):238–250, 2005.

[29] Kim A Brogden, Anthony J De Lucca, John Bland, and Shirley Elliott. Isolation of an ovine pulmonary surfactant-associated anionic peptide bactericidal for pasteurella haemolytica. *Proceedings of the National Academy of Sciences*, 93(1):412–416, 1996.

[30] Azza Eissa, Vanessa Amodeo, Christopher R Smith, and Eleftherios P Diamandis. Kallikrein-related peptidase-8 (klk8) is an active serine protease in human epidermis and sweat and is involved in a skin barrier proteolytic cascade. *Journal of Biological Chemistry*, 286(1):687–706, 2011.

[31] H Brötz, Gabriele Bierbaum, Astrid Markus, Ernst Molitor, and Hans-Georg Sahl. Mode of action of the lantibiotic mersacidin: inhibition of peptidoglycan biosynthesis via a novel mechanism? *Antimicrobial agents and chemotherapy*, 39(3):714–719, 1995.

[32] Aleksander Patrzykat, Carol L Friedrich, Lijuan Zhang, Valentina Mendoza, and Robert EW Hancock. Sublethal concentrations of pleurocidin-derived antimicrobial peptides inhibit macromolecular synthesis in escherichia coli. *Antimicrobial agents and chemotherapy*, 46(3):605–614, 2002.

[33] Hans G Boman, Birgitia Agerberth, and Anita Boman. Mechanisms of action on escherichia coli of cecropin p1 and pr-39, two antibacterial peptides from pig intestine. *Infection and Immunity*, 61(7):2978–2984, 1993.

[34] David Andreu, Luis Rivas, et al. Animal antimicrobial peptides: an overview. *Biopolymers*, 47(6):415–433, 1998.

[35] Deirdre A Devine and Robert EW Hancock. Cationic peptides: distribution and mechanisms of resistance. *Current pharmaceutical design*, 8(9):703–714, 2002.

[36] Andreas Peschel, Michael Otto, Ralph W Jack, Hubert Kalbacher, Günther Jung, and Friedrich Götz. Inactivation of the dlt operon instaphylococcus aureus confers sensitivity to defensins, protegrins, and other antimicrobial peptides. *Journal of Biological Chemistry*, 274(13):8405–8410, 1999.

[37] Sascha A Kristian, Manuela Dürr, Jos AG Van Strijp, Birgid Neumeister, and Andreas Peschel. Mprf-mediated lysinylation of phospholipids in staphylococcus aureus leads to protection against oxygen-independent neutrophil killing. *Infection and immunity*, 71(1):546–549, 2003.

[38] Michelle GJL Habets and Michael A Brockhurst. Therapeutic antimicrobial peptides may compromise natural immunity. *Biology letters*, page rsbl20111203, 2012.

[39] Lin Guo, Kheng B Lim, Cristina M Poduje, Morad Daniel, John S Gunn, Murray Hackett, and Samuel I Miller. Lipid a acylation and bacterial resistance against vertebrate antimicrobial peptides. *Cell*, 95(2):189–198, 1998.

[40] Miguel A Campos, Miguel A Vargas, Verónica Regueiro, Catalina M Llompart, Sebastián Albertí, and José A Bengoechea. Capsule polysaccharide mediates bacterial resistance to antimicrobial peptides. *Infection and immunity*, 72(12):7107–7114, 2004.

[41] Thomas K Held, Charlotte Adamczik, Matthias Trautmann, and Alan S Cross. Effects of mics and sub-mics of antibiotics on production of capsular polysaccharide of klebsiella pneumoniae. *Antimicrobial agents and chemotherapy*, 39(5):1093–1096, 1995.

[42] Magdalena Sieprawska-Lupa, Piotr Mydel, Katarzyna Krawczyk, Kinga Wójcik, Magdalena Puklo, Boguslaw Lupa, Piotr Suder, Jerzy Silberring, Matthew Reed, Jan Pohl, et al. Degradation of human antimicrobial peptide ll-37 by staphylococcus aureus-derived proteinases. *Antimicrobial agents and chemotherapy*, 48(12):4673–4679, 2004.

[43] Dieter Vandamme, Bart Landuyt, Walter Luyten, and Liliane Schoofs. A comprehensive summary of ll-37, the factotum human cathelicidin peptide. *Cellular Immunology*, 280(1):22 – 35, 2012.

[44] Robert Belas, Jim Manos, and Rooge Suvanasuthi. Proteus mirabilis zapa metalloprotease degrades a broad spectrum of substrates, including antimicrobial peptides. *Infection and immunity*, 72(9):5159–5167, 2004.

[45] Erika V Valore, Christina H Park, Alison J Quayle, Kerry R Wiles, Paul B McCray Jr, and Tomas Ganz. Human beta-defensin-1: an antimicrobial

peptide of urogenital tissues. *Journal of Clinical Investigation*, 101(8):1633, 1998.

[46] Sarah Sundelacruz, Michael Levin, and David L Kaplan. Role of membrane potential in the regulation of cell proliferation and differentiation. *Stem cell reviews and reports*, 5(3):231–246, 2009.

[47] Stephen H. Wright. Generation of resting membrane potential. *Advances in Physiology Education*, 28(4):139–142, 2004.

[48] Geoffrey M. Geise, Harrison J. Cassady, Donald R. Paul, Bruce E. Logan, and Michael A. Hickner. Specific ion effects on membrane potential and the permselectivity of ion exchange membranes. *Phys. Chem. Chem. Phys.*, 16:21673–21681, 2014.

[49] B Hubbell Honig, Wayne L Hubbell, and Ross F Flewelling. Electrostatic interactions in membranes and proteins. *Annual review of biophysics and biophysical chemistry*, 15(1):163–193, 1986.

[50] H Felle, JS Porter, CL Slayman, and HR Kaback. Quantitative measurements of membrane potential in escherichia coli. *Biochemistry*, 19(15):3585–3590, 1980.

[51] WE Alborn, NE Allen, and DA Preston. Daptomycin disrupts membrane potential in growing staphylococcus aureus. *Antimicrobial agents and chemotherapy*, 35(11):2282–2287, 1991.

[52] Clarence D Cone and Max Tongier. Contact inhibition of division: involvement of the electrical transmembrane potential. *Journal of cellular physiology*, 82(3):373–386, 1973.

[53] Thomas Starke-Peterkovic, Nigel Turner, Paul L Else, and Ronald J Clarke. Electric field strength of membrane lipids from vertebrate species: membrane lipid composition and na+-k+-atpase molecular activity. *American Journal of Physiology-Regulatory, Integrative and Comparative Physiology*, 288(3):R663–R670, 2005.

[54] Bruno Maggio. Modulation of phospholipase a2 by electrostatic fields and dipole potential of glycosphingolipids in monolayers. *Journal of lipid research*, 40(5):930–939, 1999.

[55] Mark W Barnett and Philip M Larkman. The action potential. *Practical neurology*, 7(3):192–197, 2007.

[56] John C Rogers, Yusheng Qu, Timothy N Tanada, Todd Scheuer, and William A Catterall. Molecular determinants of high affinity binding of α-scorpion toxin and sea anemone toxin in the s3-s4 extracellular loop in domain iv of the na+ channel α subunit. *Journal of Biological Chemistry*, 271(27):15950–15962, 1996.

[57] Bruce P Bean. Nitrendipine block of cardiac calcium channels: high-affinity binding to the inactivated state. *Proceedings of the National Academy of Sciences*, 81(20):6388–6392, 1984.

[58] Martin Foltz, Carmen Oechsler, Michael Boll, Gabor Kottra, and Hannelore Daniel. Substrate specificity and transport mode of the proton-dependent amino acid transporter mpat2. *European Journal of Biochemistry*, 271(16):3340–3347, 2004.

[59] Donato Terrone, Stephane Leung Wai Sang, Liya Roudaia, and John R Silvius. Penetratin and related cell-penetrating cationic peptides can translocate across lipid bilayers in the presence of a transbilayer potential. *Biochemistry*, 42(47):13787–13799, 2003.

[60] Eberhard Neumann, M Schaefer-Ridder, Y Wang, and PH Hofschneider. Gene transfer into mouse lyoma cells by electroporation in high electric fields. *The EMBO journal*, 1(7):841, 1982.

[61] Andrew R. Leach. *Molecular modelling: principles and applications*. Pearson Education, 2001.

[62] *Gromacs 4.5.4 Manual: http://www.gromacs.org/Documentation/Manual*.

[63] Sander Pronk, Szilárd Páll, Roland Schulz, Per Larsson, Pär Bjelkmar, Rossen Apostolov, Michael R Shirts, Jeremy C Smith, Peter M Kasson, David van der Spoel, et al. Gromacs 4.5: a high-throughput and highly parallel open source molecular simulation toolkit. *Bioinformatics*, page btt055, 2013.

[64] Dirk Matthes and Bert L. de Groot. Secondary Structure Propensities in Peptide Folding Simulations: A Systematic Comparison of Molecular Mechanics Interaction Schemes. *Biophysical Journal*, 97(2):599–608, July 2009.

[65] Oliver F. Lange, David van der Spoel, and Bert L. de Groot. Scrutinizing molecular mechanics force fields on the submicrosecond timescale with NMR data. *Biophysical journal*, 99(2):647–655, July 2010.

[66] Jay W. Ponder and David A. Case. *Force Fields for Protein Simulations*, volume 66 of *Advances in Protein Chemistry*, pages 27–85. Elsevier, 2003.

[67] Oren M. Becker, Alexander D. MacKerell, Benoit Roux, and Masakatsu Watanabe. *Computational Biochemistry and Biophysics*. 2001.

[68] James C Phillips, Rosemary Braun, Wei Wang, James Gumbart, Emad Tajkhorshid, Elizabeth Villa, Christophe Chipot, Robert D Skeel, Laxmikant Kale, and Klaus Schulten. Scalable molecular dynamics with namd. *Journal of computational chemistry*, 26(16):1781–1802, 2005.

[69] S. Kumar, C. Huang, G. Zheng, E. Bohm, A. Bhatele, J. C. Phillips, H. Yu, and L. V. Kale. Scalable molecular dynamics with NAMD on the IBM Blue Gene/L system. *IBM Journal of Research and Development*, 52(1):177–188, January 2008.

[70] Robert B Best, Xiao Zhu, Jihyun Shim, Pedro EM Lopes, Jeetain Mittal, Michael Feig, and Alexander D MacKerell Jr. Optimization of the additive charmm all-atom protein force field targeting improved sampling of the backbone ϕ, ψ and side-chain $\chi 1$ and $\chi 2$ dihedral angles. *Journal of chemical theory and computation*, 8(9):3257–3273, 2012.

[71] A. T. Hagler, E. Huler, and S. Lifson. Energy functions for peptides and proteins. I. Derivation of a consistent force field including the hydrogen bond from amide crystals. *Journal of the American Chemical Society*, 96(17):5319–5327, August 1974.

[72] William L. Jorgensen, Jeffry D. Madura, and Carol J. Swenson. Optimized intermolecular potential functions for liquid hydrocarbons. *Journal of the American Chemical Society*, 106(22):6638–6646, October 1984.

[73] Oliver F. Lange, David van der Spoel, and Bert L. de Groot. Scrutinizing molecular mechanics force fields on the submicrosecond timescale with NMR data. *Biophysical journal*, 99(2):647–655, July 2010.

[74] Callum J Dickson, Benjamin D Madej, Åge A Skjevik, Robin M Betz, Knut Teigen, Ian R Gould, and Ross C Walker. Lipid14: the amber lipid force field. *Journal of chemical theory and computation*, 10(2):865–879, 2014.

[75] Oliver Berger, Olle Edholm, and Fritz Jähnig. Molecular dynamics simulations of a fluid bilayer of dipalmitoylphosphatidylcholine at full hydration, constant pressure, and constant temperature. *Biophysical journal*, 72(5):2002, 1997.

[76] SHŪICHI Nosé. A molecular dynamics method for simulations in the canonical ensemble. *Molecular Physics: An International Journal at the Interface Between Chemistry and Physics*, 100(1):191–198, 2002.

[77] William G. Hoover. Canonical dynamics: Equilibrium phase-space distributions. *Physical Review A*, 31(3):1695–1697, March 1985.

[78] Koji Hukushima and Koji Nemoto. Exchange Monte Carlo Method and Application to Spin Glass Simulations. December 1995.

[79] Y. Sugita. Replica-exchange molecular dynamics method for protein folding. *Chemical Physics Letters*, 314(1-2):141–151, November 1999.

[80] T. Okabe. Replica-exchange Monte Carlo method for the isobaricisothermal ensemble. *Chemical Physics Letters*, 335(5-6):435–439, March 2001.

[81] Avanti Polar Lipids Inc. Phase transition temperatures for glycerophospholipids, http://avantilipids.com/index.php?option=com_content&id=1700&itemid=419.

[82] Sunhwan Jo, Taehoon Kim, Vidyashankara G Iyer, and Wonpil Im. Charmm-gui: a web-based graphical user interface for charmm. *Journal of computational chemistry*, 29(11):1859–1865, 2008.

[83] Sunhwan Jo, Joseph B Lim, Jeffery B Klauda, and Wonpil Im. Charmm-gui membrane builder for mixed bilayers and its application to yeast membranes. *Biophysical journal*, 97(1):50–58, 2009.

[84] Kalp in dppc tutorial, http://www.bevanlab.biochem.vt.edu/pages/personal /justin/gmx-tutorials/membrane_protein/03_solvate.html.

[85] Richard M Venable, Yuhong Zhang, Barry J Hardy, and Richard W Pastor. Molecular dynamics simulations of a lipid bilayer and of hexadecane: an investigation of membrane fluidity. *Science*, 262(5131):223–226, 1993.

[86] See-Wing Chiu, M Clark, V Balaji, Shankar Subramaniam, H Larry Scott, and Eric Jakobsson. Incorporation of surface tension into molecular dynamics simulation of an interface: a fluid phase lipid bilayer membrane. *Biophysical journal*, 69(4):1230–1245, 1995.

[87] Donna Bassolino-Klimas, Howard E Alper, and Terry R Stouch. Solute diffusion in lipid bilayer membranes: an atomic level study by molecular dynamics simulation. *Biochemistry*, 32(47):12624–12637, 1993.

[88] Jonathan N Sachs, Paul S Crozier, and Thomas B Woolf. Atomistic simulations of biologically realistic transmembrane potential gradients. *The Journal of chemical physics*, 121:10847–10851, 2004.

[89] Siewert J Marrink and Alan E Mark. The mechanism of vesicle fusion as revealed by molecular dynamics simulations. *Journal of the American Chemical Society*, 125(37):11144–11145, 2003.

[90] Chrystal D Bruce, Max L Berkowitz, Lalith Perera, and Malcolm DE Forbes. Molecular dynamics simulation of sodium dodecyl sulfate micelle in water: micellar structural characteristics and counterion distribution. *The Journal of Physical Chemistry B*, 106(15):3788–3793, 2002.

[91] Peter L Freddolino, Anton S Arkhipov, Steven B Larson, Alexander McPherson, and Klaus Schulten. Molecular dynamics simulations of the complete satellite tobacco mosaic virus. *Structure*, 14(3):437–449, 2006.

[92] B. R. Brooks, C. L. Brooks, III, A. D. Mackerell, Jr., L. Nilsson, R. J. Petrella, B. Roux, Y. Won, G. Archontis, C. Bartels, S. Boresch, A. Caflisch, L. Caves, Q. Cui, A. R. Dinner, M. Feig, S. Fischer, J. Gao, M. Hodoscek, W. Im, K. Kuczera, T. Lazaridis, J. Ma, V. Ovchinnikov, E. Paci, R. W. Pastor, C. B. Post, J. Z. Pu, M. Schaefer, B. Tidor, R. M. Venable, H. L.

Woodcock, X. Wu, W. Yang, D. M. York, and M. Karplus. CHARMM: The Biomolecular Simulation Program. *Journal of Computational Chemistry*, 30:1545–1614, 2009.

[93] NAMD Scalable Molecular Dynamics: http://www.ks.uiuc.edu/Research/namd/.

[94] Matteo Frigo and Steven G. Johnson. The design and implementation of FFTW3. *Proceedings of the IEEE*, 93(2):216–231, 2005. Special issue on "Program Generation, Optimization, and Platform Adaptation".

[95] Gcc, https://gcc.gnu.org/.

[96] William J Allen, Justin A Lemkul, and David R Bevan. Gridmat-md: A grid-based membrane analysis tool for use with molecular dynamics. *Journal of computational chemistry*, 30(12):1952–1958, 2009.

[97] Vytautas Gapsys, Bert L de Groot, and Rodolfo Briones. Computational analysis of local membrane properties. *Journal of computer-aided molecular design*, 27(10):845–858, 2013.

[98] Matthew Carr and Cait E. MacPhee. Membrainy: a 'smart', unified membrane analysis tool. *Source Code for Biology and Medicine*, (1):3+, March 2015.

[99] Christofer Hofsäß, Erik Lindahl, and Olle Edholm. Molecular dynamics simulations of phospholipid bilayers with cholesterol. *Biophysical Journal*, 84:2192–2206, April 2003.

[100] O. Berger, O. Edholm, and F. Jähnig. Molecular dynamics simulations of a fluid bilayer of dipalmitoylphosphatidylcholine at full hydration, constant pressure, and constant temperature. *Biophysical Journal*, 72:2002–2013, May 1997.

[101] R. M. Venable, Y. Zhang, B. J. Hardy, and R. W. Pastor. Molecular dynamics simulations of a lipid bilayer and of hexadecane: an investigation of membrane fluidity. *Science*, 262:223–226, October 1993.

[102] Joachim Seelig, Peter M. MacDonald, and Peter G. Scherer. Phospholipid head groups as sensors of electric charge in membranes. *Biochemistry*, 26:7535–7541, December 1987.

[103] Giulio Caracciolo, Daniela Pozzi, Heinz Amenitsch, and Ruggero Caminiti. Multicomponent cationic lipid dna complex formation: Role of lipid mixing. *Langmuir*, 21:11582–11587, November 2005.

[104] Carsten Kutzner, Helmut Grubmüller, Bert L. de Groot, and Ulrich Zachariae. Computational electrophysiology: The molecular dynamics of ion channel permeation and selectivity in atomistic detail. *Biophysical Journal*, 101:809–817, August 2011.

[105] Andrey A Gurtovenko and Ilpo Vattulainen. Pore formation coupled to ion transport through lipid membranes as induced by transmembrane ionic charge imbalance: atomistic molecular dynamics study. *Journal of the American Chemical Society*, 127(50):17570–17571, 2005.

[106] Shihu Wang and Ronald G Larson. Water channel formation and ion transport in linear and branched lipid bilayers. *Physical Chemistry Chemical Physics*, 16(16):7251–7262, 2014.

[107] Thomas Heimburg. The capacitance and electromechanical coupling of lipid membranes close to transitions. the effect of electrostriction. *Biophysical Journal*, 103:918–929, June 2012.

[108] Andrey A Gurtovenko and Ilpo Vattulainen. Molecular mechanism for lipid flip-flops. *The Journal of Physical Chemistry B*, 111(48):13554–13559, 2007.

[109] George S. Attard, Richard H. Templer, Wendy S. Smith, Alan N. Hunt, and Suzanne Jackowski. Modulation of ctp:phosphocholine cytidylyltransferase by membrane curvature elastic stress. *Proceedings of the National Academy of Sciences*, 97:9032–9036, August 2000.

[110] Louic S. Vermeer, Bert L. de Groot, Valérie Réat, Alain Milon, and Jerzy Czaplicki. Acyl chain order parameter profiles in phospholipid bilayers: computation from molecular dynamics simulations and comparison with 2h nmr experiments. *European biophysics journal : EBJ*, 36:919–931, November 2007.

[111] E Egberts and HJC Berendsen. Molecular dynamics simulation of a smectic liquid crystal with atomic detail. *The Journal of chemical physics*, 89:3718–3732, 1988.

[112] Lukas K. Tamm and Suren A. Tatulian. Infrared spectroscopy of proteins and peptides in lipid bilayers. *Quarterly Reviews of Biophysics*, 30:365–429, November 1997.

[113] Andrey A. Gurtovenko and Ilpo Vattulainen. Calculation of the electrostatic potential of lipid bilayers from molecular dynamics simulations: Methodological issues. *The Journal of Chemical Physics*, 130:215107, June 2009.

[114] Norbert Kučerka, Mu-Ping Nieh, and John Katsaras. Fluid phase lipid areas and bilayer thicknesses of commonly used phosphatidylcholines as a function of temperature. *Biochimica et Biophysica Acta (BBA)-Biomembranes*, 1808(11):2761–2771, 2011.

[115] Barbara A Lewis and Donald M Engelman. Lipid bilayer thickness varies linearly with acyl chain length in fluid phosphatidylcholine vesicles. *Journal of molecular biology*, 166(2):211–217, 1983.

[116] O Alvarez and R Latorre. Voltage-dependent capacitance in lipid bilayers made from monolayers. *Biophysical journal*, 21(1):1, 1978.

[117] Rainer A. Böckmann, Bert L. de Groot, Sergej Kakorin, Eberhard Neumann, and Helmut Grubmüller. Kinetics, Statistics, and Energetics of Lipid Membrane Electroporation Studied by Molecular Dynamics Simulations. *Biophysical Journal*, 95(4):1837–1850, August 2008.

[118] Horia I Petrache, Steven W Dodd, and Michael F Brown. Area per lipid and acyl length distributions in fluid phosphatidylcholines determined by¡ sup¿ 2¡/sup¿ h nmr spectroscopy. *Biophysical journal*, 79(6):3172–3192, 2000.

[119] RP Rand, Nola Fuller, VA Parsegian, and DC Rau. Variation in hydration forces between neutral phospholipid bilayers: evidence for hydration attraction. *Biochemistry*, 27(20):7711–7722, 1988.

[120] Christopher F Higgins. Flip-flop: the transmembrane translocation of lipids. *Cell*, 79:393–395, 1994.

[121] Philippe F Devaux and Alain Zachowski. Maintenance and consequences of membrane phospholipid asymmetry. *Chemistry and Physics of Lipids*, 73:107–120, 1994.

[122] JE Hall. Voltage-dependent lipid flip-flop induced by alamethicin. *Biophysical journal*, 33(3):373–381, 1981.

[123] Katsumi Matsuzaki, Osamu Murase, Nobutaka Fujii, and Koichiro Miyajima. An antimicrobial peptide, magainin 2, induced rapid flip-flop of phospholipids coupled with pore formation and peptide translocation. *Biochemistry*, 35(35):11361–11368, 1996.

[124] Antje Pokorny and Paulo FF Almeida. Kinetics of dye efflux and lipid flip-flop induced by δ-lysin in phosphatidylcholine vesicles and the mechanism of graded release by amphipathic, α-helical peptides. *Biochemistry*, 43(27):8846–8857, 2004.

[125] Elias Fattal, Shlomo Nir, Roberta A Parente, and Francis C Szoka Jr. Pore-forming peptides induce rapid phospholipid flip-flop in membranes. *Biochemistry*, 33(21):6721–6731, 1994.

[126] A Tardieu, Vittorio Luzzati, and FC Reman. Structure and polymorphism of the hydrocarbon chains of lipids: a study of lecithin-water phases. *Journal of molecular biology*, 75(4):711–733, 1973.

[127] VMD: Visual Molecular Dynamics, http://www.ks.uiuc.edu/Research/vmd/.

[128] The PyMOL molecular graphics system, version 1.3r1, http://www.pymol.org/.

[129] Gerard Stulen. Electric field effects on lipid membrane structure. *Biochimica et Biophysica Acta (BBA) - Biomembranes*, 640:621–627, February 1981.

[130] E. J. Dufourc, C. Mayer, J. Stohrer, G. Althoff, and G. Kothe. Dynamics of phosphate head groups in biomembranes. comprehensive analysis using phosphorus-31 nuclear magnetic resonance lineshape and relaxation time measurements. *Biophysical Journal*, 61:42–57, January 1992.

[131] Joachim Seelig, Hans-Ulrich Gally, and Roland Wohlgemuth. Orientation and flexibility of the choline head group in phosphatidylcholine bilayers. *Biochimica et Biophysica Acta (BBA) - Biomembranes*, 467:109–119, June 1977.

[132] Thomas Heimburg, Brigitta Angerstein, and Derek Marsh. Binding of peripheral proteins to mixed lipid membranes: effect of lipid demixing upon binding. *Biophysical journal*, 76(5):2575–2586, 1999.

[133] C Russ, T Heimburg, and HH von Grünberg. The effect of lipid demixing on the electrostatic interaction of planar membranes across a salt solution. *Biophysical journal*, 84(6):3730–3742, 2003.

[134] Galyna P Gorbenko, Valeriya M Trusova, Julian G Molotkovsky, and Paavo KJ Kinnunen. Cytochrome¡ i¿ c¡/i¿ induces lipid demixing in weakly charged phosphatidylcholine/phosphatidylglycerol model membranes as evidenced by resonance energy transfer. *Biochimica et Biophysica Acta (BBA)-Biomembranes*, 1788(6):1358–1365, 2009.

[135] Ryan S Davis, PB Sunil Kumar, Maria Maddalena Sperotto, and Mohamed Laradji. Predictions of phase separation in three-component lipid membranes by the martini force field. *The Journal of Physical Chemistry B*, 117(15):4072–4080, 2013.

[136] Davit Hakobyan and Andreas Heuer. Phase separation in a lipid/cholesterol system: comparison of coarse-grained and united-atom simulations. *The Journal of Physical Chemistry B*, 117(14):3841–3851, 2013.

[137] H Jelger Risselada and Siewert J Marrink. The molecular face of lipid rafts in model membranes. *Proceedings of the National Academy of Sciences*, 105(45):17367–17372, 2008.

[138] Giovanni B. Brandani, Marieke Schor, Cait E. MacPhee, Helmut Grubmüller, Ulrich Zachariae, and Davide Marenduzzo. Quantifying disorder through conditional entropy: An application to fluid mixing. *PLoS ONE*, 8:e65617, June 2013.

[139] Hans G Boman. Antibacterial peptides: key components needed in immunity. *Cell*, 65(2):205–207, 1991.

[140] Hans G Boman, Ingrid Faye, Gudmundur H Gudmundsson, Jong-Youn LEE, and Dan-Anders LIDHOLM. Cell-free immunity in cecropia. *European Journal of Biochemistry*, 201(1):23–31, 1991.

[141] Jong-Youn Lee, Anita Boman, CX Sun, Mats Andersson, Hans Jörnvall, Viktor Mutt, and Hans G Boman. Antibacterial peptides from pig intestine: isolation of a mammalian cecropin. *Proceedings of the National Academy of Sciences*, 86(23):9159–9162, 1989.

[142] David Wade, Anita Boman, B Wåhlin, CM Drain, David Andreu, Hans G Boman, and Ri B Merrifield. All-d amino acid-containing channel-forming antibiotic peptides. *Proceedings of the National Academy of Sciences*, 87(12):4761–4765, 1990.

[143] Burkhard Bechinger. Structure and functions of channel-forming peptides: magainins, cecropins, melittin and alamethicin. *Journal of Membrane Biology*, 156(3):197–211, 1997.

[144] Håkan Steiner. Secondary structure of the cecropins: antibacterial peptides from the moth¡ i¿ hyalophora cecropia¡/i¿. *FEBS letters*, 137(2):283–287, 1982.

[145] Hueih Min Chen, Wei Wang, David Smith, and Siu Chiu Chan. Effects of the anti-bacterial peptide cecropin b and its analogs, cecropins b-1 and b-2, on liposomes, bacteria, and cancer cells. *Biochimica et Biophysica Acta (BBA)-General Subjects*, 1336(2):171–179, 1997.

[146] Frank S Cordes, Joanne N Bright, and Mark SP Sansom. Proline-induced distortions of transmembrane helices. *Journal of molecular biology*, 323(5):951–960, 2002.

[147] Donghoon Oh, Song Yub Shin, Sangwon Lee, Joo Hyun Kang, Sun Don Kim, Pan Dong Ryu, Kyung-Soo Hahm, and Yangmee Kim. Role of the hinge region and the tryptophan residue in the synthetic antimicrobial peptides, cecropin a (1-8)-magainin 2 (1-12) and its analogues, on their antibiotic activities and structures. *Biochemistry*, 39(39):11855–11864, 2000.

[148] Wai-Ming Yau, William C Wimley, Klaus Gawrisch, and Stephen H White. The preference of tryptophan for membrane interfaces. *Biochemistry*, 37(42):14713–14718, 1998.

[149] FHC Crick. Is α-keratin a coiled coil? *Nature*, 170:882–883, 1952.

[150] Ingo Schwaiger, Clara Sattler, Daniel R Hostetter, and Matthias Rief. The myosin coiled-coil is a truly elastic protein structure. *Nature materials*, 1(4):232–235, 2002.

[151] D. S. Goodsell. Kinesin, http://dx.doi.org/10.2210/rcsb_pdb/mom_2005_4. *RCSB Protein Data Bank*, April 2005.

[152] Derek N Woolfson. The design of coiled-coil structures and assemblies. *Advances in protein chemistry*, 70:79–112, 2005.

[153] Erin K O'Shea, Kevin J Lumb, and Peter S Kim. Peptide velcro: design of a heterodimeric coiled coil. *Current Biology*, 3(10):658–667, 1993.

[154] Carolyn Cohen and David AD Parry. α-helical coiled coils and bundles: how to design an α-helical protein. *Proteins: Structure, Function, and Bioinformatics*, 7(1):1–15, 1990.

[155] Derek N Woolfson and Tom Alber. Predicting oligomerization states of coiled coils. *Protein Science*, 4:1596–1607, 1995.

[156] Andrei Lupas, Marc Van Dyke, Jeff Stock, et al. Predicting coiled coils from protein sequences. *Science*, 252:1162–1164, 1991.

[157] Dennis A Benson, Ilene Karsch-Mizrachi, David J Lipman, James Ostell, and David L Wheeler. Genbank. *Nucleic acids research*, 33:D34–D38, 2005.

[158] Maxim G Ryadnov, Galina V Mukamolova, Ayman S Hawrani, James Spencer, and Roscoe Platt. Re coil: An antimicrobial peptide regulator. *Angewandte Chemie International Edition*, 48(51):9676–9679, 2009.

[159] Michael R Yeaman and Nannette Y Yount. Mechanisms of antimicrobial peptide action and resistance. *Pharmacological reviews*, 55(1):27–55, 2003.

[160] Lloyd Ryan, Baptiste Lamarre, Ting Diu, Jascindra Ravi, Peter J Judge, Adam Temple, Matthew Carr, Eleonora Cerasoli, Bo Su, Howard F Jenkinson, et al. Anti-antimicrobial peptides folding-mediated host defense antagonists. *Journal of Biological Chemistry*, 288(28):20162–20172, 2013.

[161] C. Schwieters. The Xplor-NIH NMR molecular structure determination package. *Journal of Magnetic Resonance*, 160(1):65–73, January 2003.

[162] Charles D. Schwieters, John J. Kuszewski, and G. Marius Clore. Using Xplor-NIH for NMR Molecular Structure Determination. *ChemInform*, 37(44):no, 2006.

[163] Kresten Lindorff-Larsen, Stefano Piana, Kim Palmo, Paul Maragakis, John L. Klepeis, Ron O. Dror, and David E. Shaw. Improved side-chain torsion potentials for the Amber ff99SB protein force field. *Proteins*, 78(8):1950–1958, June 2010.

[164] Viktor Hornak, Robert Abel, Asim Okur, Bentley Strockbine, Adrian Roitberg, and Carlos Simmerling. Comparison of multiple amber force fields and development of improved protein backbone parameters. *Proteins: Structure, Function, and Bioinformatics*, 65(3):712–725, 2006.

[165] Stefano Piana, Kresten Lindorff-Larsen, and David E Shaw. How robust are protein folding simulations with respect to force field parameterization? *Biophysical journal*, 100(9):L47–L49, 2011.

[166] Peter L Freddolino, Sanghyun Park, Benoît Roux, and Klaus Schulten. Force field bias in protein folding simulations. *Biophysical journal*, 96(9):3772–3780, 2009.

[167] David C Chan, Christine T Chutkowski, and Peter S Kim. Evidence that a prominent cavity in the coiled coil of hiv type 1 gp41 is an attractive drug target. *Proceedings of the National Academy of Sciences*, 95(26):15613–15617, 1998.

[168] James F Conway and David AD Parry. Intermediate filament structure: 3. analysis of sequence homologies. *International Journal of Biological Macromolecules*, 10(2):79–98, 1988.

[169] Bonnie Berger, David B Wilson, Ethan Wolf, Theodore Tonchev, Maria Milla, and Peter S Kim. Predicting coiled coils by use of pairwise residue correlations. *Proceedings of the National Academy of Sciences*, 92(18):8259–8263, 1995.

[170] Angel Pineiro, Alessandra Villa, Toni Vagt, Beate Koksch, and Alan E Mark. A molecular dynamics study of the formation, stability, and oligomerization state of two designed coiled coils: possibilities and limitations. *Biophysical journal*, 89(6):3701–3713, 2005.

[171] Francis HC Crick. The packing of-helices: simple coiled-coils. *Acta crystallographica*, 6(8-9):689–697, 1953.

[172] Martha G Oakley and Jessica J Hollenbeck. The design of antiparallel coiled coils. *Current opinion in structural biology*, 11(4):450–457, 2001.

[173] Robert L Baldwin. How hofmeister ion interactions affect protein stability. *Biophysical Journal*, 71(4):2056–2063, 1996.

[174] Rainer A Böckmann, Agnieszka Hac, Thomas Heimburg, and Helmut Grubmüller. Effect of sodium chloride on a lipid bilayer. *Biophysical journal*, 85(3):1647–1655, 2003.

[175] Ilian Jelesarov, Eberhard Dürr, Richard M Thomas, and Hans Rudolf Bosshard. Salt effects on hydrophobic interaction and charge screening in the folding of a negatively charged peptide to a coiled coil (leucine zipper). *Biochemistry*, 37(20):7539–7550, 1998.

[176] Enrico Brandenburg, Hans von Berlepsch, Ulla IM Gerling, Christoph Böttcher, and Beate Koksch. Inhibition of amyloid aggregation by formation of helical assemblies. *Chemistry-A European Journal*, 17(38):10651–10661, 2011.

[177] Elisabetta Bianchi, Marco Finotto, Paolo Ingallinella, Renee Hrin, Anthony V Carella, Xiaoli S Hou, William A Schleif, Michael D Miller, Romas Geleziunas, and Antonello Pessi. Covalent stabilization of coiled coils of the hiv gp41 n region yields extremely potent and broad inhibitors

of viral infection. *Proceedings of the National Academy of Sciences of the United States of America*, 102(36):12903–12908, 2005.

[178] Daniel Lamb, AW Schuttelkopf, DM Van Aalten, and David W Brighty. Highly specific inhibition of leukaemia virus membrane fusion by interaction of peptide antagonists with a conserved region of the coiled coil of envelope. *Retrovirology*, 5(1):70, 2008.

[179] Joe Lutkenhaus. Assembly dynamics of the bacterial mincde system and spatial regulation of the z ring. *Annu. Rev. Biochem.*, 76:539–562, 2007.

[180] William Margolin. Ftsz and the division of prokaryotic cells and organelles. *Nature Reviews Molecular Cell Biology*, 6(11):862–871, 2005.

[181] Tim H Szeto, Susan L Rowland, Cheryl L Habrukowich, and Glenn F King. The mind membrane targeting sequence is a transplantable lipid-binding helix. *Journal of Biological Chemistry*, 278(41):40050–40056, 2003.

[182] Henrik Strahl and Leendert W Hamoen. Membrane potential is important for bacterial cell division. *Proceedings of the National Academy of Sciences*, 107(27):12281–12286, 2010.

[183] Takashi Katsu, Tomofusa Tsuchiya, and Yuzaburo Fujita. Dissipation of membrane potential of escherichia coli cells induced by macromolecular polylysine. *Biochemical and biophysical research communications*, 122(1):401–406, 1984.

[184] Joel M Kralj, Daniel R Hochbaum, Adam D Douglass, and Adam E Cohen. Electrical spiking in escherichia coli probed with a fluorescent voltage-indicating protein. *Science*, 333(6040):345–348, 2011.

[185] Shirley Mazor, Tomer Regev, Eugenia Mileykovskaya, William Margolin, William Dowhan, and Itzhak Fishov. Mutual effects of mind-membrane interaction: Ii. domain structure of the membrane enhances mind binding. *Biochimica et Biophysica Acta (BBA)-Biomembranes*, 1778(11):2505–2511, 2008.

[186] Julian G Hurdle, Alex J O'Neill, Ian Chopra, and Richard E Lee. Targeting bacterial membrane function: an underexploited mechanism for treating persistent infections. *Nature Reviews Microbiology*, 9(1):62–75, 2010.

[187] JL Gifford, HN Hunter, and HJ Vogel. Lactoferricin. *Cellular and molecular life sciences*, 62(22):2588–2598, 2005.

[188] LilyAnn Jeu and Horatio B Fung. Daptomycin: a cyclic lipopeptide antimicrobial agent. *Clinical therapeutics*, 26(11):1728–1757, 2004.

[189] E Schäffer and U Thiele. Dynamic domain formation in membranes: thickness-modulation-induced phase separation. *The European Physical Journal E: Soft Matter and Biological Physics*, 14(2):169–175, 2004.

[190] Guillaume Drin, Jean-François Casella, Romain Gautier, Thomas Boehmer, Thomas U Schwartz, and Bruno Antonny. A general amphipathic α-helical motif for sensing membrane curvature. *Nature structural & molecular biology*, 14(2):138–146, 2007.

[191] Bruno Antonny. Mechanisms of membrane curvature sensing. *Annual review of biochemistry*, 80:101–123, 2011.

[192] Assaf Zemel, Avinoam Ben-Shaul, and Sylvio May. Modulation of the spontaneous curvature and bending rigidity of lipid membranes by interfacially adsorbed amphipathic peptides. *The Journal of Physical Chemistry B*, 112(23):6988–6996, 2008.

[193] Toshihiko Takenobu, Kazuhito Tomizawa, Masayuki Matsushita, Sheng-Tian Li, Akiyoshi Moriwaki, Yun-Fei Lu, and Hideki Matsui. Development of p53 protein transduction therapy using membrane-permeable peptides and the application to oral cancer cells. *Molecular cancer therapeutics*, 1(12):1043–1049, 2002.

[194] May C Morris, Julien Depollier, Jean Mery, Frederic Heitz, and Gilles Divita. A peptide carrier for the delivery of biologically active proteins into mammalian cells. *Nature biotechnology*, 19(12):1173–1176, 2001.

[195] HM Seeger, G Marino, A Alessandrini, and P Facci. Effect of physical parameters on the main phase transition of supported lipid bilayers. *Biophysical journal*, 97(4):1067–1076, 2009.

[196] James C Weaver and Yu A Chizmadzhev. Theory of electroporation: a review. *Bioelectrochemistry and bioenergetics*, 41(2):135–160, 1996.

[197] C Chen, SW Smye, MP Robinson, and JA Evans. Membrane electroporation theories: a review. *Medical and Biological Engineering and Computing*, 44(1-2):5–14, 2006.

[198] Jill Glasspool-Malone, Stella Somiari, Joseph J Drabick, and Robert W Malone. Efficient nonviral cutaneous transfection. *Molecular Therapy*, 2(2):140–146, 2000.

[199] Joseph J Drabick, Jill Glasspool-Malone, Stella Somiari, Alan King, and Robert W Malone. Cutaneous transfection and immune responses to intradermal nucleic acid vaccination are significantly enhanced by in vivo electropermeabilization. *Molecular Therapy*, 3(2):249–255, 2001.

[200] Michel Belehradek, Christian Domenge, Bernard Luboinski, Stéphane Orlowski, Jean Belehradek, and Lluis M Mir. Electrochemotherapy, a new antitumor treatment. first clinical phase i-ii trial. *Cancer*, 72(12):3694–3700, 1993.

[201] Lluis M Mir, Stephen Orlowski, J Belehradek Jr, J Teissie, MP Rols, G Serša, D Miklavčič, R Gilbert, and R Heller. Biomedical applications

of electric pulses with special emphasis on antitumor electrochemotherapy. *Bioelectrochemistry and Bioenergetics*, 38(1):203–207, 1995.

[202] Tian Y Tsong. Electroporation of cell membranes. *Biophysical journal*, 60(2):297–306, 1991.

[203] D Peter Tieleman. The molecular basis of electroporation. *BMC biochemistry*, 5(1):10, 2004.

[204] D Peter Tieleman, Hari Leontiadou, Alan E Mark, and Siewert-Jan Marrink. Simulation of pore formation in lipid bilayers by mechanical stress and electric fields. *Journal of the American Chemical Society*, 125(21):6382–6383, 2003.

[205] Andrey A. Gurtovenko and Ilpo Vattulainen. Pore Formation Coupled to Ion Transport through Lipid Membranes as Induced by Transmembrane Ionic Charge Imbalance: Atomistic Molecular Dynamics Study. *J. Am. Chem. Soc.*, 127(50):17570–17571, November 2005.

[206] M Casciola, D Bonhenry, M Liberti, F Apollonio, and M Tarek. A molecular dynamic study of cholesterol rich lipid membranes: comparison of electroporation protocols. *Bioelectrochemistry*, 2014.

[207] Andrey A Gurtovenko and Anastasia S Lyulina. Electroporation of asymmetric phospholipid membranes. *The Journal of Physical Chemistry B*, 118(33):9909–9918, 2014.

[208] Ramon Reigada. Electroporation of heterogeneous lipid membranes. *Biochimica et Biophysica Acta (BBA)-Biomembranes*, 1838(3):814–821, 2014.

[209] Andraž Polak, Daniel Bonhenry, François Dehez, Peter Kramar, Damijan Miklavčič, and Mounir Tarek. On the electroporation thresholds of lipid bilayers: molecular dynamics simulation investigations. *The Journal of membrane biology*, 246(11):843–850, 2013.

[210] Maria Miteva, Mats Andersson, Andrey Karshikoff, and Gottfried Otting. Molecular electroporation: a unifying concept for the description of membrane pore formation by antibacterial peptides, exemplified with nk-lysin. *FEBS letters*, 462(1):155–158, 1999.

[211] Andrey A Gurtovenko and Ilpo Vattulainen. Calculation of the electrostatic potential of lipid bilayers from molecular dynamics simulations: Methodological issues. *The Journal of chemical physics*, 130(21):215107, 2009.

[212] Andrey A Gurtovenko and Ilpo Vattulainen. Membrane potential and electrostatics of phospholipid bilayers with asymmetric transmembrane distribution of anionic lipids. *The Journal of Physical Chemistry B*, 112(15):4629–4634, 2008.

[213] Hans Binder and Göran Lindblom. Charge-dependent translocation of the trojan peptide penetratin across lipid membranes. *Biophysical journal*, 85(2):982–995, 2003.

[214] Jehangir S Wadia and Steven F Dowdy. Transmembrane delivery of protein and peptide drugs by tat-mediated transduction in the treatment of cancer. *Advanced drug delivery reviews*, 57(4):579–596, 2005.

[215] Paul A Wender, Dennis J Mitchell, Kanaka Pattabiraman, Erin T Pelkey, Lawrence Steinman, and Jonathan B Rothbard. The design, synthesis, and evaluation of molecules that enable or enhance cellular uptake: peptoid molecular transporters. *Proceedings of the National Academy of Sciences*, 97(24):13003–13008, 2000.

[216] Stephen M. Kennedy, Erik J. Aiken, Kaytlyn A. Beres, Adam R. Hahn, Samantha J. Kamin, Susan C. Hagness, John H. Booske, and William L. Murphy. Cationic peptide exposure enhances pulsed-electric-field-mediated membrane disruption. *PLoS ONE*, 9(3):e92528, 03 2014.

[217] Yigong Ge, Dorothy L MacDonald, Kenneth J Holroyd, Clyde Thornsberry, Hannah Wexler, and Michael Zasloff. In vitro antibacterial properties of pexiganan, an analog of magainin. *Antimicrobial agents and chemotherapy*, 43(4):782–788, 1999.

[218] Michael Zasloff, Brian Martin, and Hao-Chia Chen. Antimicrobial activity of synthetic magainin peptides and several analogues. *Proceedings of the National Academy of Sciences*, 85(3):910–913, 1988.

[219] Hao-Chia Chen, Judith H Brown, John L Morell, and CM Huang. Synthetic magainin analogues with improved antimicrobial activity. *Febs Letters*, 236(2):462–466, 1988.

[220] Katsumi Matsuzaki, Ken-ichi Sugishita, Mitsunori Harada, Nobutaka Fujii, and Koichiro Miyajima. Interactions of an antimicrobial peptide, magainin 2, with outer and inner membranes of gram-negative bacteria. *Biochimica et Biophysica Acta (BBA)-Biomembranes*, 1327(1):119–130, 1997.

[221] Julio H Cuervo, B Rodriguez, and RA Houghten. The magainins: sequence factors relevant to increased antimicrobial activity and decreased hemolytic activity. *Peptide research*, 1(2):81–86, 1987.

[222] Roberto Bessalle, H Haas, A Goria, I Shalit, and M Fridkin. Augmentation of the antibacterial activity of magainin by positive-charge chain extension. *Antimicrobial agents and chemotherapy*, 36(2):313–317, 1992.

[223] Kevin J Hallock, Dong-Kuk Lee, and A Ramamoorthy. Msi-78, an analogue of the magainin antimicrobial peptides, disrupts lipid bilayer structure via positive curvature strain. *Biophysical journal*, 84(5):3052–3060, 2003.

[224] Shoji Shima, HIROYOSHI Matsuoka, TOSHIRO Iwamoto, and HEIICHI Sakai. Antimicrobial action of epsilon-poly-l-lysine. *The Journal of antibiotics*, 37(11):1449–1455, 1984.

[225] Chun Li, Dong-Fang Yu, Robert A Newman, Fernando Cabral, L Clifton Stephens, Nancy Hunter, Luka Milas, and Sidney Wallace. Complete regression of well-established tumors using a novel water-soluble poly (l-glutamic acid)-paclitaxel conjugate. *Cancer research*, 58(11):2404–2409, 1998.

[226] Xin Wang, Tomofumi Uto, Takami Akagi, Mitsuru Akashi, and Masanori Baba. Poly (γ-glutamic acid) nanoparticles as an efficient antigen delivery and adjuvant system: Potential for an aids vaccine. *Journal of medical virology*, 80(1):11–19, 2008.

[227] Julien Michel, Elizabeth A Harker, Julian Tirado-Rives, William L Jorgensen, and Alanna Schepartz. In silico improvement of β3-peptide inhibitors of p53 hdm2 and p53 hdmx. *Journal of the American Chemical Society*, 131(18):6356–6357, 2009.

Carr and MacPhee *Source Code for Biology and Medicine* _####################_
DOI 10.1186/s13029-015-0033-7

SOURCE CODE FOR
BIOLOGY AND MEDICINE

SOFTWARE Open Access

Membrainy: a 'smart', unified membrane analysis tool

Matthew Carr and Cait E MacPhee*

Abstract

Background: The study of biological membranes using Molecular Dynamics has become an increasingly popular means by which to investigate the interactions of proteins, peptides and potentials with lipid bilayers. These interactions often result in changes to the properties of the lipids which can modify the behaviour of the membrane. Membrainy is a unified membrane analysis tool that contains a broad spectrum of analytical techniques to enable: measurement of acyl chain order parameters; presentation of 2D surface and thickness maps; determination of lateral and axial headgroup orientations; measurement of bilayer and leaflet thickness; analysis of the annular shell surrounding membrane-embedded objects; quantification of gel percentage; time evolution of the transmembrane voltage; area per lipid calculations; and quantification of lipid mixing/demixing entropy.

Results: Each analytical component within Membrainy has been tested on a variety of lipid bilayer systems and was found to be either comparable to or an improvement upon existing software. For the analytical techniques that have no direct comparable software, our results were confirmed with experimental data.

Conclusions: Membrainy is a user-friendly, intelligent membrane analysis tool that automatically interprets a variety of input formats and force fields, is compatible with both single and double bilayers, and capable of handling asymmetric bilayers and lipid flip-flopping. Membrainy has been designed for ease of use, requiring no installation or configuration and minimal user-input to operate.

Keywords: Molecular dynamics, Membrane analysis, Order parameters, Headgroup orientations, Mixing/Demixing entropy, Bilayer/Leaflet thickness, Area per lipid, Double bilayer, Asymmetric bilayer, Lipid flip-flopping

Background

The cell membrane plays a crucial role in many biological systems, not only as a container for intracellular contents but also as an osmotic barrier, a platform for transmembrane proteins and fusion events, a means for maintenance of chemical and electrostatic potentials, and a barrier for drug and antibody delivery into the cell [1]. Cell membranes are primarily composed of phospholipids arranged in a bilayer and have been studied heavily with a host of experimental techniques including nuclear magnetic resonance, electron paramagnetic resonance and electron microscopy [2-5]. Recent developments in lipid force field parameters have lead to a wide range of molecular dynamics (MD) studies involving lipid bilayers which aim to improve the spatial and temporal resolution over existing experimental techniques [6]. In many of these studies, the membrane can be seen as a dynamic system that changes in response to environmental perturbations. Understanding the behaviour of the lipids can be crucial to understanding the behaviour of the system, e.g. to understand why certain amphipathic peptides prefer to insert into fluid or curved regions of the membrane [7,8], or to understand the effect a membrane-embedded object has on the mechanical properties of the surrounding lipids [9]. An improved understanding of the lipid behaviour in response to environmental perturbations may lead to advances such as improved drug design and delivery into the cell [10].

There are several tools freely available to analyse individual components of the membrane such as its thickness, curvature, area per lipid, or acyl chain order parameters [11-13]; however, we were unable to locate tools that provide measurements of other membrane properties such as headgroup orientations, gel/fluid ratios,

*Correspondence: Cait.Macphee@ed.ac.uk
Institute for Condensed Matter and Complex Systems, School of Physics and Astronomy, The University of Edinburgh, Mayfield Road, Edinburgh, UK

lipid mixing/demixing entropy, etc. Furthermore, many of these existing tools are targeted towards the experienced user, requiring complicated installations and configuration files to operate. Existing platforms for the creation of analytical tools such as MDTraj [14] and MDAnalysis [15] rely on the installation of additional packages to operate and as such may be problematic for non-Linux users.

We present Membrainy, an intelligent membrane analysis tool that endeavours to provide both the inexperienced and experienced user access to a wide range of analytical techniques to enable the measurement of various membrane-specific properties from planar bilayer trajectories. Membrainy was designed for simplicity and ease of use, requiring no compilation and minimal user-input to operate. As the range of lipid bilayer studies is broad, Membrainy was designed to automatically interpret a variety of bilayer compositions and force fields, and is capable of interpreting single, double and asymmetric bilayers. Membrainy can interpret dynamic membranes that undergo structural changes such as lipid flip-flopping, and employs different analytical approaches when switching between atomistic, united-atom or coarse grained force fields. A suite of analytical techniques is integrated within Membrainy. Acyl chain order parameters quantify the degree of order in the lipid tails, a measure often associated with lipid fluidity [16-18]. Headgroup orientations provide a measurement of the angles observed in the lipid headgroup relative to the membrane surface, and have been shown to be sensitive to electric charges and dipole fields [19]. Lipid mixing/demixing entropy is a quantification of the level of mixing between two or more lipid types, which plays an important role in a wide variety of cellular functions including DNA fusion and phase transitions [20]. The transmembrane voltage (TMV) across a double bilayer can be measured over time, and may be of particular importance in electrophysiology or electroporation simulations [21-23]. Generation of surface maps provide a high resolution 2D representation of the bilayer surface and is particularly helpful when looking at defects, undulations and gel clusters that may not be easily observable in 3D visualisation software. Gel percentages quantify the fluidity of the bilayer by measuring the linearity of the lipid tails. Measurements of leaflet and membrane thickness may be of importance in simulations where bilayers undergo electrostriction [24]. The detection and measurement of lipid flip-flopping may be useful in bilayers containing transient water pores [25]. Finally, the ability to perform a separate analysis on the annular shell of lipids surrounding molecules, whether inserted or in close contact with the membrane surface, may be helpful in understanding how these molecules affect the local properties of the membrane, such as changes in lipid tail flexibility [26].

Implementation

Membrainy has been written in Java, which provides maximum compatibility across a range of operating systems, requires no compilation and enables the safe and efficient execution of multithreaded code. Membrainy contains various multithreaded algorithms to optimise efficiency and processor use across a range of architectures. These include algorithms for using multiple threads to load larger trajectory files, for preloading the next frame in the trajectory while the current frame is being analysed, and for running each analytical technique in parallel. Membrainy has been primarily designed for use with the GROMACS MD package [13], and contains a user interface that should be intuitive to GROMACS users. Membrainy is capable of reading GROMACS xtc, trr, tpr, cpt and gro trajectory file types, along with the standard pdb trajectory file type used by other MD packages (e.g. AMBER [27], CHARMM [28], NAMD [29], etc.). Membrainy has been implemented with the CHARMM36 [30], Berger/GROMOS87 [31] and Martini v2.0 [32] force fields, and is expandable to include other force fields and trajectory formats. Asymmetric bilayers and lipid flip-flops are detected by assigning each lipid to a corresponding leaflet depending on the height of its phosphorous atom relative to the geometric centre of the bilayer. All output graphs are readable by the Grace plotting software [33] and are preprogrammed with appropriate axis labels and titles. Double bilayer systems are automatically detected and incur additional output plots which contain averages of the inner and outer leaflets for certain analytical techniques.

Order parameters

Order parameters for saturated and unsaturated lipid tails in atomistic force fields are calculated from the equation

$$S_{CD} = \left\langle \frac{3cos^2\theta - 1}{2} \right\rangle \quad (1)$$

where θ is the angle the C−H bond vectors along the lipid tails make with the membrane normal [34], taken as the z-axis for planar bilayers. This approach utilises each individual C−H bond in the lipid tails. As united-atom force fields lack non-polar hydrogen atoms, the above equation is modified to include the relation

$$S_{CD} = \frac{2}{3}S_{xx} + \frac{1}{3}S_{yy} \quad (2)$$

which is derived from the order parameter tensor [35], and achieved by defining molecular axes where the z-axis encompasses the C_{i-1}−C_{i+1} vector, the y-axis lies on the plane containing C_{i-1}−C_i−C_{i+1}, and the x-axis is orthogonal to the y and z axes. The angles that the x and y axes make with the membrane normal is then

used to determine S_{xx} and S_{yy} from Eqn. 1. Martini order parameters are calculated from the equation

$$P_2 = \frac{1}{2}\left(3\,cos^2\,\langle\theta\rangle - 1\right) \quad (3)$$

where θ is the angle between the lipid tail bonds and the membrane normal.

The final order parameter for each technique is averaged over all leaflets in the system, and Membrainy will also produce separate order parameters for each lipid type and leaflet. For atomistic and united-atom force fields, Membrainy plots the values of $-S_{CD}$ for each carbon along the lipid tails. This experiences maximum order at 0.5 and disorder at -1, whereas the Martini force field experiences maximum order at $P_2 = 1$ and disorder at $P_2 = -0.5$. Membrainy can also produce histograms of the angles measured by each technique. To maximise performance, the order parameter algorithms are multithreaded, where each lipid tail type (e.g. POPE-palmitoyl, POPE-oleoyl, etc.) is assigned its own thread, allowing much of the analysis to be conducted in parallel.

Headgroup orientations

Membrainy calculates lateral and axial headgroup orientations, producing a histogram for each lipid type. The lateral angles are calculated by establishing a headgroup vector from two reference atoms, one being the phosphorous atom and the other being another atom on the headgroup. This vector is then projected onto the membrane normal to produce an angle. The histograms are plotted in the range -90 to 90 degrees, where a value of 0 indicates the headgroup is parallel to the membrane surface and positive angles indicate the headgroup is pointing away from the membrane. Axial angles are calculated by projecting the headgroup vector onto the membrane surface, taken as the xy plane, to produce a radial angle between 0 and 2π. Each axial angle is plotted for each lipid over time. This algorithm has been multithreaded, where each lipid type is assigned its own thread and run in parallel.

2D surface maps

The membrane surface can be represented in a 2D map by binning the heights of each atom in each leaflet into a 2D lattice and applying the Gauss-Seidel method

$$\phi_{i,j}^{n+1} = -\frac{1}{4}\left[A_{i,j} - \left(\phi_{i-1,j}^{n} + \phi_{i+1,j}^{n} + \phi_{i,j-1}^{n} + \phi_{i,j+1}^{n}\right)\right] \quad (4)$$

where $A_{i,j}$ is the highest atom in cell i, j, $\phi_{i,j}^{n+1}$ is the resulting scalar value produced by the method, and the final term is the sum of the neighbouring cells' scalar values. Iterating over this method produces a scalar field of successive displacement, generating a series of Gaussians that can be scaled and mapped to a colour to produce a contour map of the leaflet surface. These maps also behave as density maps, producing more prominent Gaussians in regions of the lattice containing a high density of atoms, such as lipid tails in the gel phase. The scalar field is colour-coded such that blue regions indicate thin or sparsely populated regions of the leaflet, red indicates thick or densely populated regions, with green between the two. Black areas represent a hole or pore in the leaflet, which is identified by unpopulated regions of the lattice. A map for each leaflet is displayed through a graphical interface in real-time and can be saved as an image. Membrainy will also overlay the positions of molecules and ions on the maps. As iterative approaches can be computationally expensive, each leaflet is assigned its own thread allowing the maps to be generated in parallel.

Leaflet/membrane thickness, area per lipid and gel percentage

Membrane thickness is determined by calculating the average height of a user-specified reference atom, typically the phosphorous atom, for each leaflet. The average height of the reference atom for two opposing leaflets can then be subtracted. Leaflet thickness is calculated by subtracting the average height of the reference atom with the geometric centre of the bilayer. A 2D thickness map can also be produced by binning the reference atoms into a 2D lattice and applying the same algorithm used by the 2D surface maps. Membrainy offers a simple area per lipid (APL) calculation by dividing the box area by the number of lipids per leaflet, and will automatically produce multiple APLs for asymmetric bilayers or when lipid flip-flopping is detected. Gel percentages can be approximated by comparing the force field distance between the first and last carbon atoms in the lipid tails with the distance found in the trajectory files. As fluid lipid tails are non-linear, this distance is typically much less than the force field distance. A user-specified tolerance is assigned to the force field distance, and any lipid with a trajectory distance above this tolerance is counted as a 'gel' lipid.

Annular shell analysis

Membrainy isolates the annular shell of lipids around molecules by calculating a distance vector between each atom in the bilayer with each atom in the molecule. If the distance between any two atoms is within a user-specified radius, the lipid is counted as being within the shell. These lipids can then be analysed to determine their properties. A control group can also be established by selecting random lipids outside of the shell from the same leaflet, comprising either a fixed number of lipids, an identical number of lipids to those found within the shell or all lipids outside of the shell. An option exists to exclude gel lipids from the control group, as many proteins

and peptides are known to show selectivity for inserting into fluid regions [36]. Gel lipids are identified using the same technique described above. If multiple molecules are present, the user may specify one, several or all molecules to construct annular shells for, and Membrainy will assign a thread to each molecule, populating the shells in parallel. The output plots contain an average of all shells in the system. Membrainy is also fitted with an annular shell analysis algorithm to produce detailed records of which lipids occupy the shell at any given time and which lipids spent the longest time in the shell. In mixed bilayer compositions, Membrainy will plot the ratio of lipid types found within the shell over time.

Evolution of the TMV

In double bilayer systems, the TMV can be extrapolated from the average electrostatic potential between the two bilayers, which is calculated from a double integral of Poisson's equation

$$\Psi(z) = -\frac{1}{\varepsilon_0}\int_0^z dz' \int_0^{z'} \rho\left(z''\right) dz'' \tag{5}$$

and is achieved by splitting the simulation box into 'slices' along the z-axis and calculating the charge density in each slice [37]. The box is then corrected such that $\Psi(0) = 0$. Membrainy utilises the GROMACS tool `g_potential` by splitting the full trajectory into smaller trajectories and calculating the electrostatic potential in each trajectory. The TMV can then be extrapolated from each smaller trajectory and recombined to produce a voltage against time measurement over the full trajectory.

Lipid mixing/demixing entropy

Membranes containing two or more lipid types can have their lipid mixing/demixing quantified as an entropy with the equation

$$S(x_1,..,x_N) = N \sum_{x_i,nb_i} p(x_i, nb_i)\ log\ p(x_i \mid nb_i) \tag{6}$$

as described by Brandani et al. [38], where $p(x_i, nb_i)$ is the probability to find a lipid of type x_i neighboured to a lipid of type nb_i, and $p(x_i \mid nb_i)$ indicates the conditional probability that a lipid is of type x_i given that its neighbour is of type nb_i. To calculate the entropy, a distance vector is established between the phosphorous atoms on each lipid in a leaflet to determine the nearest neighbouring lipid and its type. This information is then binned into a probability matrix and normalised such that the total probability is always 1, and then used with Eqn. 6 to produce an entropy. A theoretical maximum entropy can be calculated from

$$S_{max} = -\sum \rho_{x_i}\ log\ \rho_{x_i} \tag{7}$$

where ρ_{x_i} is the density of a lipid of type x_i. A scaled entropy is also produced such that $S_{max} = 1$.

Results and discussion

Membrainy was tested on Linux 64-bit machines containing 2-8 cores on a selection of single and double bilayer trajectories employing the CHARMM, GROMOS and Martini force fields. Where appropriate, results were compared with either existing software, experimental values, or judged for logical consistency.

Order parameters

Order parameters are a measure of the level of order or entropy in the lipid tails and can give insight into the fluidity of the membrane, as gel lipids exhibit a greater degree of order over fluid lipids. Membrainy was used to generate order parameters for various bilayer compositions, which found saturated lipid tails to be comparable to those produced by the GROMACS tool `g_order` in the CHARMM and GROMOS force fields. For bilayers employing the CHARMM force field, Membrainy yields more accurate order parameters to `g_order` by utilising each C−H bond vector, whereas `g_order` ignores these vectors and instead reconstructs them from the C_{i-1}−C_{i+1} vector in a similar approach used by Membrainy with united-atom force fields. The order parameters for unsaturated lipids were also comparable, excluding the region around the double bond in which `g_order` calculates incorrectly. Membrainy automatically generates the necessary lipid tail information required to calculate order parameters, requiring no user-input. This is a significant improvement over `g_order` which requires a lengthy setup of user-constructed index files. This also restricts the order parameter analysis to a fixed number of lipids and as such it would be difficult to conduct an annular shell analysis with `g_order`.

Annular shell analysis

The properties of the lipids in close proximity to other molecules, whether inserted or in close contact with the membrane surface, may be modified by the presence of such molecules and result in local changes to the membrane. Membrainy isolates an annular shell of lipids surrounding a peptide, protein or other molecule, and compares its properties to lipids outside of the shell. As an exemplar, we inserted the MinD membrane targeting sequence (MinD-MTS) into the headgroup region of a POPE/POPG (3:1) double bilayer. This peptide is an 11-residue cationic amphipathic helix located at the C-terminus of the MinD protein that plays an important role in the cell division of *Bacillus subtilis* [39]. Using a shell radius of 4 Å, the order parameters of the lipids located within the shell were analysed over 50 ns and compared with a control group, comprising an identical

number of lipids selected randomly from outside of the shell within the same leaflet. The order parameters reveal an increase in disorder for lipid tails within the shell when compared to those outside of the shell (Figure 1), which suggests the presence of splayed lipid tails. This phenomenon has previously been predicted for amphipathic peptides inserted into the headgroup region of lipid bilayers [26]. The option to ignore all gel lipids from the control group was enabled as our chosen peptide had inserted into a fluid region of the bilayer that contained ~27% gel at 300 K. Without this option, the control group was observed to sample a more ordered phase of lipids, providing an inaccurate comparison with the fluid lipids found within the shell. The annular shell analysis algorithm revealed that lipids were continuously entering and exiting the shell, and saw approximately 10-14 lipids occupy the shell at any given time. Membrainy can also determine lipid type ratios within the shell for mixed bilayer compositions, which may be useful when studying molecules that give rise to an enrichment of certain lipid types. This measurement revealed an average lipid ratio of 2.6:1 POPE:POPG within the shell, suggesting that MinD-MTS gives rise to an enrichment of POPG lipids, likely mediated by the increased electrostatics between the cationic peptide and anionic POPG headgroups.

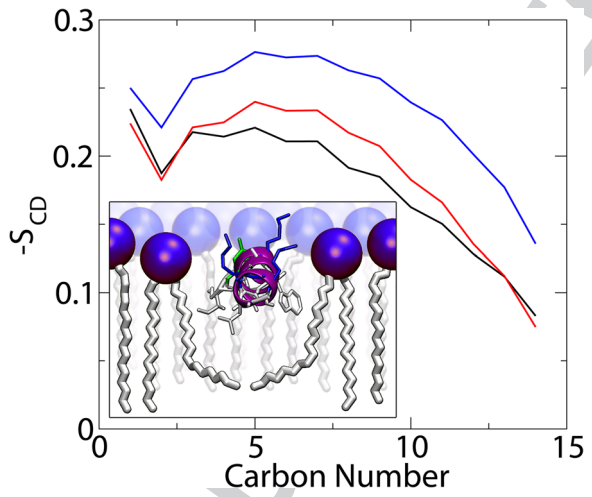

Figure 1 Annular shell order parameters. The order parameters of saturated lipid tails from an annular shell analysis of MinD-MTS, an amphipathic helical peptide inserted into a POPE/POPG (3:1) double bilayer at 300K. The shell order parameters are shown in black, along with two control groups: the red plot uses the option built into Membrainy to ignore all gel lipids, which produces a more accurate control group for this peptide as it resides in a fluid region of the bilayer; and the blue plot contains both gel and fluid lipids. The differences between the black and red plots indicate the presence of splayed lipid tails in the annular shell, whereas the blue plot is sampling the wrong phase of lipids and provides an inaccurate comparison to the lipids within the annular shell.

Evolution of the TMV

The TMV is the electrical potential found across biological cell membranes and plays a crucial role in a wide range of cellular processes, including the transport of nutrients into and out of the cell, biophysical signaling, and cell proliferation [40-42]. Membrainy is capable of measuring the time evolution of the TMV across a double bilayer, which may be of importance in electrophysiology and electroporation simulations. As an exemplar, numerous electroporation simulations were conducted for 30 ns using POPE/POPG (3:1) double bilayers. These systems were initially established with ion imbalances of +20, achieved by moving 10 cations from the inner (anodic) water compartment to the outer (cathodic) water compartment, similar to the approach taken by Sachs et al. [43]. Transient water pores were observed to form after a random time interval, allowing both cations and anions to travel through the pores in opposite directions, resulting in a loss of the initial ion imbalance. Membrainy was used to produce TMV against time measurements for each simulation, one of which is depicted in Figure 2. This measurement reveals an initial TMV of -2.65 V, which lowers to -2.35 V during the first 5 ns due to the lateral expansion of the bilayers undergoing electrostriction. Once a pore had formed, a sharp drop in TMV is observed at a rate of 0.75 V/ns, corresponding to ion transport through the pore at a rate of 3 ions/ns. The resulting TMV is indicative of the remaining ion imbalance (+2). These measurements provide an informative way to monitor

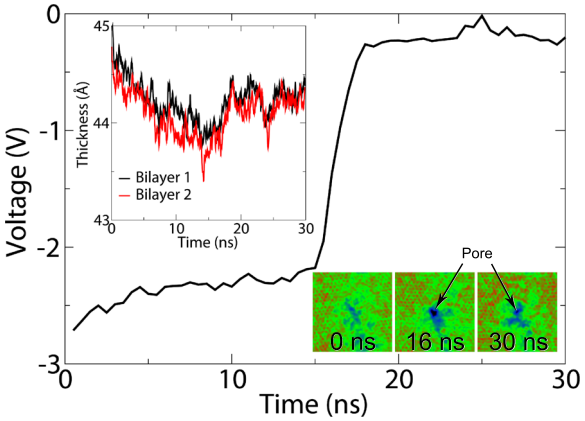

Figure 2 Evolution of the TMV and membrane thickness. A POPE/POPG (3:1) double bilayer was subject to an ion imbalance of +20, achieving an initial TMV of -2.65 V. Within 5 ns, the TMV lowers to -2.35 V as the bilayers expand laterally and experience a thickness reduction due to electrostriction. At 15 ns, a transient water pore formed through electroporation, allowing ions to travel through the pore in opposite directions. This resulted in a rapid loss of the initial ion imbalance which incurs a sharp drop in TMV. By 17 ns, the TMV is insufficient to maintain electrostriction, allowing the bilayer thickness to increase.

changes to the TMV during a trajectory, and can be used in electroporation simulations to determine the time at which a pore is formed and the rate at which the TMV is dissipated.

Leaflet/membrane thickness and area per lipid

Using the same electroporation simulation as above, Membrainy was used to measure the leaflet and membrane thickness over the trajectory (with the membrane thickness depicted in Figure 2). This membrane thickness steadily decreases prior to pore formation, corresponding to the electrostriction effects experienced by the bilayers from the TMV. After pore formation, the bilayer thickness sharply increases as the TMV is dissipated, suggesting that the electrostriction effects had diminished and the bilayers were able to relax towards their initial thickness. Similar results were obtained for the leaflet thickness, and interestingly the anodic leaflets were observed to be consistently thinner than the cathodic leaflets prior to pore formation, which was also observed by Böckmann et al. in a similar electroporation study [44]. Membrainy was used to calculate the APL during the simulation, which revealed an increase in APL prior to pore formation, and a decrease afterwards. This result was identical to the APL produced with the GROMACS tool `g_order`, which can output the box dimensions over time to be converted to an APL.

Lipid flip-flopping

Transmembrane lipid translocation, more commonly known as lipid flip-flopping, is the process in which lipids are translocated between the two opposing leaflets of a bilayer [45]. This translocation occurs from both passive and active transport mechanisms and plays a crucial role in the maintenance of asymmetric cell membranes [46]. Lipid flip-flopping has also been observed in simulated DMPC bilayers through electroporation, whereby lipids translocate through transient water pores in both directions [25].

Membrainy was used to detect lipid flip-flopping during a 30 ns simulation of a POPE/POPG (3:1) double bilayer, in which an ion imbalance of +20 was maintained with position restraints. A pore formed within 5 ns and remained open for the duration of the simulation. Figure 3 depicts the TMV and leaflet symmetry measurements during the simulation, where the leaflet symmetry is calculated by subtracting the number of lipids in the cathodic leaflets from the number of lipids in the anodic leaflets, and therefore a value of -2 indicates a single flip-flop to the cathodic leaflet. Upon pore formation, the leaflet symmetry reveals that the toroidal structure of the pore mainly comprised POPE and POPG lipids from the anodic leaflet. This is likely due to the tendency for transient water pores to initiate formation from the anodic water

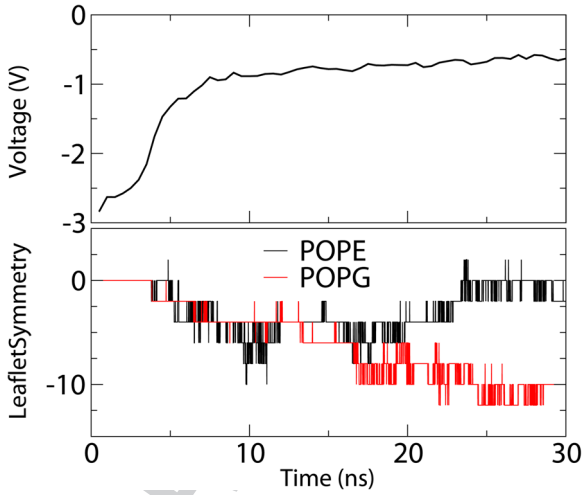

Figure 3 Lipid flip-flopping. TMV and leaflet symmetry measurements of a POPE/POPG (3:1) double bilayer undergoing electroporation over 30 ns. A value of -2 in leaflet symmetry indicates a single flip-flop from the anodic to the cathodic leaflet. A pore was formed within 5 ns, which saw both POPE and POPG lipids from the anodic leaflet form the toroidal structure of the pore. After 15 ns, the POPE lipids within the pore return to the anodic leaflet while additional POPG lipids translocate to the cathodic leaflet. By 30 ns, one POPE lipid had flip-flopped from both leaflets (producing a symmetry of 0) and five POPG lipids had flip-flopped to the cathodic leaflet. This suggests that POPG lipids are more susceptible to flip-flopping towards the cathodic leaflet through transient water pores when under the influence of a TMV.

compartments, as observed by Böckmann et al. [44]. After 15 ns, the POPE symmetry returns to zero, indicating that the distribution of POPE lipids across both leaflets has equalised; however, the POPG symmetry steadily decreases, indicating that POPG lipids are translocating through the pore towards the cathodic leaflet. By 30 ns, one POPE lipid in each leaflet had flip-flopped and five POPG lipids had flip-flopped to the cathodic leaflet. This suggests that POPG lipids experience a greater tendency to flip-flop through transient water pores in bilayers subject to a high voltage TMV, in which the POPG lipids are translocated towards the cathodic leaflet, likely due to the additional forces acting on the anionic POPG headgroups from the electric field. Membrainy has therefore detected and interpreted lipid flip-flopping through a transient pore within this system.

2D surface maps and gel percentage

Surface maps were generated for POPE/POPG (3:1) bilayers at 297 K, 300 K and 320 K, and DPPC and POPC bilayers at 297 K using the CHARMM force field (Figure 4). The 300 K POPE/POPG bilayer contained the MinD-MTS inserted into the headgroup region, and the 297 K POPE/POPG bilayer was imaged before and during

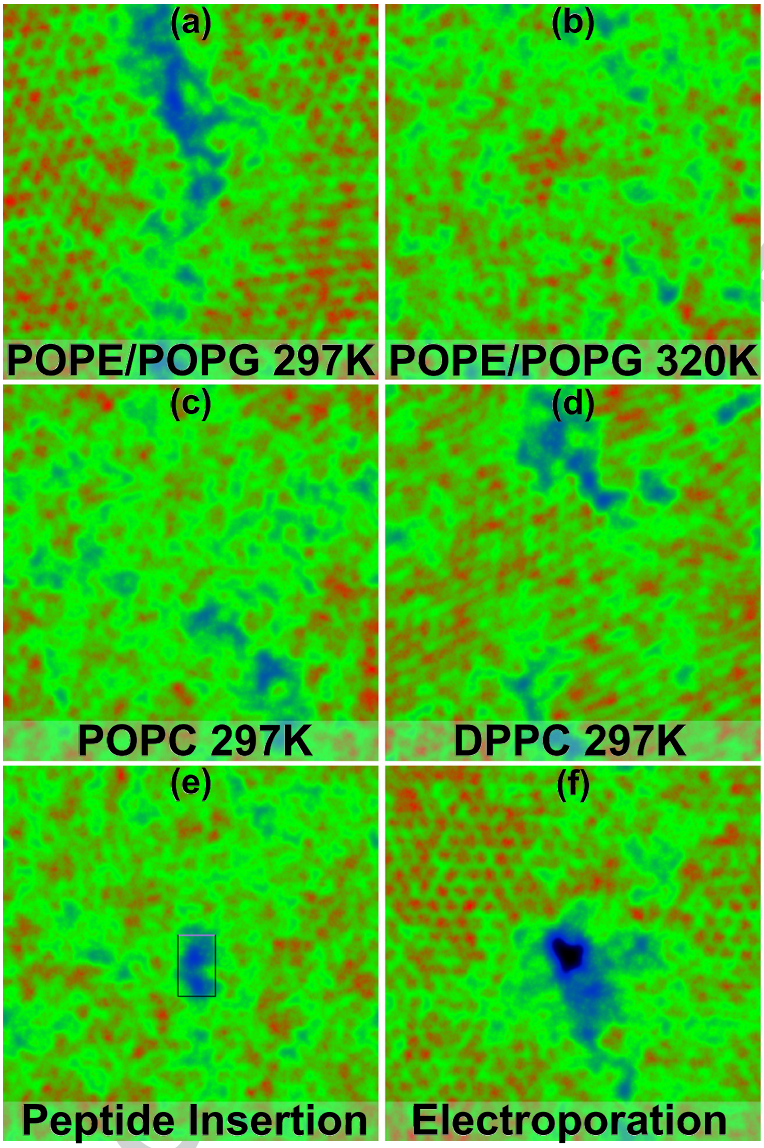

Figure 4 2D surface maps. These maps depict leaflets taken from a variety of lipid bilayer simulations. Red hexagonally packed dots represents gel clusters and black areas indicate the presence of a pore or hole in the leaflet. **(a)** and **(b)** depict POPE/POPG (3:1) bilayers at two temperatures, where (a) is near the transition temperature and contains ∼53% gel, and (b) is in the fluid phase and contains ∼14% gel. **(c)** and **(d)** depict POPC and DPPC bilayers at 297 K, containing ∼16% and ∼85% gel respectively. These percentages correspond with the correct phase of each bilayer as 297 K is above the transition temperature for POPC and below that of DPPC. The DPPC map also reveals a smudged appearance to the gel clusters which is indicative of lipids in the tilted $L_{\beta'}$ phase. **(e)** depicts an inserted MinD-MTS peptide in a POPE/POPG (3:1) bilayer at 300 K. **(f)** depicts a leaflet containing a transient water pore established through electroporation in a POPE/POPG (3:1) bilayer at 297 K.

electroporation. As 297 K is approximately the transition temperature for POPE/POPG bilayers [47], Membrainy detected ∼53% gel within the bilayer. This percentage is accurately portrayed in the surface map (Figure 4a) where approximately half of the map appears as gel, represented by hexagonally packed red dots (the hexagonal packing of lipid tails occurs naturally in gel domains). The same bilayer was analysed at 320 K and showed ∼14% gel, which is also portrayed in the surface map (Figure 4b) by showing fewer gel clusters. The POPC bilayer at 297 K shows a highly fluid bilayer with ∼16% gel (Figure 4c), whereas the DPPC bilayer at 297 K shows ∼85% gel (Figure 4d). These measurements are in agreement with their corresponding transition temperatures of 271 K for POPC bilayers and 314 K for DPPC bilayers [48]. Interestingly, the DPPC bilayer exhibits gel lipids in the tilted $L_{\beta'}$ phase which is portrayed in the surface map by the smudged appearance of the gel clusters. Finally, surface

maps were generated for the bilayer containing an inserted MinD-MTS peptide (Figure 4e) and the bilayer from the previous electroporation simulation containing a transient water pore (Figure 4f). These 2D surface maps provide an alternative representation of the bilayer, capable of producing both a contour and density map that portrays gel clusters, pores, surface undulations and defects that may not be easily seen in 3D visualisation software such as VMD [49] and Pymol [50].

Headgroup orientation

The lipid headgroup is the polar interface between the membrane core and the intracellular/extracellular spaces and has been observed to exhibit sensitivity to electric charges, dipole fields, and temperature effects [51,52]. Experimental techniques have shown the lipid headgroup to sit roughly perpendicular to the lipid tails with a variation of around 30 degrees to the membrane surface [19,53]. In MD simulations, measurements of lipid headgroup orientations can provide an effective means to compare bilayers undergoing environmental perturbations, such as those under the influence of a TMV. As an exemplar, a POPC double bilayer was equilibrated for 100 ns without a TMV, after which a 30 ns simulation was conducted using an ion imbalance of +28, achieving a TMV of -1.95 V. Membrainy was used to measure the headgroup orientations before and after applying a TMV, which yielded a mean angle of 23 degrees in both leaflets without a TMV, and mean angles of 25.5 and 21.5 degrees in the anodic and cathodic leaflets respectively after applying a TMV. This reveals a shift of +2.5 degrees in the anodic leaflets and -1.5 degrees in the cathodic leaflets, suggesting that the headgroups in both leaflets are tending to align with the electric field. These measurements are comparable to those found by Böckmann et al. [44].

Lipid mixing/demixing entropy

The entropy of lipid mixing/demixing provides a measure of the two-dimensional spatial heterogeneity of any lipid bilayer system, and a means to study changes following an environmental perturbation. A bilayer was constructed containing 1512 POPE and 504 POPC Martini lipids, where the POPC lipids were initially clustered together in a quadrant of the bilayer creating a perfectly demixed system. This bilayer was simulated for 200 ns and its trajectory was analysed by Membrainy to produce a scaled mixing entropy over time (Figure 5). These measurements reveal an initial entropy of 0.3, which immediately increases as the system began to mix. By ~150 ns the entropy settles just below the theoretical maximum entropy, indicating the bilayer was fully mixed. Membrainy has therefore quantified the level of mixing/demixing in this system.

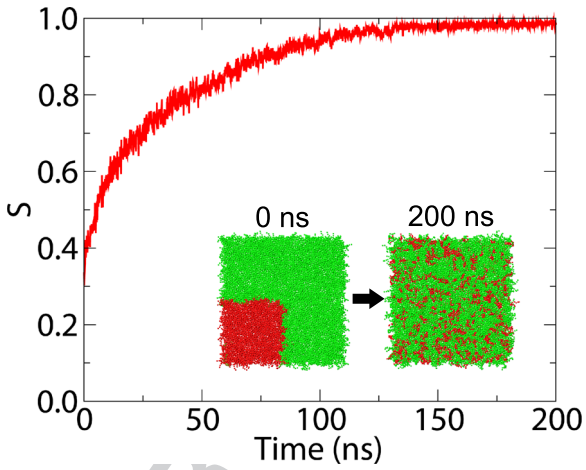

Figure 5 Mixing entropy. The mixing entropy of a POPE/POPC (3:1) bilayer over 200 ns, scaled such that $S_{max} = 1$. The bilayer is initialised such that POPC lipids (shown in red) encompass the lower left quadrant of the bilayer and the remaining bilayer contains POPE lipids (shown in green), creating a perfectly demixed system. An initial entropy of 0.3 is observed, which increases as the lipid types mix together. By 150 ns, the resulting entropy settles just below the theoretical maximum entropy, indicating a perfectly mixed system.

Conclusions

Membrainy is an important tool for any membrane simulation where the lipids may undergo changes in response to environmental perturbations. Membrainy was designed to be simple and powerful, requiring no compilation and minimal user-input to run, and offers a wide range of analytical techniques for the calculation of various membrane-specific properties including those that, to our knowledge, are not currently available with existing software. Membrainy is capable of automatically interpreting a wide range of lipid bilayer systems, including those with complex lipid compositions, or those utilising single, double or asymmetric bilayers. Membrainy will automatically detect the force field in use, and is able to adapt to dynamic membranes that undergo structural changes such as lipid flip-flopping. We have shown Membrainy to be a useful and effective tool for analysing a broad scope of biological effects and environmental perturbations acting on lipid bilayers that may incur changes to the lipids and therefore modify the properties of the membrane.

Availability and requirements

Project Name: Membrainy
Project home page: www.membrainy.net
Operating systems: Platform independent
Programming language: Java
Other requirements: Java v1.6 or higher, GROMACS v4 or higher (to enable some features)
License: GNU GPL v2
Any restrictions to use by non-academics: None

Abbreviations
APL: Area per lipid; MD: Molecular dynamics; MinD-MTS: MinD membrane targeting sequence; POPC: 1-palmitoyl-2-oleoyl-sn-glycero-3-phosphocholine; POPE: 1-palmitoyl-2-oleoyl-sn-glycero-3-phosphoethanolamine; POPG: 1-palmitoyl-2-oleoyl-sn-glycero-3-phosphoglycerol; TMV: Transmembrane voltage.

Competing interests
The authors declare that they have no competing interests.

Authors' contributions
MC carried out the experiments, analysis, and programming. Both authors read and approved the final manuscript.

Acknowledgements
We thank the EPSRC for funding MC, EPSRC EP/J007404/1 for funding CM, and acknowledge Dr. Marieke Schor and Giovanni Brandani for their contributions to the mixing/demixing data and useful discussions. This work made use of the facilities of HECToR, the UK's national high-performance computing service, which is provided by UoE HPCx Ltd at the University of Edinburgh, Cray Inc and NAG Ltd, and funded by the Office of Science and Technology through EPSRC's High End Computing Programme.

Received: 9 September 2014 Accepted: 19 February 2015

References
1. van Meer G, Voelker DR, Feigenson GW. Membrane lipids: where they are and how they behave. Nat Rev Mol Cell Biol. 2008;9:112–24.
2. Bloom M, Evans E, Mouritsen OG. Physical properties of the fluid lipid-bilayer component of cell membranes: a perspective. Q Rev Biophys. 1991;24:293–397.
3. Penkett S, Flook A, Chapman D. Physical studies of phospholipids. ix. nuclear resonance studies of lipid-water systems. Chem Phys Lipids. 1968;2:273–90.
4. Schindler H, Seelig J. Epr spectra of spin labels in lipid bilayers. J Chem Phys. 1973;59:1841–50.
5. De Kruijff B, Verkley A, Van Echteld C, Gerritsen W, Mombers C, Noordam P, et al. The occurrence of lipidic particles in lipid bilayers as seen by 31P NMR and freeze-fracture electron-microscopy. Biochimica et Biophysica Acta (BBA)-Biomembranes. 1979;555:200–9.
6. Feller SE. Molecular dynamics simulations of lipid bilayers. Curr Opin Colloid Interface Sci. 2000;5:217–23.
7. Polozov IV, Polozova AI, Molotkovsky JG, Epand RM. Amphipathic peptide affects the lateral domain organization of lipid bilayers. Biochimica et Biophysica Acta (BBA) - Biomembranes. 1997;1328:125–39.
8. Cui H, Lyman E, Voth GA. Mechanism of membrane curvature sensing by amphipathic helix containing proteins. Biophys J. 2011;100:1271–9.
9. Lee AG. Lipid-protein interactions in biological membranes: a structural perspective. Biochimica et biophysica acta. 2003;1612:1–40.
10. Jackman JA, Cho N-JJ. Model membrane platforms for biomedicine: case study on antiviral drug development. Biointerphases. 2012;7:18.
11. Allen WJ, Lemkul JA, Bevan DR. Gridmat-md: a grid-based membrane analysis tool for use with molecular dynamics. J Comput Chem. 2009;30:1952–8.
12. Gapsys V, de Groot BL, Briones R. Computational analysis of local membrane properties. J Computer-aided Mol Des. 2013;27:845–58.
13. Pronk S, Páll S, Schulz R, Larsson P, Bjelkmar P, Apostolov R, et al. Gromacs 4.5: a high-throughput and highly parallel open source molecular simulation toolkit. Bioinformatics. 2013;29:845–54.
14. McGibbon RT, Beauchamp KA, Schwantes CR, Wang L-P, Hernández CX, Harrigan MP, et al. Mdtraj: a modern, open library for the analysis of molecular dynamics trajectories. 2014. bioRxiv, 008896.
15. Michaud-Agrawal N, Denning EJ, Woolf TB, Beckstein O. Mdanalysis: a toolkit for the analysis of molecular dynamics simulations. J Comput Chem. 2011;32:2319–27.
16. Hofsäß C, Lindahl E, Edholm O. Molecular dynamics simulations of phospholipid bilayers with cholesterol. Biophys J. 2003;84:2192–206.
17. Berger O, Edholm O, Jähnig F. Molecular dynamics simulations of a fluid bilayer of dipalmitoylphosphatidylcholine at full hydration, constant pressure, and constant temperature. Biophys J. 1997;72:2002–13.
18. Venable RM, Zhang Y, Hardy BJ, Pastor RW. Molecular dynamics simulations of a lipid bilayer and of hexadecane: an investigation of membrane fluidity. Science. 1993;262:223–6.
19. Seelig J, MacDonald PM, Scherer PG. Phospholipid head groups as sensors of electric charge in membranes. Biochemistry. 1987;26:7535–41.
20. Caracciolo G, Pozzi D, Amenitsch H, Caminiti R. Multicomponent cationic lipid dna complex formation: Role of lipid mixing. Langmuir. 2005;21:11582–7.
21. Kutzner C, Grubmüller H, de Groot BL, Zachariae U. Computational electrophysiology: The molecular dynamics of ion channel permeation and selectivity in atomistic detail. Biophys J. 2011;101:809–17.
22. Gurtovenko AA, Vattulainen I. Pore formation coupled to ion transport through lipid membranes as induced by transmembrane ionic charge imbalance: atomistic molecular dynamics study. J Am Chem Soc. 2005;127:17570–1.
23. Wang S, Larson RG. Water channel formation and ion transport in linear and branched lipid bilayers. Phys Chem Chem Phys. 2014;16:7251–62.
24. Heimburg T. The capacitance and electromechanical coupling of lipid membranes close to transitions. the effect of electrostriction. Biophys J. 2012;103:918–29.
25. Gurtovenko AA, Vattulainen I. Molecular mechanism for lipid flip-flops. J Phys Chem B. 2007;111:13554–9.
26. Attard GS, Templer RH, Smith WS, Hunt AN, Jackowski S. Modulation of ctp:phosphocholine cytidylyltransferase by membrane curvature elastic stress. Proc Nat Acad Sci. 2000;97:9032–6.
27. Case DA, Darden TA, Cheatham TE, Simmerling CL, Wang J, Duke RE. AMBER 14. 2014. [http://ambermd.org/]
28. Brooks BR, Brooks CL III, Mackerell AD Jr, Nilsson L, Petrella RJ, Roux B, et al. CHARMM: The Biomolecular Simulation Program. J Comput Chem. 2009;30:1545–614.
29. Phillips JC, Braun R, Wang W, Gumbart J, Tajkhorshid E, Villa E, et al. Scalable molecular dynamics with NAMD. J Comput Chem. 2005;26:1781–802.
30. Klauda JB, Venable RM, Freites JA, O'Connor JW, Tobias DJ, Mondragon-Ramirez C, et al. Update of the charmm all-atom additive force field for lipids: validation on six lipid types. J Phys Chem B. 2010;114:7830–43.
31. Berger O, Edholm O, Jähnig F. Molecular dynamics simulations of a fluid bilayer of dipalmitoylphosphatidylcholine at full hydration, constant pressure, and constant temperature. Biophys J. 1997;72:2002–13.
32. Marrink SJ, de Vries AH, Mark AE. Coarse grained model for semiquantitative lipid simulations. J Phys Chem B. 2004;108:750–60.
33. Grace 2D Plotting Tool. [http://plasma-gate.weizmann.ac.il/Grace/]
34. Vermeer LS, de Groot BL, Réat V, Milon A, Czaplicki J. Acyl chain order parameter profiles in phospholipid bilayers: computation from molecular dynamics simulations and comparison with 2h nmr experiments. Eur Biophys J: EBJ. 2007;36:919–31.
35. Egberts E, Berendsen H. Molecular dynamics simulation of a smectic liquid crystal with atomic detail. J Chem Phys. 1988;89:3718–32.
36. Tamm LK, Tatulian SA. Infrared spectroscopy of proteins and peptides in lipid bilayers. Q Rev Biophys. 1997;30:365–429.
37. Gurtovenko AA, Vattulainen I. Calculation of the electrostatic potential of lipid bilayers from molecular dynamics simulations: Methodological issues. J Chem Phys. 2009;130:215107.
38. Brandani GB, Schor M, MacPhee CE, Grubmüller H, Zachariae U, Marenduzzo D. Quantifying disorder through conditional entropy: An application to fluid mixing. PLoS ONE. 2013;8:65617.
39. Szeto TH, Rowland SL, Habrukowich CL, King GF. The mind membrane targeting sequence is a transplantable lipid-binding helix. J Biol Chem. 2003;278:40050–6.
40. Wright SH. Generation of resting membrane potential. Adv Phys Educ. 2004;28:139–42.
41. Sundelacruz S, Levin M, Kaplan DL. Role of membrane potential in the regulation of cell proliferation and differentiation. Stem Cell Rev Rep. 2009;5:231–46.
42. Cone CD, Tongier M. Contact inhibition of division: involvement of the electrical transmembrane potential. J Cell Physiol. 1973;82:373–86.
43. Sachs JN, Crozier PS, Woolf TB. Atomistic simulations of biologically realistic transmembrane potential gradients. J Chem Phys. 2004;121:10847–51.

44. Böckmann RA, de Groot BL, Kakorin S, Neumann E, Grubmüller H. Kinetics, statistics, and energetics of lipid membrane electroporation studied by molecular dynamics simulations. Biophys J. 2008;95:1837–50.
45. Higgins CF. Flip-flop: the transmembrane translocation of lipids. Cell. 1994;79:393–5.
46. Devaux PF, Zachowski A. Maintenance and consequences of membrane phospholipid asymmetry. Chem Phys Lipids. 1994;73:107–20.
47. Silvius J. Thermotropic phase transitions of pure lipids in model membranes and their modifications by membrane proteins. Lipid-protein Interact. 1982;2:239–81.
48. Avanti Polar Lipids Inc., Phase Transition Temperatures for Glycerophospholipids. http://avantilipids.com/index.php?option=com_content&id=1700&Itemid=419.
49. VMD: Visual Molecular Dynamics. [http://www.ks.uiuc.edu/Research/vmd/]
50. The PyMOL Molecular Graphics System, Version 1.3r1. [http://www.pymol.org/]
51. Stulen G. Electric field effects on lipid membrane structure. Biochimica et Biophysica Acta (BBA) - Biomembranes. 1981;640:621–7.
52. Dufourc EJ, Mayer C, Stohrer J, Althoff G, Kothe G. Dynamics of phosphate head groups in biomembranes. comprehensive analysis using phosphorus-31 nuclear magnetic resonance lineshape and relaxation time measurements. Biophys J. 1992;61:42–57.
53. Seelig J, Gally H-U, Wohlgemuth R. Orientation and flexibility of the choline head group in phosphatidylcholine bilayers. Biochimica et Biophysica Acta (BBA) - Biomembranes. 1977;467:109–119.

⌘ *Author's Choice*

THE JOURNAL OF BIOLOGICAL CHEMISTRY VOL. 288, NO. 28, pp. 20162–20172, July 12, 2013

Anti-antimicrobial Peptides

FOLDING-MEDIATED HOST DEFENSE ANTAGONISTS[*S]

Received for publication, February 6, 2013, and in revised form, May 11, 2013 Published, JBC Papers in Press, June 4, 2013, DOI 10.1074/jbc.M113.459560

Lloyd Ryan[‡§], Baptiste Lamarre[‡], Ting Diu[‡¶], Jascindra Ravi[‡], Peter J. Judge[‖], Adam Temple[**], Matthew Carr[**], Eleonora Cerasoli[‡], Bo Su[¶], Howard F. Jenkinson[¶], Glenn Martyna[‡‡], Jason Crain[**], Anthony Watts[‖], and Maxim G. Ryadnov[‡1]**

From the [‡]National Physical Laboratory, Teddington, Middlesex TW11 0WL, United Kingdom, the [§]Division of Biomedical Sciences, St. George's University of London, London SW17 0RE, United Kingdom, the [¶]School of Oral and Dental Sciences, University of Bristol, Bristol BS1 2LY, United Kingdom, the [‖]Department of Biochemistry, University of Oxford, Parks Road, Oxford OX1 3QU, United Kingdom, the [**]School of Physics and Astronomy, University of Edinburgh, Edinburgh EH9 3JZ, Scotland, United Kingdom, and the [‡‡]IBM T. J. Watson Research Center, Yorktown Heights, New York 10598

Background: Direct antagonists of native antimicrobial peptide (AMP) sequences are unknown.
Results: Complementary antagonistic sequences can co-fold with AMPs into functionally inert assemblies.
Conclusion: Antagonists act as anti-AMPs.
Significance: The findings offer a molecular rationale for anti-AMP responses with potential implications for antimicrobial resistance.

Antimicrobial or host defense peptides are innate immune regulators found in all multicellular organisms. Many of them fold into membrane-bound α-helices and function by causing cell wall disruption in microorganisms. Herein we probe the possibility and functional implications of antimicrobial antagonism mediated by complementary coiled-coil interactions between antimicrobial peptides and *de novo* designed antagonists: anti-antimicrobial peptides. Using sequences from native helical families such as cathelicidins, cecropins, and magainins we demonstrate that designed antagonists can co-fold with antimicrobial peptides into functionally inert helical oligomers. The properties and function of the resulting assemblies were studied in solution, membrane environments, and in bacterial culture by a combination of chiroptical and solid-state NMR spectroscopies, microscopy, bioassays, and molecular dynamics simulations. The findings offer a molecular rationale for anti-antimicrobial responses with potential implications for antimicrobial resistance.

Intermolecular recognition by peptides is a critical aspect of regulatory processes at cellular interfaces (1). Native systems ranging from viral fusion proteins (2) and SNARE complexes (3) to membrane skeletal networks (4) and harbor domains of enteric pathogens (5) rely on specific α-helical coiled coils to maintain interfacial contacts in a highly cooperative manner. Amphipathic helical monomers can be designed to incorporate alternative interfaces into such assemblies, thereby disrupting regulatory processes (6). By contrast, amphipathic antimicrobial helices bind to microbial membranes without *a priori* requirements for specific assemblies (7). Given their sequence similarities with coiled coils, antimicrobial peptides may be challenged by co-assembly with antagonistic helices, a proposition that has so far been unexplored. Thus, the overall aim of this study is to explore the hypothesis that antimicrobial activity in peptides can be effectively neutralized by the formation of inert coiled-coil complexes.

Coiled-coil sequences show heptad repeats of hydrophobic and polar residues (usually designated *abcdefg*), in which *a* and *d* form hydrophobic interfaces (8). To form contiguous interfaces the *a*/*d* patterns of corresponding helices must be in register, which is prevented by the average spacing of hydrophobic residues along a coiled-coil sequence being 3.5 residues. This is less than one complete turn (3.6 residues) of a monomeric α-helix (9). To rectify this discrepancy *a*/*d* patterns impose a slight left-handed twist enabling left-handed helix-crossing angles in the coiled-coil bundle, which permits, but does not guarantee, stable coiled coils. Further stabilization is required through complementary electrostatic interactions at *e* and *g* sites of successive heptads between partner strands (*i.e. g*-*e*′ interactions: *g* of one heptad and *e*′ of the following heptad on the other helix) (Fig. 1) (8, 9). Therefore, in assigning coiled-coil patterns in antimicrobial sequences it is necessary to consider hydrophobic *a*/*d* pairs in conjunction with charged *e*/*g* pairs.

Antimicrobial peptides (AMPs)[2] are cationic amphipathic structures that fold and oligomerize in anionic phospholipid

* This work was supported by the United Kingdom Department of Business, Innovation and Skills, European Metrology Research Programme Grant HLT10, the Strategic Research Programme of the National Physical Laboratory, the Scottish Universities Physics Alliance, IBM Research, and Engineering and Physical Sciences Research Council Grants EP/I029443/1 (to J. C.) and EP/I029516/1 (to A. W. and P. J. J.).
⌘ *Author's Choice*—Final version full access.
[S] This article contains supplemental text and Figs. S1–S6.
[1] To whom correspondence should be addressed: National Physical Laboratory, Teddington, Middlesex TW11 0LW, United Kingdom. E-mail: max.ryadnov@npl.co.uk.

[2] The abbreviations used are: AMP, antimicrobial peptide; DIPEA, *N*,*N*-diisopropylethylamine; DLPC, 1,2-dilauroylphosphatidylcholine; DLPG, 1,2-dilauroyl-*sn*-glycero-3-phospho-(1′-rac-glycerol); DMPC, 1,2-dimyristoyl-*d*54-*sn*-glycero-3-phosphocholine; DMPG, 1,2-dimyristoyl-*sn*-glycero-3-phospho-(1′-rac-glycerol); HCTU, 2-(6-chloro-1H-benzotriazole-1-yl)-1,1,3,3-tetramethylaminium hexafluorophosphate; LD, linear dichroism; MIC, minimum inhibitory concentration.

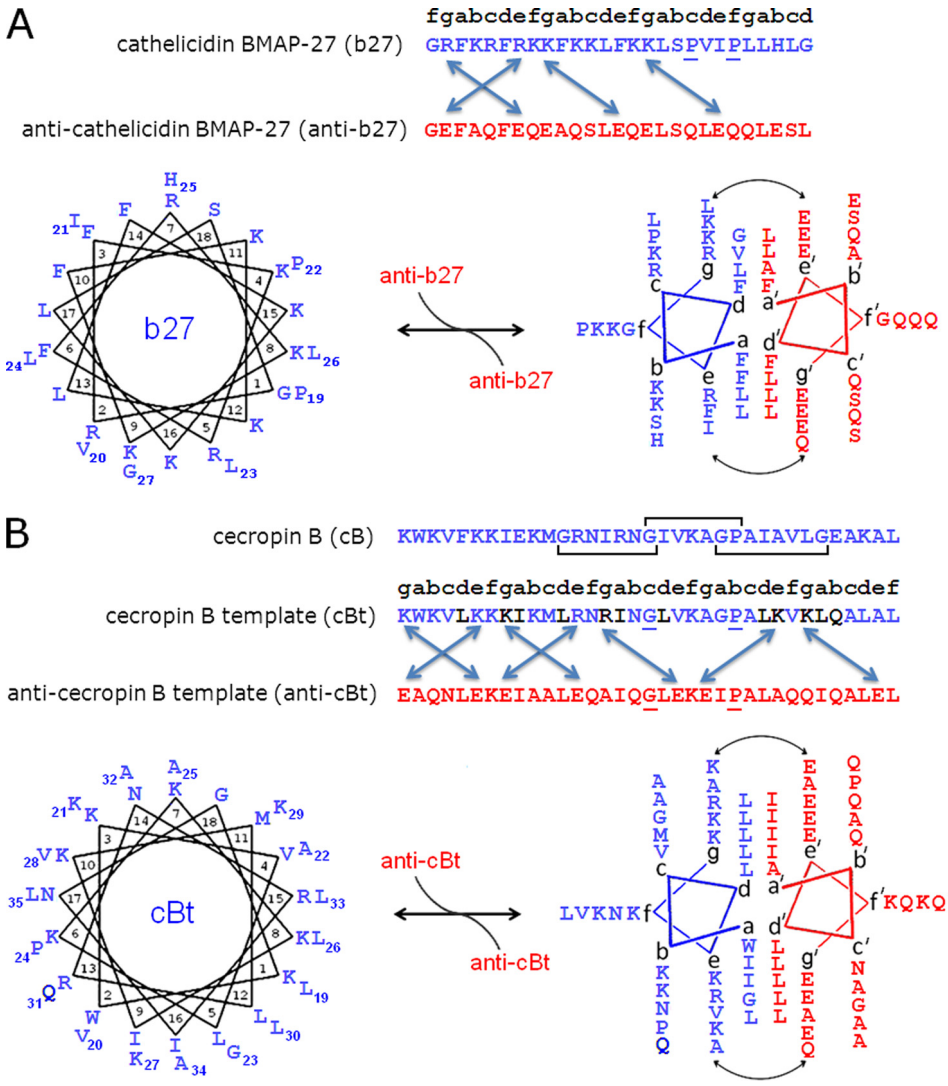

FIGURE 1. **Peptide design.** *A*, cathelicidin type: bovine myeloid antimicrobial peptide-27 (b27) and anti-b27. *B*, cecropin type: native cecropin B (cB), cecropin B template (cBt), and anti-cecropin B template (anti-cBt). Linear sequences (*top*) and configured onto helical wheels (*bottom*) are monomeric with 3.6 residues (*left*) and coiled-coil with 3.5 residues (*right*) per turn. Antimicrobial peptides and antagonists are shown in *blue* and *red*, respectively. Mutations in cBt are in *black*, and key residues in helix-disrupting motifs are *underlined*. Three overlapping G(*X*)$_n$G motifs are highlighted by *horizontal brackets*. *Double-headed arrows* denote electrostatic *e-g′* interactions.

membranes (7). By this convention, antagonistic sequences are anionic amphipathic helices that remain unfolded in solution and in membrane environments but fold upon binding to cationic AMPs (Fig. 1). The strength and stability of this binding depend on helical propensity and persistence length. An antimicrobial sequence can comprise up to 50 amino acid residues (7, 10; see also antimicrobial sequences database at the bbcm Web site at the University of Trieste, Italy), and most helical AMPs contain 20–35 residues which should be sufficient for coiled-coil formation (11). However, and importantly, native antimicrobial helices often incorporate helix-disrupting motifs to facilitate membrane insertion. Common examples include glycine zipper G(*X*)$_n$G motifs, where *X* is any residue and $n = 3–6$ (12, 13). Length correlations between these motifs and antimicrobial peptides are not obvious. For instance, bombinins prefer $n = 3$ as do membrane proteins that incorporate glycine zippers for transmembrane helix dimerization, whereas cecropins, defensins, and magainins tend to have variable *n*, a strategy also used by proteins to specify phosphate binding and domain folding (14–19). Given these dependences and preferences for longer coiled coils in membrane proteins (2–5) it was appropriate to probe one sequence having a relatively long and uninterrupted helical stretch and another longer sequence containing G(*X*)$_n$G motifs. A cathelicidin, bovine myeloid antimicrobial peptide-27 (b27) (20), and cecropin B (cB), originally isolated from the cecropia moth *Hyalophora cecropia* (21) met the requirements (Fig. 1).

EXPERIMENTAL PROCEDURES

Peptide Synthesis—All peptides were synthesized on a Liberty microwave peptide synthesizer (CEM Corporation) using standard solid phase Fmoc (*N*-(9-fluorenyl)methoxycarbonyl) protocols on Rink amide-4-methylbenzhydrylamine resins with HCTU/DIPEA as coupling reagents. Peptides were purified by semipreparative RP-HPLC on a JASCO HPLC system (model PU-980; Tokyo, Japan) and confirmed by MALDI-TOF mass

spectrometry (Bruker Daltonics) with α-cyano-4-hydroxycinnamic acid as the matrix.

MS $[M+H]^+$: b27, *m*/*z* 3282.2 (calc.), 3283.2 (found); anti-b27, 3138.3 (calc.), 3139.3 (found); cB, *m*/*z* 3834.5 (calc.), 3836.0 (found); cBt, *m*/*z* 3968.1 (calc.), 3969.1 (found); anti-cBt, *m*/*z* 3843.4 (calc.), 3843.4 (found); m2, *m*/*z* 2465.9 (calc.), 2467.0 (found); m2t, *m*/*z* 2526.1 (calc.), 2526.1 (found); m2t2, *m*/*z* 2555.3 (calc.), 2556.2 (found); anti-m2, *m*/*z* 2529.8 (calc.), 2529.8 (found); anti-m2t2, *m*/*z* 2560.9 (calc.), 2562.0 (found). $[M+Na]^+$ and $[M+K]^+$ were also found.

High Performance Liquid Chromatography—Analytical and semipreparative gradient RP-HPLC was performed on a JASCO HPLC system using Vydac C18 analytical (5 μm) and semipreparative (5 μm) columns. Both analytical and semipreparative runs used a 10–60% B gradient over 50 min at 1 ml/min and 4.5 ml/min, respectively, with detection at 230 and 220 nm. Buffer A was 5% and buffer B was 95% aqueous CH_3CN, 0.1% TFA.

Lipid Vesicle Preparation—The lipids, 1,2-dilauroylphosphatidylcholine (DLPC) and 1,2-dilauroyl-*sn*-glycero-3-phospho-(1′-rac-glycerol) (DLPG), 75%/25% (w:w) used for liposome construction were from Avanti Polar Lipids. The lipids were weighted up, dissolved in chloroform-methanol (2:1, v:v), dried under a nitrogen stream, and placed under vacuum overnight. The resulting film was hydrated to 10 mg/ml total lipid concentration in 10 mM phosphate buffer, pH 7.4. The suspension was then extensively vortexed, sonicated (30 °C), and extruded using a hand-held extruder (Avanti Polar Lipids) (15 times, polycarbonate filter, 0.05 μm) to give a clear solution containing small unilamellar vesicles, which were analyzed (50 nm) by photon correlation spectroscopy.

Photon Correlation Spectroscopy—Vesicles were resuspended to a final concentration of 1 mg/ml and were analyzed on a Zetasizer Nano (ZEN3600, Malvern Instruments, Worcestershire, UK). Dynamic light scattering batch measurements were carried out in a low volume disposable cuvette at 25 °C. Hydrodynamic radii were obtained through the fitting of autocorrelation data using the manufacture's software, Dispersion Technology Software (DTS version 5.10).

Circular Dichroism Spectroscopy—All CD spectra were recorded on a JASCO J-810 spectropolarimeter fitted with a Peltier temperature controller. All measurements were taken in ellipticities in millidegrees and converted to molar ellipticities ($[\theta]$, deg cm^2 $dmol^{-1}$) by normalizing for the concentration of peptide bonds. Aqueous peptide solutions (300 μl, at a given concentration) were prepared in filtered (0.22 μm) 10 mM phosphate buffer, pH 7.4. CD spectra recorded in the presence of synthetic membranes are for lipid:peptide molar ratio of 100:1. CD titrations were performed at 20 °C by titrating anti-cBt (177.5 μM) into cBt (30 μM) to achieve anti-cBt/cBt molar ratios from 0.1 to 2.

Linear Dichroism Spectroscopy—Solution-phase flow linear dichroism spectroscopy was performed on a JASCO-810 spectropolarimeter using a photo elastic modulator 1/2 wave plate, and a micro-volume quartz Couette flow cell with ~0.25 mm annular gap and quartz capillaries (all from Kromatec Ltd.). Molecular alignment was achieved through the constant flow of the sample solution between two coaxial cylinders: a stationary quartz rod and a rotating cylindrical capillary. Linear dichroism (LD) spectra were acquired with laminar flow obtained by maintaining the rotation speed at 3000 rpm and processed by subtracting nonrotating base-line spectra. LD spectra recorded in the presence of synthetic membranes, DLPC and DLPC:DLPG (3:1), were prepared at a lipid:peptide molar ratio of 100:1 (2 mM total lipid, 20 μM peptide).

FTIR Spectroscopy—All FTIR spectra were collected using a Tensor-37 series FTIR spectrophotometer with a BioATR II unit (Bruker Optics) as the sampling platform with a photovoltaic MCT detector and a Bruker Optics work station, which was equipped with OPUS software. Aqueous samples of very low volume (15 μl, 50–130 μM) were placed in a circular sampling area of radius 2 mm with a path length of 6 μm. This multireflection ATR accessory is based on a dual crystal technology, which has an upper silicon crystal and a hemispherical zinc-selenide (ZnSe) lower crystal that does not come into contact with the sample. The temperature of the sample was maintained at 20 °C by means of flow connectors to a circulating water bath. This accessory was purged continuously throughout the experiment with dry nitrogen via telescopic inserts that seals the optical path inside the spectrometer sample compartment. All FTIR spectra were collected with resolution 4 cm^{-1}, scanner velocity 20 kHz, 256 scans, phase resolution 32, and zero filling factor 4.

Analytical Ultracentrifugation—Sedimentation equilibrium experiments for anti-cBt and cBt peptides and their equimolar mixture were carried out at 20 °C in a Beckman Optima XL-I analytical ultracentrifuge fitted with absorbance and interference optics. Sedimentation equilibrium curves were measured by interference optics in the 1.2-cm path length cells. 100-μl samples of 100 μM peptides, individually and as equimolar mixtures buffered to pH 7 with 20 mM potassium phosphate, were used. Buffer density was taken as 1.0007 mg/ml, and samples were equilibrated for 24 h at rotor speeds of 30,000, 37,000 and 50,000 rpm. The data were fitted using routines in Origin (Origin Lab). The average partial specific volumes for the peptides were calculated from the amino acid sequences and were 0.73 ml/mg for all samples.

Isothermal Titration Calorimetry—Measurements were obtained using a Microcal VP-isothermal titration calorimeter and a calorimetric cell (initial volume 1.46 ml) with a 260-s equilibration time and a 120-s initial delay after each addition. The titrations were performed at 20 °C with stirring until no further enthalpy changes were observed. Binding isotherms were recorded for cBt (30 μM) following the injection of anti-cBt (2 μl aliquots, 1.4 mM) into the cell. The observed heats were corrected for dilution effects by titrating peptide solutions, as appropriate, into the buffer and using the heat of last injections due to negligible differences between the first and last injections. All the data were corrected for the volume of the added titrant and analyzed by proprietary software (Microcal Origin 7) using a one-site binding model to allow for the determination of association constants (K_a), changes in enthalpy (ΔH) and enthropy (ΔS). Each experiment was performed in triplicate.

Solid-state NMR—DMPC-d54 and DMPG were purchased from Avanti Polar Lipids and used without further purification. A 3:1 (molar ratio) of DMPC:DMPG (8 mg of total lipid) was

solubilized in a 2:1 mixture (v/v) of chloroform and methanol and dried under a stream of N_2 gas to generate a thin film. The lipid film was subsequently rehydrated with 20 mM HEPES buffer (containing deuterium-depleted H_2O and peptide) at pH 7 to a final volume of 30 μl. 1 mg/ml stock solutions of cecropin mutant and blocker peptides were prepared in deuterium-depleted HEPES buffer at pH 7 and were added to the hydrated lipid to give a final total lipid:peptide molar ratio of 25:1. In samples in which the cecropin mutant and blocker were both present, the individual stock peptide solutions were combined before being diluted and added to the lipid film for rehydration. Static ssNMR experiments were carried out on a Varian Infinityplus 500-MHz spectrometer equipped with a 4-mm MAS HXY probe at 30 °C. All samples were prepared with total lipid concentrations of 10 mg/ml in 20 mM pH 7 HEPES buffer. Static ^{2}H ssNMR spectra were acquired at 76.8 MHz using a quadrupolar echo sequence with a recycle delay of 0.5 s. 200,000 scans were collected, and ^{2}H pulse lengths of 4 μs were used.

Molecular Dynamics Simulations—Molecular dynamics simulations of the cecropin assembly inserted in aqueous solution were performed in GROMACS (v4.5.5) using the AMBER99SB-ILDN force field with 150 mM concentration of sodium and chloride molecules for charge neutralization. AMBER99SB-ILDN was chosen following testing of four force fields, and correctly reproduced phenomena were observed in the primary monomeric spectra whereas other force fields showed helical bias. Monomeric structures were simulated for 50 ns in the NPT ensemble following energy minimization, 200-ps equilibration in the NVT ensemble, and 200-ps equilibration in the NPT ensemble. The dimer structure was run for 100 ns with 200ips equilibration steps in the NVT and NPT ensembles, both with and without peptide position restraints. These extra steps allowed for relaxation of the solvent and the dimer in each ensemble. The initial helical configuration was obtained using the XPlor-NIH structure determination algorithm. In detail, the temperature was coupled using a velocity-rescaling thermostat (coupling time 0.1 ps) with separate peptide and solvent coupling groups. Pressure coupling was isotropic and achieved through a Parrinello-Rahman coupling scheme (coupling time 2.0 ps).

Bond lengths were constrained using the LINCS algorithm. The TIP3P water model was used, and a time step of 2 fs was used throughout. Coulomb and van der Waals forces were treated by a twin range cut-off scheme, with short range electrostatics experiencing a cutoff of 1 nm and long range by particle-mesh Ewald with grid spacing of 0.12 nm. Pair-lists were updated every five steps.

Minimum Inhibitory Concentration (MIC) Assay—MICs were determined by broth microdilution on *Pseudomonas aeruginosa* ATCC 27853, *Escherichia coli* K12, *Staphylococcus aureus* ATCC 25723, *Micrococcus luteus* NCIMB 13267, and *Bacillus subtilis* ATCC 6633 according to the Clinical and Laboratory Standards Institute. Typically, 100 μl of 0.5–1 $\times$ 10^6 cfu/ml of each bacterium in Mueller-Hinton medium broth (Oxoid) was incubated in 96-well microtiter plates with 100 μl of serial 2-fold dilutions of the peptides (from 100 to 0 μM) at 37 °C on a three-dimensional orbital shaker. The absorbance was measured after peptide addition at 600 nm using a Victor 2 plate reader (PerkinElmer Life Sciences). MICs were defined as the lowest peptide concentration after 24 h at 37 °C. All tests were done in triplicate.

*Stain-dead Antimicrobial Assay—S. aureus (*ATCC 25723) culture (1 ml) was centrifuged to give a cell pellet, which was washed twice with 10 mM phosphate buffer, pH 7.4, before being reconstituted in phosphate buffer to give $A_{600\ nm} = 0.008$. 1 ml of the solution was dispensed in a 2-well glass chamber (LabTek) with diluted (1/500) propidium iodide (1 mg/ml, from Invitrogen). The chambers with surface-settled bacteria (60 min) were mounted on a confocal microscope (Olympus) equipped with an incubation chamber at 37 °C. Propidium iodide fluorescence emission was monitored at 625 nm for 60 min (three frames/min) using an appropriate filter after the addition of peptide (1 ml). Recorded images (XYZ) were analyzed using Fiji software to plot the number of fluorescent (stain-dead) cells as a function of time.

Hemolysis Assay—Hemolysis was determined by incubating 10% (v/v) suspension of human erythrocytes with peptides. Erythrocytes were rinsed four times in 10 mM PBS, pH 7.2, by repeated centrifugation and resuspension (3 min at 3000 $\times$ *g*). Erythrocytes were incubated at room temperature for 1 h in either deionized water (fully hemolysed control), PBS, or with peptide in PBS. After centrifugation at 10,000 $\times$ *g* for 5 min, the supernatant was separated from the pellet and the absorbance measured at 550 nm. Absorbance of the suspension treated with deionized water defined complete hemolysis. The values below correspond to the percentage of hemolysis at tested concentrations. All tests were done in triplicate.

Gram Stain Assays—20 μl of a bacterium culture was dispensed onto a glass slide and spread well. The slide was swiftly passed through a Bunsen flame to dry and fix cells before staining. The fixed bacteria were first covered in crystal violet (0.25%) for 30 s followed by washing with water (distilled, filtered 0.22 μm) until all of the excess stain was washed off, and then with iodine (1.0%) for 2 min before washing with a minimum amount of acetone needed to rinse off the iodine color. The cells were counterstained with safranin (0.5%) for 30 s, washed with water, and dried by a Bunsen flame. The obtained slides were viewed under a Leica DMLB fluorescent microscope. The images were obtained at $\times$100 magnification under oil and analyzed by ImageJ.

RESULTS

Cathelicidin Assembly Design— b27 consists of 27 amino acid residues with one glycine at each terminus (20). The C-terminal heptad of the peptide is predominantly hydrophobic and contains a P*XX*P motif, which is believed to promote membrane insertion (22). A larger N-terminal stretch has three incomplete coiled-coil heptads starting with a charged arginine at *g* followed by putative *a*/*d* and *g*/*e* patterns. An antagonist sequence, anti-b27, was designed to match these patterns in a parallel arrangement. *a* and *d* positions were occupied by core-stabilizing combinations of phenylalanine and leucine residues to favor low oligomers while promoting cooperative folding (23–25). Negatively charged glutamates were used in *g* and *e* positions of anti-b27 to pair corresponding *g*′, *e*′ lysines and arginines in b27. The remaining *b*, *c*, and *f* sites were made neutral polar and

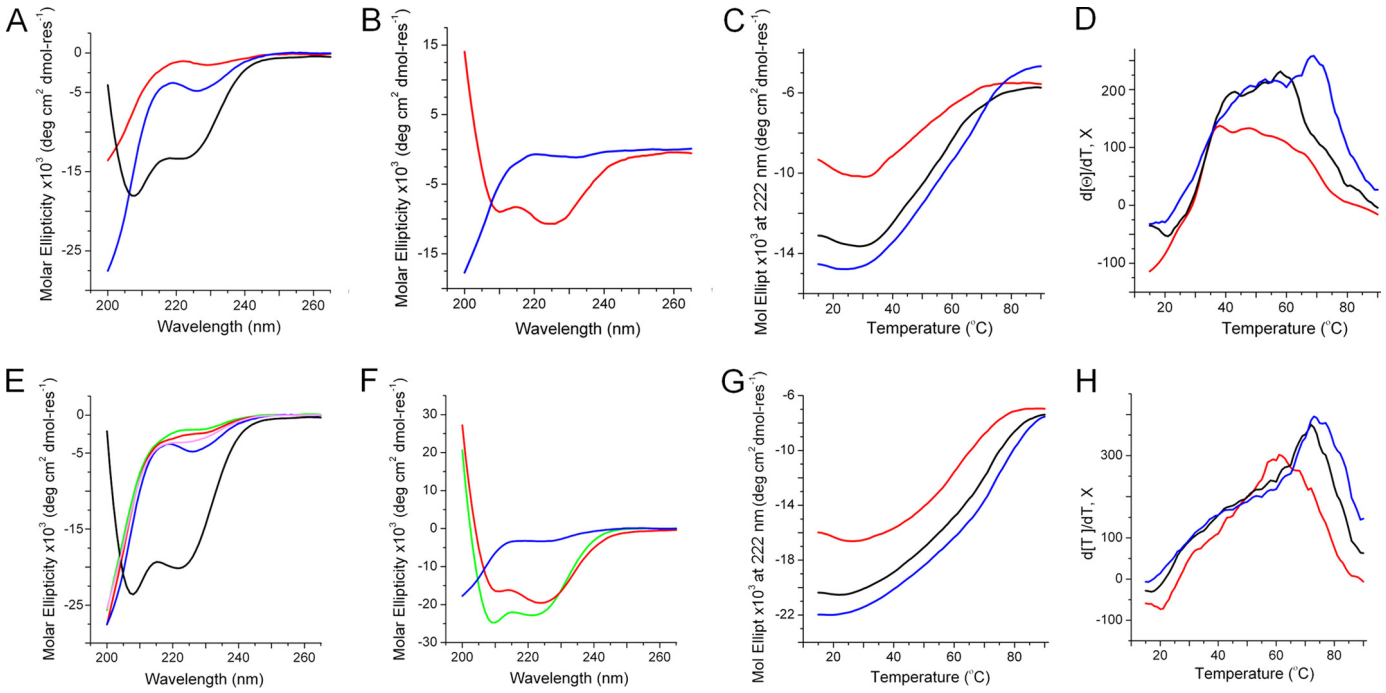

FIGURE 2. **Peptide folding probed by CD spectroscopy.** *A*, CD spectra for b27 (*red line*), anti-b27 (*blue line*), and anti-b27:b27 (*black line*) in 10 mM phosphate buffer. *B*, CD spectra for b27 (*red line*) and anti-b27 (*blue line*) in anionic membranes. *C* and *D*, thermal unfolding curves (*C*) and their first derivatives for anti-b27:b27 (*D*) as a function of temperature at 222 nm. *E*, CD spectra for cB (*green line*), cBt (*red line*), anti-cBt (*blue line*), anti-cBt:cB (*magenta line*), and anti-cBt:cBt (*black line*) in 10 mM phosphate buffer. *F*, CD spectra for cB (*green line*), cBt (*red line*), and anti-cBt (*blue line*) in anionic membranes. *G* and *H*, thermal unfolding curves (*G*) and their first derivatives (*H*) for anti-cBt:cBt as a function of temperature at 222 nm. CD spectra are for 30 μM concentration of each peptide, pH 7.4, room temperature. Thermal unfolding curves are for 15 μM (*red line*), 30 μM (*black line*), and 50 μM (*blue line*) concentration of each peptide. Lipid-peptide ratio for CD spectra in anionic membranes was 100:1.

TABLE 1
Biological activity of peptides

Peptide	Minimum inhibitory concentration (MIC)					HE (LC_{50})[a]
	E. coli (K12)	*P. aeruginosa* (ATCC27853)	*B. subtilis* (ATCC6633)	*S. aureus* (ATCC6538)	*M. luteus* (NCIMB 13267)	
	μM	μM	μM	μM	μM	μM
b27	3.13 ± 0.43	4.51 ± 1.56	0.78 ± 0.01	>100	0.74 ± 0.33	≫250
Anti-b27	>200	>200	>200	>200	>200	≫250
cB	0.62 ± 0.01	1.56 ± 0.01	50.7 ± 0.10	>100	0.46 ± 0.20	≫250
cBt	1.28 ± 0.04	1.55 ± 0.01	6.33 ± 0.12	25.9 ± 0.06	0.36 ± 0.10	≫250
Anti-cBt	>200	>200	>200	>200	>200	≫250

[a] Human erythrocytes, 50% cell death compared with untreated cells, 1–9% at 250 μM.

alanine residues. The P*XX*P motif in the antagonist was deemed redundant and was replaced to stabilize coiled-coil formation. Fig. 1*A* summarizes the design.

Cathelicidin Assembly Folding—Consistent with the design, the peptides did not fold individually in aqueous solutions at micromolar concentrations. Circular dichroism (CD) spectra were characteristic of random coil or disordered conformations (Fig. 2*A*). Similarly, none of the peptides folded in the presence of zwitterionic unilamellar vesicles whose composition mimics that of mammalian membranes (supplemental Fig. S1). In contrast, CD spectra for equimolar peptide mixtures showed appreciable helical signals indicative of coiled-coil formation (Fig. 2*A*). The behavior of the peptides in anionic unilamellar vesicles, which mimicked microbial membranes, was consistent with the observations. Unlike anti-b27, which remained disordered, b27 underwent a coil-helix transition suggesting membrane binding (Fig. 2*B*).

The helix content in both cases did not exceed 35% (supplemental Fig. S1). The percentage of α-helix was estimated using the equation: $-100([\theta]_{222} + 3000)/33{,}000$ (26). However, the thermal denaturation of pair mixtures gave sigmoidal unfolding curves indicative of cooperatively folded structures (Fig. 2*C*). Low temperature CD and FTIR spectra recorded before and after thermal unfolding revealed almost complete reversibility of folding (supplemental Fig. S1). The first derivatives of the unfolding curves comprised several overlapping transitions with two clear cut-offs of transition midpoints (T_m) at approximately 37 °C and 70 °C, with the higher T_m becoming more pronounced at higher concentrations (Fig. 2*D*). The transitions were broadly within the biokinetic temperature ranges. However, the lower cut-off remained apparent at all concentrations and was dominating at lower concentrations (Fig. 2*D*). Although b27 was strongly antimicrobial (Table 1) the effect of the antagonist on the activity of b27 could not be measured with certainty (results not shown). Therefore, anti-b27-b27 interactions were deemed insufficiently stable under physiological conditions. The lack of stability can be attributed to that *g-e′* interactions available in b27 can support the assembly of only

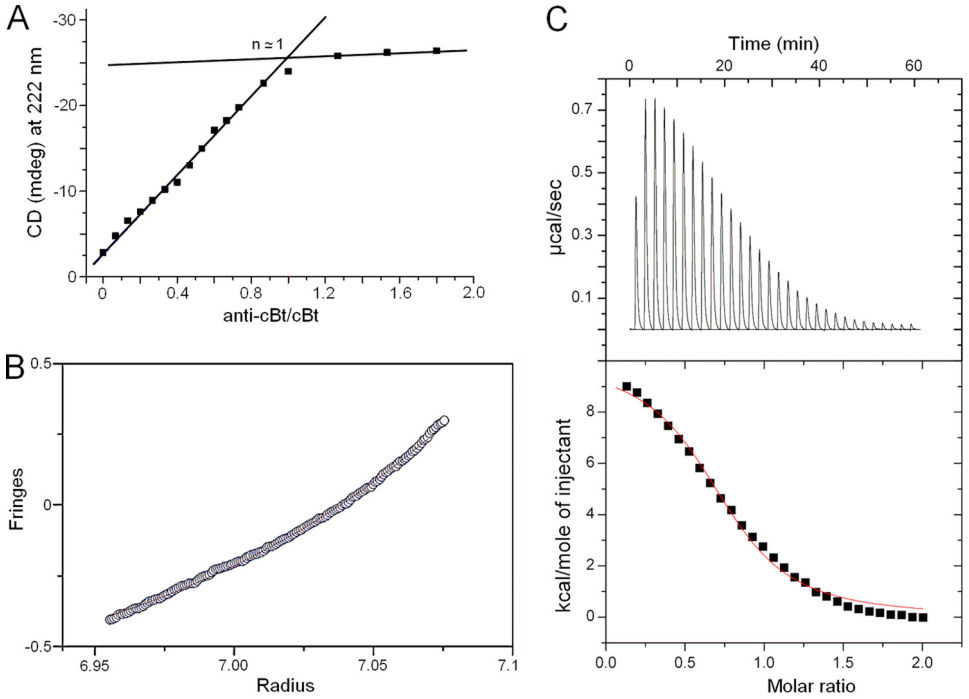

FIGURE 3. **Stoichiometry of anti-cBt:cBt interactions.** *A*, CD points recorded for 222 nm by titrating anti-cBt into cBt (30 μM). The *intersection* of the *lines* fitted on the titration curve indicates a 1:1 binding stoichiometry. *B*, sedimentation equilibrium analysis. Experimental data (*open circles*) were collected at 37,000 rpm for a 100 μM sample at 20 °C. The *line* is a calculated curve for an ideal dimer. *C*, isothermal titration calorimetry of the interactions. Heat absorbed (μcal/s) for each isotherm is plotted *versus* titration time (min) and shows endothermic binding (*top panel*). Integrated heats (kcal/mol) are plotted *versus* anti-cBt:cBt molar ratios (*bottom panel*).

two combined heptads, which falls short of a stable coiled coil formed by three contiguous heptads (Fig. 1*A*) (11). The longer cB sequence was thus probed.

Cecropin Assembly Design— cB comprises 35 amino acid residues and three G(*X*)$_n$G motifs, which in principle can span five canonical coiled-coil repeats. However, all three G(*X*)$_n$G motifs form a contiguous stretch starting in the second heptad from the N terminus which makes the assigning of contiguous coiled-coil patterns problematic. Searches using coiled-coil prediction algorithms (Paircoil2, COILS, Multicoil), albeit biased toward stand-alone sequences, did not give any apparent pattern either. Therefore, selective point mutations were allowed.

The central G(*X*)$_4$GP motif and the tryptophan residue, important for activity (27), were kept in the sequence. The N-terminal lysine was assigned to the first *g* position. This ensured minimum mutations by placing isoleucines and leucines in *a* and *d* and by swapping hydrophobic and polar residues in *g* and *a* to enable contiguous *a-d*/*e-g* pairs (23–25). A single Ala→Lys mutation at an *e* position was adapted to enable a continuous network of electrostatic interhelical interactions, whereas a Glu→Gln mutation at a *b* position excluded an intrahelical *i, i*+4 electrostatic interaction. This completes a cB template, cBt. Similar to the anti-b27, anti-cBt was designed to mirror the *a-d*/*e-g* arrangements in cBt. Glutamates were used at all *e* and *g* sites, whereas isoleucines and leucines occupied *a* and *d* sites. The G(*X*)$_4$GP was simplified to G(*X*)$_5$P. This stretch is functionally irrelevant for anti-cBt, which is meant to be biologically inactive, but structurally it is sufficient to prevent the sequence of such length to fold autonomously. In the resulting anti-cBt:cBt arrangement all five heptads of cBt contribute to the binding with anti-cBt with the number of *e-g*′ pairs being nearly doubled compared with b27 (Fig. 1*B*).

Cecropin Assembly Folding—The CD spectra of the pair in aqueous solutions revealed 20% increases in helicity (26) *versus* those recorded for anti-b27:b27 (Fig. 2, *A* and *E*, and supplemental Fig. S1). Comparable helical signals were recorded for cBt and cB in anionic membranes (Fig. 2*F*). None of the peptides folded in zwitterionic membranes (supplemental Fig. S1). CD spectra for individual peptides and the equimolar mixtures of cB with anti-cBt in solution as well as anti-cBt in anionic membranes were characteristic of random coils (Fig. 2, *E* and *F*). CD titrations performed by adding anti-cBt into the buffered cBt, which was kept at a constant concentration, provided quantitative information of coiled-coil interactions. The CD values (millidegrees at 222 nm) showed saturation after reaching an equimolar anti-cBt:cBt ratio (n = 1) allowing thus the stoichiometry of the complex being calculated from the titration curve as 1:1 (Fig. 3*A*). Sedimentation equilibrium data, which fitted an analysis that assumed a single ideal species, returned a M_r of 7148 (93% confidence limits of 6766 and 7527) for the 1:1 anti-cBt:cBt mixture, which was close to that expected for an anti-cBt:cBt dimer (7811), *versus* a M_r of 3508 (3328, 3691) for the monomeric anti-cBt (3843) (Fig. 3*B*). Further evidence comes from isothermal titration calorimetry experiments. Binding isotherms obtained for cBt titrated with anti-cBt support endothermic binding characteristic of native coiled-coil systems (28), and the integrated heats fitted into a single site binding model gave a stoichiometry of 1:1 (n = 0.8) and a strong association (binding) constant (K_a) of 2.8 ± 0.2 × 10^6 M^{-1}. The endothermic binding enthalpy (ΔH) for this inter-

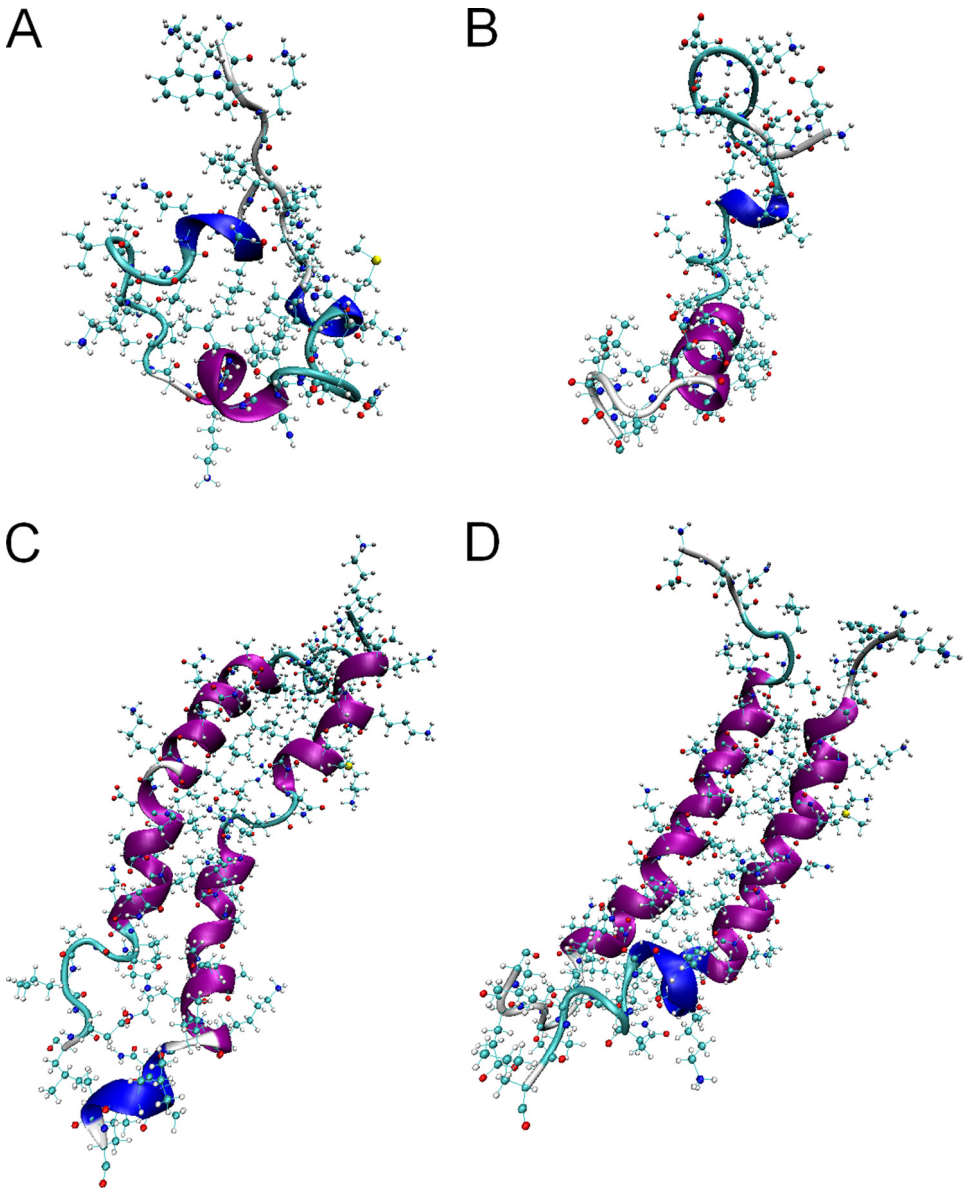

FIGURE 4. **Molecular dynamics simulations of cecropin assembly.** Secondary structure visualization after 50 ns for cBt (*A*) and anti-cBt (*B*), and for anti-cBt:cBt (*C*) at the initial configuration (0 ns) and after 100 ns (*D*).

action was 9.7 kcal/mol with a favorable ΔG of −7.8 kcal/mol (Fig. 3*C*).

Consistent with the design, the results are comparable with those for other native and designed coiled-coil systems (28–30) and indicate that cB and cBt efficiently and selectively bind to anionic membranes and anti-cBt bundles up with cBt. Collectively, the data confirm cooperative and strong anti-cBt-cBt interactions, which remain at equilibrium with cBt.

To gain a better insight into oligomerization we performed molecular dynamics simulations using the Amber99SB-ILDN force field (supplemental text) (31). The 20-ns simulations of individual peptides revealed random conformations with no further significant changes to the peptides observed into 50 ns of simulations. Elements of helical structure in individual residues and short peptide stretches were present in both peptides which can be accounted for by their high helical propensities (Fig. 4, *A* and *B*, and supplemental Fig. S2). When visualized together following an equilibration phase, anti-cBt and cBt appeared to align in parallel supported by hydrophobic (*a-d*) and charged (*e-g*) contacts (Fig. 4*C*). At initial configurations (0 ns) the C-terminal fragments and hinge regions proved to be partly unfolded, but over 100 ns the assembly evolved into a rigid α-helical structure (Fig. 4*D*), which was consistent with the secondary structure analysis of each residue using the STRIDE secondary structure algorithm (supplemental Fig. S2). The C-terminal fragments retained a degree of unfolding, suggesting some fraying of the assembly. This arrangement was maintained over 100 ns conforming to the formation of a stable and cooperatively folded structure.

The findings were further supported by sigmoidal unfolding curves of anti-cBt:cBt (Fig. 2*G*). The first derivatives of the curves gave dominating transition midpoints at >60 °C, which at higher concentrations increased to >70 °C (Fig. 2*H*). The obtained spectra had some structure suggesting partial unfold-

ing, consistent with the simulations, or α-to-β conformational transitions. CD spectra recorded after the thermal denaturation agreed with incomplete reversibility of folding, whereas FTIR spectra recorded before and after thermal denaturation showed nearly identical helical bands at 1650 cm^{-1} and 1550 cm^{-1}, with no indication of a β-sheet switch (1610–1625 cm^{-1}) (supplemental Fig. S1). CD spectroscopy can only reveal averaged or relative changes in helicity corresponding to mixed types of binding comprising membrane-bound antimicrobial peptides and assembled coiled coils, both of which are associated with helix formation.

Further evidence for antagonist effects on antimicrobial peptides may be ascertained from changes in membrane binding monitored by LD spectroscopy. LD arises from differential absorption of light linearly polarized parallel and perpendicular to an orientation axis and thereby provides a convenient probe of relative peptide orientation to the membrane surface (32). LD spectra for cB and cBt in anionic membranes were similar and showed positive and negative bands at approximately 200–210 nm and 220–230 nm, respectively, which are characteristic of π-π^* and n-π^* electronic transitions of peptide helices lying flat on membrane surfaces (33). This is consistent with the proposed carpet-like mechanism of action for cB (34) and indicates that cBt should retain this mode of action (Fig. 5*A* and supplemental Fig. S3).

Negligible signals were recorded for anti-cBt in anionic membranes (Fig. 5*A* and supplemental Fig. S3) and for all peptides in zwitterionic membranes (supplemental Fig. S3). In the presence of anti-cBt no absorption patterns could be identified, suggesting interfering contributions from anti-cBt (Fig. 5*A* and supplemental Fig. S3). LD spectra for preformed anti-cBt:cBt complexes at different ratios were also negligible without specific binding or orientation, but revealed shape similarities with the spectra for cBt implying competing interactions of cBt for anti-cBt and membrane surfaces (Fig. 5*A* and supplemental Fig. S3). Further support for this conclusion comes from solid-state NMR studies.

Fig. 5*B* shows static ^2H spectra of anionic membranes with chain-deuterated lipids (DMPC-d54) in the absence and presence of the peptides. Spectra for the membrane alone showed maximum and minimum splittings of 28 and 4.9 kHz, respectively. Intermediate peaks that correspond to CD_2 groups along the fatty acid acyl chains were well resolved. On addition of cBt, no individual peaks could be resolved, suggesting that the peptide interacts with and disorders the lipid molecules along the length of the acyl chains. In marked contrast, the innermost and outermost splittings for anti-cBt:cBt were consistent with the lipid only spectrum, suggesting that anti-cBt prevents cBt from disrupting the lipids. In all of the spectra, the innermost splitting corresponding to the CD_3 groups on the ends of the acyl chains was apparent, implying that the lipid termini remained buried within the lipid bilayer, which together with that there were no dominant peaks observed at 0 kHz suggests that micellization did not take place (Fig. 5*B*). The observations are consistent with the CD and LD data in that cBt folds onto anionic membranes and binds with its antagonist through cooperative interactions that interfere with membrane binding (35).

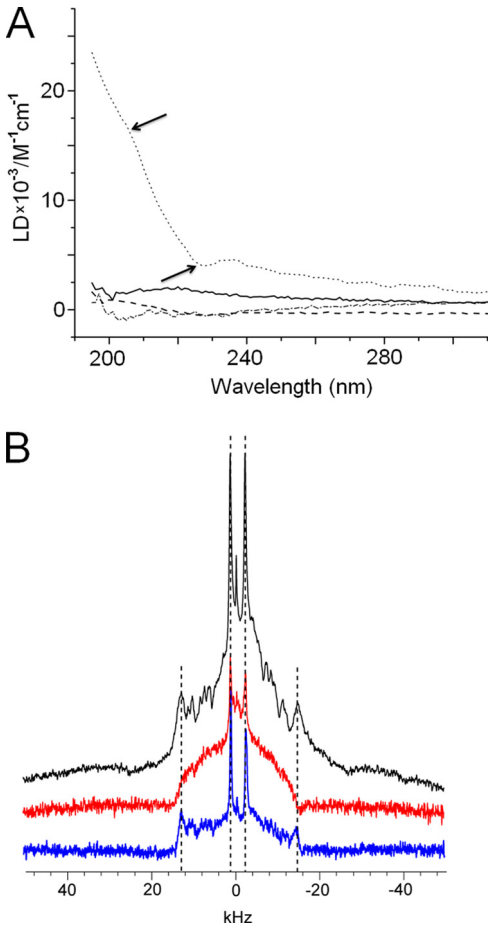

FIGURE 5. **Cecropin folding in anionic membranes.** *A*, LD spectra for cBt (*dotted line*), anti-cBt (*bold line*), cBt added to anti-cBt (*dashed line*) and preformed anti-cBt:cBt (*dot-dashed line*). Lipid-peptide ratio was 100:1 (20 μM peptide), pH 7.4, room temperature. *Arrows* point to π-π^* and n-π^* electronic transition bands. *B*, solid-state NMR spectra for blank (no peptide, *black*), cBt (*red*), and anti-cBt:cBt (*blue*). Lipid-peptide ratio was 25:1, pH 7.4, room temperature. *Vertical dashed lines* are to assist comparison between the innermost and outermost splittings of the three spectra.

Cecropin Assembly in Bacterial Culture—The results discussed so far support the formation of anti-cBt:cBt complexes that can exist in dynamic membrane environments. However, to be competitive under equilibrium conditions the interactions are likely to require anti-cBt in excess. In physiological terms, this is consistent with that AMPs must respond to microbial challenge within their proteolytic life time (*i.e.* minutes) and that inhibitory effects on antimicrobial activity should become apparent within the same time scale.

To probe this, we performed stain-dead assays using a log-phase planktonic culture of *S. aureus*. MICs against the bacterium were at 15–30 μM ranges (25 μM, Table 1), at which anti-cBt:cBt were stable up to 70 °C (Fig. 2*H*). In these assays the fluorescence emission of propidium iodide used as a dead cell marker was measured after peptide addition as a function of time (Fig. 6).

To directly assess the inhibition of cBt by anti-cBt the total number of cells lysed by cBt at the MIC after 1 h was taken as 100% killing rates. Thus, in the first 30 min killing rates for cB and cBt were ~60 and ~40%, respectively (Fig. 6, *A* and *B*). No effects observed for anti-cBt at concentrations ≥100 μM, and marginal killing rates (10%) at higher concentrations (>250

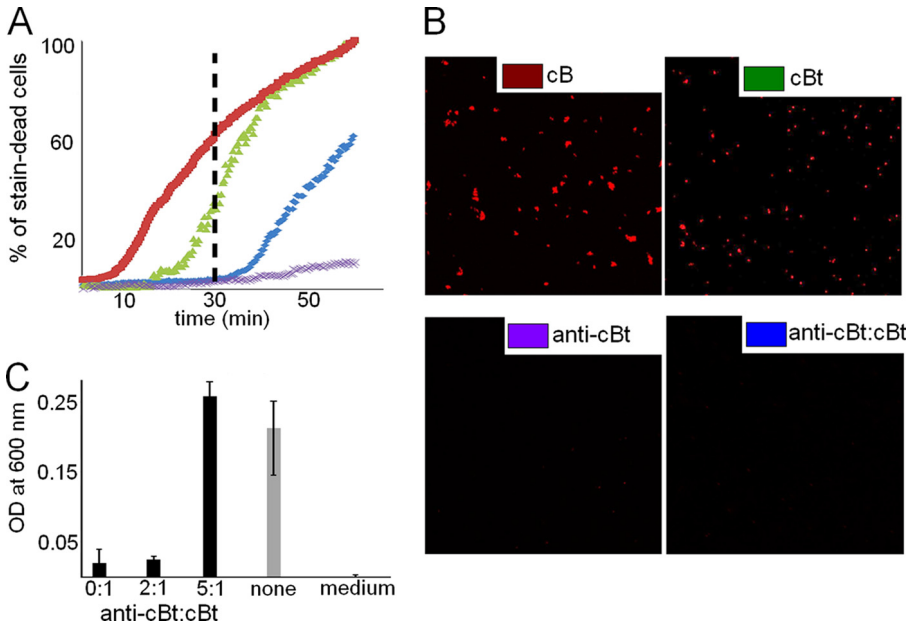

FIGURE 6. **Stain-dead *S. aureus* cells.** *A*, percentage of stain-dead cells as a function of time for cB (100 μM, *red squares*), cBt (25 μM, *green triangles*), anti-cBt (250 μM, *purple crosses*), and anti-cBt:cBt (125:25 μM, *blue diamonds*). *B*, confocal microscopy images of cells stained with propidium iodide after incubation with corresponding peptide. *C*, absorbances measured overnight at 600 nm for the bacterium incubated with anti-cBt:cBt at different ratios (*black pillars*), for the bacterium without peptide and for the culture medium only (*gray pillars*). *Error bars*, S.D.

μM) were consistent with the medium cytotoxicity of the peptide at hemolytic concentrations (Table 1). For anti-cBt:cBt at 5–10:1 molar ratios a continuous lag-phase in killing rates of <10% was observed over the first 40 min of incubation (Fig. 6, *A* and *B*). The effect then became less apparent with gradual exponential increases in killing rates up to 60% after 60 min accounting for 40% decreases in the activity of cBt. The optical density measurements of bulk culture overnight (MIC assays) at 5–10:1 ratios gave the visible growth of *S. aureus* which was comparable with that of the bacterium without peptide (Fig. 6*C*). In contrast, lower anti-cBt:cBt ratios (<5:1) imposed no inhibition on the antimicrobial activity of cBt (Fig. 5*C*). *E. coli* and *P. aeruginosa* that were found to be more susceptible to cBt (Table 1) gave varied and irreproducible MIC differences between cBt and anti-cBt:cBt. Because optical density measurements take no account of changes at the cellular level we sought additional evidence from Gram stain assays for these strains. *E. coli* and *P. aeruginosa* incubated with peptide for 16 h were Gram-stained and imaged by optical microscopy (Fig. 7*A* and supplemental Fig. S4). Nearly complete inhibition of cell growth by cBt was apparent for both strains. No obvious effects were found for anti-cBt and anti-cBt:cBt samples (10:1) in which cell populations were remarkably similar for both strains (Fig. 7, *A* and *B*). Round and blue-stained spheroplasts, particularly for *P. aeruginosa*, were observed for cBt and anti-cBt:cBt samples, but not in anti-cBt samples. This is consistent with spheroplast-forming activities of cell wall or membrane-active antibiotics (36), which implies that anti-cBt:cBt may retain residual antimicrobial activity of cBt giving rise to cell wall deficient-forms (Fig. 7).

DISCUSSION

The results prompt several conclusions. Firstly, anti-antimicrobial activity may occur at a microscopic level, which is not necessarily detected by changes in optical density. Second, the 5–10:1 ratios of anti-AMP to AMP give detectable anti-antimicrobial effects. Third, coiled-coil stability, which directly links to primary structure, determines all of these points. Indeed, other antimicrobial sequences that are biologically and structurally similar to cB and b27 are shorter. This decreases the probability of shorter antagonists and their assemblies with AMPs. Magainin 2 (m2) can serve as an example. The peptide is a 23-mer with one $G(X)_4G$ motif, which thus can represent a shorter version of cB. Although it was possible to assign a coiled-coil template in the sequence our attempts to find an efficient antagonist were unsuccessful (supplemental Figs. S5 and S6). Furthermore, mutations used to generate suitable magainin templates significantly compromised membrane binding (supplemental Fig. S6). This lack in sequence plasticity may not come as a surprise if one considers that shorter antimicrobial helices may aim at minimizing the possibility of co-folding with potential antagonists, which in turn are challenged to produce stronger binders. Such a competition is pre-defined in native AMPs which contain the patterns of both antimicrobial helices and coiled coils. The former is thus designed to prevail in membrane environments but can become "frustrated" by a competitive trigger, an antagonist, which gives way to the latter.

Antimicrobial peptides are being considered as new drug candidates in the post-antibiotic era (7). Their clinical potential is largely attributed to that widespread microbial resistance against them has yet to emerge (10, 37, 38). In this context, it is plausible to suggest that antagonistic sequences secreted by bacterial cells or expressed on their surfaces may elicit anti-antimicrobial responses. Although this remains to be shown in nature, this report, to the best of our knowledge, provides the first example of peptide sequences capable of

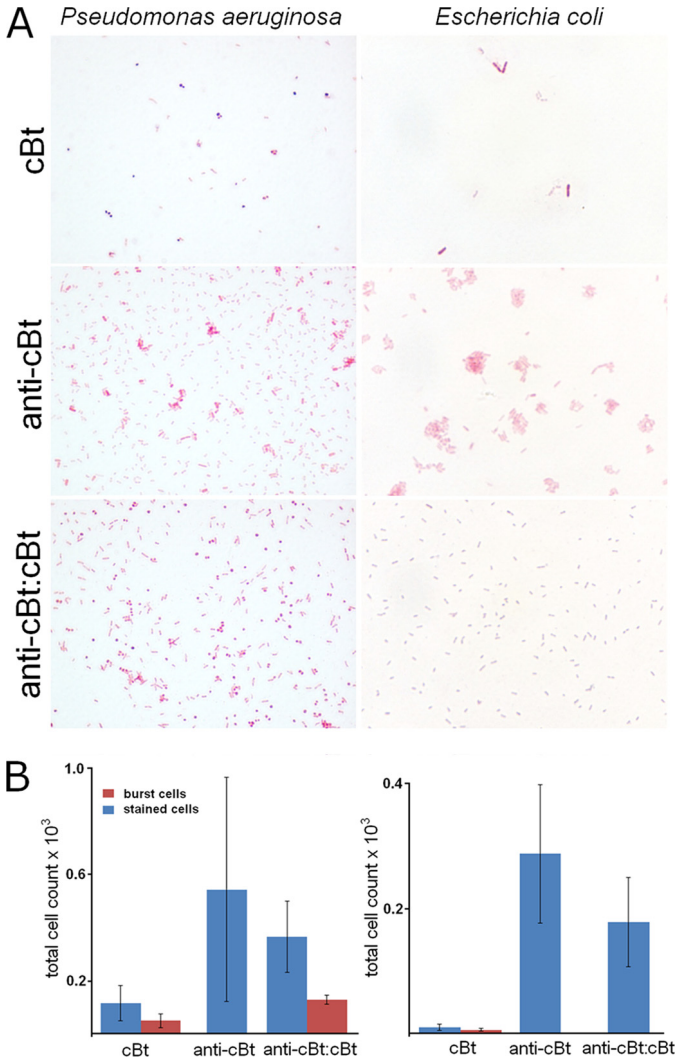

FIGURE 7. *A*, 100× light micrographs of Gram-stained *E. coli* and *P. aeruginosa* after overnight incubations with peptide. *B*, averaged total of Gram-stained cells. Shown is anti-cBt:cBt at (100:10 μM).

antagonistic responses to the action of host defense peptides. Specifically, the combination of experimental and computational approaches confirms a coiled-coil-mediated antagonistic mechanism which is consistent with the functional basis of antimicrobial peptides as local and short contact time immune regulators.

REFERENCES

1. Rose, A., and Meier, I. (2004) Scaffolds, levers, rods and springs: diverse cellular functions of long coiled-coil proteins. *Cell Mol. Life Sci.* **61,** 1996–2009
2. Boucrot, E., Pick, A., Çamdere, G., Liska, N., Evergren, E., McMahon, H. T., and Kozlov, M. M. (2012) Membrane fission is promoted by insertion of amphipathic helices and is restricted by crescent BAR domains. *Cell* **149,** 124–136
3. Lin, R. C., and Scheller, R. H. (2000) Mechanisms of synaptic vesicle exocytosis. *Annu. Rev. Cell Dev. Biol.* **16,** 19–49
4. De Matteis, M. A., and Morrow, J. S. (2000) Spectrin tethers and mesh in the biosynthetic pathway. *J. Cell Sci.* **113,** 2331–2343
5. Knodler, L. A., Ibarra, J. A., Pérez-Rueda, E., Yip, C. K., and Steele-Mortimer, O. (2011) Coiled-coil domains enhance the membrane association of *Salmonella* type III effectors. *Cell Microbiol.* **13,** 1497–1517
6. Naider, F., and Anglister, J. (2009) Peptides in the treatment of AIDS. *Curr. Opin. Struct. Biol.* **19,** 473–482
7. Fjell, C. D., Hiss, J. A., Hancock, R. E., and Schneider, G. (2012) Designing antimicrobial peptides: form follows function. *Nat. Rev. Drug Discov.* **11,** 37–51
8. Grigoryan, G., and Keating, A. E. (2008) Structural specificity in coiled-coil interactions. *Curr. Opin. Struct. Biol.* **18,** 477–483
9. Lupas, A. N., and Gruber, M. (2005) The structure of α-helical coiled coils. *Adv. Protein Chem.* **70,** 37–78
10. Peschel, A., and Sahl, H. G. (2006) The co-evolution of host cationic antimicrobial peptides and microbial resistance. *Nat. Rev. Microbiol.* **4,** 529–536
11. Rozzelle, J. E., Jr., Tropsha, A., and Erickson, B. W. (1994) Rational design of a three-heptad coiled-coil protein and comparison by molecular dynamics simulation with the GCN4 coiled coil: presence of interior three-center hydrogen bonds. *Protein Sci.* **3,** 345–355
12. Senes, A., Engel, D. E., and DeGrado, W. F. (2004) Folding of helical membrane proteins: the role of polar, GxxxG-like and proline motifs. *Curr. Opin. Struct. Biol.* **14,** 465–479
13. Kim, S., Jeon, T. J., Oberai, A., Yang, D., Schmidt, J. J., and Bowie, J. U. (2005) Transmembrane glycine zippers: physiological and pathological roles in membrane proteins. *Proc. Natl. Acad. Sci. U.S.A.* **102,** 14278–14283
14. Simmaco, M., Kreil, G., and Barra, D. (2009) Bombinins, antimicrobial peptides from *Bombina* species. *Biochim. Biophys. Acta* **1788,** 1551–1555
15. MacKenzie, K. R., Prestegard, J. H., and Engelman, D. M. (1997) A transmembrane helix dimer: structure and implications. *Science* **276,** 131–133
16. Glukhov, E., Stark, M., Burrows, L. L., and Deber, C. M. (2005) Basis for selectivity of cationic antimicrobial peptides for bacterial versus mammalian membranes. *J. Biol. Chem.* **280,** 33960–33967
17. Mygind, P. H., Fischer, R. L., Schnorr, K. M., Hansen, M. T., Sönksen, C. P., Ludvigsen, S., Raventós, D., Buskov, S., Christensen, B., De Maria, L., Taboureau, O., Yaver, D., Elvig-Jørgensen, S. G., Sørensen, M. V., Christensen, B. E., Kjaerulff, S., Frimodt-Moller, N., Lehrer, R. I., Zasloff, M., and Kristensen, H. H. (2005) Plectasin is a peptide antibiotic with therapeutic potential from a saprophytic fungus. *Nature* **437,** 975–980
18. Gourley, D. G., Schüttelkopf, A. W., Leonard, G. A., Luba, J., Hardy, L. W., Beverley, S. M., and Hunter, W. N. (2001) Pteridine reductase mechanism correlates pterin metabolism with drug resistance in trypanosomatid parasites. *Nat. Struct. Biol.* **8,** 521–525
19. Veit, G., Kobbe, B., Keene, D. R., Paulsson, M., Koch, M., and Wagener, R. (2006) Collagen XXVIII, a novel von Willebrand factor A domain-containing protein with many imperfections in the collagenous domain. *J. Biol. Chem.* **281,** 3494–3504
20. Zanetti, M. (2004) Cathelicidins, multifunctional peptides of the innate immunity. *J. Leukoc. Biol.* **75,** 39–48
21. Boman, H. G. (2003) Antibacterial peptides: basis facts and emerging concepts. *J. Intern. Med.* **254,** 197–215
22. Yang, S. T., Jeon, J. H., Kim, Y., Shin, S. Y., Hahm, K. S., and Kim, J. I. (2006) Possible role of a P*XX*P central hinge in the antibacterial activity and membrane interaction of PMAP-23, a member of cathelicidin family. *Biochemistry* **45,** 1775–1784
23. Yoder, N. C., and Kumar, K. (2006) Selective protein-protein interactions driven by a phenylalanine interface. *J. Am. Chem. Soc.* **128,** 188–191
24. Tripet, B., Wagschal, K., Lavigne, P., Mant, C. T., and Hodges, R. S. (2000) Effects of side-chain characteristics on stability and oligomerization state of a de novo-designed model coiled coil: 20 amino acid substitutions in position "d." *J. Mol. Biol.* **300,** 377–402
25. Ryadnov, M. G., Bella, A., Timson, S., and Woolfson, D. N. (2009) Modular design of peptide fibrillar nano- to microstructures. *J. Am. Chem. Soc.* **131,** 13240–13241
26. Morrisett, J. D., Jackson, R. L., and Gotto, A. M., Jr. (1977) Lipid-protein interactions in the plasma lipoproteins. *Biochim. Biophys. Acta* **472,** 93–133
27. Oh, D., Shin, S. Y., Lee, S., Kang, J. H., Kim, S. D., Ryu, P. D., Hahm, K. S., and Kim, Y. (2000) Role of the hinge region and the tryptophan residue in the synthetic antimicrobial peptides, cecropin A(1–8)-magainin 2(1–12) and its analogues, on their antibiotic activities and structures. *Biochemis-*

try **39,** 11855–11864
28. Sharma, A. K., Zhou, G. P., Kupferman, J., Surks, H. K., Christensen, E. N., Chou, J. J., Mendelsohn, M. E., and Rigby, A. C. (2008) Probing the interaction between the coiled-coil leucine zipper of cGMP-dependent protein kinase Iα and the C terminus of the myosin binding subunit of the myosin light chain phosphatase. *J. Biol. Chem.* **283,** 32860–32869
29. De Crescenzo, G., Litowski, J. R., Hodges, R. S., and O'Connor-McCourt, M. D. (2003) Real-time monitoring of the interactions of two-stranded *de novo* designed coiled-coils: effect of chain length on the kinetic and thermodynamic constants of binding. *Biochemistry* **42,** 1754–1763
30. Ryadnov, M. G., Ceyhan, B., Niemeyer, C. M., and Woolfson, D. N. (2003) "Belt and braces": a peptide-based linker system of *de novo* design. *J. Am. Chem. Soc.* **125,** 9388–9394
31. Cerasoli, E., Ravi, J., Gregor, C., Hussain, R., Siligardi, G., Martyna, G., Crain, J., and Ryadnov, M. G. (2012) Membrane mediated regulation in free peptides of HIV-1 gp41: minimal modulation of the hemifusion phase. *Phys. Chem. Chem. Phys.* ***14,*** 1277–1285
32. Hicks, M. R., Kowałski, J., and Rodger, A. (2010) LD spectroscopy of natural and synthetic biomaterials. *Chem. Soc. Rev.* **39,** 3380–3393
33. Bulheller, B. M., Rodger, A., Hicks, M. R., Dafforn, T. R., Serpell, L. C., Marshall, K. E., Bromley, E. H., King, P. J., Channon, K. J., Woolfson, D. N., and Hirst, J. D. (2009) Flow linear dichroism of some prototypical proteins. *J. Am. Chem. Soc.* **131,** 13305–13314
34. Gazit, E., Lee, W. J., Brey, P. T., and Shai, Y. (1994) Mode of action of the antibacterial cecropin B2: a spectrofluorometric study. *Biochemistry* **33,** 10681–10692
35. Bonev, B. B., Chan, W. C., Bycroft, B. W., Roberts, G. C., and Watts, A. (2000) Interaction of the lantibiotic nisin with mixed lipid bilayers: a ^{31}P and ^{2}H NMR study. *Biochemistry* **39,** 11425–11433
36. Isono, F., Katayama, T., Inukai, M., and Haneishi, T. (1989) Mureidomycins A–D, novel peptidylnucleoside antibiotics with spheroplast forming activity. III. Biological properties. *J. Antibiot.* **42,** 674–679
37. Yeung, A. T., Gellatly, S. L., and Hancock, R. E. (2011) Multifunctional cationic host defence peptides and their clinical applications. *Cell Mol. Life Sci.* **68,** 2161–2176
38. Afacan, N. J., Yeung, A. T., Pena, O. M., and Hancock, R. E. (2012) Therapeutic potential of host defense peptide in antibiotic-resistant infections. *Curr. Pharm. Des.* **18,** 807–819

Nanoscale imaging reveals laterally expanding antimicrobial pores in lipid bilayers

Paulina D. Rakowska[a,b,1], Haibo Jiang[c,1], Santanu Ray[a,1], Alice Pyne[a,d], Baptiste Lamarre[a], Matthew Carr[e], Peter J. Judge[f], Jascindra Ravi[a], Ulla I. M. Gerling[g], Beate Koksch[g], Glenn J. Martyna[h], Bart W. Hoogenboom[d,i], Anthony Watts[f], Jason Crain[a,e], Chris R. M. Grovenor[c], and Maxim G. Ryadnov[a,e,2]

[a]National Physical Laboratory, Teddington TW11 0LW, United Kingdom; [b]Department of Chemistry, University College London, London WC1H 0AJ, United Kingdom; [c]Department of Materials, University of Oxford, Oxford OX1 3PH, United Kingdom; [d]London Centre for Nanotechnology, University College London, London WC1H 0AH, United Kingdom; [e]School of Physics and Astronomy, University of Edinburgh, Edinburgh EH9 3JZ, United Kingdom; [f]Department of Biochemistry, University of Oxford, Oxford OX1 3QU, United Kingdom; [g]Institut für Chemie und Biochemie, Freie Universität Berlin, 14195 Berlin, Germany; [h]IBM T. J. Watson Research Center, Yorktown Heights, NY 10598; and [i]Department of Physics and Astronomy, University College London, London WC1E 6BT, United Kingdom

Edited by Hiroshi Nikaido, University of California, Berkeley, CA, and approved April 16, 2013 (received for review January 2, 2013)

Antimicrobial peptides are postulated to disrupt microbial phospholipid membranes. The prevailing molecular model is based on the formation of stable or transient pores although the direct observation of the fundamental processes is lacking. By combining rational peptide design with topographical (atomic force microscopy) and chemical (nanoscale secondary ion mass spectrometry) imaging on the same samples, we show that pores formed by antimicrobial peptides in supported lipid bilayers are not necessarily limited to a particular diameter, nor they are transient, but can expand laterally at the nano-to-micrometer scale to the point of complete membrane disintegration. The results offer a mechanistic basis for membrane poration as a generic physicochemical process of cooperative and continuous peptide recruitment in the available phospholipid matrix.

innate host defense | de novo protein design | nanometrology | antibiotics | nanoscopy

Structurally compromised phospholipid membranes can lead to premature cell death, which is particularly critical for unicellular microorganisms (1, 2). Multicellular organisms take the full advantage of such vulnerability by using host defense or antimicrobial peptides (AMPs) (1–6). Although there are >1,000 AMPs known to date (7), only a few have been studied to expose the molecular mechanisms of action. The proposed barrel-stave pore (4, 8), torroidal pore (3), and carpet models (9) differ according to the ways in which AMPs interact within phospholipid bilayers, but all are believed to involve two distinct peptide–lipid states—an inactive surface-bound S-state and a pore-like insertion I-state (1, 10, 11). However, the link between these two states and membrane disintegration remains unresolved.

Despite their apparent diversity in structure and modes of action, AMPs share common features that make their modulation in model sequences possible. The peptides preferentially target anionic microbial surfaces, upon binding to which (S-state) they adopt amphipathic conformations by partitioning polar and hydrophobic amino acid side chains (2, 12, 13). Neutron diffraction and solid-state nuclear magnetic resonance (ssNMR) spectroscopy suggest that these conformations assemble into perpendicular stacks that close into the pore-like (I-state) structures (5, 11, 14). Here, positive curvature strains (15) and membrane thinning (16) are induced and may precede poration. In lipid vesicles (17, 18) and supported bilayers (16), kinetic studies imply the formation of transient pores (6), suggesting that antimicrobial peptides may expand through the monolayers of the lipid bilayers (15–18). Much research has focused on small and stabilized pores (5, 14, 15, 17). Growth arrest and uniform sizes of pores conform to the functional and structural rationale of specialized transmembrane proteins but may not be consistent with that of antimicrobial peptides.

Indeed, bacterial protein toxins such as α-hemolysins oligomerize into small 2- to 4-nm pores of defined structure, which is sufficient to cause the rapid discharge of vital resources (ions, ATP) from host cells (19, 20). Cell death in this case is a consequence, but not an aim. In contrast, AMPs are designed to kill microbial cells, not necessarily specifically (21), but rapidly within the time limits of their proteolytic stability. The behavior of other protein toxins is somewhat similar to these two scenarios. For example, perforins (22) that activate intrinsic suicide programs (apoptosis) of various cells, thus mediating cell lysis rather than causing it directly, use different avenues for membrane targeting and can form heterogeneous transmembrane pores (23). Heterogeneity in pore formation for AMPs may derive from the fact that, unlike the case of membrane proteins (24), there are no a priori topological constraints on assembled structures that the peptides must adopt in bilayers. Therefore, their pore sizes may be governed as much by progressive peptide aggregation as they are by local energetics. Because AMPs are typically cationic, free-energy changes in the edges of pores can be affected by peptide positions and local variations in the dielectric medium between peptide molecules, suggesting strong electrostatic repulsion. In this light, poration can be described as a physical phenomenon accommodating peptide diffusion in the membrane matrix with no strict predisposition for a particular pore size, but with sufficient freedom of movement for lateral expansion. To address this phenomenon in a sufficient molecular detail, the direct observation of pore architecture and dynamics is needed, but thus far has been lacking.

One reason for the lack of direct observation is the intrinsic complexity of imaging poration in live cells. Membrane binding of AMPs is kinetically driven and, in live cells, occurs over timescales of microseconds to minutes (2, 25). Pores need not expand substantially because cell death can occur concomitantly as a result of membrane leakage and swelling under osmotic pressure and because AMPs can reach and bind to intracellular targets or disrupt processes that are crucial to cell viability (protein, DNA, or cell-wall syntheses) within the same timescales (2, 25). Furthermore, microbial membranes are curved 3D architectures whose diameters do not exceed 2 μm. Pore formation in these membranes can cause significant variations in membrane tension, which can lead to

Author contributions: B.W.H., A.W., J.C., C.R.M.G., and M.G.R. designed research; P.D.R., H.J., S.R., A.P., B.L., M.C., P.J.J., J.R., U.I.M.G., and G.J.M. performed research; U.I.M.G. and B.K. contributed new reagents/analytic tools; P.D.R., H.J., S.R., A.P., B.L., M.C., P.J.J., J.R., B.K., G.J.M., B.W.H., A.W., J.C., C.R.M.G., and M.G.R. analyzed data; and M.G.R. wrote the paper.

The authors declare no conflict of interest.

This article is a PNAS Direct Submission.

Freely available online through the PNAS open access option.

[1]P.D.R., H.J., and S.R. contributed equally to this work.

[2]To whom correspondence should be addressed. E-mail: max.ryadnov@npl.co.uk.

This article contains supporting information online at www.pnas.org/lookup/suppl/doi:10.1073/pnas.1222824110/-/DCSupplemental.

"premature" membrane rupture before individual pores can expand substantially. A visible expansion in live cells depends on these interrelated factors, which makes its direct observation problematic.

In contrast, longer time and length scale studies are accessible in supported lipid bilayers (SLBs) (26). SLBs provide ideal experimental models for fluid-phase membranes and can be imaged by atomic force microscopy (AFM) (27, 28). Combining AFM with high-resolution secondary-ion mass spectrometry (SIMS), which has been shown to provide compositional chemical imaging of small lipid domains with lateral resolution of <100 nm (29), permits the detailed visualization of poration in SLBs.

To mitigate the complexities of direct live cell studies, we introduce and explore here a model system designed to expose the fundamental physicochemical processes relevant in the peptide–bilayer interactions. A model antimicrobial peptide, which combines main features of helical AMPs, was designed to integrate into SLBs that were then used as substrates for detailed nanoscale imaging and analysis by AFM and high resolution SIMS.

Results

To enable pore formation, a de novo amino acid sequence, KQKLAKLKAKLQKLKQKLAKL, dubbed amhelin (for "antimicrobial helix insert"), was generated as an archetypal model of transmembrane AMPs. The peptide comprises three *PPPHPPH* heptads, in which *P* is polar or small (alanine) and *H* is hydrophobic. This arrangement allows for the formation of a contiguous amphipathic helix in SLBs spanning ~3.15 nm (0.54 nm per turn) to match the bilayer thickness of ~3.2 nm (30, 31). The heptads in the sequence place *i* and *i* + 7 residues (32), which are of the same type, next to each other when viewed along the helical axis (Fig. 1*A* and Fig. S1). This order ensures the segregation of hydrophobic and polar residues onto distinct regions or faces, giving rise to an amphipathic helix. The hydrophobic face was kept short at the 1:1.5 ratio of hydrophobic (leucine) to cationic (lysine) residues to avoid hemolytic activities common for venom peptides that have broader hydrophobic clusters (4, 33). To support the ratio, small alanines and neutral glutamines, which do not contribute to membrane binding, were alternately arranged in the polar face as a neutral cluster opposite to the hydrophobic face (*SI Text*).

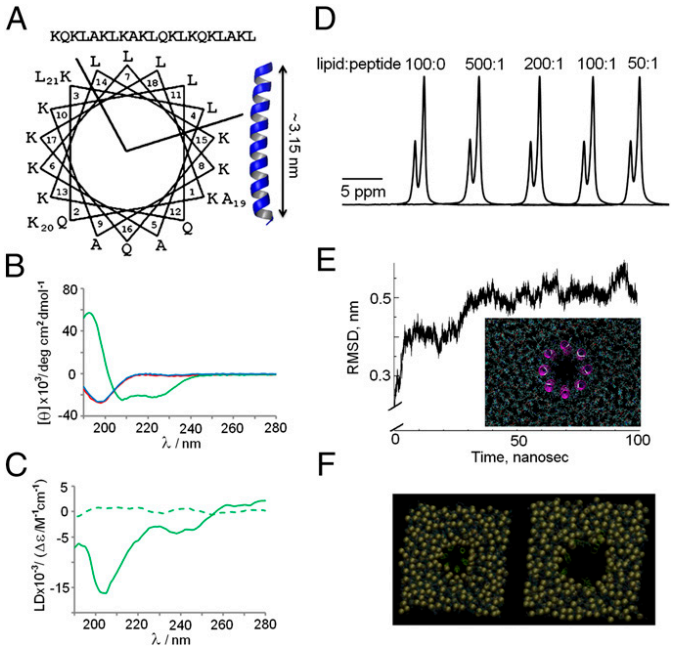

Fig. 1. Peptide design and folding. (*A*) Amhelin sequence, linear and on a helical wheel, and as an amphipathic helix spanning ~3.15 nm (in blue, 2ZTA PDB entry rendered with PyMoL). (*B*) CD spectra of amhelin (20 μM) in 10 mM phosphate buffer (red line), ZUVs (blue line), and AUVs (green line). (*C*) LD spectra of amhelin (solid line) and the non-AMP (dashed line) (both at 20 μM) in AUVs. (*D*) ^{31}P MAS ssNMR spectra of AUVs mixed with amhelin at different lipid–peptide ratios, –0.9 ppm (large peak) and 0.2 ppm (small peak) resonances arise from the PC and PG headgroups, respectively. (*E*) The rmsd for the molecular dynamics simulation of a model octameric amhelin pore (initial configuration in *Inset*) in an AUV bilayer. (*F*) Initial (*Left*) and later stage (*Right*) configurations of a model hexameric amhelin pore in the bilayer.

Peptide folding in solution was probed using zwitterionic unilamellar vesicles (ZUVs) and anionic unilamellar vesicles (AUVs) mimicking mammalian and microbial membranes, respectively (33, 34). Dilauroylphosphatidylcholine (DLPC) was used to assemble ZUVs whereas its mixtures with dilaurylphosphatidylglycerol (DLPG) at 3:1 ratios were used to assemble AUVs (30, 33). These lipid compositions yield fluid-phase membranes at room and physiological temperatures (27, 30, 31). Circular dichroism (CD) spectroscopy revealed that amhelin did not fold in aqueous buffers or in the presence of ZUVs at micromolar concentrations. In contrast, an appreciable helical signal was recorded for the peptide in AUV samples (Fig. 1*B*). Linear dichroism (LD) spectroscopy, which gives a convenient probe for relative peptide orientation in membranes, showed band patterns comprising maxima at 190–195 nm and 220–230 nm, and a minimum at 205–210 nm, which are indicative of peptide insertion into AUVs in a transmembrane manner (Fig. 1*C*) (35). In contrast, no signal was observed for a designed non-AMP, which cannot bind and order in membranes (Fig. 1*C*) (33). ^{31}P magic angle spinning ssNMR (MAS ssNMR) spectra of AUV mixed with amhelin revealed increasing broadening of phospholipid peaks as a function of decreasing lipid–peptide ratios (Fig. 1*D*). This broadening effect relates to an increase in line width caused by a decrease in the T2 relaxation time (36), which corresponds to an increase in correlation time of the phospholipid groups. This increase suggests a decrease in motion of phospholipid groups in contact with the peptide, which is more pronounced at higher peptide concentrations and is more noticeable in thicker membranes (Fig. S1). Taken together, the data is consistent with a transmembrane insertion of the peptide.

Early oligomers of helical inserts are believed to arrange into small pores whose projections can be obtained by crystallizing peptide–lipid assemblies in fluid bilayers as a function of hydration and temperature (14). Diffraction patterns of such assemblies show regular hexagonal arrays of pores comprising just a few helices. To probe the dynamics of poration and expansion, amhelin inserts in AUVs were explored with molecular dynamics simulations using the Chemistry at HARvard Macromolecular Mechanics (CHARMM)36 force field (37). Amhelin helices remained stable with slightly tilted orientations over timescales of 100 ns whereas rudimentary hexameric and octameric pores constructed in the bilayers expanded with the root-mean-square displacement (rmsd) separations doubling in diameter over timescales of order 100 ns (Fig. 1 *E* and *F* and Movies S1 and S2). These results imply that early oligomers have a tendency for expansion, which may occur at the expense of further peptide recruitment in the pores.

Consistent with the folding and simulation data, amhelin exhibited antimicrobial activity with minimum inhibitory concentrations typical of AMPs, while showing negligible hemolytic activity (Table S1 and Fig. S2) (1, 2, 12, 21). AFM revealed the surface corrugation of amhelin-treated bacterial cells (*Escherichia coli*) (Fig. S2). The analysis of pore-like structures was deemed ambiguous due to the considerable roughness of the cell surfaces (Fig. S2) (25). A comparative analysis was performed on SLBs prepared by the surface deposition of AUV in aqueous solution using adapted protocols (26, 29). Silicon wafers used as substrates were coated with a 9-nm layer of silicon dioxide to (*i*) support

homogeneous and stable bilayers maintained in the fluid phase at room temperature and (*ii*) avoid charge build-up during SIMS measurements, which is necessary as SIMS relies on the detection of secondary ions extracted from the surface by a focused beam of primary ions ($^{133}Cs^{+}$) rastered across the sample (29).

The SLB samples were incubated with solutions containing amhelin, which was ^{15}N-labeled at all alanine and leucine residues and washed to remove excess peptide. To arrest poration and preserve structural changes in the membrane, the hydrated samples were then rapidly frozen and freeze-dried (29). Secondary ion images of the $^{12}C^{14}N^{-}$ and $^{12}C^{15}N^{-}$ signals, which are commonly used in imaging SIMS experiments of biological materials (38), revealed pores of varied forms and sizes supporting the conjecture of pore expansion across the whole scanned area (Fig. 2*A* and Fig. S3).

In these samples, we expect a higher signal intensity from regions of the surface rich in peptide because each unlabeled residue in amhelin contributes to $^{12}C^{14}N^{-}$, but the $^{12}C^{15}N^{-}$ signals will come predominantly from the labeled residues. Thus, SIMS images have a strong degree of component specificity providing direct evidence for the location of the peptide, which prompts the conclusion that the observed pores are peptide-specific. The conclusion was reinforced by the images of the $^{12}C^{15}N^{-}/^{12}C^{14}N^{-}$ ratio and hue saturation intensity (HSI) images (Fig. 2*B* and Fig. S3). Complementary images of control samples (bare and non-AMP-treated SLBs and bare and amhelin-treated silicon wafer substrates) were featureless (Fig. 2*C* and Figs. S4 and S5).

Firstly, all these images suggest that the interior of the pores in the amhelin-exposed samples is completely free of peptide, as are the control samples, as expected. Secondly, $^{12}C^{15}N^{-}/^{12}C^{14}N^{-}$ ratios far above natural abundance values (0.37%) are recorded from the surface of the sample away from the pores and are particularly evident at the edges of the pores, where the peptide content appears to be highest (40%) and increases with increasing pore sizes (Fig. 2*B*). Thirdly, high peptide accumulations can be seen running across the NanoSIMS images, presumably pore-connecting ridges that are spread across the imaged area suggesting peptide migration dynamics (Fig. 2 *A* and *B* and Fig. S3).

It should be emphasized here that SIMS measurements relate to the chemical composition of the surface with only a minor contribution from topography. Therefore, AFM measurements on the same samples were performed to support the SIMS data (Fig. 3). AFM-scanned pore sizes revealed that the pore edges protruded from the surface to the heights of ~4 nm (Fig. 3*A*). The long axis of the peptide can account for ~3.2 nm whereas the remaining is consistent with the size of a lipid head group (Fig. 3*B*). Although other explanations are possible, the height difference could be interpreted as due to a staggered arrangement of the peptides at the pore edges, with every other peptide being shifted slightly upward, while retaining their roughly vertical alignment on the edge (4, 5) and maximizing the contact with the hydrophic lipid tails (Fig. 3*B*). In addition, small white-dot deposits observed predominantly inside the pores and on their edges are most likely due to the aggregation of peptide–lipid material ejected from the membrane. These observations altogether (*i*) suggest that the peptide incorporates into the bilayer by distorting and partially displacing the lipids of the outer leaflet and (*ii*) imply an efficient migration mode of lipid–peptide assemblies through fluidic pores and ridges in a highly cooperative manner.

An intriguing question provoked by the observations is the peaking of pore edges. Although the heights of the edges were fairly consistent, the depth values of the perforations could not be determined reliably. The holes would appear as deep as ~2 nm in relation to the surrounding surfaces, but an explicit cross-section analysis was hampered by high noise levels from the surfaces in the 1- to 2-nm range. The peaking itself may become negligible under equilibrium conditions at which outer leaflet lipids detach irreversibly and too fast to be observed without deliberately arresting the system by freezing. An insight into this scenario can be obtained only in solution.

Therefore, we monitored real-time changes of SLBs incubated with amhelin by time-lapse AFM in water (25). Amhelin solution at low concentration was directly introduced into a liquid cell that contained an AUV lipid bilayer assembled on flat mica. After the first 10 min of incubation, small pores started forming on the surface and continued to grow in size and numbers over the period of 2 h, culminating in the total removal of the lipid from the mica surface (Fig. 4*A*). The lipids are likely to dissolve in the form of micelles, possibly including peptides. On removal of larger amounts of the SLB, material increasingly precipitates on the surface (Fig. 4*A* and Fig. S6). As expected, the pores appeared as

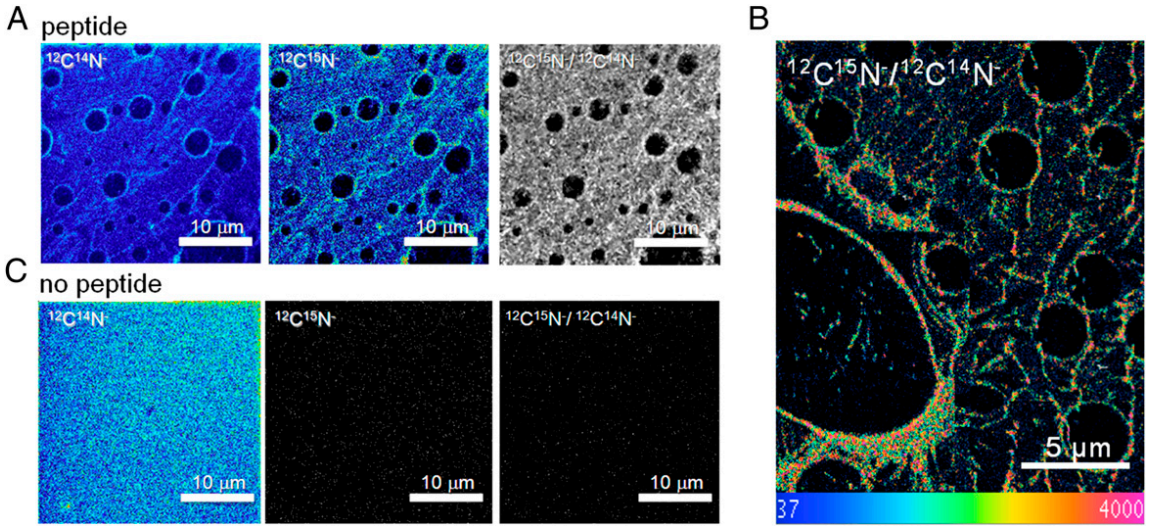

Fig. 2. SIMS analysis of amhelin-treated supported lipid bilayers. (*A*) SIMS images of $^{12}C^{14}N^{-}$, $^{12}C^{15}N^{-}$, and $^{12}C^{15}N^{-}/^{12}C^{14}N^{-}$ signals from the supported lipid bilayers treated with the isotopically labeled peptide. (*B*) $^{12}C^{15}N^{-}/^{12}C^{14}N^{-}$ ratio expressed as HSI images. The rainbow scale changes from blue (natural abundance ratio of 0.37%) to red (40%, >100 times the natural ratio). This image is the sum of several sequential images to enhance the statistical significance of the measured ratios. (*C*) SIMS images of $^{12}C^{14}N^{-}$, $^{12}C^{15}N^{-}$, and $^{12}C^{15}N^{-}/^{12}C^{14}N^{-}$ signals from the supported lipid bilayers with no peptide. Incubation conditions: 10 μM, pH 7.4, 20 °C.

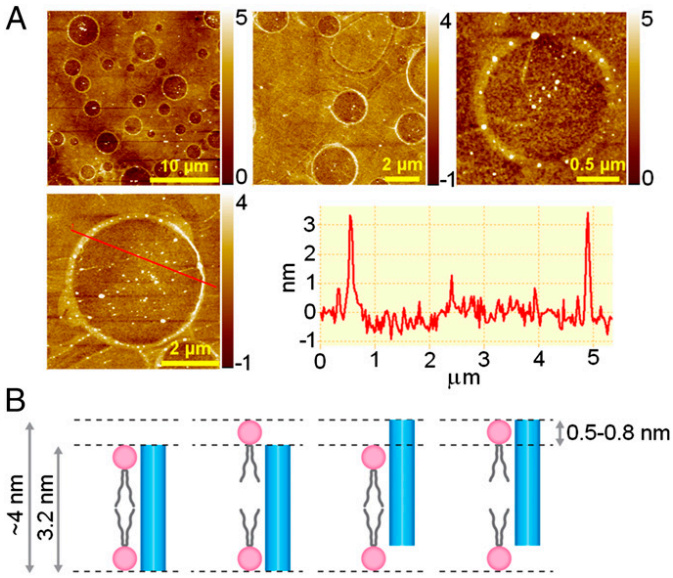

Fig. 3. Amhelin-treated supported lipid bilayers. (*A*) In-air AFM topographic images with a cross-section along the highlight line. (*B*) Schematic representation of pore edges showing the thickness of the SLB (3.2 nm), the maximum observed height (4 nm), and the difference between the two (0.5–0.8 nm) accounted for by possible protrusion variants, three shown. For clarity, only one peptide (blue cylinder) and one phospholipid per layer are shown (aliphatic chains in gray, headgroups in pink). Incubation conditions: 10 μM, pH 7.4, 20 °C.

expanding holes, suggesting the displacement of outer lipids from the surface into the water, which is characteristic of equilibrated systems (17). The depths of perforations reached ~2.7 nm, conforming to the amhelin spanning the bound hydrophobic core of the bilayer (Fig. 4*B*). Similar real-time changes were observed for another amphipathic AMP (AMP2) whose pore expansion in SLBs provides an additional example (Figs. S1 and S6).

Discussion

Collectively our findings provide evidence for pore expansion, or an E-state, of amphipathic antimicrobial peptides in lipid bilayers (Fig. 5). The E-state promotes cooperative peptide migration through the lipid matrix and can persist to complete membrane disintegration. Our proposed model of pore expansion is the synergistic interplay of two physical processes.

In the first, peptide adsorption induces surface tension on membrane surfaces, which, when sufficiently large, leads to poration. The pore formation promotes peptide migration from the surface to the edges of the pores. This variation of surface tension with composition (Gibbs surface excess) is driven by amphipathic peptides having higher affinity to the membrane edges (3, 4). The process is likely to reduce the tension between peptide and lipid bilayers, thereby stabilizing the formed pores. However, it is challenged by strong electrostatic repulsion between inserted helices in the pore edges (3, 4). In live cells, this conflict can be avoided both because excess peptide on cell membranes can migrate through small pores directly into the cytoplasm targeting intracellular components and because continuous peptide incorporation and diffusion in lipid bilayers can be preempted by membrane swelling (6, 12, 22). For flat and extended 2D lipid matrices, pore expansion is more thermodynamically favorable and is determined by both incorporation and repulsion of peptides to the pore edges. In this way, inserting helices can be viewed as charged equipotential surfaces with a degree of translational freedom (4, 14) conforming to toroidal type poration, which is characterized by shallow energy minima leading to substantial variations in pore sizes (4, 6, 18).

Pores of 10 μm in size can be physically generated in giant unilamellar vesicles (100 μm in diameter) by strong optical illumination in a viscous medium (39). The edges of the generated pores make up a "line" of lipid bilayer edges that, unless stabilized or expanded, reseal due to the line tension (17, 18). Detergent molecules (e.g., Tween 20) can reduce the tension and partially stabilize the line (17, 39) but cannot fold and propagate. Instead, they form micellar aggregates above a critical concentration. In contrast, antimicrobial peptides become amphipathic only upon folding, which, in conjunction with sustained hydrophobic and electrostatic interactions, enables their progressive self-assembly in lipid bilayers. Pore expansion is also different from mechanisms of fusion and transmembrane proteins whose conserved topologies impose specific self-assembly modes and pore architectures (22). For example, HIV glycoprotein 41 (gp41) controls each step in fusion, including pore nucleation, through a sequence of highly specialized conformations rendering the dimensions and lifetime of induced pores precisely optimized for viral entry.

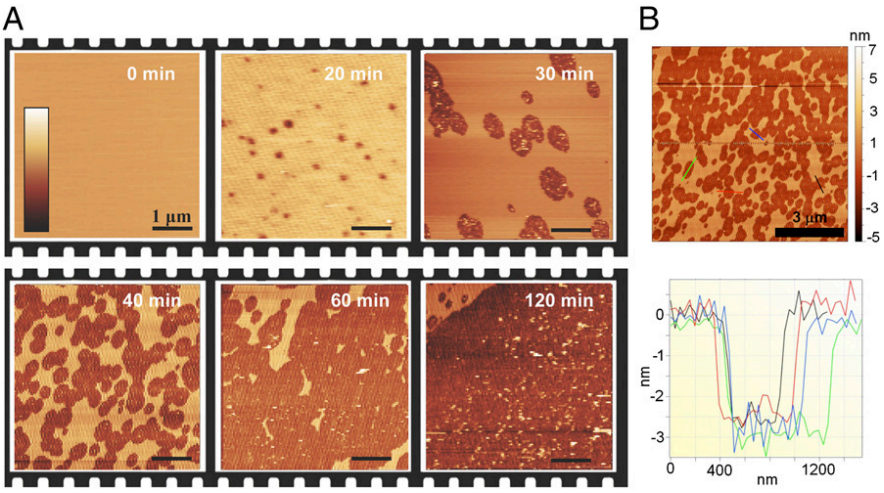

Fig. 4. In-water AFM imaging of amhelin-treated supported lipid bilayers. (*A*) Topography of supported lipid bilayers during incubation with amhelin. Color scale (see *Inset*, 0 min): 3 nm (0–20 min); 9 nm (30–120 min). (*B*) Topography image after 40 min incubation with cross-sections along the highlighted lines. Incubation conditions: 0.5 μM, pH 7.4, 20 °C.

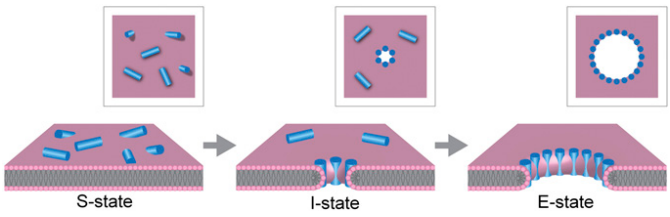

Fig. 5. Proposed pore expansion mechanism for amphipathic antimicrobial peptides. Antimicrobial peptides (blue cylinders) bind to the surface of the membrane (S-state), insert into lipid bilayers forming pores (I-state), which can then expand indefinitely (E-state).

Thus, our findings support the biological rationale of antimicrobial peptides as nonspecific and fast-reacting molecules that target microbial membranes and whose action depends on concentration and matrix availability rather than on pore uniformity and global structural parameters such as folding topology.

Materials and Methods

Peptide Design and Synthesis. Amhelin and a non-AMP control, QIAALEQEIAALEQEIAALQ and AMP2 were designed, synthesized, and characterized according to protocols published elsewhere (33) (*SI Materials and Methods*). ^{15}N-amhelin labeled at all alanine and leucine residues was purchased from AnaSpec. All peptides were identified by reverse phase high performance liquid chromatography (RP-HPLC) and MALDI-TOF mass spectrometry. MS $[M+H]^+$: amhelin, *m/z* 2448.2 (calculated), 2447.7 (found); non-AMP, *m/z* 2152.4 (calculated), 2152.4 (found); ^{15}N-amhelin, *m/z* 2458.2 (calculated), 2458.1 (found); AMP2, *m/z* 2319.1 (calculated), 2320.1 (found). $[M+Na]^+$ and $[M+K]^+$ were also found.

Circular and Linear Dichroism Spectroscopy. All CD spectra were recorded on a JASCO J-810 spectropolarimeter fitted with a Peltiertemperature controller. All measurements were taken in ellipticities in mdeg and converted to molar ellipticities ([θ], deg $cm^2 \cdot dmol^{-1}$) by normalizing for the concentration of peptide bonds. Aqueous peptide solutions (300 μL, 20 μM) were prepared in filtered (0.22 μm) 10 mM phosphate buffer, pH 7.4. CD spectra recorded in the presence of synthetic membranes are for lipid:peptide molar ratio of 100:1. Solution-phase flow LD spectra were recorded on a Jasco-810 spectropolarimeter using a photo-elastic modulator 1/2 wave plate, and a microvolume quartz cuvette flow cell with ∼0.25 mm annular gap and quartz capillaries (all from Kromatec). Molecular alignment was achieved through the constant flow of the sample solution between two coaxial cylinders—a stationary quartz rod and a rotating cylindrical capillary. LD spectra were acquired with laminar flow obtained by maintaining a cell rotation speed of 3,000 rpm and processed by subtracting nonrotating baseline spectra. LD spectra recorded in the presence of synthetic membranes were prepared at a lipid:peptide molar ratio of 100:1 (2 mM total lipid, 20 μM peptide).

Solid-State NMR Spectroscopy. ssNMR experiments were carried out on a Varian Infinityplus 500 MHz spectrometer equipped with a 4 mm MAS triple resonance (HXY) probe at 30 °C. ^{31}P ssNMR spectra were acquired at 202 MHz. A single 4 μs 90° pulse was used to excite directly the ^{31}P nuclei, and broadband proton decoupling of 20 kHz was applied during the acquisition period. Samples were rotated at 8 kHz MAS at 20 °C. The 8k scans were collected, and the pulse delay was 4 s. Spectra were referenced to $NH_4H_2PO_4$.

Molecular Dynamics Simulations. Molecular dynamics simulations were performed using the CHARMM36 force field using chloride counter ions for charge neutralization. The initial helical configuration was obtained using the XPlor-NIH structure determination algorithm (http://nmr.cit.nih.gov/xplor-nih/). DLPC/DLPG (3:1) membranes were constructed with dimensions of 12 × 12nm and simulated with a semiisotopic moles, pressure, temperature (NPT) ensemble with equilibrations of 20 ns. Production runs were then performed for ∼100 ns.

In-Air Atomic Force Microscopy Imaging. Topographic, amplitude, and phase AFM images were recorded using tapping mode AFM on an MFP-3D Asylum AFM instrument (for imaging bacteria) and on a Cypher Instrument (Asylum Research) (for imaging supported lipid bilayers). All AFM images were flattened with a first-order line-wise correction fit. AFM tips used were supersharp silicon probes (Nanosensors; resonant frequency ∼330 kHz, tip radius of curvature <5 nm, force constant 42 N/m). Images were processed using proprietary SPIP software, version 5.1.3.

In-Water Atomic Force Microscopy Imaging. Topographic images of supported lipid bilayers in liquid were recorded in contact mode on a JPKNanoWizard I AFM, mounted on an Olympus IX71 inverted optical microscope, as well as in tapping mode on the Asylum Cypher mentioned above. The AFM probes used for all experiments in liquid were MSNL Silicon Nitride probes with spring constants of 0.005–0.03 N/m (Bruker AFM probes) for contact mode imaging, and Olympus BL-AC40 (∼0.1 N/m, Olympus) for tapping mode. Images were processed using Gwyddion (http://gwyddion.net) first-order line-wise flattening and cross-section measurements.

High Resolution Secondary Ion Mass Spectrometry. SIMS images of chemical and isotopic distributions were acquired on a CAMECA NanoSIMS 50 with lateral resolution down to 50 nm. The instrument uses a 16 keV primary $^{133}Cs^+$ beam to bombard the sample surface and collects five selected secondary negative ions using a Mauttach–Herzog mass analyzer with electrostatic sector and asymmetric magnet configuration. $^{12}C^{14}N^-$ and $^{12}C^{15}N^-$ secondary ions were collected. Three of the following signals were also recorded simultaneously to give information on sample morphology: $^{12}C^-$, $^{13}C^-$, $^{16}O^-$ and $^{31}P^-$. The ratio images ($^{12}C^{15}N^-/^{12}C^{14}N^-$) (30 by 30 μm, 256 by 256 pixels) were collected with a large primary aperture to match the pixel size in the images with the incident ion beam diameter (∼120 nm). A smaller primary aperture was used to achieve higher lateral resolution images (10 by 10 μm). The data were collected without preliminary $^{133}Cs^+$ implantation to avoid sputtering away the thin samples. The images were calculated and processed using OpenMIMS software (MIMS, Harvard University; www.nrims.harvard.edu), were multiplied by a scale factor 10,000, and processed by a median filter with one pixel radius. Ratios of the control samples were calculated as: ratio = $^{12}C^{15}N^-/(^{12}C^{14}N^- + ^{12}C^{15}N^-) \times 100\%$.

ACKNOWLEDGMENTS. We thank Ian Gilmore and Alex Shard for their advice and support for the work. We acknowledge funding from the United Kingdom's Department of Business, Innovation and Skills, European Metrology Research Programme Grant HLT10, the Strategic Research Programme of the National Physical Laboratory, the Scottish Universities Physics Alliance, IBM Research, Biotechnology and Biological Sciences Research Council Grant BB/G011729/1 (to B.W.H.), Engineering and Physical Sciences Research Council Grants EP/I029443/1 (to J.C.), EP/I029516/1 (to A.W. and P.J.J.), and EP/G036675/1 (to B.W.H. and A.P.), and a Chinese Scholarship Council Research Scholarship (to H.J.).

1. Zasloff M (2002) Antimicrobial peptides of multicellular organisms. *Nature* 415(6870): 389–395.
2. Fjell CD, Hiss JA, Hancock REW, Schneider G (2012) Designing antimicrobial peptides: Form follows function. *Nat Rev Drug Discov* 11(1):37–51.
3. Matsuzaki K, Murase O, Fujii N, Miyajima K (1996) An antimicrobial peptide, magainin 2, induced rapid flip-flop of phospholipids coupled with pore formation and peptide translocation. *Biochemistry* 35(35):11361–11368.
4. Yang L, Harroun TA, Weiss TM, Ding L, Huang HW (2001) Barrel-stave model or toroidal model? A case study on melittin pores. *Biophys J* 81(3):1475–1485.
5. Qian S, Wang W, Yang L, Huang HW (2008) Structure of transmembrane pore induced by Bax-derived peptide: evidence for lipidic pores. *Proc Natl Acad Sci USA* 105(45): 17379–17383.
6. Matsuzaki K, Yoneyama S, Miyajima K (1997) Pore formation and translocation of melittin. *Biophys J* 73(2):831–838.
7. Fjell CD, Hancock REW, Cherkasov A (2007) AMPer: A database and an automated discovery tool for antimicrobial peptides. *Bioinformatics* 23(9):1148–1155.
8. He K, Ludtke SJ, Worcester DL, Huang HW (1996) Neutron scattering in the plane of membranes: Structure of alamethicin pores. *Biophys J* 70(6):2659–2666.
9. Pouny Y, Rapaport D, Mor A, Nicolas P, Shai Y (1992) Interaction of antimicrobial dermaseptin and its fluorescently labeled analogues with phospholipid membranes. *Biochemistry* 31(49):12416–12423.
10. Huang HW (2000) Action of antimicrobial peptides: Two-state model. *Biochemistry* 39(29):8347–8352.
11. Mani R, et al. (2006) Membrane-dependent oligomeric structure and pore formation of a β-hairpin antimicrobial peptide in lipid bilayers from solid-state NMR. *Proc Natl Acad Sci USA* 103(44):16242–16247.
12. Schmitt MA, Weisblum B, Gellman SH (2007) Interplay among folding, sequence, and lipophilicity in the antibacterial and hemolytic activities of α/β-peptides. *J Am Chem Soc* 129(2):417–428.
13. Sinthuvanich C, et al. (2012) Anticancer β-hairpin peptides: Membrane-induced folding triggers activity. *J Am Chem Soc* 134(14):6210–6217.

14. Yang L, Weiss TM, Lehrer RI, Huang HW (2000) Crystallization of antimicrobial pores in membranes: Magainin and protegrin. *Biophys J* 79(4):2002–2009.
15. Hallock KJ, Lee D-K, Ramamoorthy A (2003) MSI-78, an analogue of the magainin antimicrobial peptides, disrupts lipid bilayer structure via positive curvature strain. *Biophys J* 84(5):3052–3060.
16. Mecke A, Lee D-K, Ramamoorthy A, Orr BG, Banaszak Holl MM (2005) Membrane thinning due to antimicrobial peptide binding: An atomic force microscopy study of MSI-78 in lipid bilayers. *Biophys J* 89(6):4043–4050.
17. Lee M-T, Hung W-C, Chen F-Y, Huang HW (2008) Mechanism and kinetics of pore formation in membranes by water-soluble amphipathic peptides. *Proc Natl Acad Sci USA* 105(13):5087–5092.
18. Yu Y, Vroman JA, Bae SC, Granick S (2010) Vesicle budding induced by a pore-forming peptide. *J Am Chem Soc* 132(1):195–201.
19. Fang Y, Cheley S, Bayley H, Yang J (1997) The heptameric prepore of a staphylococcal α-hemolysin mutant in lipid bilayers imaged by atomic force microscopy. *Biochemistry* 36(31):9518–9522.
20. Song L, et al. (1996) Structure of staphylococcal α-hemolysin, a heptameric transmembrane pore. *Science* 274(5294):1859–1866.
21. Shai Y (2002) Mode of action of membrane active antimicrobial peptides. *Biopolymers* 66(4):236–248.
22. Law RHP, et al. (2010) The structural basis for membrane binding and pore formation by lymphocyte perforin. *Nature* 468(7322):447–451.
23. Praper T, et al. (2011) Human perforin employs different avenues to damage membranes. *J Biol Chem* 286(4):2946–2955.
24. Shea J-E, Onuchic JN, Brooks CL, 3rd (1999) Exploring the origins of topological frustration: design of a minimally frustrated model of fragment B of protein A. *Proc Natl Acad Sci USA* 96(22):12512–12517.
25. Fantner GE, Barbero RJ, Gray DS, Belcher AM (2010) Kinetics of antimicrobial peptide activity measured on individual bacterial cells using high-speed atomic force microscopy. *Nat Nanotechnol* 5(4):280–285.
26. Mingeot-Leclercq M-P, Deleu M, Brasseur R, Dufrêne YF (2008) Atomic force microscopy of supported lipid bilayers. *Nat Protoc* 3(10):1654–1659.
27. Lin W-C, Blanchette CD, Ratto TV, Longo ML (2006) Lipid asymmetry in DLPC/DSPC-supported lipid bilayers: A combined AFM and fluorescence microscopy study. *Biophys J* 90(1):228–237.
28. Dufrêne YF (2004) Using nanotechniques to explore microbial surfaces. *Nat Rev Microbiol* 2(6):451–460.
29. Kraft ML, Weber PK, Longo ML, Hutcheon ID, Boxer SG (2006) Phase separation of lipid membranes analyzed with high-resolution secondary ion mass spectrometry. *Science* 313(5795):1948–1951.
30. Leckband DE, Helm CA, Israelachvili J (1993) Role of calcium in the adhesion and fusion of bilayers. *Biochemistry* 32(4):1127–1140.
31. Kučerka N, et al. (2005) Structure of fully hydrated fluid phase DMPC and DLPC lipid bilayers using X-ray scattering from oriented multilamellar arrays and from unilamellar vesicles. *Biophys J* 88(4):2626–2637.
32. Akerfeldt KS, Lear JD, Wasserman ZR, Chung LA, DeGrado WF (1993) Synthetic peptides as models for ion channel proteins. *Acc Chem Res* 26(4):191–197.
33. Ryadnov MG, Mukamolova GV, Hawrani AS, Spencer J, Platt R (2009) RE coil: An antimicrobial peptide regulator. *Angew Chem Int Ed Engl* 48(51):9676–9679.
34. Nomura K, et al. (2005) Induction of morphological changes in model lipid membranes and the mechanism of membrane disruption by a large scorpion-derived pore-forming peptide. *Biophys J* 89(6):4067–4080.
35. Hicks MR, Kowałski J, Rodger A (2010) LD spectroscopy of natural and synthetic biomaterials. *Chem Soc Rev* 39(9):3380–3393.
36. Yeagle PL (1990) *Phosphorus NMR of Membranes* (Plenum, New York).
37. Klauda JB, et al. (2010) Update of the CHARMM all-atom additive force field for lipids: Validation on six lipid types. *J Phys Chem B* 114(23):7830–7843.
38. Moore KL, Schröder M, Grovenor CRM (2012) Imaging secondary ion mass spectroscopy. *Handbook of Nanoscopy* (Wiley-VCH, Weinheim, Germany), pp 709–744.
39. Sandre O, Moreaux L, Brochard-Wyart F (1999) Dynamics of transient pores in stretched vesicles. *Proc Natl Acad Sci USA* 96(19):10591–10596.